The Role of Cyclic Nucleotide Signalling in *L. mexicana* Flagellar Motility

A thesis submitted for the degree of
Doctor of Philosophy at the University of Oxford

Sophia Fochler

Sir William Dunn School of Pathology | University of Oxford | Lincoln College
2018 – 2022 Michaelmas Term

Acknowledgements

This thesis would not have been possible without my supervisor, Eva Gluenz. I am certain no one else could have given me such a perfect balance of freedom and support to explore the themes of this thesis venture, be it in Oxford or Glasgow! Thank you Eva, there is not a moment I would change. A big shout out to the Sir William Dunn School of Pathology, including Matthew Freeman, Rita, Samantha and Phil. You all made the Dunn School feel like a home away from home for me. Thanks to my wonderful colleagues over the years, especially James, Andreia, Ciaran, Matthew and Tom, and all passing visitors and students for making the lab a light-hearted and safe place to handle the excitement and dread of experimental research. Thanks to my wonderful collaborators in the Wheeler Lab, Cecile and Richard without whom I would not have a Chapter 4. A massive thank you to all the past members of the Gull lab in Oxford, (especially Amy, Sam and Helen) and members of the Hammarton and McCulloch Labs in Glasgow (especially Jessie, Olu, Jane, Cat, and Jeziel) who made me feel very welcome and never fell short on time to help or have a pint down the pub. Last of all, a huge thank you to my glorious mother, Uschi, who sat and read through this thesis, correcting my frequent tendencies to spell words my own way, and eccentric father, Graham, who provided endless opportunities and excuses to escape from the thesis and explore the Cornish coastal creeks.

1. Table of Contents

ACKNOWLEDGEMENTS I

LIST OF FIGURES VI

LIST OF TABLES IX

ACRONYMS AND ABBREVIATIONS X

DECLARATIONS XIII

1. INTRODUCTION 2

1.1. EUKARYOTIC FLAGELLAR BIOLOGY 2

1.1.1. Motile flagella and cilia 2

1.1.1.1. Ultrastructure 3

1.1.1.2. Flagellar and ciliary waveforms 9

1.1.2. Essential axonemal structures and dynein contribution 12

1.1.3. Models for spatiotemporal dynein regulation 16

1.1.4. Second messengers contribute to flagellar beat regulation 19

1.2. CYCLIC AMP IN KINETOPLASTID SPECIES 21

1.2.1. Classical cAMP signalling pathway 21

1.2.2. Divergent cAMP signalling pathway in kinetoplastid species 23

1.3. PROPOSED ROLES FOR CAMP IN THE DIGENETIC LIVES OF KINETOPLASTIDS 25

1.3.1. Lifecycle of kinetoplastid species 25

1.3.1.1. Flagellar motility 27

1.3.1.2. Immunomodulation 31

1.3.1.3. Osmoregulation 31

1.3.1.4. Targets for Trypanocidal drugs 32

1.3.1.5. Differentiation 35

1.4. PROJECT APPROACH 38

1.4.1. Aims, strategy and rationale 38

2. CAMP CONTRIBUTES TO FLAGELLUM BEAT DIRECTION AND POPULATION SWIM SPEED VIA AXONEMAL CARP1 43

2.1. INTRODUCTION 43

2.2. RESULTS 45

2.2.1. The Leishmania mexicana genome encodes 35 putative cyclic nucleotide signalling components 45

2.2.1.1. L. mexicana genomes encode a highly divergent set of cyclic nucleotide transducers 52

2.2.2. Fluorescent tagging libraries revealed cAMP signalling is confined to precise sub-cellular domains 62

2.2.2.1. Six of the seven phosphodiesterase are detectable in the flagellum 63
2.2.2.2. Leishmania adenylate cyclase are predominantly flagellar tip enriched 66
2.2.2.3. Over half of the putative cyclic nucleotide transducers were detectable in the flagellum 68
2.2.2.4. CARP1 is embedded in the flagellar axoneme, but localisation is not dependent on components of the radial spokes, outer dynein arms, inner dynein arms, central pair, or nexin dynein regulatory complex. 74
2.2.2.5. Corroboration of tagging localisations through comparison with published proteome data. 78
2.2.3. A null mutant library demonstrated that cyclic nucleotide signalling components within the flagellum can increase as well as decrease parasite swim speed 81
2.2.3.1. Nearly half of the null mutant from our library swam significantly different to the parental control 84
2.2.3.2. Change in population swim speed is attributable to altered proportions of cells propagating forward motility and changes in beat frequency 89
2.2.3.3. Dissection of flagellar beating parameters suggests cAMP contributes to beat frequency but not amplitude 94
2.2.3.4. Deletion of flagellar localised PDE A, but not PDE D or B2, can rescue the slow swimming phenotype of ΔRAC-a 96
2.2.4. Pharmacological manipulation and genetic rescue of ΔRAC-a slow swimming phenotype corroborates a role in speed modulation 99
2.2.4.1. Pharmacological rescue of slow swimming ΔRAC-a.....104
2.3. DISCUSSION 106
2.3.1. Limitations of techniques and proposed next experiments.....106
2.3.1.1. Only one to four predicted cAMP transducers encoded in the L. mexicana genome.....106
2.3.1.2. Residues of the phosphate binding cassette are (almost) invariable throughout diverse CNBD containing proteins 109
2.3.1.3. Endogenous fluorescent tagging of putative cyclic nucleotide signalling components was successful in establishing likely signalling microdomains.....111
2.3.1.4. The unknown localisation of axonemal CARP1 113
2.3.1.5. Motility phenotypes in the null mutant library.....115
2.3.2. Proposing a model for cAMP modulation of flagellar motility.....119

3. AN ESSENTIAL ROLE FOR DIVERGENT PKA IN FORWARD MOTILITY 126

3.1. INTRODUCTION.....126
3.2. RESULTS.....131
3.2.1. The genome of Leishmania spp encode two divergent regulatory and three catalytic PKA subunits.....131

3.2.2. L. mexicana PKACs and PKARs show distinct localisation patterns in the flagellar axoneme, nucleus and cell body cortex *141*
3.2.3. Localisation dependencies *148*
3.2.4. Toyocamycin and inosine exposure dissociates PKAC1 signal from the axonemal cytoskeleton *152*
3.2.5. PKAC1 is essential for forward motility of parasites *155*
3.2.6. All PKAC subunits contribute in different ways to beat amplitude and frequency *158*
3.3. DISCUSSION 166

4. THE OUTER DYNEIN ARMS ARE NEEDED FOR DIRECTIONAL CELL MOTILITY 172

4.1. INTRODUCTION 172
4.2. RESULTS 177
4.2.1. Selection of proteins for functional interrogation *177*
4.2.1.1. Identification of axonemal dyneins in L. mexicana 177
4.2.1.2. Selection of non-dynein axonemal proteins included in the mutant analysis 184
4.2.2. The double headed dynein heavy chains of the ODA and IDA are both necessary for forward motility *186*
4.2.2.1. Population overview waveform analysis 186
4.2.2.2. Flagellum length and curling propensity 187
4.2.2.3. Mutant population displacement fitness 192
4.2.3. Flagellar waveform parameters *196*
4.2.3.1. ODA deficiency causes reduced dominant beat frequency and elevated beat amplitude 196
4.2.3.2. Single headed IDA dynein IDA5c contributes to beat frequency only, whilst IDA3, IDA4b and IDA5b contribute to angular amplitude only 199
4.2.3.3. Rare propagation of rhythmic tip-to-base flagellar movement by ΔIDAα and ΔIDAβ cells when unhindered by flagellar curl 201
4.3. DISCUSSION 204

5. MATERIALS AND METHODS 210

5.1. CELL CULTURING, MUTANT PRODUCTION AND GENOTYPE VERIFICATION 210
5.1.1. Cell culturing *210*
5.1.2. PCR based gene knockout validation *211*
5.2. MICROSCOPY 213
5.2.1. Fluorescence microscopy of live cells *213*
5.2.2. Imaging axenic amastigotes *213*
5.2.3. Cytoskeleton preparation in a tube *214*
5.2.4. Salt extraction of cytoskeletons settled on a slide *214*

5.3. WAVEFORM ANALYSIS 215
5.3.1. Population Overview Waveform analysis (POWA) *215*
5.3.2. High Speed Video Microscopy *216*
5.4. GROWTH CURVES 217
5.5. MOTILITY ASSAY WITH PHARMACOLOGICAL INTERVENTION 218
5.6. PHYLOGENETIC TREE FOR THE NOVEL AXONEMAL DYNEIN (LMXM.27.2590) 219
5.7. HOMOLOGY MODELLING AND LIGAND DOCKING TO ASSESS CNBDS 220

6. REFERENCES 222

List of Figures

Figure 1-1: Features of the motile flagellar axoneme. _____4

Figure 1-2: The repeating structure of motile flagella. _____6

Figure 1-3: Leishmania promastigote cell with a '9 + 2' motile flagellum. _____8

Figure 1-4: Waveform types in Leishmania and Chlamydomonas._____11

Figure 1-5: Life cycles of example kinetoplastid species. _____26

Figure 2-1: Protein domain architecture for L. mexicana putative cyclic nucleotide signalling components. _____50

Figure 2-2: Important residues within the phosphate binding cassette (PBC)._____52

Figure 2-3: Sequence alignment of proteins which are bound to cAMP. _____54

Figure 2-4: Categorisation of PBC sequences in the Leishmania PNUTs. _____56

Figure 2-5: Full CNBD sequence alignment of Leishmania 'classical' CNBDs. _____58

Figure 2-6: Homology modelling of classical CNBDs of L. mexicana and predicted cAMP docking position._____60

Figure 2-7: cAMP repulsion out of the PBC binding pocket in Leishmania classical PNUTs. 61

Figure 2-8: Localisation of phosphodiesterases._____64

Figure 2-9: Punctate cell body signal of PDE B2._____65

Figure 2-10: Localisation of adenylate cyclase._____67

Figure 2-11: Localisation of PNUTs. _____71

Figure 2-12: Cell cycle dependent localisation of PNUT19. _____73

Figure 2-13: Cell cycle dependent localisation of PNUT51. _____73

Figure 2-14: Axonemal localisation of CARP1. _____76

Figure 2-15: Salt extraction of CARP1 axonemal signal. _____78

Figure 2-16: Detection of cAMP signalling components in proteome dataset. _____80

Figure 2-17: Functional disruption of RAC1. _____82

Figure 2-18: Gene knockout verification. _____83

Figure 2-19: Null mutant swimming behaviour. _____85

Figure 2-20: Motility behaviour of PDE null mutants._____90

Figure 2-21: Flagellar waveform and cell track analysis._____93

Figure 2-22: Waveform parameters for slow swimming mutants. _____95

Figure 2-23: Genetic rescue of ΔRAC-a mutant slow motility._____98

Figure 2-24: Pharmacological manipulation of parental control swim speed. _____100

Figure 2-25: CpdB likely has targets outside of PDE B1/B2. _____103

Figure 2-26: CpdB treatment can rescue slow swimming motility of ΔRAC-a. _____105

Figure 2-27: Unconventional cAMP binding positions._____110

Figure 2-28: Microdomains involved in flagellar motility._____118

Figure 2-29: Model for cAMP modulation of flagellar movement._____122

Figure 3-1: Classical and divergent PKA signalling. _____128

Figure 3-2: PKAC and PKAR synteny._____132

Figure 3-3: Sequence analysis of PKAR1. _____134

Figure 3-4: Sequence analysis of PKAR3. _____137

Figure 3-5: Sequence analysis of PKAC. _____139

Figure 3-6: Localisations of tagged L. mexicana PKAC and PKAR subunits._____142

Figure 3-7: Cell cycle localisation of PKAC. _____146

Figure 3-8: Cell cycle localisation of PKAR. _____148

Figure 3-9: Localisation dependencies of L. mexicana PKAC and PKAR subunits._____149

Figure 3-10: PKAR1 is not anchored in the radial spokes._____151

Figure 3-11: Pharmacological displacement of PKAC1 signal from the axoneme. _____155

Figure 3-12: Population motility of PKAR and PKAC mutants. _____157

Figure 3-13: Fourier decomposition of the flagellar waveform in PKA mutants. _____159

Figure 3-14: Correlations between flagellum length and waves/flagellum in PKA mutants.

_____163

Figure 3-15: PCR validation of knock out mutants._____164

Figure 4-1: Phylogeny of dynein heavy chains (DHC) encoded in H. sapiens, L. mexicana and C. reinhardtti._____179

Figure 4-2: Gene knockout validation. _____180

Figure 4-3: Axonemal dynein localisations in L. mexicana._____183

Figure 4-4: Axonemal dynein localisations in T. brucei. _____183

Figure 4-5: Waveform analysis of DHC and DHC associated mutants. _____186

Figure 4-6: Example flagellum morphologies._____188

Figure 4-7: Absent and curled flagella quantification. _____189

Figure 4-8: Population motility assay of DHC and dynein associated component._____193

Figure 4-9: Fourier analysis of waveforms from ODA mutants. _____197

Figure 4-10: Fourier analysis of waveforms from IDA mutants. _____200

Figure 4-11: Rare flagellar wave of IDAalpha and IDAbeta. _____202

List of Tables

Table 2-1: Putative cyclic nucleotide signalling components in L. mexicana. _____46

Table 2-2: Population motility measurements for Leishmania null mutants. _____86

Table 2-3: Motility measurements for parental controls._____88

Table 3-1: Kinetoplastid PKAR and PKAC genes. _____133

Table 3-2: Summary numbers for the flagellar waveform of PKA null mutants._____161

Table 4-1: Dynein heavy chains encoded in the T. brucei, L. major, L. mexicana genomes.

_____181

Table 4-2: Non-dynein proteins included in the study._____185

Table 4-3: Quantification of flagellum length, absence, and curling. _____191

Table 4-4: Population motility measurements._____194

Table 4-5: Waveform parameters of mutant flagella._____199

Table 5-1: Bespoke primer design for knockout verification. _____212

Table 5-2: Accession numbers for Chlamydomonas DHCs used in the phylogenetic tree.219

Table 5-3: Accession numbers for H. sapiens DHCs used in the phylogenetic tree. _____220

Acronyms and Abbreviations

IFT	Intra-Flagellar Transport
CSF	Cerebro Spinal Fluid
ODA	Outer Dynein Arm
DHC	Dynein Heavy Chain
CP	Central Pair
RS	Radial Spoke
EM	Electron Microscopy
IDA	Inner Dynein Arm
N-DRC	Nexin-Dynein Regulatory Complex
DRC	Dynein Regulatory Complex
MIP	Microtubule Inner Protein
pDC	Proximal Docking Complex
dDC	Distal Docking Complex
PFR	Paraflagellar Rod
EM	Electron Microscopy
cAMP	Cyclic Adenosine Monophosphate
cGMP	Cyclic Guanosine Monophosphate
PKA	cAMP Dependent Protein Kinase
PKG	cGMP Dependent Protein Kinase
MNNG	N-Methyln'-Nitro-N-Nitrosoguanidine
UV	Ultraviolet

DNAAF	Dynein Axonemal Assembly Factor
FAZ	Flagellar Attachment Zone
TEM	Transition Electron Microscopy
SDS-PAGE	Sodium
cryo-ET	Cryogenic Electron Tomography
LC	Light Chain
CNBD	Cyclic Nucleotide Binding Domain
GPCR	G-Protein Coupled Receptor
sAC	Soluble Adenylate Cyclase
tAC	Transmembrane Adenylate Cyclase
RAC	Receptor Type Adenylate Cyclase
CREB	Camp Response Element Binding Protein
CNG	Camp Gated Ion Channel
MRP	Multi-Drug Resistance Protein
EPAC	Exchange Protein Directly Activated By Camp
PDE	Phosphodiesterase
PBC	Phosphate Binding Cassette
CAP	Catabolite Gene Activator Protein
CRP	cAMP Response Protein
CDN	Cyclic Dinucleotides
FRET	Förster Resonance Energy Transfer
PKAR	PKA Regulatory Subunit
PKAC	PKA Catalytic Subunit

VSG	Variant Surface Glycoprotein
TMD	Transmembrane Domains
SoMo	Social Motility
CARP	cAMP Response Protein
ESAG	Expression Site Associated Genes
GRESAG	Genes Related To Esag
TNFα	Tumour Necrosis Factor Alpha
CVC	Contractile Vacuole Complex
CpdA/B	Compound A And B
JME	Juvenile Myoclonic Epilepsy
PNUT	Putative Nucleotide/Nucleoside Transducer
CARPT	cAMP-Binding Receptor Protein
VASP	Platelet Vasodilator Stimulated Phosphoprotein
△	Null Mutant
DYNC	Cytoplastic Dynein
pf	Paralysed Flagellum
ROS	Reactive Oxygen Species
ADCP	Ancient Conserved Domain Proteins
CNBH	Cyclic Nucleotide Binding Homology
PDB	Protein Database
LRR	Leucine Rich Repeat
PCD	Primary Ciliary Dyskinesia

Declarations

No portion of the work referred to in this thesis has been submitted in support of an application for another degree or qualification of this or any other university or other institute of learning.

Excluding references, the text of this thesis consists of 40,525 words.

Abstract

Cyclic AMP (cAMP) is a ubiquitous conserved second messenger involved in diverse biological function across the Eukaryotic kingdom. Here we explore components of the divergent cAMP signalling pathway, including divergent protein kinase A (PKA), in the early diverging protozoan *Leishmania mexicana,* with an aim to understand how cAMP contributes to its canonical motile flagellum. While cAMP may transduce external signals, it is ultimately the regulation of dynein activity that determines the waveform. Therefore, we assessed the contribution of all 10 axonemal dyneins to gain a deeper understanding how each one contributes to *L. mexicana* waveforms. To tackle these aims, we used CRISPR-Cas9 gene deletion and endogenous fluorescent tagging combined with microscopy techniques to localise our proteins of interest and assess their contributions to flagellar wave shape and direction. We found that 24 of 35 putative cyclic nucleotide signalling components were present in the flagellum, notably in either the distal, proximal or entire axoneme. We identified cAMP at the flagellar tip serves as the main regulator of parasite swim speed. Sequence analysis, homology modelling and predicted cAMP docking suggested that only CARP1, firmly embedded in the flagellar cytoskeleton, binds cAMP via classical binding mechanisms. *⊿CARP1* flagella demonstrated reduced beat frequencies and a higher propensity for ciliary beating. Moreover, we described the pairing preferences of PKAR1 with PKAC1/ PKAC2 in the flagellar cytoskeleton, and PKAR3 with PKAC3 to the cell body. Loss-of-function phenotypes showing distinct effects on motility with loss of PKAC1 being the most severe. Lastly, we found that the double headed axonemal dyneins were indispensable for cell displacement, however the single headed dyneins contributed more specifically to either beat frequency or amplitude. Ultimately, the findings of this thesis have systematically pinpointed the contributing components of the divergent cAMP signalling pathway to flagellar motility. What remains, is to unpick the mechanistic details of how CARP1 is interacting within its local axoneme environment to affect wave shape and direction of travel.

CHAPTER 1

Introduction

1. Introduction

1.1. Eukaryotic flagellar biology

1.1.1. Motile flagella and cilia

Many cells have mechanisms for locomotion and amongst them, whip like appendages called flagella are common in prokaryotes and eukaryotes. However, mechanistically, eukaryotic flagella differ in all aspects from prokaryotic flagella found in bacteria, asides from their primary function of motility. In the former, dynein motor proteins mediate microtubule sliding which is converted to flagellar bending (1–3). Here, the beating that we observe is propagated by machinery positioned periodically along the entire flagellum length (3). Alternatively, prokaryotic flagellar movement is coordinated by motor driven rotation of the basal body anchor which whips the flagellin based filaments comprising the flagellum (4).

Motile flagella serve diverse functions across the Eukaryota domain. In ciliates, the flagellum serves as a mechanism of navigating the environment (5) and filter feeding (6). In mammals, the motile flagellum may be found to contribute in various organs and processes, such as embryonic development (7), fluid displacement; mucosal clearing in the lungs (8) and cerebral spinal fluid (CSF) circulation in the brain ventricles and central nervous system (9), and fertility; movement of the egg down the fallopian tube (10) and sperm chemotaxis towards the egg (11). Despite such diversity in function, the structure and waveforms of the motile flagellum are highly conserved.

1.1.1.1. Ultrastructure

Altogether, the flagellar proteome contains at least 500-700 proteins which all contribute to the structure, signalling and motor features of this multi-functional organelle (12–15). By electron microscopy (EM), a cross-section taken from the axonemes of mammalian ciliated epithelia, to sea urchin sperm, to *Chlamydomonas* and *Leishmania* flagella, will typically reveal the same underlying ultrastructure. A 9 + 2 microtubule arrangement, with two single microtubules in the centre and 9 radially positioned doublet microtubules (16) (Figure 1-1A). Anchored to the cell by a pair of modified centrioles called the basal body, the flagellum is constructed and maintained via the intra-flagellar-transport (IFT) system (17). Here, kinesin-2 motor protein carry cargo anteriorly, whilst cytoplasmic dynein 2 (DYNC2) mediates the retrograde transport (18,19).

Decorating the central singlet microtubules (C1, C2) are central pair (CP) projections (20) (Figure 1-1B) which are thought to communicate signals via the highly electronegative radial spoke (RS) heads (21), through the RS stalks and finally to the outer nine encircling microtubule doublets. The outer doublets comprise of so-called A- and B-tubules, from which outer and inner dynein arm (ODA and IDA respectively) complexes protrude off the A-tubules and extend towards the adjacent B-tubules (Figure 1-1C). Dynein heavy chain (DHC) motors provide the driving force of flagella and ciliary motion. The majority of species harbour dyneins that project off both the inner and outer microtubule regions. The exceptions include species of higher plants, red algae and Entamoeba which lack dyneins entirely (22), and eel sperm which naturally lacks just the ODA (23). Typically, either two or three ODA DHCs may be observed, where *Trypanosoma, Ciona* and *Homo sapiens* have two

(alpha, beta) (22,24,25), and *Chlamydomonas* and *Tetrahymena* have three (alpha, beta, gamma) (26,27).

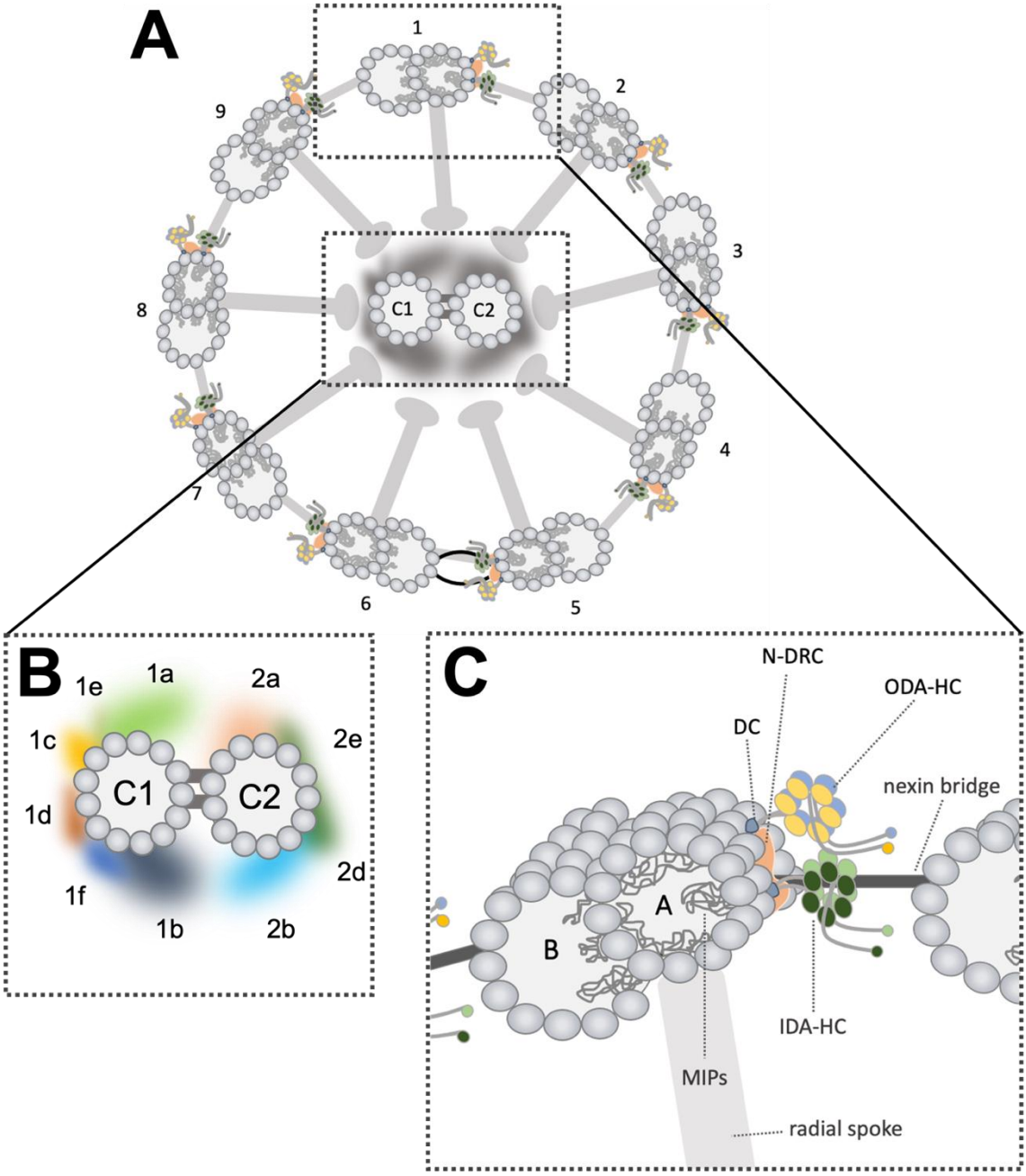


Figure 1-1: Features of the motile flagellar axoneme.

(A) Detailed overview of traverse section of the 9 + 2 axoneme indicating the outer microtubule doublets numbered 1-9, and indicating the crossbridge between doublets 5 and 6 (coloured in black). A magnified view of the (B) central pair (CP) with central pair projections which decorate the C1 and C2 central microtubules, CP projections based on

Chlamydomonas and T. brucei data (24,28) and (C) the outer dynein arm heavy chain (ODA-HC) and inner dynein arm heavy chain (IDA-HC) motor proteins anchored to the A-tubule. Key structures which contribute to flagellar motility are highlighted i.e. the MIPs (Microtubule Inner Proteins – crude cartoon representation) within the lumens of A/B microtubules, radial spoke, nexin bridge, nexin-dynein regulatory complex (N-DRC) and the outer dynein arm docking complex (DC).

As the dynein motors iteratively bind, pull and release the adjacent microtubules, the shear force created by this relative sliding is converted into bending by sliding restrictions imposed by nexin links, which bridge the outer microtubule doublets (Figure 1-1C) (1,29).

Radial spokes form a connection with the A-tubule and the nexin-dynein regulatory complex (N-DRC), a regulatory hub which communicates with both the inner and outer dynein complexes (21,30). The N-DRC, positioned adjacent to RS2, proves to be an essential coordinator of dynein activity, where DRC1/2/4 comprises the core scaffold for this structure and DRC7 provides a link with the ODA (31). This N-DRC is positioned closest to dynein heavy chains IDAc, IDAe and IDAg (31) with dynamic association noted with IDAc (21). Distinct and conserved periodicities have been described along the flagellum length (Figure 1-2). Whilst DHCs in the ODA apparatus overlap with one another and are anchored with 24 nm repetition by docking complex (DC) proteins (32,33), the IDA periodicity repeats every 96 nm, with IDA-alpha, -beta, IDAa, IDAc positioned by RS1, followed by IDAc, IDAa, IDAg, adjacent to RS2 and the N-DRC, then finally IDAd positioned close to a vestigial RS3 found is some species (31).

In recent decades there has been growing interest in the role of proteins localised within the microtubule lumen themselves, named microtubule inner proteins (MIPs). Studies using cryogenic electron microscopy (cryo-EM) have detailed MIP arrangements in *Tetrahymena*

and *Chlamydomonas* model organisms, whilst proteomic approaches in MIP deficient mutants (34) have discovered that calcium sensing EF-hand containing proteins are intriguingly highly represented in this domain (27,34). MIPs are structurally well resolved to the point where precise periodicities have been described within the lumen (35). Although functions have not been assigned to many of the MIPs, it appears a role in motility is evident for some. Firstly, RIB72a/b mutants in *Tetrahymena* demonstrate slower motility (36).

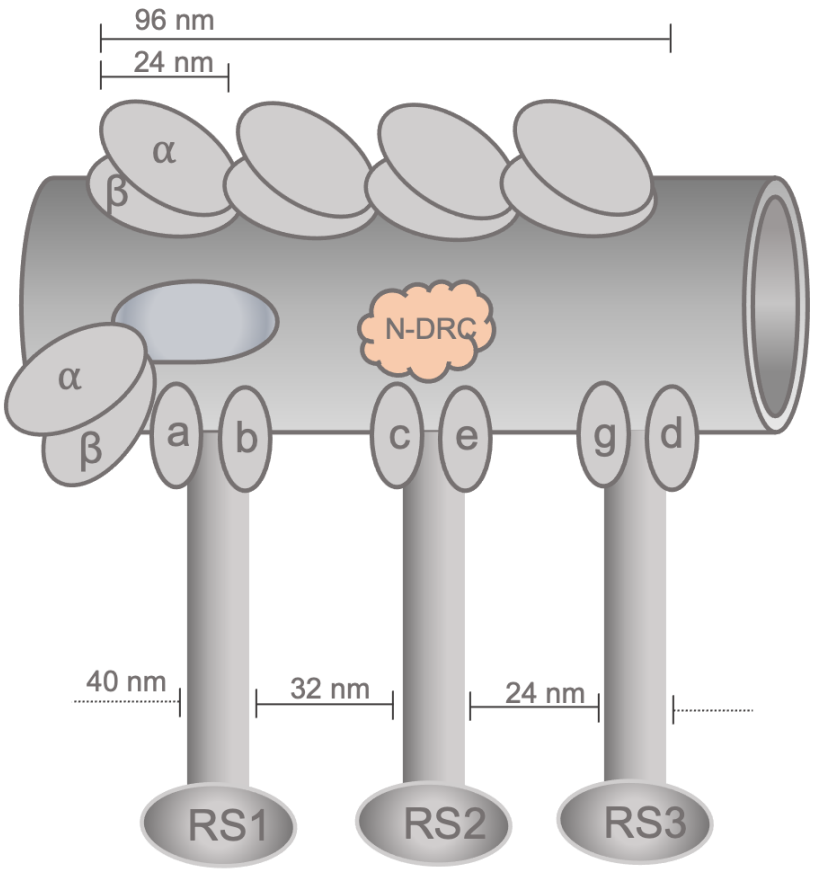


Figure 1-2: The repeating structure of motile flagella.

Longitudinal section of the flagellar axoneme unit consisting of three radial spokes (RS1-3), a row of inner dynein arms (IDA) with ~7 dynein heavy chains (DHC) (a, b, c, d, e, g, alpha and beta) repeating every 96 nm, and an outer row of dyneins consisting of 2 DHC in L. mexicana, H. sapiens and sea urchin, repeating every 24 nm. Nexin dynein regulatory complex (N-DRC) in orange positioned above RS2. Figure adapted from (Oda et al. 2014).

Additionally, it has been demonstrated that the rigidity and elasticity of isolated microtubules changes in the presence of different pH and calcium environments (37), an observation that could suggest the bending properties of axonemes are dynamic, responding to different environmental cues. Lastly, some MIPs (FAP85, FAP29 and FAP182) have been observed to protrude through the microtubule protofilaments and contact external ODA-docking complexes (DC) that anchor ODA DHCs (27), and indeed similar cross protofilament connections have been seen for the RS and IDA apparatus in *Tetrahymena* (38). Other than this direct contact, MIPs are hypothesised to also mediate microtubule stability, especially in context of the structural dynamic bending stresses imposed on the axoneme during rapid beat cycles (34,39).

Unique to the species of kinetoplastids, is an extra-axonemal structure named the paraflagellar rod (PFR). The PFR is anchored to outer doublets 4-7 and is comprised of at least 40 proteins which form the trilaminar latticed organelle. In *T. brucei* bloodstream forms, the PFR is essential for flagellar motility and cytokinesis (40), two biological processes which appear to be linked in bloodstream forms parasites specifically (Figure 1-3B) (41). Recent work has described a 54 nm structural repeat within the PFR where its positioning at 45^{o} to the axoneme is described to assist the non-planar helical wave used by *T. brucei* spp. Although similar mechanistically detailed contributions of the PFR have not been described for the symmetric planar wave of *Leishmania* spp, its role has been described in terms of aberrant forward motility in PFR mutant cell lines (42,43).

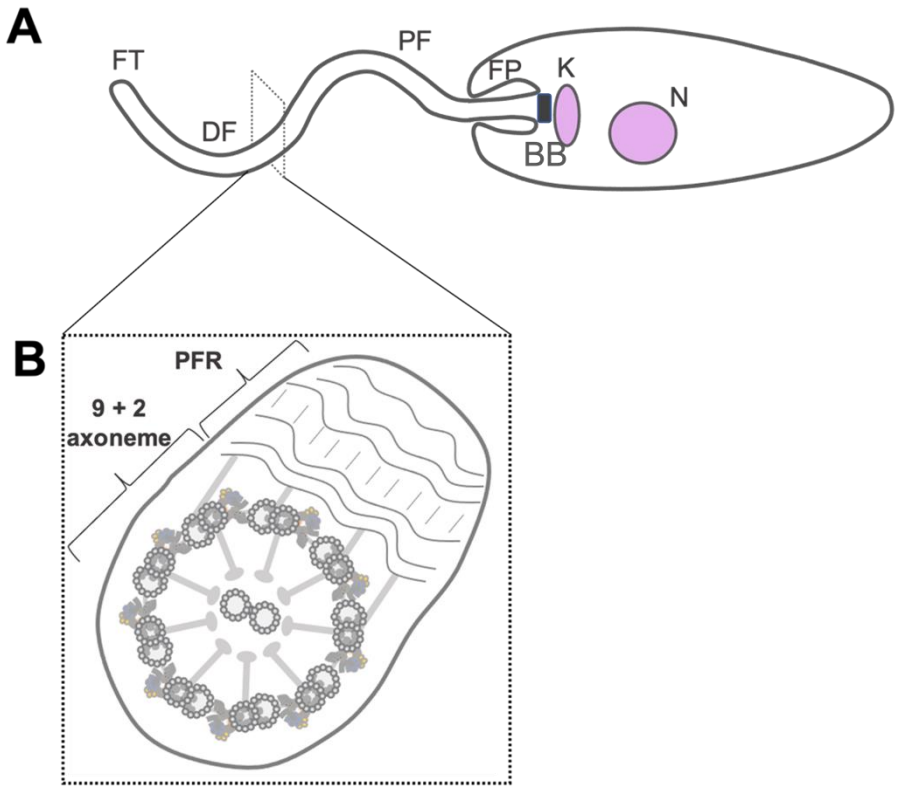


Figure 1-3: Leishmania promastigote cell with a '9 + 2' motile flagellum.

(A) Promastigote cell morphology. Annotated cellular domains abbreviated as FT-flagellar tip, DF-distal flagellum, PF-proximal flagellum, FP-flagellar pocket, BB-basal body, K-kinetoplast, N-nucleus and (B) cross section of the flagellum highlighting the canonical 9+2 microtubule arrangement of motile flagella and the extra-axonemal paraflagellar rod (PFR) structure found in kinetoplastid species.

Although at first glance by EM, the ultrastructure of eukaryotic axonemes appears to have radial symmetry (Figure 1-1A), there have been important structural asymmetries detailed which appear to hold clues as to how wave shape and direction may be coordinated. Firstly, the CP-projections on C1 and C2 microtubules (Figure 1-1B) are distinct from one another, where proteins comprising the C1 CP-projections have been identified, and the C2 CP-projections remain less well characterised (20). This C1 C2 asymmetry is thought to be a

mechanism of communicating the opposing dynein on/off signals through the RS/N-DRC to the dynein apparatus (44,45). Dynein motor proteins in the CP mutant *pf19* are described to be pulling against one-another resulting in rigid flagellar paralysis (3). Paralysed flagella are also described in several other CP-projection mutants, most notably *pf16* mutants which are deficient in pf16/pf20/C1a (pf6), e, c ,d (FAP221) and often the C1 microtubule altogether (Figure 1-1B) (20). Moreover, interesting work in *Leishmania* has described a flagellar curling phenomenon that occurs when the C2 CP-projection hydin is removed (12).

Additional to this, there is also longitudinal proximal-distal flagellar asymmetry described in the outer dynein arm apparatus. Kinetoplastid parasites maintain a proximal docking complex (pDC) comprised of pDC1/2, and a distal pair of dDC1/2, each spanning ~50% of the flagellum length in *T. brucei* and with distributions favouring dDC (~70%) in *L. mexicana* (46) (Figure 1-3A). Although the ODA DHCs are localised along the entire axoneme visible by EM, it appears that a calcium sensitive protein, LC4-like, localises to the dDC complex to negatively regulate population swim speed (46). The same work showed that deletion of the dDC altogether results in an increased proportion of cells propagating the reverse ciliary beat, suggesting this machinery could be the switch centre between forward (flagellar wave) or tumbling (ciliary wave) motility (46).

1.1.1.2. Flagellar and ciliary waveforms

Across the diverse eukaryotic ciliated cell types, we typically observe the same well-described wave shapes being propagated by cilia and flagella, the so-called ciliary and flagellar beats. The overall periodic beating of flagella may be decomposed into a static and dynamic component, whereby the static component is 'the average angle over one

beat cycle at each position along the axoneme' and the dynamic component is the 'travelling wave that provides propulsion' (47).

Ciliary beating is defined by its asymmetry and high static angle component, classically propagating from the flagellum base to the tip in a whip like motion. This ciliary beat is what wafts the mucous up out of our lungs (8), the egg along the fallopian tube (10) and mediates the dominant form of forward motility in several unicellular organisms (such as *Chlamydomonas* and *Tetrahymena*) (47,48). On the other hand, the flagellar beat is defined by its symmetry with a low static angular component and propagated from either base-to-tip (*Chlamydomonas* reverse swimming and sperm motility (48)) or, unusually, tip-to-base in kinetoplastid species (including *Leishmania* and *Trypanosoma*) (46). After decades of observation and experimental study, the flagellar motility behaviour of many organisms is now very well described.

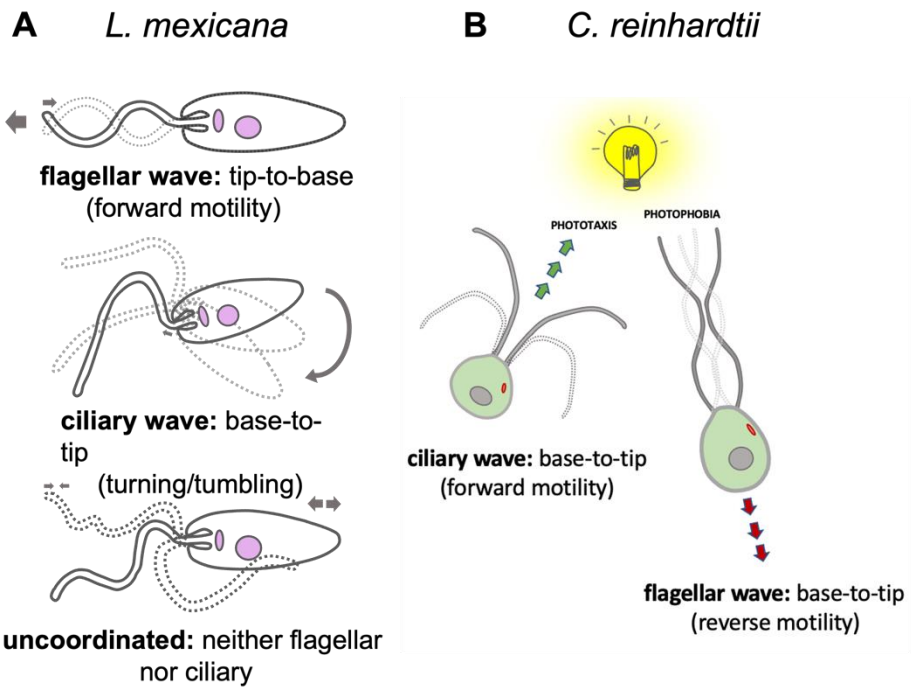


Figure legend on following page.

Figure 1-4: Waveform types in Leishmania and Chlamydomonas.

(A) cartoons of the tip-to-base flagellar wave (symmetric) for forward motility, base-to-tip ciliary wave (asymmetric) for tumbling/turning and the uncoordinated flagellum movement which results in little net cell movement in Leishmania spp. Large grey arrow indicates direction of cell displacement. Small grey arrow indicates direction wave travel. (B) the base-to-tip asymmetric ciliary wave for forward motility and the base-to-tip symmetric wave for reverse motility in the motile green algae Chlamydomonas.

In the motile green algae, *Chlamydomonas reinhardtii*, the biflagellate wild type cells typically default to the forward swimming asymmetric breaststroke motion which they use to photo-tax (49). On occasions when sudden bright light is encountered, a photophobic response is triggered which promotes a 'wave reversal' to the symmetric base-to-tip beat, resulting in cells moving away from the light source (Figure 1-4) (50,51). Both waveforms are rapidly propagated at over 60 beats per second (Hz) (47,52).

The swimming behaviour of mammalian sperm depends on environmental cues and begins with the encounter of high $HCO3^-$ within the female reproductive tract (53). This triggers the capacitation process, defined as a series of physiological and biochemical events that mature the sperm ready for egg fertilisation. Activated sperm cell flagella beat with a symmetrical base-to-tip flagellar wave, where a chemotactic response to a progesterone gradient guides their swimming towards the egg (11). Second messengers calcium and cyclic adenosine monophosphate (cAMP), as well as $HCO3^-$ all play a role in leading up to the final asymmetric frantic beating behaviour prior to egg fertilisation referred to as hyperactivation (53–55) (detailed in Section 1.1.3).

Finally, several species of kinetoplastids, including *Leishmania* and *Trypanosoma*, fulfil a digenetic life cycle between an insect and mammalian host (see Section 1.2) (56). Within

the insect, directional flagellar motility is essential for promastigote form parasites to navigate from the mid-gut to the mouthparts ready for infecting the next mammalian host (12,57). In *Leishmania* promastigotes, the dominant beat observed in more than 75% of the population is the symmetric forward tip-to-base motility (flagellar waveform) which pulls the cell in the direction of the flagellar tip (46,58). This forward motility is sporadically broken up by brief propagation of the turning/tumbling asymmetrical beats (ciliary waveform) which can be observed in 1 - 10% cells of a population at any given time (Figure 1-4) (46,59). Several studies in various *Trypanosoma* species have already outlined the typical waveform parameters for wild type swimming behaviour. For the flagellar tip-to-base wave, species of *Crithidia* appear to beat over 40 Hz, *L. major* and *L. mexicana* beat at 27 Hz and ~25-30 Hz respectively and *Trypanosoma brucei* beat with around 15 Hz (58,60,61). In addition to forward motility, the ciliary wave has also been described in *L. mexicana*, beating at ~5 Hz with a preference for the PFR (see Section 1.1.1.1) on the inside of the asymmetric beat recovery stroke (62). In *L. mexicana*, there is a third less understood flagellar movement referred to as uncoordinated (Figure 1-4), where the beats possess no obvious rhythm, direction or symmetry (46). It is unknown whether this uncoordinated flagellum movement serves a biological purpose or is an artifact of *in vitro* culturing conditions.

1.1.2. Essential axonemal structures and dynein contribution

Decades have been spent piecing together the components that make up the flagellar organelle, with most recent cryo-EM leading to a significant leap in resolution. This has resulted in a detailed 3D architectural model of the main components of axonemes at near-atomic resolution from a variety of organisms (20,21,24,27,32,34,63). In combination with

an understanding of dynein conformational changes during the mechanochemical cycle during binding and hydrolysis of ATP (64–68), these studies have amounted in a robust understanding of the basic principles of axonemal bending (see Section 1.1.3).

What is still to be fully understood is how precisely the hydrolysis of ATP by DHC motors in the ODA and IDA apparatus ultimately ends up as complex behaviours of cell motility that we observe as changes in flagellar beat or swimming direction (Figure 1-4).

A plethora of work from model organisms have resulted in a comprehensive understanding of which axonemal components are essential for flagellar motility. Use of random DNA mutagens such as N-methyln'-nitro-N-nitrosoguanidine (MNNG), methyl methano-sulfate (MMS) or UV treatment in the motile green algae *Chlamydomonas* has resulted in the establishment of a diverse library of structurally defective mutants, for which flagellar movement has been described for many. Released in a series of linked papers called 'Bending patterns of *Chlamydomonas* flagella' by Brokaw *et al*., during 1980s (52,69,70), the wave shape for flagellar and ciliary beats are quantified for a variety of structural mutants. Most noteworthy are *oda41*, *oda38* (both lacking ODA), *pf30*, *ida98,* (both IDA) (69), *pf1*, *pf17* (both radial spoke head) (70), *pf2*, *pf3* (both N-DRC) (71,72), *pf15*, *pf16* (both central pair) (70), and most recently LC1 (73). Additionally, the paralysed *Chlamydomonas pf23* mutant, a mutant of the dynein axonemal assembly factor gene (DNAAF), DNAAF4, resulting in a severe deficiency of all axonemal DHCs apart from moderate levels of the ODA DHCs and IDAa (74,75).

Intriguingly, despite the paralysed phenotype associated with deficiencies in the RS-head (*pf17*) and CP (*pf15*), several so called suppressor mutants have been described, where symmetric and asymmetric beating has been restored, to some extent, by introduction of DRC (*pf3*) and RSP or DRC4 (*pf1* or *pf2*) mutations respectively on top of the aforementioned

mutants backgrounds (70). Although it has not been directly tested, it would be interesting to see whether suppressor mutations of the DRC or RSP on mutants with constitutively active dyneins (*pf19*) would correct for this dynein tug-of-war situation described (3). Interestingly, a similar concept of rescuing targeted flagellar mutants with extra mutations has been applied to *T. brucei*. RNAi knockdown of trypanin (part of the N-DRC, analogous to *Chlamydomonas pf2* mutant) is reported to have a similar rescue capability of the PF16 mutant paralysis phenotype (76). Although this rescue refers to a regain of flagellar movement relative to paralysis, which did not correlate with an increase of motile cells, concluding that the flagellum movement did not equate in cell propulsion (77). As *T. brucei* flagella are attached along the entire cell body via a flagellar attachment zone (FAZ) (78,79), it may prove difficult to precisely quantify differences in flagellum beat shape upon manipulation of the axonemal structure. It would be intriguing to assess the biological outcome of a similar motility rescue approach in *Leishmania* spp where the waveforms of the single external flagellum (79) can be readily quantified using automated tracing methods (80,80).

Several studies manipulating motile flagella throughout the 1970-80s have amounted in the establishment of a model for the respective contributions of inner and outer dynein arms, where the IDA propagates the wave, and the ODA contributes the power but is otherwise dispensable for wave formation (Figure 1-1). In 1973 by Gibbons and Gibbons, observations that the ODA were not essential for wave propagation was by KCl extraction of sea urchin sperm cytoskeletons which were then reactivated by ATP. This partial removal of outer dynein resulted in a proportional decrease of beat frequency but little change in other waveform parameters (81–83). Over a decade later, a more targeted analysis of *Chlamydomonas* motility mutants highlighted that mutants deficient in ODA displayed the

same diminished beat frequency by 50%, where deficiencies in IDA components resulted in aberrant sliding velocity resulting in decreased shear amplitudes (69). Both studies categorised these mutants visually by assessing the loss of electron density in either the ODA or IDA regions by transmission electron microscopy (TEM). Moreover, the techniques used to create the deficiency in ODA structure were salt extraction for the sea urchin sperm and random mutagenesis for *Chlamydomonas*, thus hard to know exactly which other structures were also altered during the process. Supporting the model that the ODA supply mostly just the power, is the observation that in ODA mutants, ATPase activity is described to be 10-20% of wild type activity, where IDA mutants were 60-80% (75).

Based on these studies, and observations that the naturally occurring motile eel sperm which lack the ODA structure but have otherwise normal axonemal structures (23), it is widely believed that the ODA are dispensable for wave formation.

There is, however, evidence that this dogma might not apply universally, or that the ODA contributions may vary depending on the species, waveform, and cell type. Firstly, work prior to the generation of *oda1/38* and *oda40* from Brokaw *et al*, (1987), yielded several ODA mutants described as immotile (*pf13* and *pf22*) (75), and one ODA mutant made by Kamiya which displayed an abolished flagellar wave (no photophobic response), and a halved ciliary beat frequency (84). This latter unique ODA mutant was visualised by EM and shown by SDS-PAGE to be missing four of the ten high molecular weight bands seen normally in control axonemes, and its finding suggested that the ODA contribute power to the asymmetric ciliary beat, but is an essential structure for propagation of the symmetric flagellar wave (84). In agreement with this work, it was shown that *T. brucei* mutants lacking the ODA are defective in forward motility, suggesting that the ODA are needed for the flagellar wave which drives forward cell displacement (85,86). Lastly, mice with mutations

within the ODA DHC DNAH11 are described to have immotile tracheal cilia, reduced sperm motility, however, normal fertility fitness (87). Given the variation of observations described across cell types and species, it would be useful to systematically address this question of distinct ODA and IDA contributions to flagellar motility in a more diverse set of eukaryotic organisms, beyond *Chlamydomonas* and sea urchin. Recent advances in gene editing technology and availability of wide range of eukaryotic genome sequences, it is now possible to ask how *individual* dyneins contribute to wave formation (see Chapter 4).

1.1.3. Models for spatiotemporal dynein regulation

Several models have been proposed as an answer to the question how dyneins coordinate their opposing activation/inactivation to allow for the rapid wave propagation and variation in waveform shapes observed across cell types. In order for bending to occur, the dyneins distributed on opposing lengths of the flagellar axoneme must complement each other's activation so that they do not pull all at once.

Brokaw was among the first to apply some quantitative parameters such as elastic resistance, internal longitudinal shear force (active moments) and external forces imposed by viscous mediums (viscous moment), to symmetric and asymmetric beat mechanism (2). This built on previous EM work which summarised a likely sliding filaments system of flagellar movement, ruling out structural contraction and extension as a mechanism of bend propagation (1,2,88). Over a decade later in 1985, Brokaw declared that the simple curvature-controlled models did not account for how real flagella, rather than the computer simulations, chose their bend initiation pattern (89). The simulated flagellar model only worked when a predetermined frequency was defined, which does not apparently reflect

the weak or absent mode preference in real flagella observed in various external environments (89).

Nearly a decade on in 1994, a more specified version of a curvature control model was elaborated, the 'geometric clutch', which described several possible relevant parameters (90–92). Here it is understood that the proximity of the dynein to the adjacent microtubule defines the likelihood of forming a crossbridge and contribution to the beat. The nexin links are described to give flexibility to the structure, where a bend propagating through the axoneme causes a force traverse to the bend (called the t-force) resulting in some doublets being compressed and thus increasing the likelihood of dynein binding. As dyneins bind, the energy released by ATP hydrolysis causes a relative sliding, which in turn causes a longitudinal force, which together with the t-force, are what ends the bind-pull-release iteration by ripping the dyneins off the adjacent microtubule (90). Torsional force has also been proposed, imposed on the axoneme due to its asymmetric structure and potentially also contributing to determining the termination point of dynein mechanochemical cycles (93).

Several studies throughout the 1980s considered central pair rotation to be at the crux mediating opposing dynein activation via the asymmetrically distributed CP-projections (94,95), however the fact that the central pair does not rotate in many species (96–98) has dismissed the CP as a universal mechanism of dynein activity control.

The most recent addition to the field is from Lin and Nicastro who built upon a 'switching point' model first described in 1979. Originally, Wais-Steider and Satir described how the position of gill cilia from freshwater mussels arrest in the hands-up or hands-down positions when exposed to ATPase inhibitors, ionophores and various salts (99). This resulted in a model where dynein motors on the outer doublets 1 - 4 were active on the effective stroke

whilst the opposing doublets 6 - 9 were inactive, and *vice versa*, known as the 'switching mechanism' or switch point hypothesis (99). Work released in 2018 provided the latest leap in our understanding of dynein activity, using the rapid freezing of live sea urchin sperm and *Chlamydomonas* alongside cryo-electron tomography (cryo-ET) visualisation (3), amounting in the 'switch-inhibition' model. The mechanochemical cycle of dynein activation states have been described, detailing how the angle between the stalk and linker domains on a DHC *in situ* can allude to its activation state. A large angle is indicative of an active/primed dynein, and a small angle is indicative of a post-power stroke inactive conformation (100). The switch-inhibition model describes how the majority of dyneins exist in their active and primed conformations, contrary to previous thoughts (3). Moreover, that the conformation of ODA dynein clusters (on either doublets 1 - 4 or 6 - 9) in the opposing flagellar bends were in the post-power stroke inactive conformations. A similar asymmetric bend dependent distribution of inactive dynein pattern was seen for the IDA DHCs a, g, d and the double headed DHCs -alpha and -beta. ATP deprived control axonemes assessed alongside demonstrated that the ODA DHCs were in the inactive post-power stroke conformation tightly bound to adjacent microtubules. In the same study, dynein positions in paralysed *Chlamydomonas* mutant, *pf19*, which lacks the CP complex, described how the ODA DHCs were actively hydrolysing ATP and pulling against one another, causing rigid paralysis.

The combined observations suggest that DHCs reside by default in a primed and active form, which require a regulatory signal system in place to decrease the dynein binding probability on one side and thus generate a force imbalance which results in bend propagation (3). When the regulatory system is removed (such as in the CP mutant *pf19*), the DHCs are all active and forces produced on both sides are equal, resulting in rigid paralysis.

Ultimately, although we appear to be getting closer to a working model for oscillatory dynein activity within motile flagella and cilia, what has not been resolved is how the mechanism of wave initiation or waveform switching may work. Or furthermore, how the second messenger signals, which communicate cues from the external environment, integrate with the dynein motor dynamics to modulate the wave shape (amplitude, frequency, static curvature *etc*.).

1.1.4. Second messengers contribute to flagellar beat regulation

Although the flagellar ultrastructure is well understood (see Section 1.1.1.1), it is still unclear what mechanism modulates the highly ordered and rapid beat propagation in flagella, or even the switching between waveform types. Studies on sea urchin and hamster sperm models (101,102), *Chlamydomonas* (103), and uniflagellate protists like *Leishmania* (59,104) have shown that both cAMP and Ca^{2+} second messengers are involved in flagellar beat modulation. In mammalian sperm, it is the HCO_3^- activation of soluble adenylate cyclase Adcy10, creating the cAMP spike which activates cAMP dependent protein kinase (PKA) to mediate downstream CatSper channel influx of Ca^{2+}. EFCAB9, a subunit of the CatSper channel, is pH and Ca^{2+} dual sensing to modulate influx (105). This process is what mediates capacitation and is essential for fertility (106). Interestingly, in human sperm, a preliminary study observed that the irregular spiking of Ca^{2+} levels correlated with the rapid directional changes in sperm motility (55,107).

Chlamydomonas models identified calcium responsive components within RS, ODA apparatus, CP and within the microtubule lumens (108). These Microtubule Inner Proteins (MIPs) include the EF-hand containing RIB72 and FAP115 in the lumen of the outer A-

microtubule (27,109) which are postulated to modulate dynein activity and thus fine tune movement (103). Studies in *Leishmania* demonstrate that the distal ODA complex houses the machinery necessary for switching between flagellar and ciliary beats, where Ca^{2+} acts to suppress the propagation of flagellar waves through LC4-like (46). This calcium effector was first described in *Chlamydomonas* and is thought to directly associate with ODA-gamma heavy chain (108).

A common method to study flagellar movement is to extract the flagellar membrane with detergent and reactivate the flagellar cytoskeleton with Mg^{2+} and ATP. *In vitro* reactivation of demembranated *Leishmania* axonemes showed that both addition of cAMP (110) and inhibition of calmodulin/calcineurin (111), trigger wave reversal from a symmetric flagellar waveform to an asymmetric ciliary beat, suggesting cAMP and Ca^{2+} act antagonistically on wave direction and symmetry in *Leishmania*. Similar reactivation techniques in sea urchin (112) and *Paramecium* showed the opposite, that high calcium was the trigger for asymmetric wave reversal, confirmed by techniques using photolysis of caged Ca^{2+} in live *Paramecium* cells (112–114). In *Ciona* (sea squirt) sperm, asymmetric beating, essential for chemotaxis, is believed to be mediated through Ca^{2+} activated calaxin, which supposedly acts directly on outer dynein arm motors to suppress microtubule sliding and allow for the propagation of an asymmetric beat for turning (115–117).

Alternative techniques using Förster Resonance Energy Transfer (FRET) microscopy have observed that elevated cAMP levels correlate with increased beat frequency in mammalian ciliated epithelia (118). So too was increased ciliary frequency achieved by introducing elevated cAMP, calcium and cGMP together via the patch clamp method of altering the concentration of intracellular elements (119). Interestingly, a light chain (LC) associated with the ODA of *Paramecium* (p29) (120) and *Tetrahymena* (p34) (121) was found to be

phosphorylated in a cAMP dependent manner, where phosphorylation correlated with increased microtubule sliding velocity and beat frequency. This finding may allude to a pathway whereby cAMP increases ODA power contribution to the wave.

Taking together these observations across such diverse organisms, it appears the roles of cAMP and Ca^{2+} second messengers in cilia and flagellar beating are somewhat nuanced across species and cell types, however an underlying theme appears to be that these second messengers are involved in the switch between wave symmetry and asymmetry (flagellar and ciliary beats). It is likely that second messenger signalling systems are adapted to the organism's specific environment, be it the sea, or the gut of an insect. There is no doubt, however, that both play modulatory roles in eukaryotic flagellar motility. What is lacking, is the clarity of how the calcium and cyclic nucleotide effectors localised within the flagellum are transducing these signals to modulate rhythmic beating and waveform switching. And moreover, how these second messenger signals fit into the proposed models for dynein activity described in Section 1.1.2.1.

1.2. Cyclic AMP in kinetoplastid species

1.2.1. Classical cAMP signalling pathway

In 1957, Sutherland *et al*, made the link between a previously unknown heat-stable factor (cAMP) and hormones, observing that in various tissue homogenates, glucagon and epinephrine mediated phosphorylase activity via cAMP (122,123). A decade later, Fischer and Krebs worked together to discover reversible protein phosphorylation as a post translational modification, through phosphatases and kinases, identifying protein kinase A as a key cAMP effector (124). After decades of study in versatile organisms from *E. coli* to

Dictyostelium and yeast, the mechanism of cAMP binding to its effector proteins via the cyclic nucleotide binding domains (CNBD) is understood to be widely conserved (125). In mammals, the canonical description of cAMP signalling centres around stimulatory and inhibitory classes of transmembrane heterotrimeric G-protein coupled receptors (GPCRs), transducing an external stimulus (*e.g.,* hormones) to modulate internal adenylate cyclase activity, of which there are soluble (sAC) and transmembrane types (tAC) (126). These enzymes in turn, catalyse the synthesis of cAMP from ATP. The most canonical downstream effect of high cAMP abundance is the activation of the cAMP dependent protein kinase (PKA), a heterotetramer of two regulatory and two catalytic subunits ($PKAR_2PKAC_2$). From here, PKA phosphorylates serine threonine residues within target proteins, including Ser133 in the transcription factor cAMP Response Element Binding Protein (CREB), which modulates the expression of a cohort of cAMP inducible genes (127,128). Other downstream effectors of cAMP include cAMP gated ion channel (CNG), multi-drug resistance protein (MRP) and exchange protein directly activated by cAMP (EPAC) (129). Throughout the cell, phosphodiesterase enzymes (PDE) negatively regulate cAMP by hydrolysing the phosphodiester bond of the exocyclic phosphate. PDEs are observed to maintain the boundaries of subcellular micro/nanodomains and reset the signal (130,131).

The proteins which respond to cAMP or cGMP harbour a cyclic nucleotide binding domain comprised of ~120 aa, within which an eight-stranded beta barrel forms a protective binding pocket for the cyclic nucleotide, shielding it from PDE degradation (125). The most understood and conserved feature of the CNBD is the phosphate binding cassette (PBC) of ~13 amino acids, containing an invariable glutamate at position 2, which forms a hydrogen bond with the hydroxyl group of carbon 2 on the ribose sugar of cAMP (125). Another key interaction is from the arginine (R) in position 11 to the exocyclic phosphate protruding off

carbons 3 and 4 of the ribose sugar (125). So conserved is this binding mechanism, that it was first studied in the catabolite gene activator protein (CAP) (a.k.a. cAMP response protein (CRP)) of *E. coli* (132,133). It is unclear whether we can distinguish cAMP and cGMP specific binding preferences from sequence alone, however, one set of work demonstrate that switching an alanine to a threonine in the PBC favours binding affinity to cGMP (134,135). Demonstrating this residue switch in other cAMP effector types other than PKA would add strength to this observation, as it may only be relevant for cGMP/cAMP dependent protein kinase (PKG/PKA) kinase selectivity (for which this was shown) for example.

Although most research has centred around these two molecules, cAMP and cGMP, we must not overlook the existence of less widely distributed cyclic nucleotide signalling molecules, such as cyclic dinucleotides (CDN) (*e.g.,* c-di-GMP and c-di-AMP (136)), of which bacteria seem to have exploited. One well studied example is cyclic-di-GMP in biofilm formation by *Pseudomonas aeruginosa* (137).

1.2.2. Divergent cAMP signalling pathway in kinetoplastid species

Kinetoplastids species, belonging to the phylum Euglenozoa, represent a relatively early diverging eukaryotic lineage, branching off earlier than the ciliates, Apicomplexans, slime moulds and Entamoebae (138).

Although the canonical cAMP signalling pathway is well described and holds true for diverse species across the eukaryotic domain, from yeast to slime moulds to humans (128,139,140), recent work has identified the early diverging kinetoplastid species to harbour an alternative cAMP signalling pathway. It is now becoming clear that the comparison of biological systems

across a wider range of eukaryotic lineages enriches and deepens our understanding of fundamental cell biology.

Strikingly, in species of *Leishmania* and *Trypanosoma*, no recognisable GPCR, EPAC, MRP or CNG encoding genes have been identified, and nor has any concrete evidence of cGMP signalling (141). Instead of GPCRs transducing an extracellular signal, as is classical, it is hypothesised that a subset of divergent receptor-type adenylate cyclase (RAC) use their hugely variable N-termini as receptors (126).

Moreover, it was recently shown in closely related species *T. brucei* and *T. cruzi*, that their PKA exists as a heterodimer ($PKAR_1PKAC_1$) rather than a canonical heterotetramer, and the cyclic nucleotide binding domains (CNBD) of the PKA regulatory subunit (PKAR) showed precise nucleotide divergence in the glutamate and arginine which are essential for hydrogen bonding to cyclic nucleotides (cAMP/cGMP), thus rendering the PKAR subunits insensitive to cAMP (142). The same study synthesised an artificial nucleoside analogue activator of these divergent PKA, 7-CN-7-C-Ino (Jaspamycin), suggesting that the ligand which activates PKA *in vivo* is structurally more similar to toyocamycin or inosine (also shown to activate divergent-PKA), than a purine cyclic nucleotide. Moreover, it was detailed how the *Trypanosoma* PKAR contain an alanine/glutamate residue switch within the PBC, from which it was seen that the negatively charged glutamate clashes with cAMP exocyclic phosphate, thus actively repelling the molecule out of the binding pocket (142).

Perhaps the most canonical components of cyclic nucleotide signalling in kinetoplastids are the phosphodiesterase (PDE), of which 5 isoforms have been documented (A, B1, B2, C and D) (143). Several of which have been the focus of work to find novel trypanocidal drugs (PDE B1/2) (144) or understand the role of osmoregulatory organelles (PDE C) (145). The following sections discuss where studies of these components within the divergent cyclic

nucleotide signalling pathway allude to a biological function for cAMP in the lifecycle of kinetoplastid species.

1.3. Proposed roles for cAMP in the digenetic lives of kinetoplastids

1.3.1. Lifecycle of kinetoplastid species

Many parasitic protozoans belonging to the class Kinetoplastida pass through complex digenetic lifecycles between mammalian hosts and insect vectors (146). *T. brucei*, *Trypanosoma cruzi* (*T. cruzi*) and *L. mexicana* are the aetiological causes of Sleeping Sickness (African trypanosomiasis), Chagas disease (American trypanosomiasis), and Leishmaniasis respectively, diseases which cause significant suffering and economic burdens across the globe (147–151). There are over 20 species of *Leishmania,* where transmission between hosts is orchestrated by the bite of female phlebotomine sandflies, of which 90 species have been found to be vectors (148). As uniflagellate cells, the lifecycle of *Leishmania* spp. involves two morphologically distinct forms; an immotile intracellular amastigote stage which resides within the mammalian macrophage phagolysosome, and a motile extracellular promastigote stage harboured inside the insect vector (Figure 1-5A, 5C) (56,79). So too, does the life-cycle of *T. cruzi* include an intracellular amastigote stage in the mammalian host (Figure 1-5A, 5C) (153).

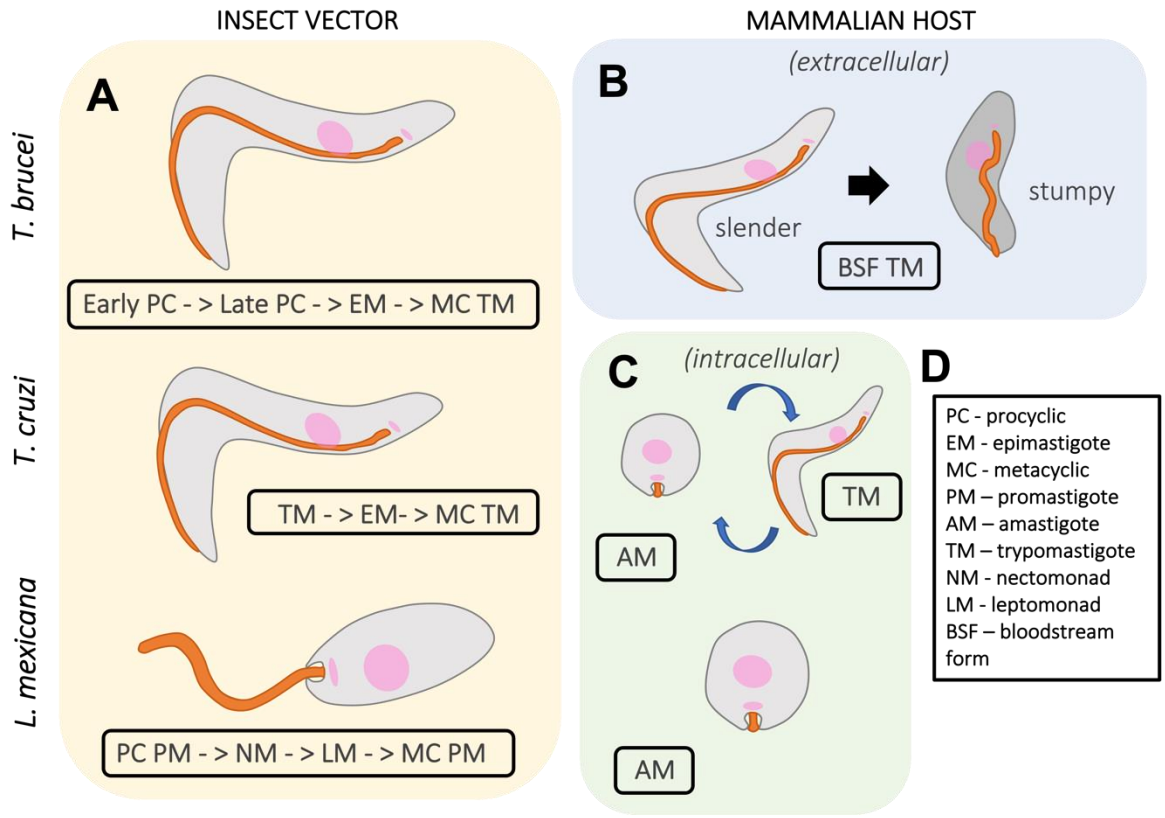


Figure 1-5: Life cycles of example kinetoplastid species.

A simplified life cycle schematic of insect and mammalian form parasites for Trypanosoma brucei (T. brucei), Trypanosoma cruzi (T. cruzi) and Leishmania mexicana (L. mexicana). (A) T. brucei early and late procyclic (PC) replicative form parasites reside in the midgut, becoming epimastigotes (EM) and finally non-replicative metacyclic (MC) trypomastigotes (TM) in the tsetse fly salivary glands (152). T. cruzi TM forms are taken up from an infected blood meal, becoming a replicative EM in the mid-gut before becoming an infective MC TM in the hind-gut of the triatomine insect vector and being passed to the host via infected faeces near the site of the bite wound (153). L. mexicana PC promastigotes (PM) replicate in the sandfly midgut before becoming nectomonad (NM) and leptomonad (LM) forms migrating to the mouthparts and finally becoming infective MC PM (154). (B) Infective MC enter the bloodstream and become replicative slender bloodstream (BSF) form TM at low parasitaemia. At higher parasitaemia, a stumpy induction factor now known to be oligopeptides (155) initiates the slender-to stumpy differentiation which are non-replicative TM forms primed to be taken up by the next biting tsetse fly vector. (C) MC TM and MC PM for T. cruzi and L. mexicana respectively enter the bloodstream of the mammalian host and

infect various host tissues and macrophages respectively. Where T. cruzi cycles between intracellular amastigotes (AM) and extracellular TM (not to scale) in the bloodstream, L. mexicana replicates as an AM inside the parasitophorous vacuole of phagocytic cells. Cell body coloured in grey and flagellum highlighted in orange to demonstrate the presence of an extracellular motile flagellum in (A) and the loss of the external motile flagellum in amastigote forms (C). Shaded in pink represents the kinetoplast (mitochondrial) and nuclear DNA.

Contrasting to this, *T. brucei* remain extracellular throughout the lifecycle and have evolved a unique Variant Surface Glycoprotein (VSG) coat alongside an expanded repertoire of adenylate cyclase to evade the mammalian host immune response (see Section 1.2.3.2) (126,156). In addition to this, *T. brucei* use a quorum sensing mechanism to coordinate differentiate from long slender proliferative bloodstream form parasites at low parasitaemia into quiescent short stumpy forms at high parasitaemia, the latter of which is primed for uptake into its tsetse fly insect vector (Figure 1-5A, 5B) (See Section 1.2.3.5) (155). Shared between these species is the need for flagellar driven motility to navigate the insect vector as procyclic form parasites and the differentiation into metacyclic form parasite which are infective and sit in the insect vector mouthparts or salivary glands primed to be inoculated into the next mammalian host which is bitten (Figure 1-5A) (57,77).

1.3.1.1. Flagellar motility

Classical adenylate cyclase (AC) enzymes synthesise cAMP from ATP, where two main families exist. In mammals, the tACs contain 12 membrane spanning helices and one large cytoplasmic region harbouring the catalytic core (157). These are associated with GPCRs which either stimulate or inhibit cAMP synthesis. The other type are sACs, whose activity is

linked to environmental HCO_3^- concentration (53). Although ACs are recognisably encoded in the genomes of all kinetoplastids, they appear somewhat diverged from mammalian homologues (158). Structurally, the parasite tACs contain 1 predicted transmembrane domains (TMD), a large variable N-terminal sequence believed to be extracellular, and a conserved intracellular C-terminal catalytic core (126). In *T. brucei*, a repertoire of insect stage tACs have been described, TbACP1-6, most of which localise to the flagellar tip domain (159). In early (but not late) procyclic (insect) form *T. brucei* parasites (Figure 1-5A), cell populations are reported to behave in a coordinated manner on semi-solid surfaces (160,161). When inoculated into the centre of a petri-dish, parasites will migrate over several days in finger like projections outwards, navigating to avoid other projections (161). This is termed Social Motility (SoMo). Intriguingly here, loss of some ACs like AC6 and AC1/2 (in combination) cause hyper-social motility behaviour, where more numerous and faster projections are formed (160). On the flip side, most recently, PDE isoform B1 and downstream effector cAMP response protein (CARP) 3 were found to be essential for SoMo, and consequently too migration through the tsetse fly vector for PDE B1 (57,162). It has now been shown a pH gradient is at the crux of this phenomenon, where CARP3 at the flagellar tip, directly interacts with ACP3 and ACP5 (adenylate cyclase) downstream of PDE B1 regulation (162,163). Taken together it appears high cAMP concentration (*e.g.,* in the PDE B1 mutant) inhibits social motility and low cAMP concentration at the flagellar tip (*e.g.,* in AC mutants) promotes social motility in a signalling pathway involving CARP3 which transduces environmental pH gradients into directional group movement. Still to be reported on is the effect of PDE B2 ablation on SoMo behaviour, especially as previous work identified PDE B1 and PDE B2 to compensate for each other's loss in bloodstream form trypanosomes (164).

Several studies in *Leishmania* also point to the cAMP pathway being involved in flagellar function. Firstly, recent work identified that the flagellar proteome of *L. mexicana* contained several adenylate cyclase and phosphodiesterase (isoforms A and D), where PDE A was found enriched at the flagellar tip and parasite swim speed was described to increase in mutants lacking these PDEs (77). In an independent study, the exposure of *Leishmania* cytoskeletons to high cAMP was shown to amount in a high proportion of asymmetric ciliary beating (110). Together these findings suggest that cAMP may modulate both population speed and wave direction.

Interestingly, the localisation of sAC in *Leishmania* promastigotes was also found to be enriched at the flagellar tip, although no role in motility has yet been described (158). The *Leishmania* sAC has partially been characterised, where two independent studies claim it to be a heme coupled protein, and thus O_2-dependent in its cAMP production (165,166). One demonstrates cAMP production upon binding O_2 or CO but reports a high K_m value for ATP of ~1.9 mM (165). Both point to a potential role for sAC in sensing and responding to harsh hypoxic environments (165) or encounters with reactive oxygen species (ROS) in macrophages (166).

In 1995, an array of 5 AC genes were described in *L. donovani*, of which two were partially sequenced, named Receptor type AC-a (RAC-a) and RAC-b, and found only expressed in the insect form (promastigotes) (167). Taking the published sequence and conducting a protein BLAST search revealed these genes to be LdBPK_170120.1 (*L. mexicana*: LmxM.17.0200) for RAC-a and LdBPK_170130.1 (*L. mexicana*: LmxM.17.0190). Expression of RAC-a and RAC-b in *Xenopus* oocystes demonstrated slight activation of downstream cAMP sensitive channel (CFTR) only with RAC-a, amounting to ~3 nmol/oocyste cAMP (167). However, a positive control was lacking so it is hard to conclude whether this is truly representative of an *L.*

donovani AC producing cAMP within that system, especially as it is not known what activates these RACs. Interestingly, the expression of both RAC-a and RAC-b together in the system nullified the cAMP production detected by RAC-a, a finding which led to the assumption of interaction within the membrane (167), supporting the previous hypothesise of AC dimerization in kinetoplastids (141,168,169).

Very little has been found about what triggers/inhibits kinetoplastid AC activity. Several studies point to the identification of calcium stimulated ACs present in *T. cruzi* (170,171) and *T. brucei* (170,172), although these findings have not been revisited for decades.

One recurring feature of ACs across kinetoplastids, is the enrichment of ACs within the flagellum, notably in the tip microdomain or PFR associated (158,159,171). Still lacking is conclusive evidence of cAMP production, which only exists for a few ACs in the form of complementation assays in AC deficient yeast models (for TcCLB.511705.10) (171) or activity in *Xenopus* oocystes (for LdBPK_170120.1) (167).

As mentioned, there has been little follow-up of these early discoveries from the 1980s and 1990s and major knowledge gaps remain. With the advances in genomics, tools for genetic manipulation tools and new methods for probing the biochemistry and cellular activities of these proteins, the field would benefit from the application of modern research tools to tackle these curious knowledge gaps. What are the ligands for kinetoplastid ACs? Are they all synthesising cAMP or have some diverged away from canonical function (as seen with PKA)? What forms the signal transduction pathway downstream of ACs? See Chapter 2.

1.3.1.2. Immunomodulation

Interestingly, it has been described that where species of *Leishmania* and *T. cruzi* parasites exist in an intracellular amastigote form within the mammalian host, and harbour a handful of adenylate cyclase, the *T. brucei* parasites, which remain extracellular in the mammalian host (Figure 1-5B), harbour an expanded repertoire (~80) of RACs called Expression Site Associated Genes (ESAGs) and Genes Related to ESAGs (GRESAGs) (141,173). ESAG expression is intrinsically linked to that of neighbouring VSGs which coat the surface of parasites to evade immune recognition by the mammalian host (156), thus ESAGs are exclusively expressed in bloodstream forms (174). It is hypothesised, that upon initial blood inoculation with a parasite load from the bite of a tsetse fly, a subset of sacrificial parasites release cAMP via activated ESAGs during cell destruction (173). This production and release of cAMP is thought to effectively inhibit tumour necrosis factor alpha (TNFα) production by myeloid cells, dampening the first line host immune response and allowing remaining invading parasites to establish an infection (173).

1.3.1.3. Osmoregulation

The contractile vacuole complex (CVC), an organelle used to regulate cell volume under varying external osmolarity, has been described in a variety of organisms which reside in water-based environments (175).

In *T. cruzi*, the CVC is positioned proximal to the flagellar pocket where all kinetoplastid endo- and exocytosis occurs (176). It is proposed that cAMP signalling pathways are involved in osmotic stress adaptations via aquaporins (177), largely because intracellular cAMP

concentrations are seen to spike when the cell is exposed to hypo-osmotic stress, and that cells treated with 1 mM dibutyryl cAMP, a membrane permeable PKA agonist, showed an increased ability for volume recovery (178). However, cell volume recovery was not observed at micromolar range dibutyryl cAMP. Moreover, the dual cAMP/cGMP hydrolysing PDE isoform C (179), has been found to be part of the CVC in *T. cruzi*, co-localising with two CVC protein markers calmodulin and an aquaporin, TcAQP (145). Interestingly, in support of this hypothesis, a yeast-two-hybrid screen revealed PDE C and aquaporin as interactors of PKAC1 in *T. cruzi* (180). That said, direct evidence of cAMP involvement is still lacking, with only a proposed mechanism hypothesised. Furthermore, since these works were published, we have an evolved understanding of the divergent nature of PKA in kinetoplastids (142,177).

1.3.1.4. Targets for Trypanocidal drugs

Relatively a lot is known about the phosphodiesterase (PDE) of kinetoplastid parasites, thanks to the work done to explore them as novel therapeutic targets to combat disease (143). Five PDE isoforms have been reported in the literature, named A, B1, B2, C and D, but only a few have been functionally explored. Complementation assays have been used in PDE deficient yeast to ascertain the activity of several isoforms. In one study, PDE A, B1 and B2 from *L. major,* and *PDE* A from *T. brucei* were all shown to rescue deficient yeast (181). Separately, *T. cruzi* PDE C was found by enzyme kinetics to be dual specific for cAMP and cGMP, and additionally rescued PDE deficient yeast (179). In the same year by a different lab, PDE C from *T. cruzi, T. vivax, L. major* were shown to rescue PDE deficient yeast, however PDE C from *T. brucei* and *T. congolense* did not (182). Curiously, characterisation of PDE D is notably lacking, with no work having attempted complementation assays. Most published

work has been focussed on characterising PDE B1 and B2, which localise to the flagellum in *T. brucei,* reportedly associating with the paraflagellar rod (PFR) (164). It has been described that dual knockdown of both B1/B2 together amounted in an increased global cAMP concentration correlating with a lethal cytokinesis defect, however, individual knockdown did not, suggesting that they compensate for one another and are together essential for bloodstream form parasites (164). On these grounds, collaborative efforts were made to create a PDE B1/B2 specific inhibitor repurposed from an existing library of *H. sapiens* PDE inhibitors. This yielded Compound (Cpd) A and several others (144) which were designed to target the parasite P-pocket, a cavity described in PDB B1/B2 and *T. cruzi* PDE C (182,183). The lethality of CpdA was demonstrated, describing an uncontrolled and sustained increase in cAMP correlating with cytokinesis defects and lethality in bloodstream form trypanosomes. However CpdA also demonstrated a higher affinity for human PDE4B which was measured alongside the trypanosome enzymes (144). Subsequent co-crystal structures demonstrated that the P-pocket designed compounds associated with the catalytic site of PDEs instead, which explained the lack of compound selectivity (184). If used as a trypanocidal drug, the off-target TNFα suppression of the human PDEs could counterintuitively render the host more vulnerable to infection (173,185) (see Section 1.2.3.2).

There have been two independent studies which set out to find what is transducing the cAMP signal. The first technique used the PDE inhibitor CpdA alongside a genome-wide RNAi knockdown screen in bloodstream form trypanosomes, revealing that knockdown of 4 genes conferred resistance to CpdA lethal effects (186). These genes were named CARP1-4, where CARP1 knockdown made the cells 100X less sensitive to CpdA. CARP1 protein contained predicted CNBDs, was found to be kinetoplastid-specific and localised to the

flagellar axoneme (Tryptag.org) (186,187). CARP2 and CARP4 represented conserved eukaryotic flagellar components, where the latter contained an EF-hand and is part of a family of four RIB72-like proteins associated with MIPs (34,186) (see Section 1.1.1.1). Intriguingly the human ortholog of CARP4, EFHC1, has been linked to juvenile myoclonic epilepsy (JME) (188,189), however, as the contributions of MIPs to the function of motile flagella have not been fully detailed, it is difficult to hypothesise a mechanism of why this may occur. Lastly, CARP3 is exclusive to *Trypanosoma* species, localising to the flagellar tip microdomain (187), and described to form associations with ACs, with involvement in SoMo of *T. brucei* alongside PDE B1 (162,186) (see Section 1.1.2.1).

Independent of this study, an *in silico* approach to find the kinetoplastid cAMP signalling pathway also identified CARP1 as the strongest candidate for cAMP binding, alongside hypothetical protein TcCLB.510297.110 (LmxM.36.0830 (PNUT19 in this project)), out of 27 hits predicted to contain cyclic nucleotide binding domains (190). For these two hits, the PBCs within the CNBDs were noted to have a consensus set of residues in accordance with canonical binding sequences (118). Moreover, a displacement assay showed that recombinant CARP1 associated with cAMP-coupled to agarose beads could be displaced by both cAMP and cGMP at 1 mM, although oddly, the same study did not report on attempting similar cAMP displacement assays with the novel hypothetical protein TcCLB.510297.110 (190).

Interestingly, neither of these approaches to find downstream cAMP effectors highlighted PKA as a likely candidate, which further supports the recent findings of PKA divergence (142).

1.3.1.5. Differentiation

Insect form differentiation

Work throughout the 1980s experimented with cAMP analogues, PDE inhibitors and AC activators in *T. cruzi* to demonstrate a role for cAMP in metacyclogenesis, the transition from non-infective proliferative epimastigote forms to infective metacyclics primed for inoculation into the bloodstream (Figure 1-5A) (191,192). In 1988, the transition of epimastigotes into metacyclic trypomastigotes was seen to correlate with a 3-fold cAMP increase, where cAMP binding was described to a protein with an Mr of 87,000 named CARPT (cAMP-binding receptor protein), noted not to be PKAR (193).

Later on, experiments by Fraidenraich *et al*, showed that the alpha D-globin oligopeptide sequence activated ACs in *T. cruzi* epimastigotes which caused differentiation into trypomastigotes (194). Similarly in *T. brucei* procyclic promastigote insect form parasites, the crude membrane fraction of the proventriculus/oesophagus from teneral tsetse flies specifically correlated with an increased global cAMP production when compared to other fly tissues assessed (195).

In other work, roles have been suggested for PKAR1 in metacyclogenesis for *L. donovani* (196,197) and *L. amazonensis* (198). It was seen that starvation conditions correlated with elevated PKAR1 expression, and PKAR1 overexpression mediated an increased proportion of the early stationary promastigotes to develop metacyclic morphology alongside decreased sensitivity to human serum and enhanced survival inside of macrophages (196). Supporting the proposed role for PKA in promastigote form parasites, the phosphorylation activity of PKA was assessed during promastigote to axenic amastigote differentiation,

where rapid dephosphorylation of target motifs was observed shortly (10 minutes) after introduction of promastigotes to differentiation conditions (199).

Cyclic AMP is not involved in slender-to-stumpy bloodstream form differentiation

Bloodstream form trypanosomes respond to a density sensing signal, named stumpy induction factor (SIF), which, in sufficient quantities when cell densities are high enough, mediates cell cycle arrest and slender-to-stumpy form differentiation (155). It was originally described to be mediated through a cAMP signalling pathway, firstly because cAMP production was seen to reach a peak at maximum parasitaemia, then fall during transitions to intermediate and stumpy forms (200), but largely due to the observation that cell permeable analogue, pCPT-cAMP, and PDE inhibitor, etazolate, had the effect of promoting differentiation (201). Almost a decade later it was identified that only hydrolysable cAMP analogues had this stumpy inducing effect, and thus it was understood that the hydrolysed products (AMP) were likely acting through transducers such as AMPK and TOR to mediate quiescence (202,203). Most recently the SIF mechanism was described to be parasite secretion of peptidases which cause a cell density dependent oligopeptide concentration. These oligopeptides are then internalised by transmembrane GPR89 by the slender form trypanosomes, and trigger a signalling pathway to stop cell replication and differentiate into the stumpy forms, primed to infect the next biting tsetse fly vector (Figure 1-5B) (155).

Ultimately, several decades of work have contributed many proposed roles for cAMP in the life cycles of kinetoplastid species. PKA is now recognised as a cAMP-independent effector of a novel endogenous ligand (unknown), where known downstream cAMP targets in

trypanosomatids are distinct from the canonical targets including PKA described in the textbook (142,190).

What is still to be pieced together, is how these components act within the cell to contribute to parasite biology and specifically, what their mechanistic contribution to flagellar beat modulation is. In this project, I performed an inclusive systematic tagging and gene deletion screen of all potential components of *L. mexicana* cAMP signalling pathways, and the divergent PKA, to assess which components (if any) are involved in flagellum function.

1.4. Project approach

1.4.1. Aims, strategy and rationale

Cyclic AMP is a highly conserved ubiquitous second messenger which, alongside calcium, has been documented in diverse eukaryotic species to modulate the movement of motile flagella (see Section 1.1.4). Still, we understand little of how these second messengers are transduced within the flagellar structure to change the wave shape and direction of travel. Recent advances in gene editing technology (*i.e.,* CRISPR-Cas9) now allow us to explore these long-standing unanswered questions in uniflagellate protozoan parasites like *Leishmania*. Although it is described well how the motile *Leishmania* promastigotes utilise their flagella to propagate several waveforms for turning and forward motility in the culture medium, it is not explored just how cyclic AMP may be acting within the organelle to modulate the behavioural changes. Given recent publications highlighting a repertoire of cAMP-insensitive-PKA within kinetoplastid parasites, it is imperative to keep in mind how these early diverging eukaryotes might have divergently evolved or repurposed the supposedly conserved cyclic nucleotide binding domain. Here, we have designed three main project chapters which use a combination of genetic and pharmacological intervention alongside fluorescence and video microscopy. This exploration is not only interesting from a fundamental biology perspective, but also serves to gauge potential areas of host pathogen discrepancy which may be built upon to tackle the growing need to combat *Leishmaniasis* as a disease.

Aim 1: To determine which cyclic nucleotide signalling components contribute to flagellar driven motility in Leishmania mexicana.

We chose to initiate our strategy by compiling a list of components which we predicted may participate in transducing a cyclic nucleotide signal in *L. mexicana*. Using the online database TriTrypDB and mining through literature, we first established a curated set of 35 signalling components to experimentally interrogate. To determine which components contribute to flagellar beating dynamics, we used CRISPR-cas9 to create fluorescently tagged and null mutant libraries. The fluorescent tagging information was used to elucidate any signalling microdomains that exist in these parasites. Then we used an array of microscopy-based motility assays to quantify whether the null mutants swam any different to parental controls, and thus contributed to flagellar beating dynamics. We explored also the manipulation of parasite motility using phosphodiesterase inhibitors and cell permeable cAMP analogues to complement our genetic approach to understanding flagellar movement.

Together these experimental data alongside *in silico* protein sequence scrutiny of cyclic nucleotide binding domains has successfully highlighted a unique parasite cAMP signalling pathway in the distal flagellum which modulates speed and wave direction.

Aim2: Establish the role of known divergent parasite protein kinase A to flagellar motility.

As PKA is an established canonical and conserved effector of the cAMP signal across the eukaryotic kingdom (excluding plants), it was assumed until very recently that kinetoplastid parasites harboured a similar signalling dogma. Now, robust evidence points towards the existence of a divergent second messenger (yet to be found), where PKA has been repurposed to transduce its signal as opposed to cAMP (142). Although several publications

have explored some potential functions of divergent PKA in kinetoplastids (196,198,204), no study as of yet, has quantified PKA contribution to the parasite flagellum, especially as PKA is known to be a core mediator of sperm behaviour during fertility from sea urchin to mammals (205).

In this Chapter 3, we ask 1. Where do the two PKAR and three PKAC subunits localise, 2. what pairing preferences exist between PKAR and PKAC, and 3. which subunits contribute to flagellar motility (and how). This strategy succeeded in identifying the PKA signalling microdomains and an essential subunit, PKAC1, indispensable for the dominant forward motility behaviour for promastigote *Leishmania*. We also demonstrate that, contrary to the predictions in literature (206), none of the PKA subunits individually, or in combination, were essential for parasite viability. Lastly, we confirm that *L. mexicana* PKAR are more sensitive to nucleoside analogues (toyocamycin and inosine) than cyclic nucleotides (cAMP), corroborating existing work described in *T. brucei* and *T. cruzi* (142).

Aim 3: Assess the effect of removing inner and outer dynein arm components on flagellar waveform.

The core principle of the motile 9 + 2 flagellum is movement. This movement is driven by giant microtubule anchored dynein motor proteins, which hydrolyse ATP to fuel the relative sliding of outer microtubule doublets (see Section 1.1.3). The axonemal dyneins are divided into those that are anchored on the outer A-tubule structure (ODA), and those that are anchored more proximal to the radial spokes on the inside of the A-tubule (IDA). Experimental data from sea urchin and *Chlamydomonas* model organisms identify separate roles for the ODA and IDA, where the former mainly contribute the power to the flagellar beat and the latter are involved in wave propagation and shape (69,82,83). These findings

have not been systematically built upon since the 1970-80s, and the CRISPR-cas9 revolution now allows us to readdress this proposed dogma for dynein driven movement with a targeted genetic approach. Our ultimate aim was to identify whether the CARP1 cAMP transducer was acting through the ODA or IDA to alter the beat frequency and wave direction observed in *⊿CARP1*.

In Chapter 4, we establish the repertoire of axonemal dyneins for *L. mexicana* and investigated the consequence of the flagellum movement upon deletion of each individual dynein. This strategy heavily relied upon waveform analysis established in collaboration with Dr Richard J Wheeler and Dr Benjamin J Walker, using the high magnification high speed video capture with semi-automated cells tracing and Fourier decomposition of the wave parameters. This Chapter found that the ODA is an essential structure for forward motility, however removing individual ODA DHCs or associated LC1, halved the beat frequency, corroborating the findings from *Chlamydomonas* and sea urchin (69,83). Moreover, we describe that of the 8 IDA DHCs, motility of double headed *⊿IDAalpha* and *⊿IDAbeta* was severely hindered by a proximal flagellar curling phenomenon, and the single headed IDA DHCs either contributed to beat frequency or amplitude. Although these observations alone were not enough for us to establish how our CARP1 may be transducing cAMP signal into complex cell swimming behaviour, we did establish a useful reference for future work of individual axonemal DHC contributions to wave shape.

CHAPTER 2

cAMP contributes to flagellum beat direction and population swim speed via axonemal CARP1

2. cAMP contributes to flagellum beat direction and population swim speed via axonemal CARP1

Data presented in this chapter is my own work, asides from section 2.2.1 and 2.3 where data was produced as part of a Masters and Undergraduate student project by Xiaojun Peng and Gabe Crossfield respectively, which I supervised. Figures were adapted by myself where indicated from the resulting dissertations. The scripts used for cell tracing and Fourier decomposition of the wave in Section 2.4.1 were supplied by Dr Richard Wheeler.

2.1. Introduction

Second messengers like Ca^{2+} and cAMP have been consistently shown to be involved in eukaryotic cilia and flagella functions (50,57,104,112,114,162,207–211), with significant bodies of evidence describing the role of cAMP in sperm fertility and calcium in wave asymmetry (see Chapter 1, Section 1.1.4). Yet a knowledge gap still exists on how precisely a signal is transduced to ultimately modulate the dynein-driven movement of flagellar and cilia. Even less understood, are the mechanisms by which cAMP affects cellular functions in early diverging eukaryotic species like the kinetoplastids, which use a single motile flagellum to navigate the environment of their insect vectors (77). Recent evidence points to alternative cyclic nucleotide signalling pathways in these early diverging eukaryotes, than the textbook pathway described in mammalian species and across diverse lineages of the eukaryotic domain (212,213). First indications of alternative second messenger signalling became evident when little consensus was reached on (a) whether parasite PKA regulatory

subunits are responsive to cAMP (198,214) and (b) whether cGMP signalling exits in these parasites (142,214). Now, it is largely accepted that kinetoplastids like *Leishmania* lack components of cGMP signalling (56,141,142), along with any recognisable EPACs, CNGs or GPRCs (141) . Furthermore, parasite PKA regulatory subunits have now conclusively been demonstrated to have diverged away from cAMP sensitivity (see Chapter 1, Section 1.2) (142,204). Comparisons of genomes of a wider range of eukaryotes and a new emphasis on evolutionary cell biology is driving a renewed interest in the true unity and diversity of so-called 'canonical' pathways, bringing to light the existence of unexplored divergent/repurposed cAMP signalling pathways within the eukaryotic domain. With this in mind, my aim here was to firstly identify the whole repertoire of putative components of cyclic nucleotide signalling encoded in the *L. mexicana* genome. Secondly, since it was shown that the PKA regulatory subunit (PKAR) of *T. brucei* does not bind cAMP despite having a predicted CNBD, I asked the question if sequence structure modelling analysis could distinguish between bona-fide cAMP-binding CNBDs and divergent CNBDs. And lastly, I conducted a tagging and a gene deletion screen to identify which components may be contributing to flagellar functions by interrogating which of the putative cyclic nucleotide signalling proteins localise to the *L. mexicana* flagellum and which null mutants present with a motility phenotype.

2.2. Results

2.2.1. The *Leishmania mexicana* genome encodes 35 putative cyclic nucleotide signalling components

Several search strategies were combined in attempts to curate an inclusive list of potential cyclic nucleotide signalling components. First, searching the TriTryp database (TriTrypDB) for any proteins that contain domains associated with cAMP synthesisers: adenylate cyclase (AC) (PF00211), cAMP degraders: phosphodiesterase (PDE) (PF00233), or cAMP effectors: cyclic nucleotide binding domains (CNBD) and cAMP-regulated phosphoprotein (PF00027, SSF51206, PF04667), yielded a list of 33 genes. It must be noted now that since these lists were compiled in 2018, the TriTrypDB has undergone several version updates and the gene PNUT36 (LmxM.31.1990) which was initially annotated as cAMP-regulated phosphoprotein (PF04667), is now listed as hypothetical protein, however we chose to still report on the data collected for this component. Additionally, as direct published experimental evidence for cAMP binding is lacking for all the *Leishmania* CNBD containing proteins, we chose to refer to them as putative (cyclic) nucleotide/nucleoside transducers (PNUT) (see Table 2-1) to emphasise this unanswered question of what the proteins bind *in vivo*. Next, we used literature searches to curate this list. Work published in 2013 (186) identified novel cAMP response proteins (CARPs) named CARP1-4 in *Trypanosoma brucei*. As CARP1 was already on our list as it contains a CNBD (PF00027), and CARP3 is *Trypanosoma* specific, we added CARP2 (LmxM.09.0780) and CARP4 (LmxM.25.1460) which form essentially a fourth category of (likely) indirect downstream effectors.

Table 2-1: Putative cyclic nucleotide signalling components in L. mexicana.

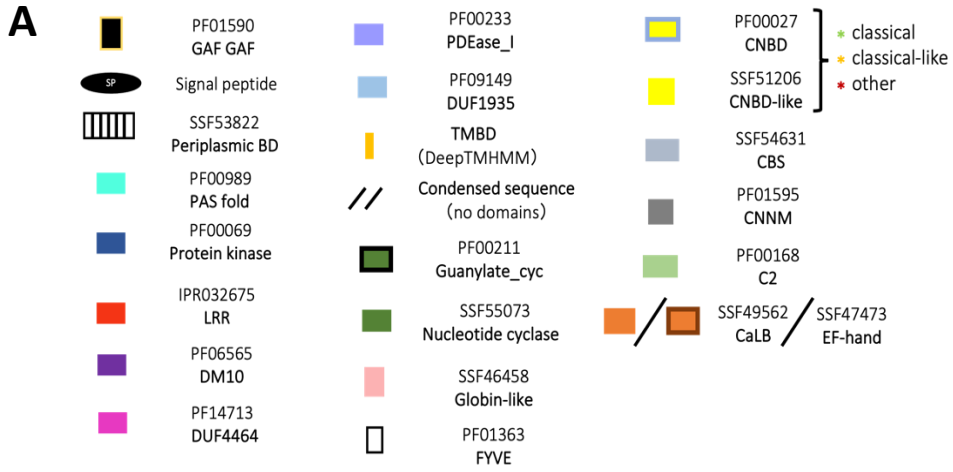
The first column indicates the complete deletion (green), incomplete deletion (orange) and unsuccessful generation (grey) of null mutants for that target gene. Leishmania Gene IDs (column 2) curated from a search for putative cyclic nucleotide signalling component detailed in section 2.2. Excluded from the list are the divergent protein kinase A regulatory subunits. Added to the list are CARPs sourced from (186). The given mutant names for each generated cell line are listed in column 3, where the respective protein length of each protein product (column 4). Columns 5-6 list the predicted PFAM and Superfamily domains within each protein with column 7 summarising the domains in each protein. Abbreviations: PK – protein kinase, DUF– domain of unknown function, CNBD – cyclic nucleotide binding domain, CBS - cyclin and cystathionine β-synthase, TMD – transmembrane domain, PBD – periplasmic binding protein.

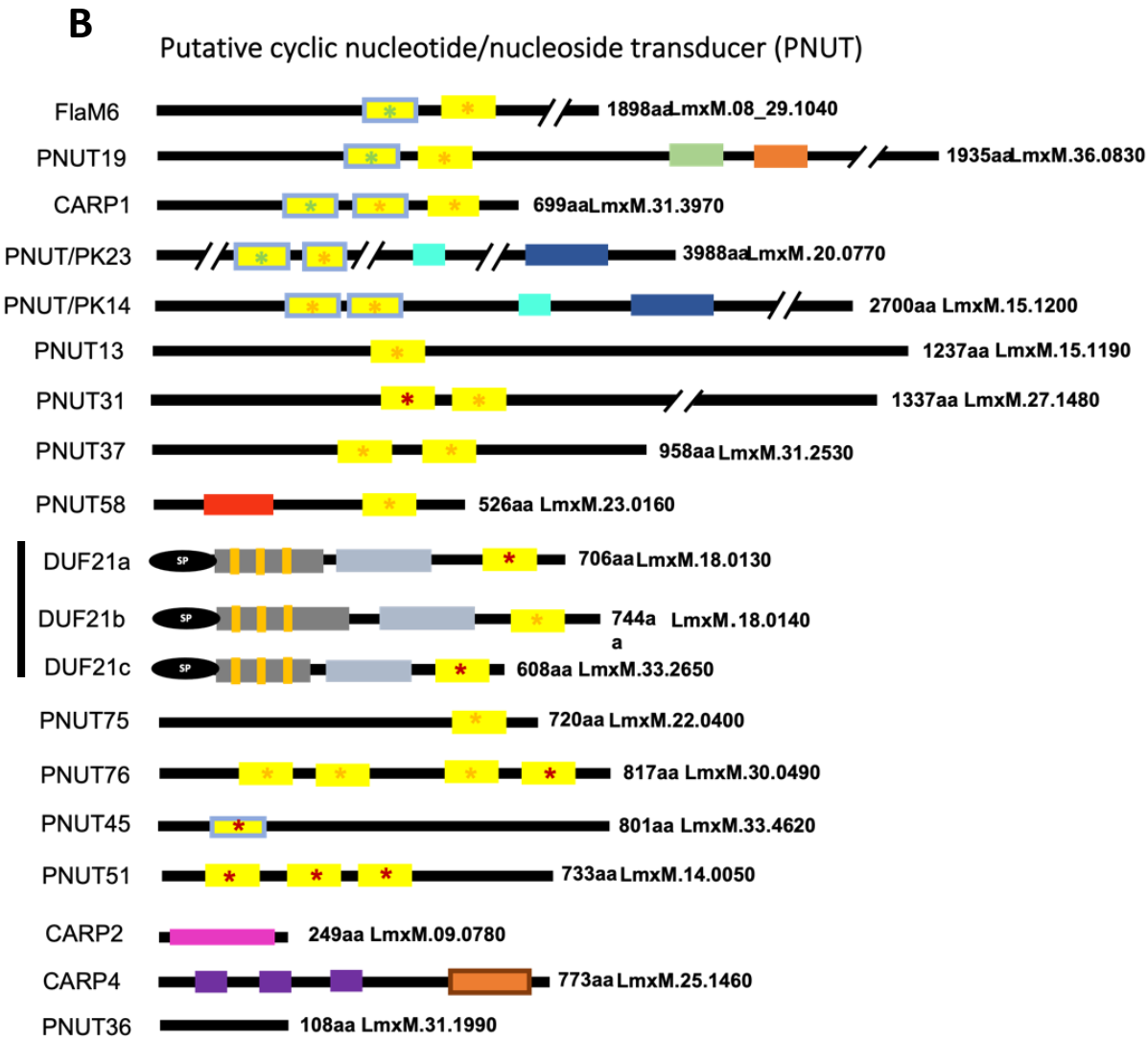
Table legend on previous page.

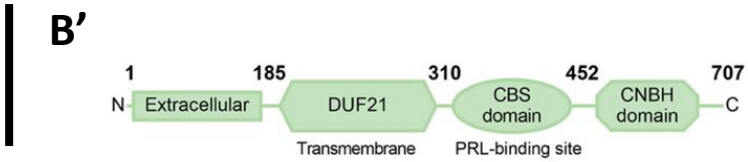
	Knockout attempt	Gene ID	Given Name	Length (aa)	PFam ID	Superfamily ID	Domains
Putative Nucleotide/Nucleoside Transducer (PNUT)		LmxM.08_29.1040	FlaM6	1898	PF00027	SSF51206	CNBD
		LmxM.09.0780	DUF4464/CARP2	249	PF14713	N/A	DUF4464
		LmxM.14.0050	PNUT51	733	N/A	SSF51206	CNBD
		LmxM.15.1190	PNUT13	1237	N/A	SSF51206	CNBD
		LmxM.15.1200	PNUT/PK14	2700	PF00027;PF00069;PF00989	SSF51206;SSF52172; SSF55785;SSF56112	CNBD;Protein kinase;PAS
		LmxM.18.0130	DUF21a	706	PF01595	SSF51206;SSF54631	CNNM;CNBD;CBS;TMD
		LmxM.18.0140	DUF21b	744	PF01595	SSF51206;SSF54631	CNNM; CNBD; CBS;TMD
		LmxM.20.0770	PNUT/PK23	3988	PF00027;PF00069;PF00989	SSF51206;SSF55785; SSF56112	CNBD;Protein kinase;PAS
		LmxM.22.0400	PNUT75	720	N/A	SSF51206	CNBD
		LmxM.23.0160	PNUT58	526	N/A	SSF51206;SSF52047	CNBD;RNI-like
		LmxM.25.1460	CARP4	773	PF06565	SSF47473	DUF1126;EF-hand
		LmxM.27.1480	PNUT31	1337	N/A	SSF51206	CNBD
		LmxM.30.0490	PNUT76	817	N/A	SSF51206	CNBD
		LmxM.31.1990	PNUT36	108	N/A	N/A	
		LmxM.31.2530	PNUT37	958	N/A	SSF51206	CNBD
		LmxM.31.3970	CARP1	699	PF00027	SSF51206	CNBD
		LmxM.33.2650	DUF21c	608	PF01595	SSF51206;SSF54631	CNNM;CNBD;CBS;TMD
		LmxM.33.4620	PNUT45	801	PF00027	SSF51206	CNBD
		LmxM.36.0830	PNUT19	1935	PF00027;PF00168	SSF49562;SSF51206	CNBD;C2-domain
adenylate cyclase		LmxM.05.0050	hypAC	841	N/A	SSF55073	Nucleotide cyclase
		LmxM.17.0190	RAC3	1411	PF00211	SSF53822;SSF55073	Nucleotide cyclase; PBP
		LmxM.17.0191	RAC4	1392	PF00211	SSF53822;SSF55073	Nucleotide cyclase; PBP
		LmxM.17.0200	RACa	1372	PF00211	SSF53822;SSF55073	Nucleotide cyclase; PBP
		LmxM.17.0235	RAC1	1400	PF00211	SSF53822;SSF55073	Nucleotide cyclase; PBP
		LmxM.17.0236	truncRAC	209	N/A	SSF53822	PBP
		LmxM.17.0237	RAC2	1330	PF00211	SSF53822;SSF55073	Nucleotide cyclase;PBP
		LmxM.28.0090	HemAC	677	PF00211	SSF46458;SSF55073	Nucleotide cyclase;Globin-like
		LmxM.36.3180	RAC-a-like	1410	PF00211;PF09149	SSF101601;SSF55073	Nucleotide cyclase;Smp1-like
phosphodiesterase		LmxM.04.0030	PDE U1	667	PF00233	SSF109604	HD-domain/PDEase-like
		LmxM.08_29.2440	PDE D	714	PF00233	SSF109604	HD-domain/PDEase-like
		LmxM.08_29.2680	PDE C	1083	PF00233;PF01363	SSF109604;SSF57903	HD-domain/PDEase-like;FYVE
		LmxM.15.1480	PDE B2	930	PF00233;PF01590	SSF109604;SSF55781	HD-domain/PDEase-like;GAF
		LmxM.15.1481	PDE B1	940	PF00233;PF01590	SSF109604;SSF55781	HD-domain/PDEase-like;GAF
		LmxM.17.0950	PDE U2	1587	PF00233	SSF109604	HD-domain/PDEase-like
		LmxM.18.1090	PDE A	631	PF00233	SSF109604	HD-domain/PDEase-like

Recent work in *T. brucei* and *T. cruzi* detailed how the kinetoplastid PKAR subunit has diverged away from binding cyclic nucleotides, where the same pattern of sequence divergence within the CNBD has been found in *Leishmania* spp (142,204). Thus, the two PKAR on our list were removed and investigated separately (see Chapter 3). Lastly, to ensure no components were missed out, we performed protein BLAST searches against the *L.*

mexicana genome. Using RAC-a (LmxM.17.0200) as query sequence revealed an additional two ACs, hypothetical AC (LmxM.05.0050), and a truncated RAC-b (LmxM.17.0236). A BLAST search using PDE A (LmxM.18.1090) or the CNBD amino acid sequences from CARP1 revealed no additional undiscovered genes to add to our list, leaving us to conclude that the *L. mexicana* genome encodes a set of at least 35 putative cyclic nucleotide signalling components comprising of 9 ACs, 7 PDEs, and 19 putative cyclic nucleotide transducers (Table 2-1). We used InterProScan (215) and DeepTMHMM (216) webtools to predict the domain architecture and presence of transmembrane domains (TMD) and signal peptides. Of these 35 signalling components (Figure 2-1), we saw that there were two large PNUTs, which we named PNUT/PK14 (2700 aa) and PNUT/PK23 (3988 aa), with very similar architecture, *i.e.* two N-terminal CNBDs, one mid protein PAS fold and one C-terminal protein kinase domain (Figure 2-1A, 1B). Also apparent was a set of three DUF21 (PF01595) containing proteins, the only PNUTs in our list predicted to have transmembrane domains. Consulting literature, it was apparent that the cyclin M family of proteins (a.k.a. ancient conserved domain proteins (ACDP)) have identical protein architecture to our DUF21 containing *L. mexicana* proteins (Figure 2-1B') (217). Published work allocates these a function of magnesium or metal ion homeostasis, as putative transporters, where the C-terminal cyclic nucleotide binding homology (CNBH) region has been evolutionarily repurposed to mediate protein dimerization within the membrane, rather than binding cyclic nucleotides (217). This would be one explanation for the divergence in phosphate binding cassette (PBC) sequence detailed in Chapter 2, Section 2.2.1, Figure 2-4C.


A
PF01590
GAF GAF
Signal peptide
SSF53822
Periplasmic BD
PF00989
PAS fold
PF00069
Protein kinase
IPR032675
LRR
PF06565
DM10
PF14713
DUF4464
PF00233
PDEase_I
PF09149
DUF1935
TMBD
(DeepTMHMM)
Condensed sequence
(no domains)
PF00211
Guanylate_cyc
SSF55073
Nucleotide cyclase
SSF46458
Globin-like
PF01363
FYVE
PF00027
CNBD
SSF51206
CNBD-like
classical
classical-like
other
SSF54631
CBS
PF01595
CNNM
PF00168
C2
SSF49562
CaLB
SSF47473
EF-hand


B
Putative cyclic nucleotide/nucleoside transducer (PNUT)
FlaM6
1898aaLmxM.08_29.1040
PNUT19
1935aaLmxM.36.0830
CARP1
699aaLmxM.31.3970
PNUT/PK23
3988aaLmxM.20.0770
PNUT/PK14
2700aa LmxM.15.1200
PNUT13
1237aa LmxM.15.1190
PNUT31
1337aa LmxM.27.1480
PNUT37
958aa LmxM.31.2530
PNUT58
526aa LmxM.23.0160
DUF21a
706aa LmxM.18.0130
DUF21b
744a
a
LmxM.18.0140
DUF21c
608aa LmxM.33.2650
PNUT75
720aa LmxM.22.0400
PNUT76
817aa LmxM.30.0490
PNUT45
801aa LmxM.33.4620
PNUT51
733aa LmxM.14.0050
CARP2
249aa LmxM.09.0780
CARP4
773aa LmxM.25.1460
PNUT36
108aa LmxM.31.1990


B'
1
185
310
452
707
N
Extracellular
DUF21
CBS
domain
CNBH
domain
C
Transmembrane
PRL-binding site

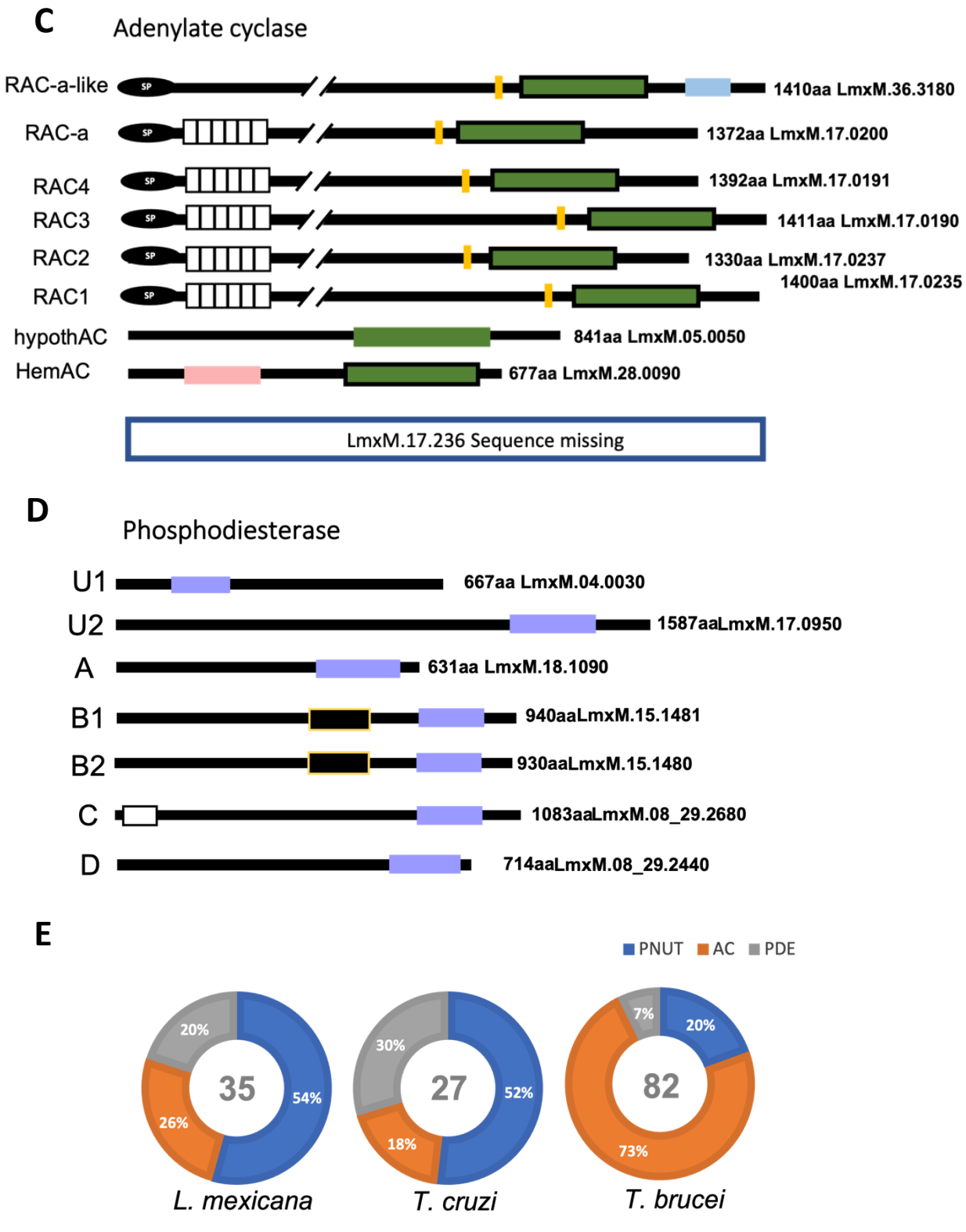


Figure 2-1: Protein domain architecture for L. mexicana putative cyclic nucleotide signalling components.

(A) Key for predicted protein domains using amino acid sequences sourced from TriTrypDB and InterProScan for domain prediction. (B) Domains within Putative Nucleotide/Nucleoside Transducers

(PNUTs). The coloured asterisks within the predicted CNBDs indicate which of the proteins contain canonical residues for cAMP binding (green asterisk) as defined in Section 2.2.1. (B') Published domain architecture for Homo sapiens CNNM3, also known as cyclin M, CNNM family or DUF21 containing proteins, demonstrating the similar protein architecture of the Leishmania DUF21 containing proteins. Sourced from (Chen et al. 2018). (C) Domains within adenylate cyclase (AC) and (D) Phosphodiesterase (PDE). (E) Infographic representing putative cyclic nucleotide signalling components from parallel searches in L. mexicana, T. cruzi and T. brucei. Centre number is the total number of components. Percentages represent proportions of total that are made up by PNUTs, AC or PDE.

Also notable in our list were proteins PNUT19 and CARP4 which contained calcium lipid binding protein (CaLB) and an EF-hand respectively, highlighting components which may serve at the potential crossroad between cyclic nucleotide and calcium second messenger signalling (Figure 2-1B). Six of the adenylate cyclase (AC) demonstrated a predicted N-terminal signal peptide and mid-protein TMD which defines them as putative receptor type adenylate cyclase (RAC) (173), where the hypothetical AC (hypothAC) and oxygen sensing AC (HemAC) were predicted to be globular proteins (Figure 2-1C). Lastly, in addition to the five known PDE isoforms (A, B1, B2, C and D), we found two extra proteins containing a PDE catalytic domain (PF00233). These proteins contained no other predicted domains, and they were named as isoforms unknown 1 (U1) and U2 (Figure 2-1D). Interestingly, none of the PDEs were predicted by DeepTMHMM to have TMDs, in contrast to TriTrypDB annotations which predicts that isoform D had one C-terminal TMD.

Performing similar parallel searches in *T. brucei* and *T. cruzi* (Figure 2-1E) reveal a similar number of phosphodiesterase (Tb: 6, Tc: 8) and PNUTs (Tb: 16, Tc: 14) to *L. mexicana*, and highlighted the expanded repertoire of *T. brucei* adenylate cyclase (Tb: 60, Tc: 5), including ACs that are expression site associated genes (ESAGs) which are hypothesised to modulate the host immune response during mammalian infection (173,218) (Section 1.3.1.2).

2.2.1.1. L. mexicana genomes encode a highly divergent set of cyclic nucleotide transducers

As it has been demonstrated that proteins containing predicted CNBDs do not necessarily bind cAMP (142), we next set out to scrutinise our set of PNUTs to identify if any have diverged similar to that reported in these *Trypanosoma* PKAR.

The mechanism of cyclic nucleotide binding to its transducer proteins is shared across protein found in pro- and eukaryotic species. The sequences of cyclic nucleotide binding domains are very conserved, being first described in the cyclic AMP receptor protein (CRP) of *E. coli* (219). An invariable glutamate (E) and arginine (R) residue reside within the CNBD phosphate binding cassette (PBC) to form hydrogen bonds with the hydroxyl group on the ribose sugar, and the exocyclic phosphate respectively (Figure 2-2) (125).

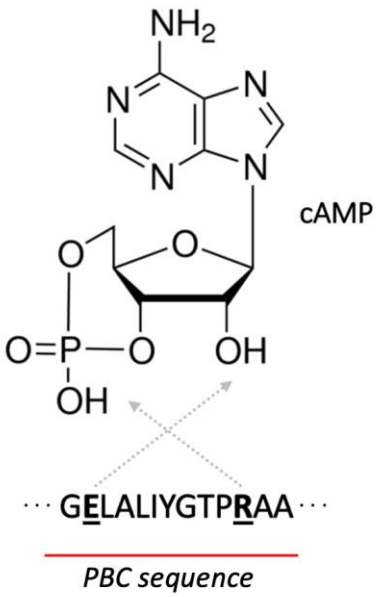


Figure 2-2: Important residues within the phosphate binding cassette (PBC).

Pictural representation of the hydrogen bond formation (dotted lines) between glutamate and arginine residues (bold underlined) and the hydroxyl and exocyclic phosphate groups of

cAMP respectively. Amino acid sequence of the PBC located within the cyclic nucleotide binding domain is shown. Sequence sourced from (142).

We started by creating a reference panel of known cAMP transducers for which a cAMP bound structure has been solved, with which to compare our putative *Leishmania* PNUTs. We identified 29 cyclic nucleotide binding domains co-crystalised with cAMP from 23 proteins on protein database (PDB) and used these as a *bona fide* reference for 3D conformation and cAMP binding position. We generated a multiple sequence alignment of these CNBDs, which mostly corroborated the literature consensus. All 29 sequences contained two conserved glycine residues separated by 11 amino acids towards the N-terminus of the CNBD (Figure 2-3). The PBC (green underlined sequence in Figure 2-3) was easily identifiable, starting with a glycine-glutamate (GE – positions 1 and 2) and containing an R in position 11 for 26 of the co-crystal structures. It was intriguing to see that the three sequences for the CNBDs of *E. coli*, *Y. pestis* and *P. aeruginosa*, had an additional 1-4 amino acids from position 8 of the PBC, highlighted in blue in Figure 2-3. This may be an underlying feature of the cyclic AMP response protein (CRP/CAP) repertoire of prokaryotes.

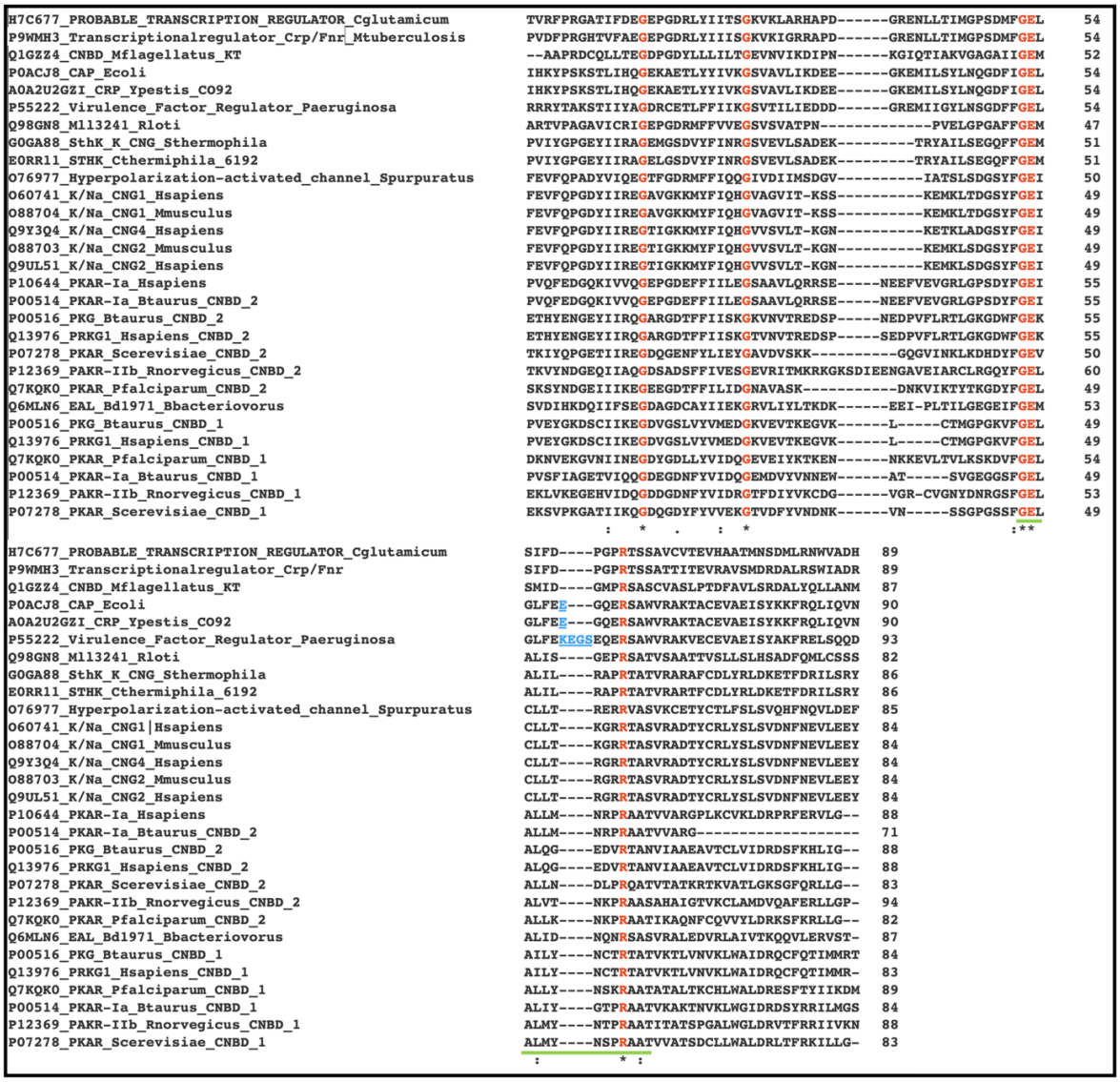


Figure 2-3: Sequence alignment of proteins which are bound to cAMP.

Reference panel alignment of 29 CNBD sequences from proteins on PDB which have been co-crystalised with a cAMP molecule. Protein accession numbers from GenBank listed to the left alongside abbreviated protein annotation and species. Red residues with an asterisk are invariable across all aligned sequences. Blue underlined residues represent non-canonical insertions within the phosphate binding cassette (PBC). PBC sequence underlined in green. Clustal Omega was used for creating alignment.

To identify the PBC sequences present in our 16 *Leishmania* proteins with CNBDs (Table 2-1), we aligned one-by-one each of the 29 CNBD sequences in these proteins against three classical reference CNBDs, namely, the *Bos taurus* PKARI-α (accession: P00514) CNBD1 (PBC sequence: **GE**LALIYGTP**R**AA), the *Mus musculus* CNG (PBC sequence: **GE**ICLLTKGR**R**TA) (accession: O88704) and the *Plasmodium falciparum* CNBD1 of PKAR (PBC sequence: **GE**LALLYNSK**R**AA) (accession: Q7KQK0).

Surprisingly, we found that only four CNBDs from four proteins contained the GE and R residues in the expected conserved positions within the PBC. This finding led us to categorise the 28 CNBDs found in *L. mexicana* proteins according to the residues in their PBC into 'classical', 'classical-like', and 'non-classical' categories (Figure 2-4). Classical CNBDs contain PBC sequences with GE at position 1 and 2, and R at position 11 of the PBC. Classical-like contain only the initial GE, and non-classical PBCs yield poor sequence similarity or no clear alignment (NCA) (exemplified in Figure 2-4D, 4E) when aligned against the three classical reference PBC sequence.

From our 29 *Leishmania* CNBDs, four *Leishmania* PNUTs (Flagellar Member 6 (FLAM6), cyclic AMP response protein (CARP1), PNUT19 and PNUT/PK23) contained at least one classical PBC (Figure 2-4A).

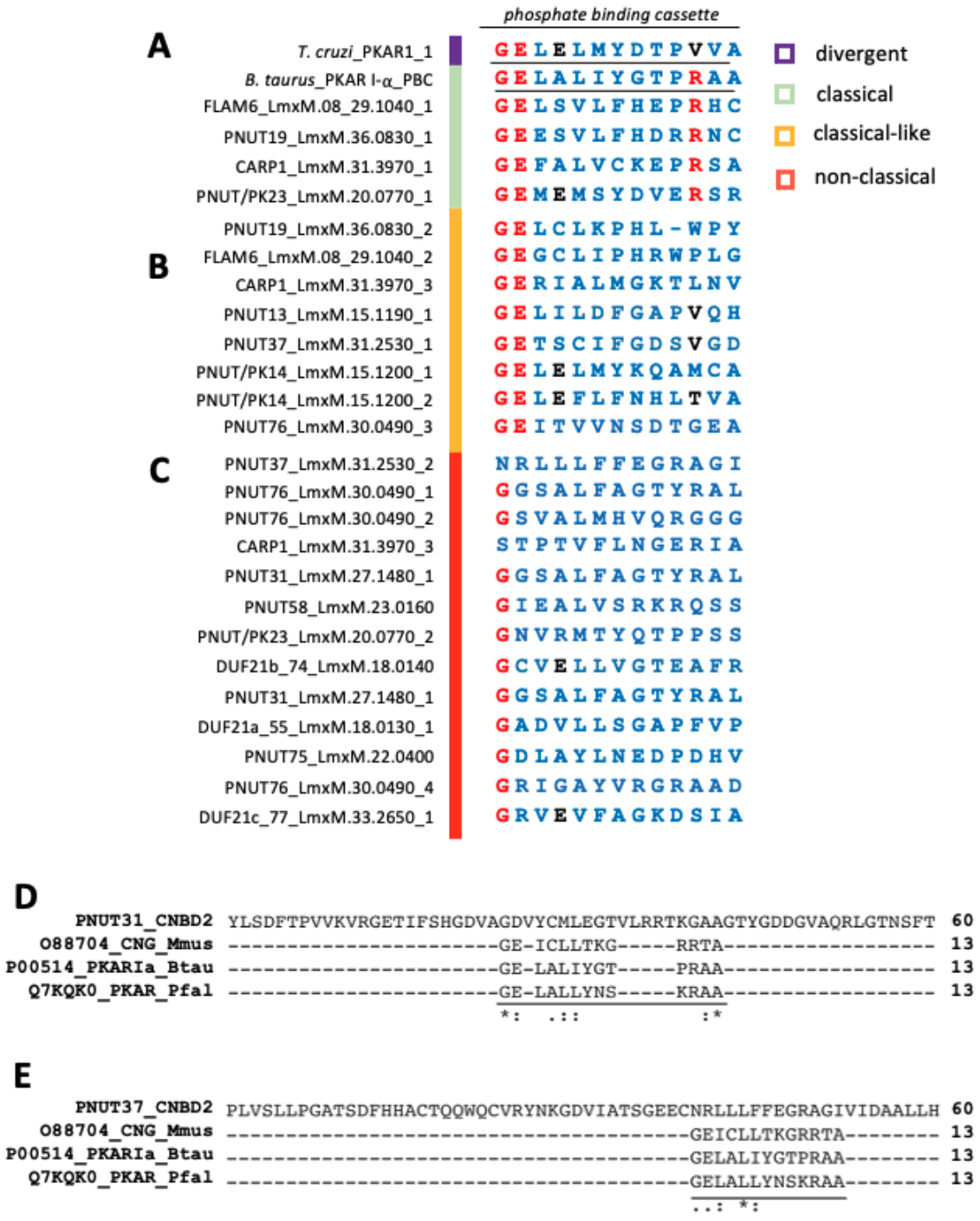


Figure 2-4: Categorisation of PBC sequences in the Leishmania PNUTs.

Amino acid sequence alignment of predicted PBCs found by aligning each of the 29 L. mexicana PNUT CNBDs, identified as SSF51206 domains by Interproscan, against three classical reference PBCs, namely, B. taurus PKAR Iα (accession: P00514) CNBD1 PBC sequence (GELALIYGTPRAA), the Muc musculus CNG PBC sequence (GEICLLTKGRRTA) (accession: O88704) and the Plasmodium falciparum CNBD1 of PKAR PBC sequence (GELALLYNSKRAA) (accession: Q7KQK0). Reference sequence for divergent T. cruzi PKAR1 (gene ID: TcCLB.506227.150) highlights key residue switches (black) which

indicate protein selectivity towards a novel nucleoside analogue (142). PBCs are categorised into (green) 'classical', (orange) 'classical-like' and (red) 'non-classical' according to consensus residues found within the reference CNBD panel. Red residues indicate the invariable GE and R of canonical PBC sequences. Example alignments of (D) PNUT31 CNBD2 and (E) PNUT37 CNBD2 demonstrate what we refer to as a 'no clear alignment' (NCL) and a clear alignment with poor sequence similarity respectively. Underlined sequences highlight the phosphate binding cassettes of reference sequences. Built on work from Xiaojun Peng Masters project. Clustal Omega used to make alignments.

Six CNBDs *i.e.* CNBD1-3 of PNUT51, CNBD2 of PNUT31, CNBD2 of CARP1 and CNBD1 of PNUT45, yielded NCA against the reference PBCs. Eight CNBDs (from 7 proteins) contained classical-like PBC sequences (Figure 2-4B). And lastly, 13 CNBDs (from 10 proteins) contained non-classical PBCs (Figure 2-4C). Interestingly, our alignment with the divergent *T. cruzi* PKAR1 (142) indicated that *L. mexicana* PNUT/PK14, a large (2700aa) kinase domain containing (PF00069) protein (Figure 2-1B) follows similar patterns of divergence (Figure 2-4A), with a negative glutamate at position 4 and the substitution of a positive arginine at position 11 to a neutral residue with a short side chain (A, T, V or N reported) (142). These residues have been described to cause selectivity to the synthetic PKA activator 7-CN-7-C-ino (a.k.a. Jaspamycin), and insensitivity towards cAMP (142).

Alignments of the full classical *Leishmania* CNBD sequences to classical reference *B. taurus* PKARI-a and divergent reference *T. cruzi* PKAR1 CNBD-A, we saw that three *Leishmania* CNBDs contained the two N-terminal glycine residues (red in Figure 2-5), however PNUT/PK23 contained a serine insertion (blue in Figure 2-5) between the two

conserved glycines. We see that in the same alignment position, the divergent TcPKAR1 also had an insertion of a threonine.



Figure 2-5: Full CNBD sequence alignment of Leishmania 'classical' CNBDs.

Protein sequence alignment of L. mexicana classical CNBDs with reference canonical Bos taurus PKAR Iα CNBD-A and reference divergent T. cruzi PKAR1 CNBD-A. Highlighted in red are invariable residues for cAMP binding according to our reference panel alignment (Figure 2-4). Residues in blue indicate divergent insertions which disagree with the canonical cAMP reference panel. Residues in green are reported to result in repulsion to cAMP binding according to the descriptions from divergent T. cruzi PKAR1 source (142). Box indicates location of the phosphate binding cassette. Clustal Omega used to make alignments.

Although the sequence of the four classical *L. mexicana* CNBDs appear to agree with the reference sequence with three key residues known to be involved in cAMP binding, we used homology modelling and docking predictions to further scrutinise whether the 3D folding of the CNBDs these proteins conformed with the reference panel of co-crystal structures.

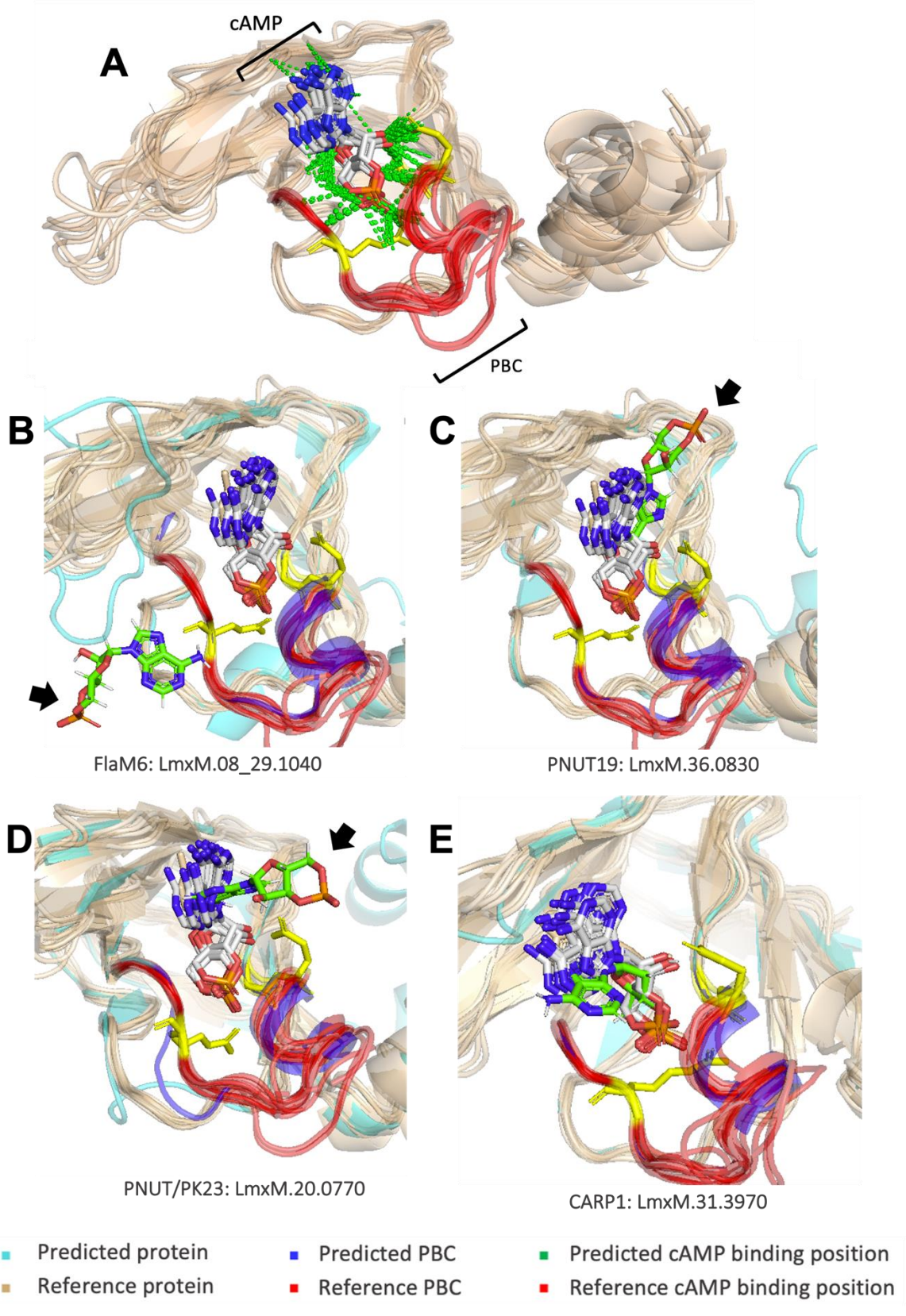


Figure legend on following page.

Figure 2-6: Homology modelling of classical CNBDs of L. mexicana and predicted cAMP docking position.

(A) Overlay of 16 reference PDB structures showing CNBDs co-crystalised with cAMP. The phosphate binding cassette (PBC) is highlighted in red, with G, E and R residues important for cyclic nucleotide docking are in yellow. (B-E) Structures of L. mexicana protein CNBDs with 'classical' PBC sequences (cyan) modelled using SWISS-MODEL, where the CNBD protein sequence was submitted and the model with the highest QMEANDisCo was chosen (FlaM6: 1hw5 (QMEANDisCo 0.55), PNUT19: 6wek (QMEANDisCo 0.64), PNUT/PK23: 3of1 (QMEANDisCo 0.69) and CARP1: 5kbf (QMEANDisCo 0.67)). Swiss Dock prediction of cAMP molecule binding site, where the closest position of cAMP to the PBC binding pocket was chosen to display (green). Black arrows indicate where the cAMP molecule is flipped so that the exocyclic phosphate is pointing away from the PBC. Built on work from Xiaojun Peng Masters project. PyMol software was used to visualise and create figures.

Firstly, the predicted cAMP docking position (Swiss Dock) for FlaM6 was far away in comparison to the reference proteins (Figure 2-6A, 6B). CARP1 and PNUT19 contained CNBDs with the most comparable 3D structure and predicted docking site for cAMP to our reference panel (see Figure 2-6), however upon closer inspection, the PNUT19 cAMP molecule appeared rotated so that the exocyclic phosphate is positioned away from the PBC region (Figures 2-6C and 2-7B). This cAMP repulsion in PNUT19 appeared to be due to a glutamate in position 3 of the PBC, highlighted in green in Figure 2-7B, which appears to be acting similar to the glutamate in position 4 of the PNUT/PK23. In divergent *T. cruzi* PKAR1, a switch from alanine to glutamate at position 4 of the PBC was associated with cAMP repulsion from the pocket due to negative charge clashing (142). This glutamate at position 4 is observed in 5 *Leishmania* CNBDs (black residues in Figure 2-4B, 4C), namely in both CNBDs of PNUT/PK14, CNBD4 of PNUT76, CNBD1 of DUF21c, and in the classical PBC of CNBD1 of PNUT/PK23. Despite having classical (GE and R) residues within the PBC of PNUT19 and PNUT/PK23, we anticipate that these residues alone are not enough to predict the

biological substrate but need to be assessed alongside the divergent residue substitutions described. Although it has not been directly documented to clash with cAMP, as aforementioned (142), it appears as though the glutamate at position 3 of the PNUT19 PBC is predicted by Swiss Dock to clash with the cAMP molecule similar to a glutamate at position 4 (Figure 2-7B), therefore unlikely to form the required hydrogen bonds for stable cAMP docking. To understand whether a negative residue may be tolerated at position 3, we consulted the classical reference panel of cAMP bound CNBD sequences, and we saw that none of the residues in position three or four were negatively charged, suggesting that glutamates within certain positions of the PBC are potentially predictive of divergence towards cAMP insensitivity.

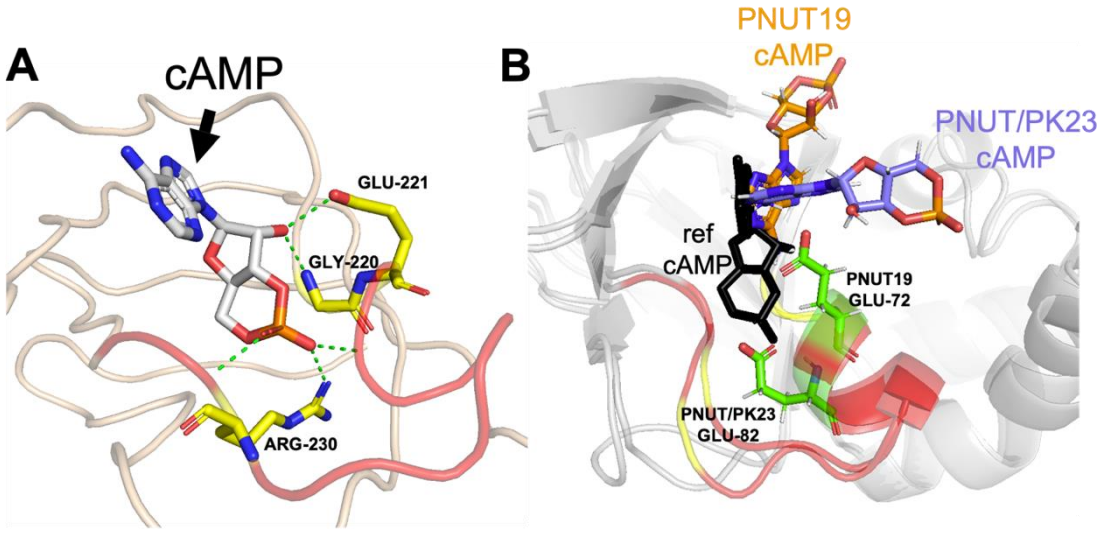


Figure 2-7: cAMP repulsion out of the PBC binding pocket in Leishmania classical PNUTs.

(A) Classical CNBD co-crystallised with cAMP, taken from PBD: 1CX4 (Rattus norvegicus PKARII-beta) demonstrating hydrogen bonds (green dashes) and positioning of cAMP (black arrow) within the binding pocket. G, E and R indicated in yellow and labelled. (B) Homology modelled CNBDs of PNUT19 and PNUT/PK23 from Figure 2-6C, 6D respectively (grey), highlighting the negatively charged glutamate residues (green) within the PBC (red PBC/yellow G, E and R residues) which are predicted by Swiss Dock to repel the cAMP molecule away from the binding site (purple and orange). The classical binging position of

cAMP from 1CX4 is in black for reference. PyMol software was used to visualise and create figures.

Ultimately, of all the predicted *L. mexicana* proteins with CNBDs, four CNBDs in four proteins (FlaM6, CARP1, PNUT23 and PNUT19) contained the classical GE and R residues within the PBC sequences (Figure 2-4A). Additional glutamates present within position three and four of the PNUT19 and PNUT/PK23 PBCs respectively allude to a potential for cAMP repulsion from the binding pocket and was reflected in our homology modelling and predicted docking of cAMP (Figure 2-7B). Lastly, as predicted docking suggested cAMP did not bind into the CNBD PBC of FlaM6, our *in silico* assessment of *Leishmania* cyclic nucleotide binding proteins ultimately concludes that CARP1 is the strongest candidate for cAMP binding. Moreover, this analysis highlighted several *L. mexicana* CNBDs, particularly that of PNUT/PK14 which resemble the divergent CNBDs that were shown not to bind cAMP and instead bind nucleoside analogues such as 7-CN-7-C-ino (142).

2.2.2. Fluorescent tagging libraries revealed cAMP signalling is confined to precise sub-cellular domains

Indirect immunofluorescence and immunogold-EM techniques have succeeded in localising the PDE B1/B2 proteins (164) as well as several ACs (159,220) to the motile flagellum, however antibody-based techniques are expensive to use on a large scale localisation screen. CRISPR gene editing tools developed for kinetoplastid spp. (221) allow for rapid and precise insertion of fluorescent protein tags at the endogenous gene locus to facilitate protein localisation. To determine the localisation of the putative cyclic nucleotide signalling

components defined in Table 2-1, we made libraries of mutants expressing fluorescent fusion proteins. Since tagging can disrupt localisation sequences (*e.g.,* signal peptides), we tagged both the N- and C-terminus for each protein separately. We targeted all 35 signalling components to express endogenously fused mNeonGreen (mNG) and successfully yielded mutants with at least one terminus tagged for 32 of the 35 components. We failed in determining the localisation of two ACs due to a lack of genomic sequence with which to design primers for this tagging strategy, and additionally one cyclic nucleotide transducer.

2.2.2.1. Six of the seven phosphodiesterase are detectable in the flagellum

PDE B1 and B2

Endogenously tagged mutants were successfully gained for all 7 phosphodiesterases. The PDE B1 and B2 signals in *L. mexicana* were most intense at the distal end of the flagellum, gradually tapering off towards the proximal end, most noticeably for the C-terminal tags (Figure 2-8B). In many but not all the cells, PDE B1 and B2 signals were seen to be also slightly enriched in the basal body (white arrows in Figure 2-8). A notable disparity between PDE B1 and B2 localisations is the presence of a singular bright dot in the cell body of PDE B2::mNG expressing mutants, (circled in Figure 2-8A). This bright dot was observed in ~18% cells (n=87), occasionally seen in the midbody and occasionally at the very posterior tip (example cells shown in Figure 2-9). It did not appear to correlate with any obvious organelle visible by phase contrast illumination (*i.e.* acidocalcisomes) (79).

The PDE B orthologs in *T. brucei* were reported to associate with the paraflagellar rod (PFR) (164), a structure that does not extend to the distal portion of the *L. mexicana* flagellum (79). We examined the localisation of tagged PFR2 (LmxM.16.1430), a major PFR component

(42,43), in the tagged PDE B2 cell line and found that the signals were distinct (Figure 2-8C). PFR2 signal was most intense in the proximal half of the external flagellum with a gradually diminishing signal in the distal half of the external flagellum, in essence, juxtaposed to the signal distribution of PDE B2.

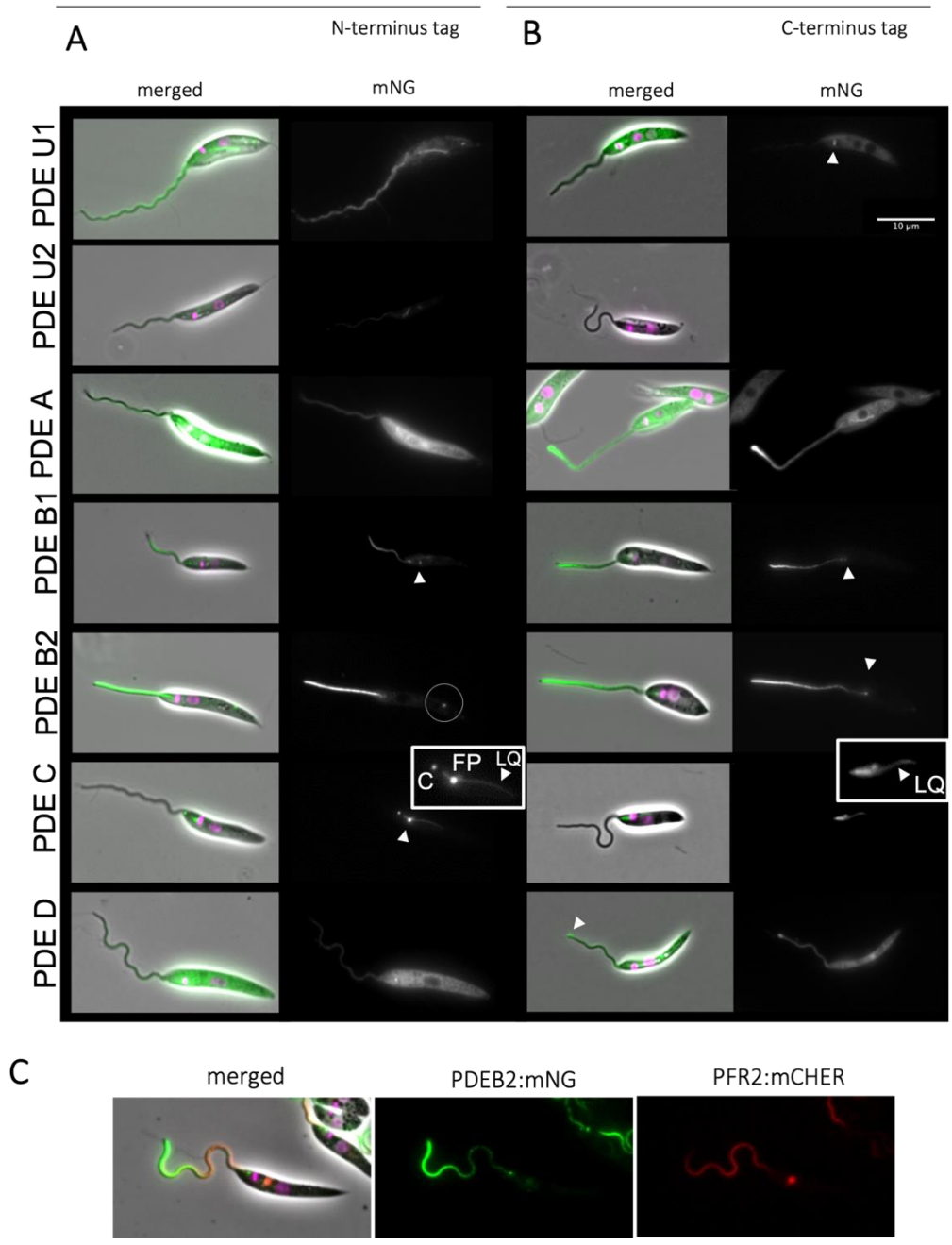


Figure 2-8: Localisation of phosphodiesterases.

(A) N-terminal tags (left) merged phase and fluorescence and (right) phase contrast. (B) C-terminal tags (left) merged phase and fluorescence and (right) phase contrast. Inset images for PDE C tags indicate the lysosomal quartet (LG), and punctate signal near the flagellar pocket (FP) and collar (C). (C) PFR2 (LmxM.16.1430) C-terminally fused with mCherry expressed on a PDEB::mNG expressing mutant background. Merged phase contract and fluorescence (left), mNG fluorescence (middle), mCherry fluorescence (right). Arrows indicate points of interest referred to in text, specifically punctate signal within the cell body. Scale bar represents 10 µM.

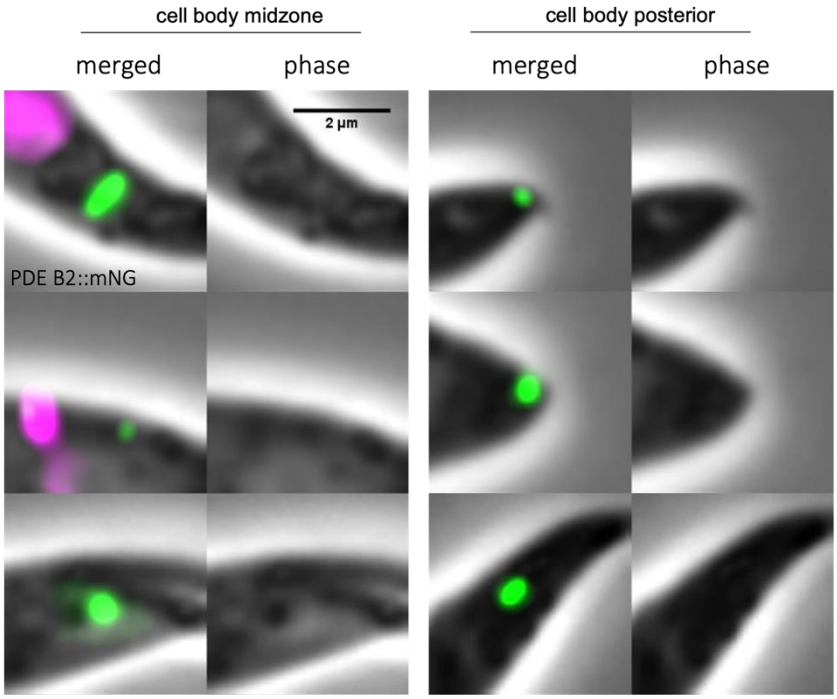


Figure 2-9: Punctate cell body signal of PDE B2.

Fluorescent micrographs of the bright punctate mNG signal observed in a significant proportion of PDE B2::mNG mutants. Signal observed in the cell body midzone (left two columns) or cell posterior (right two columns). DNA stained with Hoechst in magenta. mNG signal in green. Scale bar represents 2 µM.

PDE A and D

The N-terminal tag of PDE A appeared ubiquitous soluble with more enrichment in the cell body (Figure 2-8A). However, in contrast the C-terminal tag appeared flagellar enriched

especially towards the distal portion, with a weaker cell body signal. A similar signal disparity was observed between the PDE D N- and C-terminal tags, where the former was weak in the flagellum with a soluble cell body and punctate basal body signal (Figure 2-8A), and the latter was often enriched at the flagellar tip with a weak cell body signal (Figure 2-8B).

PDE U1 and U2

The signal from the PDE U1 N-terminal tag was weak in the cell body and enriched in the flagellum, where the C-terminal tag signal was weakly soluble in the cell body with a punctate basal body localisation. The PDE U2 N-terminal tag yielded no clear localisation.

PDE C

Lastly, PDE C isoform was the only PDE not to be detectable in the flagellum, but instead concentrated as two bright dots in the area of the flagellar pocket or basal body and collar/neck, often observed with an additional lysosomal quartet localisation (inset shown in Figure 2-8A, 8B). Published experimental evidence of PDE C isoform in *T. cruzi* points towards a role in osmoregulation and the contractile vacuole complex (CVC), where the enzyme is able to hydrolyse both cGMP and cAMP *in vitro* (145,179).

2.2.2.2. Leishmania adenylate cyclase are predominantly flagellar tip enriched

As the majority of *Leishmania* ACs have predicted signal peptides at the N-terminus (DeepTMHMM predictions, Figure 2-1C), we focused on the localisations of C-terminally fused fluorescent proteins. We successfully obtained localisations for 7 of the 9 ACs encoded

in the *L. mexicana* genome. The RAC-a-like protein localisation was unclear, localising potentially to the cell body lysosomal quartet for the C-terminal cells, however appearing reticulated in the cell body in the N-terminal expressing cells (Figure 2-10).

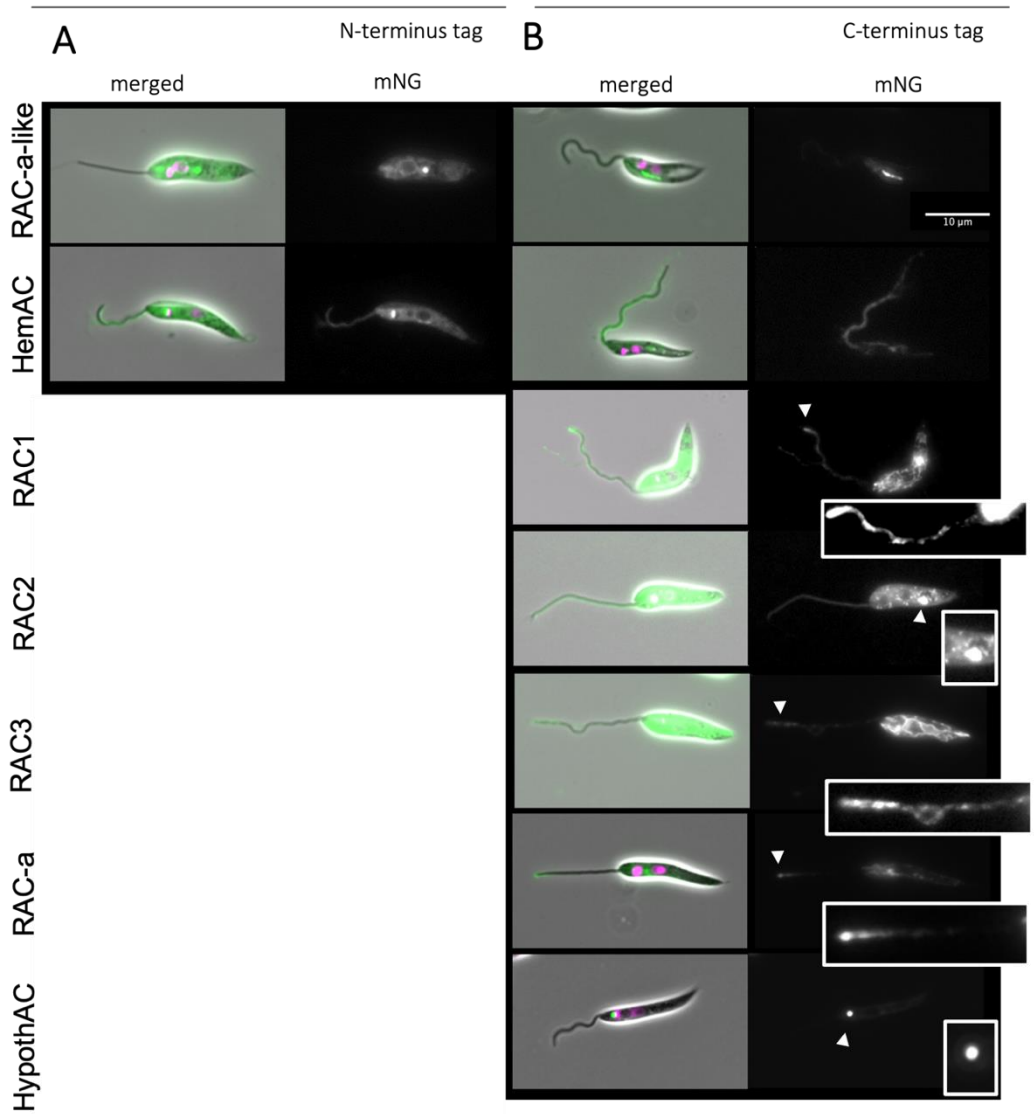


Figure 2-10: Localisation of adenylate cyclase.

(A) Micrographs of cells expressing ACs N-terminally tagged with mNG. Left panel, merged phase contrast and fluorescence signal from Hoechst DNA stain (magenta) and mNG (green). Right panel, mNG fluorescence signal only. (B) C-terminally tagged ACs, panels as for A.

Arrows point towards enriched signal at the flagellar tip and near the flagellar pocket/basal body. Inset images provide a magnified view of where the arrow points. Scale bar represents 10 µm.

Four of the RAC type proteins were obviously flagellar enriched. RAC3 (LmxM.17.0190), RAC-a (LmxM.17.0200) and RAC1 (LmxM.17.0235) displayed enrichment towards the flagellum tip membrane (inset images in Figure 2-10B) whilst the oxygen sensing AC (here named HemAC) was enriched throughout the entire flagellum (Figure 2-10B). Interestingly, the RAC4 C-terminal tag signal was faintly soluble in the flagellum however had punctate signal within the cell body. One singular large bright dot was evident centrally in the cell body of 95% cells (n = 41), mostly, but not exclusively on the posterior side of the nucleus. Interestingly, the hypothetical AC (HypothAC) we identified by BLAST searches localised to a strong punctate dot near the flagellar pocket, reminiscent of the localisation of PDE C (see Figure 2-8A).

So far, the tagging has highlighted two areas of concentration for PDEs and ACs, the contractile vacuole and the flagellum. In this study we focus on the role of cyclic nucleotides in flagellar motility and therefore the flagellar-localised proteins are of most interest for further study.

2.2.2.3. Over half of the putative cyclic nucleotide transducers were detectable in the flagellum

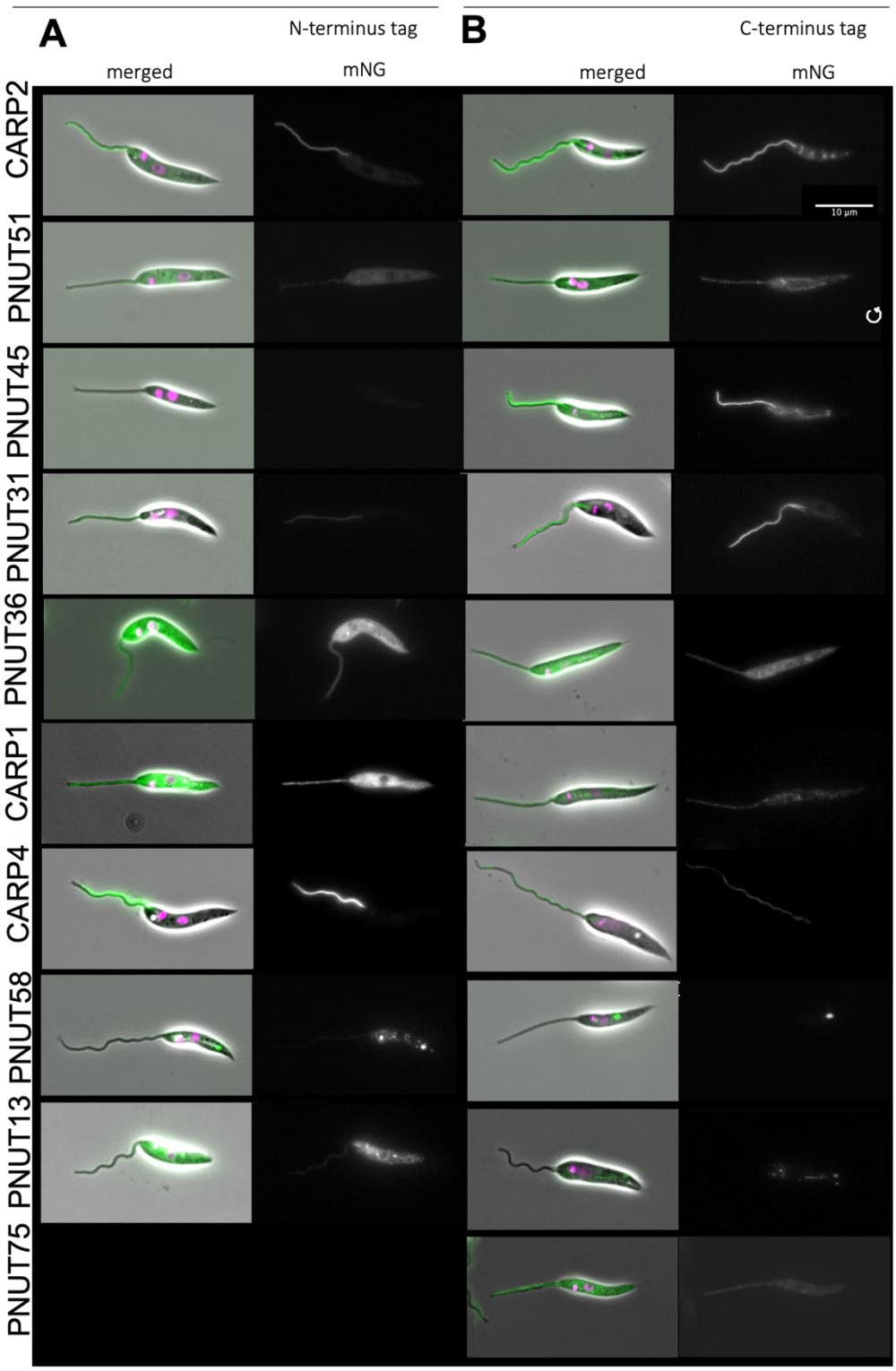
Tagging of the 19 putative cyclic nucleotide transducers yielded 18 fluorescent cell lines, of which 13 showed a flagellar signal (Figure 2-11). We observed nine distinct subcellular

microdomains for the putative transducers: flagellar axoneme, distal flagellum, proximal flagellum, flagellar pocket, flagellar collar/FAZ, contractile vacuole complex, basal body, small cytoplasmic organelles and the nucleus

Flagellum

Fluorescent signal from ten of the fluorescently tagged proteins was visible throughout the flagellar axoneme. Figure 2-11A, 11B display micrographs from CARP2, PNUT51, PNUT45, PNUT31, PNUT36, CARP1, CARP4, and PNUT75 which present a clear signal presence in the flagellum especially in C-terminal tag expressing mutants, and in Figure 2-11A, the N-terminal expressing tag cells of PNUT58 and PNUT13, present cells with extremely faint signal presence in the flagellum.

We noted that PNUT51 had a distinct cell cycle dependent localisation, enriching in the nucleus during cell division and becoming more intense towards late cell cycle (Figure 2-12).


A
N-terminus tag
merged
mNG
B
C-terminus tag
merged
mNG
CARP2
PNUT51
PNUT45
PNUT31
PNUT36
CARP1
CARP4
PNUT58
PNUT13
PNUT75
10 µm

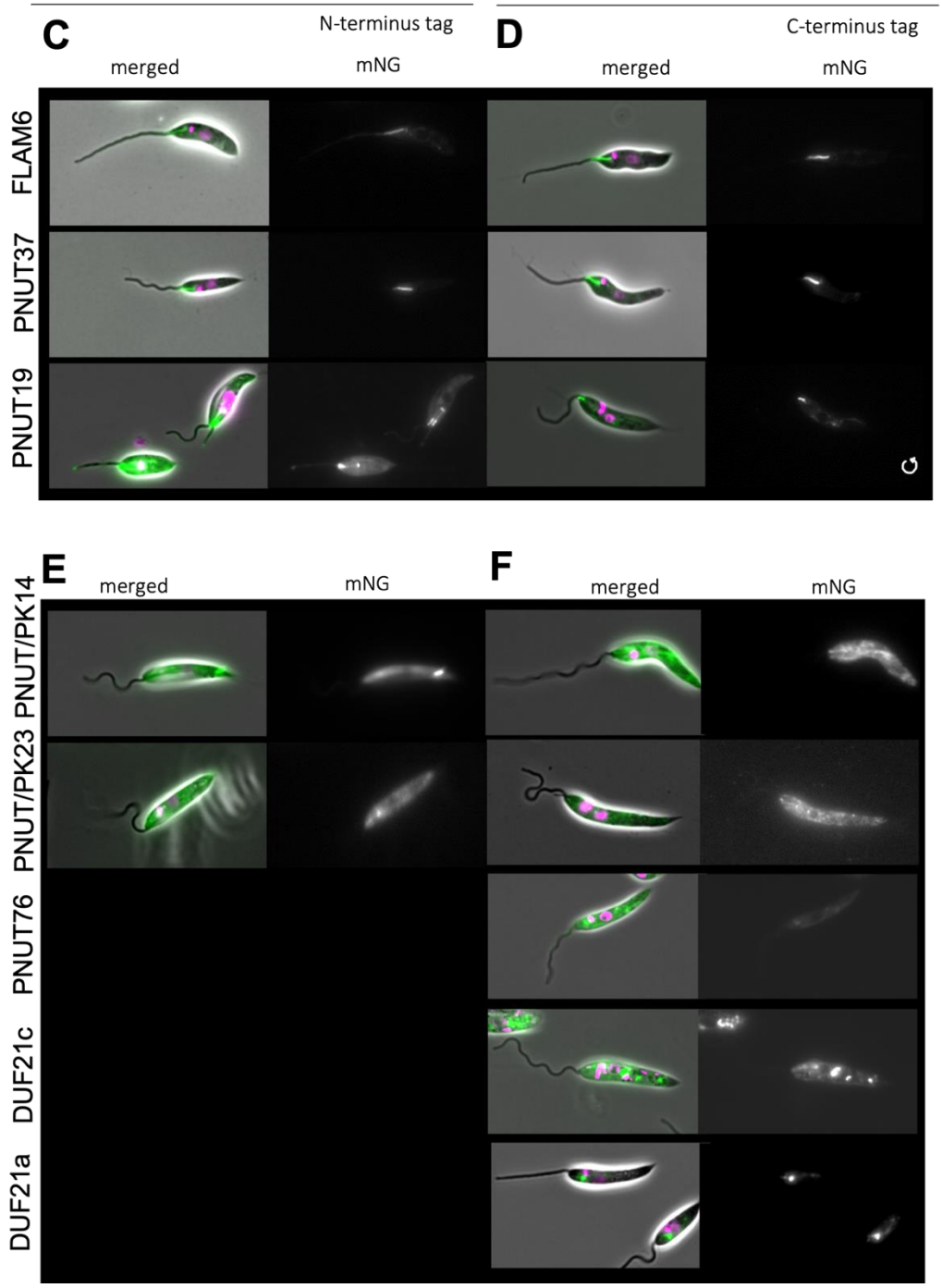


Figure 2-11: Localisation of PNUTs.

(A, C, E) Micrographs of cells expressing PNUTs N-terminally tagged with mNG. Left panel, merged phase contrast and fluorescence signal from Hoechst DNA stain (magenta) and mNG (green). Right panel, mNG fluorescence signal only. (B, D, F) C-terminally tagged PNUTs, panels as above. (A and B) PNUTs which are detectable in the flagellum for one both of the

tags. (C and D) PNUTs which localise to the proximal flagellum. (E and F) PNUTs which are not detectable in any flagellar domain. Scale bar represents 10 µm. Curly arrow in right most column indicates a cell cycle dependent localisation discussed in Section 2.3.3.

The N-terminal tag of PNUT58 localised to many bright dots in the body, potentially associated with one of the small cytoplasmic organelles (79).

Three additional proteins localised to regions neat the proximal flagellum. The signals of FlaM6 and PNUT37 (Figure 2-11C, 11D) displayed proximal flagellum localisation which tapered off once reaching the flagellar pocket. The signals from the N- and C-terminal PNUT19 tags were in disagreement. The PNUT19 N-terminal tag was heavily enriched in the flagellar collar and basal body, with faint soluble signal throughout the flagellum and an occasional punctate signal at the flagellar tip. PNUT19 signal was more often observed with a flagellar tip localisation in dividing cells (noted to be more often present in the new growing flagellum) however this was not exclusive and was also observed at the tip in some non-dividing cells (Figure 2-12). The proportions of signal observed at the flagellar tip were as follows; 40% (8/20) non-dividing, 57% (11/19) 2F1N1K, 71% (5/7), and 57% (11/19) 2F2N2K. The PNUT19 C-terminal signal however, localised quite specifically to the flagellum neck/collar region.

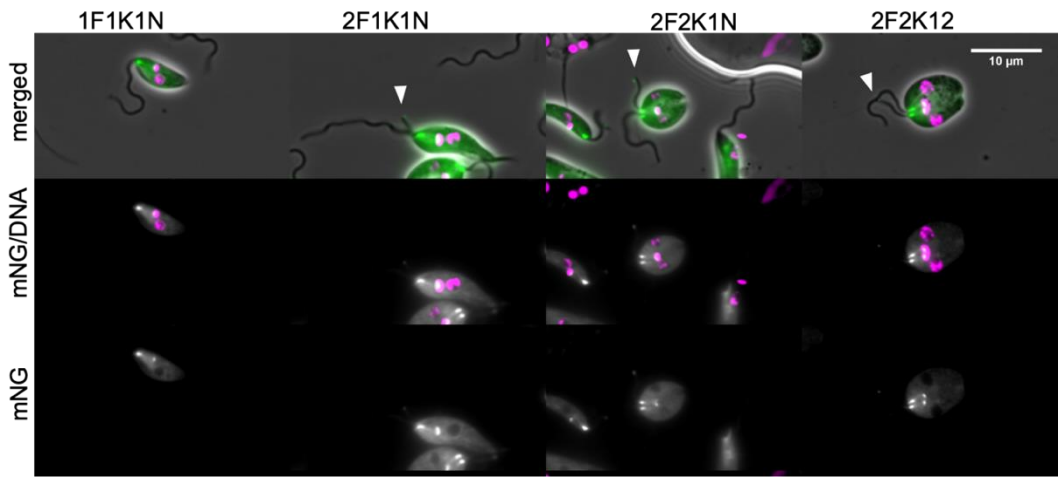


Figure 2-12: Cell cycle dependent localisation of PNUT19.

Example cells of PNUT19::mNG tagged cells in successive stages of the cell division cycle, as assessed by the number of flagella (F), nuclei (N) and kinetoplasts (222). Merged, phase contrast and fluorescence from DNA stained with Hoechst (magenta) and mNG fluorescence (green); mNG/DNA, merged fluorescence Hoechst (magenta) and mNG fluorescence (grey); mNG, PNUT19::mNG fluorescence signal only. PNUT19::mNG signal enrichment seen in the flagellar collar/neck, the basal body and a dot at the flagellar tip indicated by a white arrow. DNA stained by Hoechst in magenta, mNG fluorescence in green or grey. Scale bar represents 10 µm. Panel made by Gabe Crossfield.

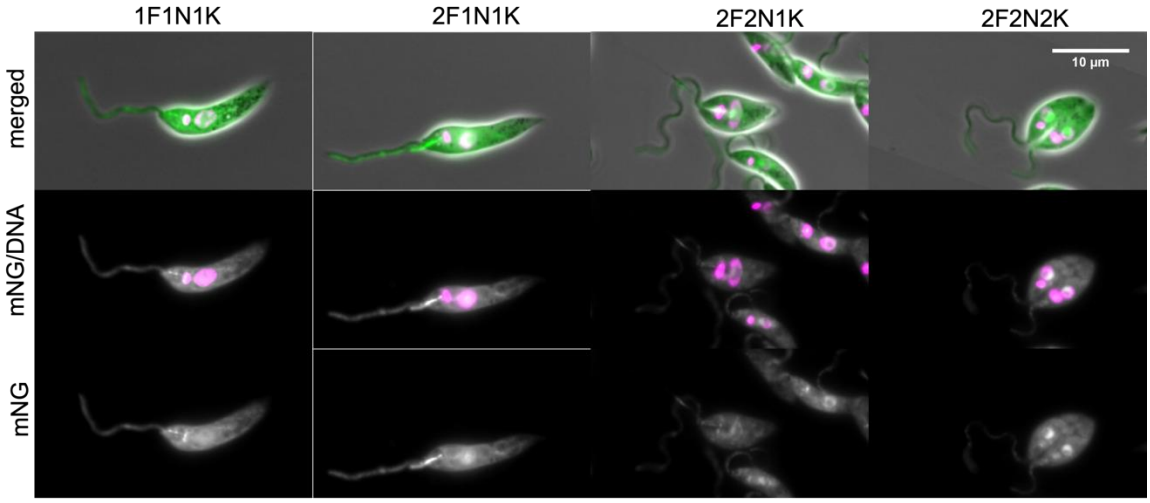


Figure 2-13: Cell cycle dependent localisation of PNUT51.

Examples of PNUT51::mNG tagged cells in successive stages of the cell division cycle, as assessed by the number of flagella (F), nuclei (N) and kinetoplasts (K) (222). Merged, phase contrast and fluorescence from DNA stained with Hoechst (magenta) and mNG fluorescence

(green); mNG/DNA, merged fluorescence Hoechst (magenta) and mNG fluorescence (grey); mNG, PNUT51::mNG fluorescence signal only. Enrichment of the PNUT51::mNG signal in the nucleus is seen during cell division. Scale bar represents 10 µm. Panel made by Gabe Crossfield.

Cell body

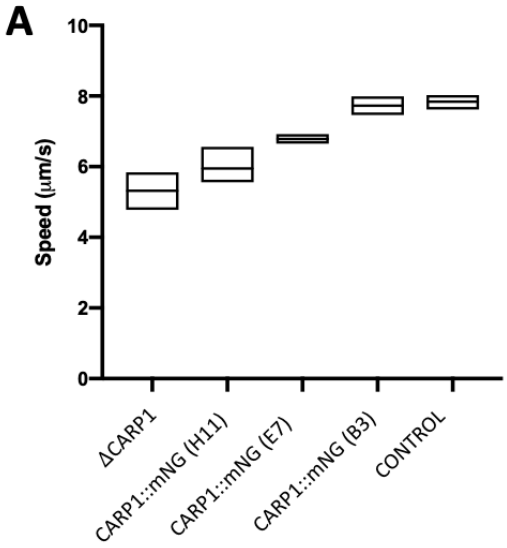
The remaining seven PNUTs were not detectable in the flagellum, most of which localised to unclear regions within the cell body (PNUT/PK14, PNUT/PK23 and PNUT76). The C-terminal tag of DUF21a appeared enriched in a region close to the flagellar pocket/basal body, with an additional faint lysosomal quartet signal reminiscent again of the localisations of PDE C and HypothAC. Lastly, the DUF21c signal appeared enriched in several large cell body organelles with a faint soluble cell body signal.

2.2.2.4. CARP1 is embedded in the flagellar axoneme, but localisation is not dependent on components of the radial spokes, outer dynein arms, inner dynein arms, central pair, or nexin dynein regulatory complex.

We next focused on a more thorough characterisation of CARP1 because it was a flagellar axoneme-localised protein (Figure 2-11A, 11B), with the strongest evidence of binding to cAMP of all the *Leishmania* CNBD containing proteins (see Chapter 2.2.1 and (186)) and as described in Chapter 2.4.1 below, the null mutant showed a distinctive motility phenotype. To identify more precisely where in the axoneme CARP1 is localised we used a genetic approach to examine the dependence of CARP1 localisation on the presence of known axonemal structures. Techniques such as creating clonal mutants expressing the fluorescently tagged protein of interest, with subsequent targeted gene deletions has

proven to yield information of this kind in previous studies (77,223). It was observed that fusion of mNG to the C-terminus of CARP1 caused a motility defect, whereas fusion of mNG to the N-terminus did not cause a change in motility relative to controls (Figure 2-14A). For this reason, we used an N-terminally fused CARP1 expressing parental cell line for the fluorescence microscopy of cytoskeletons from various targeted knockout cell lines to assess whether deletion or disruption of the targeted axonemal structures resulted in a reduction of mNG::CARP1 fluorescence to the flagellar axoneme.

We used a clonal mNG::CARP1 expressing mutant and deleted genes on which normal assembly of the radial spokes *(ΔRSP3* (224)), radial spoke head (*ΔRSP9* (224)), central pair *(ΔPF16* , *Δhydin* (225)), N-DRC (*ΔDRC5*, *ΔDRC7* (30,31)), inner dynein arm *(ΔCFAP44*, *ΔIC140* (223) and CCDC113 (226)) and outer dynein arms (*ΔdDC2* (227)) relied upon. All knock out lines were successfully generated asides from hydin, from which the mutants showed the expected high curling phenotype (77) however retained a detectable copy of the hydin coding sequence when verified by PCR (see Figure 2-14).



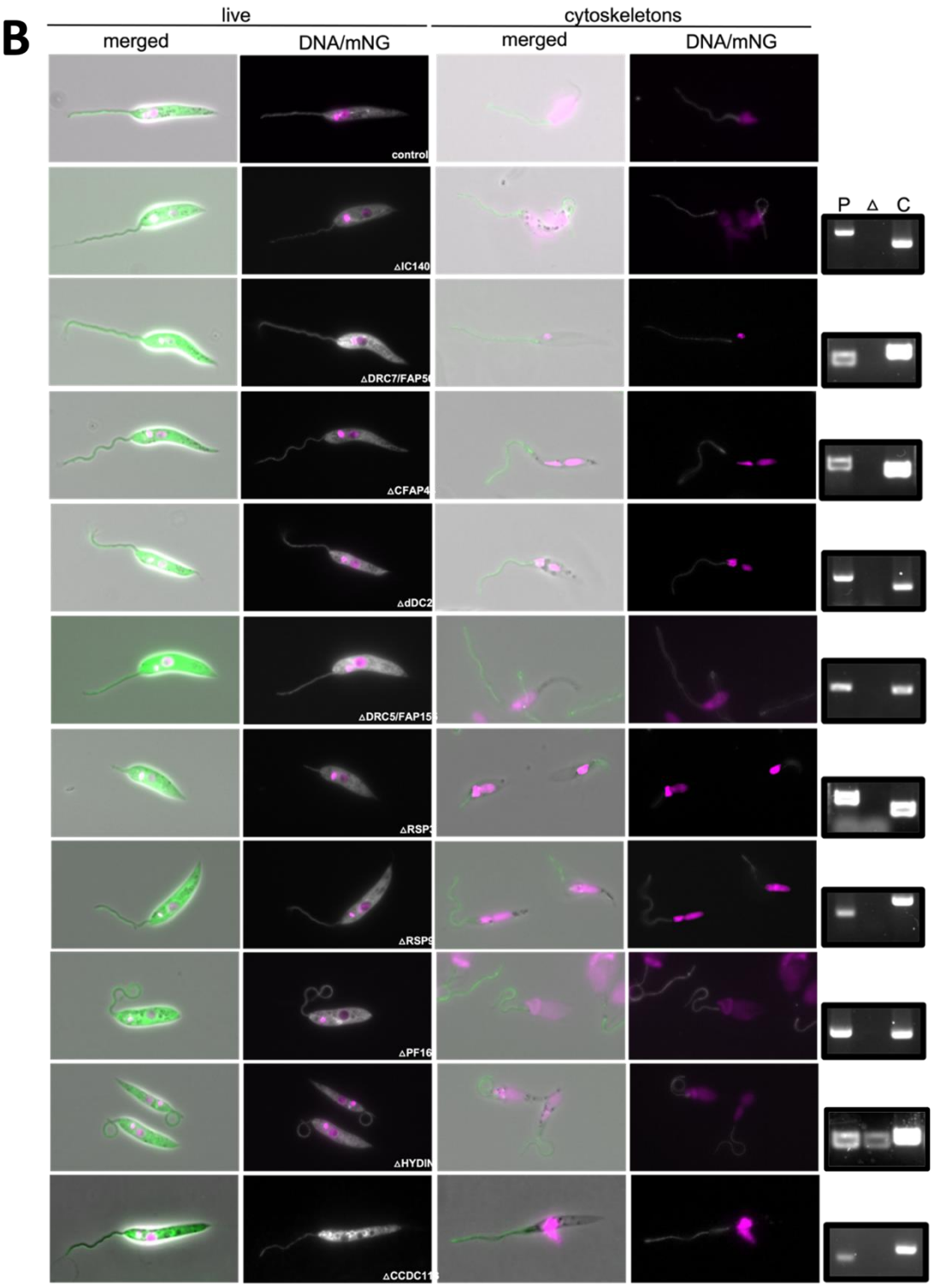


Figure 2-14: Axonemal localisation of CARP1.

(A) the population motility assay of mNG tagged CARP1 expressing cell lines where clone H11 represents a cell line with both gene copies C-terminally tag, clone E7 a single gene copy C-terminally tagged and B3 with both gene copies N-terminally tagged. Swim speed of

⊿CARP1 and parental control were measured alongside for reference. Motility was quantified to ensure the tagged parental cell line selected for targeted gene deletions was not hindered by fusion of mNG to the CARP1 protein. (B) Micrographs of live (columns 1 and 2) and cytoskeleton (columns 3 and 4) promastigote cells from a clonal cell line (clone B3) expressing mNG::CARP1 where each row represents the deletion of a target gene on which core axonemal structures depend. Columns 1 and 3 display merged phase contrast, Hoechst (magenta) and mNG fluorescence (green), where columns 2 and 4 display merged fluorescence from Hoeschst (magenta) and mNG (grey). Cytoskeletons extracted with 1% NP40 in PEME buffer. PCR validation of gene deletion shown on the far right. P - represents the target gene ORF primers used to amplify a DNA fragment on genomic parental DNA, ⊿ - represents the target gene ORF primers used to amplify on genomic mutant DNA from the respective targeted gene, and C - represents a mutant DNA quality control where a fragment within the ORF of a housekeeping gene (PF16) is amplified as a positive control.

We observed the mNG::CARP1 signal within the axoneme of live cells as well as detergent-extracted cytoskeletons in all the cell lines obtained (Figure 2-14B), indicating that we were unable to dissociate the CARP1 protein from the cytoskeletal axoneme by deletion of aforementioned core structures. This demonstrates that the localisation of CARP1 does not depend on any of the listed genes deleted, suggesting it is perhaps associated with a minor axonemal structure or perhaps a subcellular domain which is not yet fully elucidated, for example the microtubule inner protein (MIPs). In a further attempt to dissociate mNG::CARP1 from the axoneme, we treated the cells with high salt concentrations. The flagellar signal remained after treatment with 1.5M $CaCl_2$ or 5M $NaCl_2$ but was lost upon treatment with 5M $CaCl_2$ (Figure 2-15). This preliminary result, if reproducible, could serve as a future starting point to ask what other proteins are solubilised alongside 5M $CaCl_2$ extraction, using mass spectrometry.

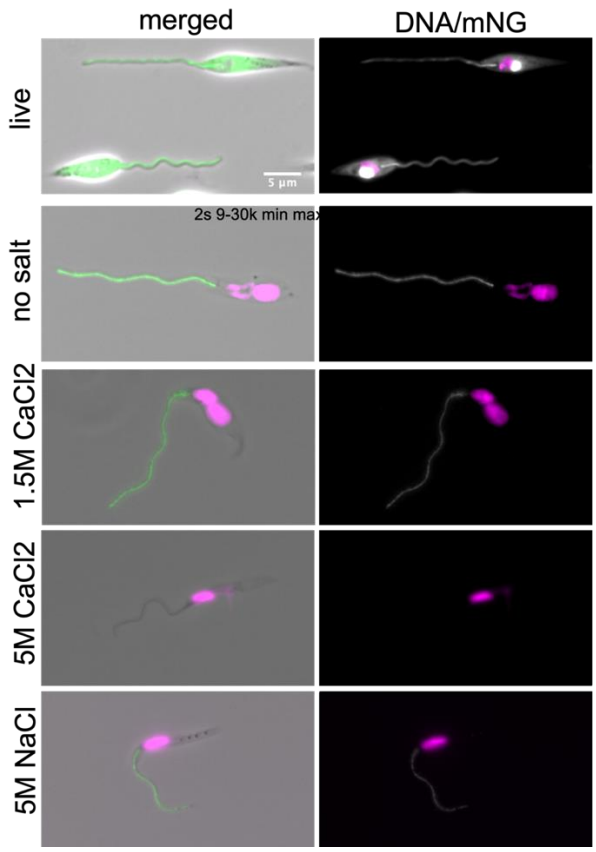


Figure 2-15: Salt extraction of CARP1 axonemal signal.

Example cells of salt extraction treatment on cytoskeletons of mNG::CARP1 expressing mutants taken from fields of view containing > 10 cytoskeletons. Merged phase contrast and fluorescence (mNG, green; Hoeachst DNA stain, magenta) on the left with just mNG (grey) and DNA stain (magenta) on the right. First row shows the live cell mNG::CARP1 expressing parental cell line. All salt extracted micrographs set to the same min-max 9000-30000 on ImageJ and exposed to 2 s fluorescent excitation for mNG channel acquisition. Scale bar represents 5 µm.

2.2.2.5. Corroboration of tagging localisations through comparison with published proteome data.

To complement the experimental localisation data gained from endogenous tagging and fluorescence microscopy, we compared our list of 35 putative cyclic nucleotide signalling

components against the proteomes of *L. mexicana* flagellum and cell body fractions (77). A total of 19 proteins were present in these datasets, of which CARP2, CARP4, PDE B1/B2 and PNUT31 were enriched in the detergent insoluble flagellar fraction, and three ACs along with PDE D/A were enriched in the soluble flagellar fraction (Figure 2-16). In agreement with our tagging localisation to a compartment near the anterior end of the cell body (possibly contractile vacuole), we found the hypothetical AC along with PDE C were among the detergent insoluble cell body fraction which suggests that if they are indeed associated with the contractile vacuole, then they were not solubilised with octylglucoside. PNUT37 was strongly enriched also in the insoluble cell body fraction, localising to the proximal flagellar cytoskeleton, which was expected because the fractionation severed the external part of the flagellum from the cell body; where the cell body fractions still contained within them the proximal proteins of the flagellum that resides within the flagellar pocket (77).

Also striking was the apparent lack of cell body soluble components (Figure 2-16).

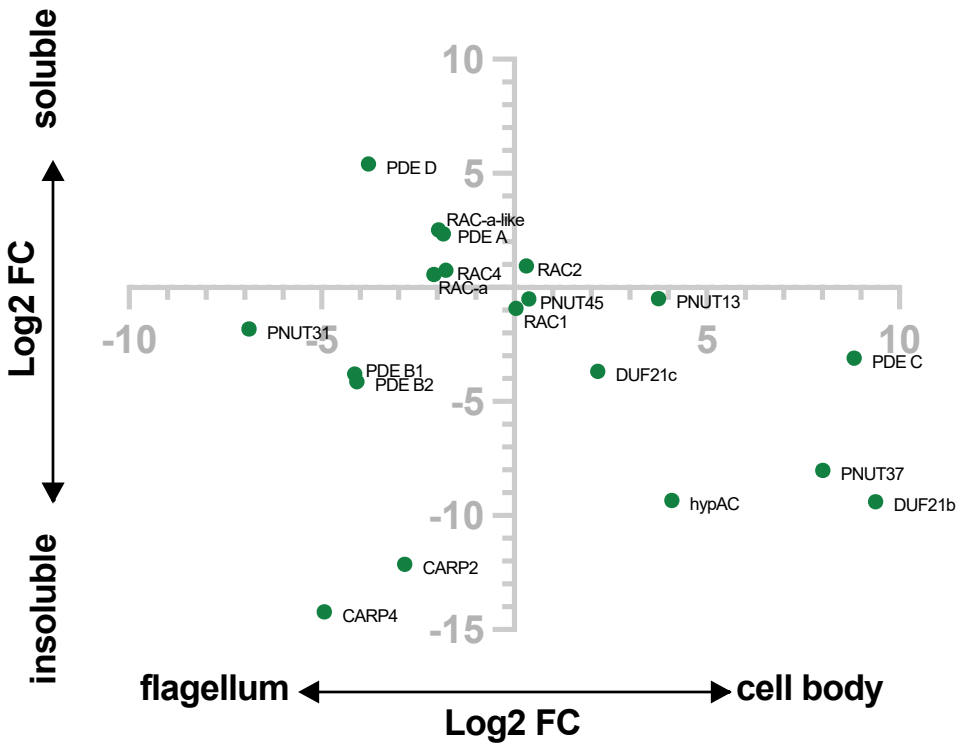


Figure 2-16: Detection of cAMP signalling components in proteome dataset.

Mass spectrometry of L. mexicana cell body and flagellar fractions detected ~2500 proteins (Proteome data acquired from LeishGEdit DB (http://leishgedit.net/leishgedit_db, Beneke et al., 2019). 19 of the 35 L. mexicana putative cyclic nucleotide signalling components analysed in this study were detected in this proteome and plotted here to show Log2 fold change (Log2 FC) of protein abundance between cell body and flagellum fractions displayed along the x-axis and Log2 FC between n-octylglucoside soluble and insoluble cell fractions displayed along the y-axis.

2.2.3. A null mutant library demonstrated that cyclic nucleotide signalling components within the flagellum can increase as well as decrease parasite swim speed

To determine whether loss of any of the 35 putative cyclic nucleotide signalling components which we identified (Table 2-1) would lead to changes in motility, we targeted all 35 putative signalling components for deletion. We successfully obtained mutants for 16 (of the 19) cyclic nucleotide transducers, all 7 PDEs and 4 of the nine ACs (see Table 2-1, column 1). As the genomic sequence was not reliable enough for successful deletion of several of the ACs using the standard LeishGEdit strategy, we designed a bespoke CRISPR strategy to truncate the catalytic domain from RAC-b (LmxM.17.0235) (Figure 2-17B), as we hypothesised this would create a functional null mutant. We fused an mNG protein to the C-terminus of the truncated product to ensure it was not localising to the flagellar tip (Figure 2-17C) and used diagnostic primers spanning from within the ORF to the 3'UTR to confirm the desired altered genomic locus by PCR (Figure 2-17B, 17D). Despite several attempts, we did not obtain null mutants for PNUT45, PNUT75 and PNUT76, which never came back from drug selection. This may be due to technical error or indicative of essentiality for these genes.

Figure 2-17 shows a complete loss of the target ORF for 25 genes, however for 3 genes (HemAC, PNUT58, and PNUT13), the diagnostic PCR still showed a band for the target ORF (Figure 2-18). All of these cell lines were included in the following studies to assess their flagellar motility.

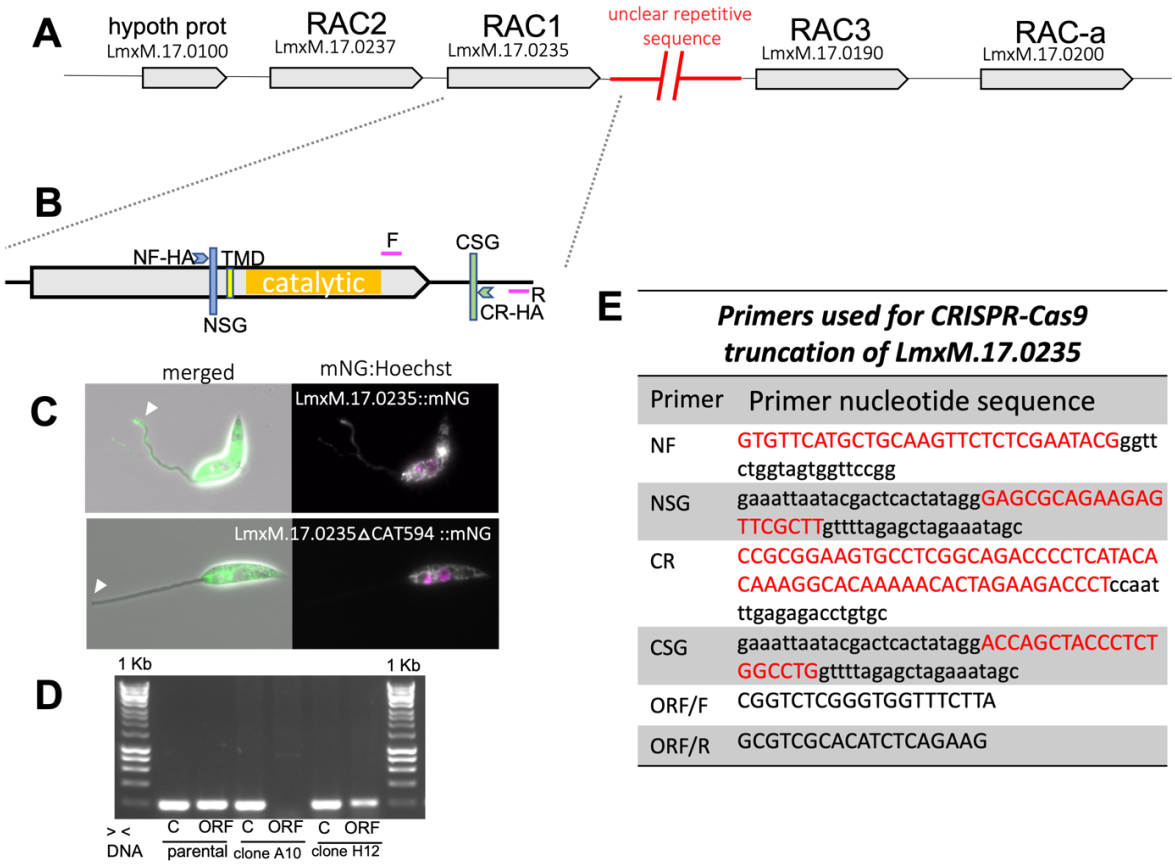


Figure 2-17: Functional disruption of RAC1.

Strategy for the functional disruption of RAC1 by truncation of the catalytic domain. (A) Cartoon representation of the gene arrangement of RACs within the genomic array gained from the nanopore genome sequence of L. mexicana generated previously from our lab. Red indicates an area of low sequence confidence where the two sequenced contigs (contig 66 and 76) adjoin and only the 3'UTRs is present for LmxM17.0191 (RAC4) whose ORF is missing from the array. Nanopore sequence was used for this strategy due to the inconclusive annotation of this gene array available of TriTrypDB at the time. (B) a close up of the RAC1 ORF showing the strategy for ORF truncation by fusing an mNG fluorescent protein to the C-terminus of the truncated product thereby deleting the AC transmembrane domain (TMD) and catalytic domain. The target sites for CRISPR-mediated insertion of an mNG fusion tag are shown: NSG indicates the location of the upstream sgRNA target sequence, NF-HA the 30nt sequences of the upstream homology arm (in blue); CSG indicates the downstream sgRNA target sequence and CR-HA the 30nt sequences of the downstream homology arm (in green). Binding sites for the forward (F) and reverse (R) diagnostic primers are shown as pink. (C) Localisation of a full length RAC1:mNG fusion protein at the flagellar tip (top) and truncated RAC1:mNG (LmxM.17.0235ΔCAT594:mNG), which does not have detectable fluorescence at the flagellum tip, indicating functional disruption of the protein. (D) PCR based validation of the truncated genomic

region. Genomic DNA was tested from two clones from the truncation experiment (A10 and H12), alongside the parental control DNA. Control primers amplifying within the PF16 (LmxM.20.1400) gene verify the genomic DNA quality in lanes labelled C with a fragment length of 212 nucleotides. Lanes labelled ORF show the products obtained with primers specified in (B). A product was amplified from the parental DNA and clone H12. No product was seen in Clone A10, suggesting successful truncation of the target. (E) primer sequences used for the CRISPR-Cas9 truncation of RAC1, where red nucleotides represent target genomic sequences shown in (B) and black nucleotides target the pPLOT plasmids or universal G00 primer for DNA product generation. Sequences for the diagnostic primers are indicated in pink in (B).

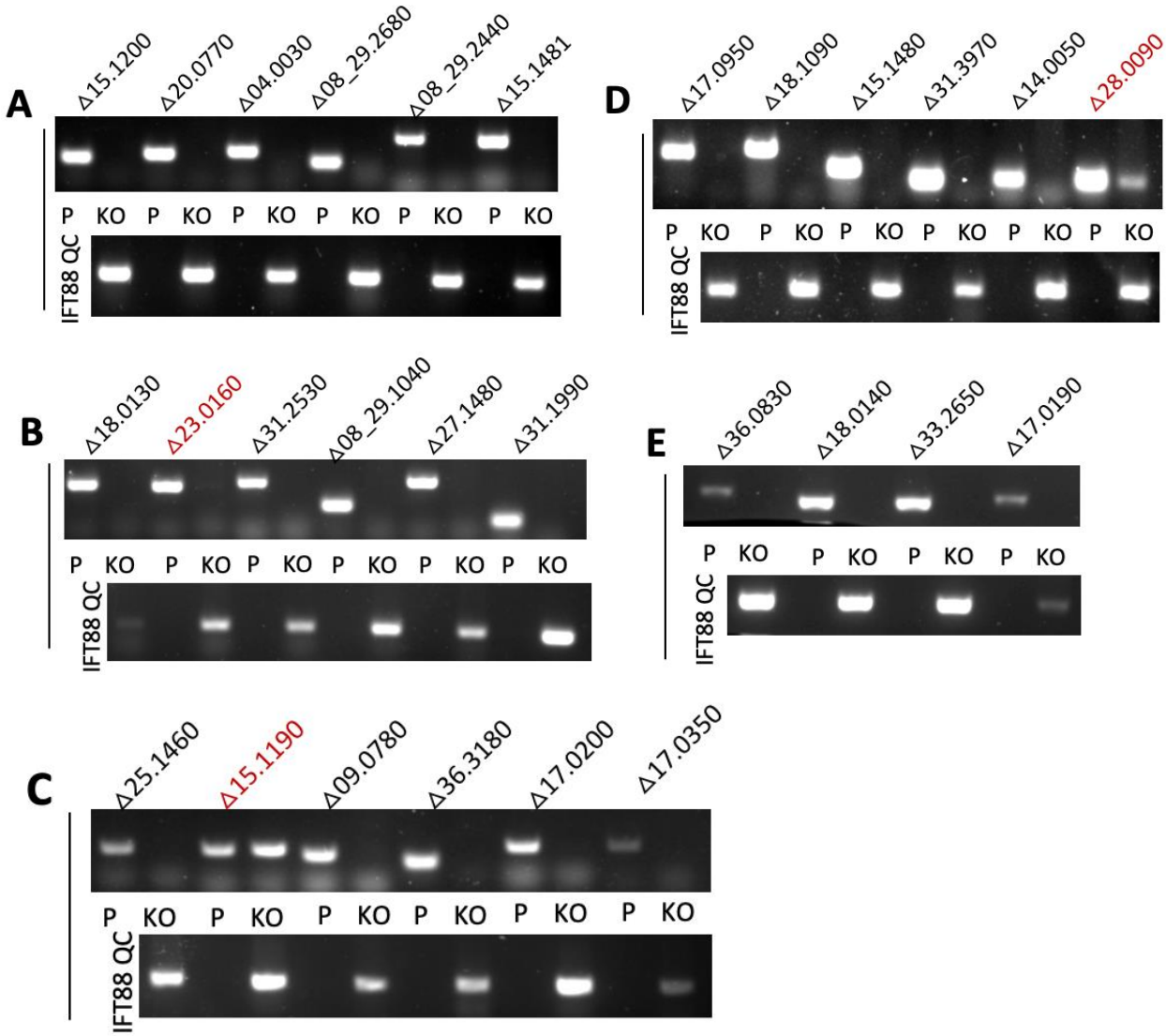


Figure 2-18: Gene knockout verification.

(A-E) represent batches of knockout verifications performed in parallel with the same PCR master-mix and run within the same thermocycler. In the upper panel, (P) represents

genomic DNA from the parental cell line, KO indicates genomic DNA from the mutant cell line. The Gene ID of the targeted gene and the mutant number used in this study are indicated above the panel. Detection of a ORF band in P and absence of a band in the KO indicates successful gene deletion. Red colouring indicates an ORF band still detectable in the mutant DNA; these lines are referred to in this screen as an incomplete gene deletion mutant. The lower panel (IFT88 QC) shows a DNA quality control PCR on DNA from the KO mutant only, targeting the gene IFT88, with a PCR fragment length of 191 nucleotides. Alternating wells were left empty.

2.2.3.1. Nearly half of the null mutant from our library swam significantly different to the parental control

A swimming motility assay (61) was used to determine crude population displacement behaviour in terms of average swim speed and directionality (velocity/speed) for up to 10000 cells for each cell line, in triplicate. Firstly we saw that our parental controls swam similarly to previously described (77), with an average speed of 7.45 µm/s. Out of 25 mutants, we saw that five mutants swam significantly slower, and seven swam faster than parental controls (Students unpaired t-test against parental motility dataset (Table 2-3), p-value <0.5, Table 2-2). Also, that the same slower five mutants demonstrated significantly lower directionality (velocity/speed), whilst only three of the seven faster mutants showed significantly elevated directionality (Table 2-2). Figure 2-19A represents the change relative to parental controls, where black points indicate significant difference in swim speed. Highly enriched in the faster swimmers were five of the cohort of PDEs (A-D).

Fi

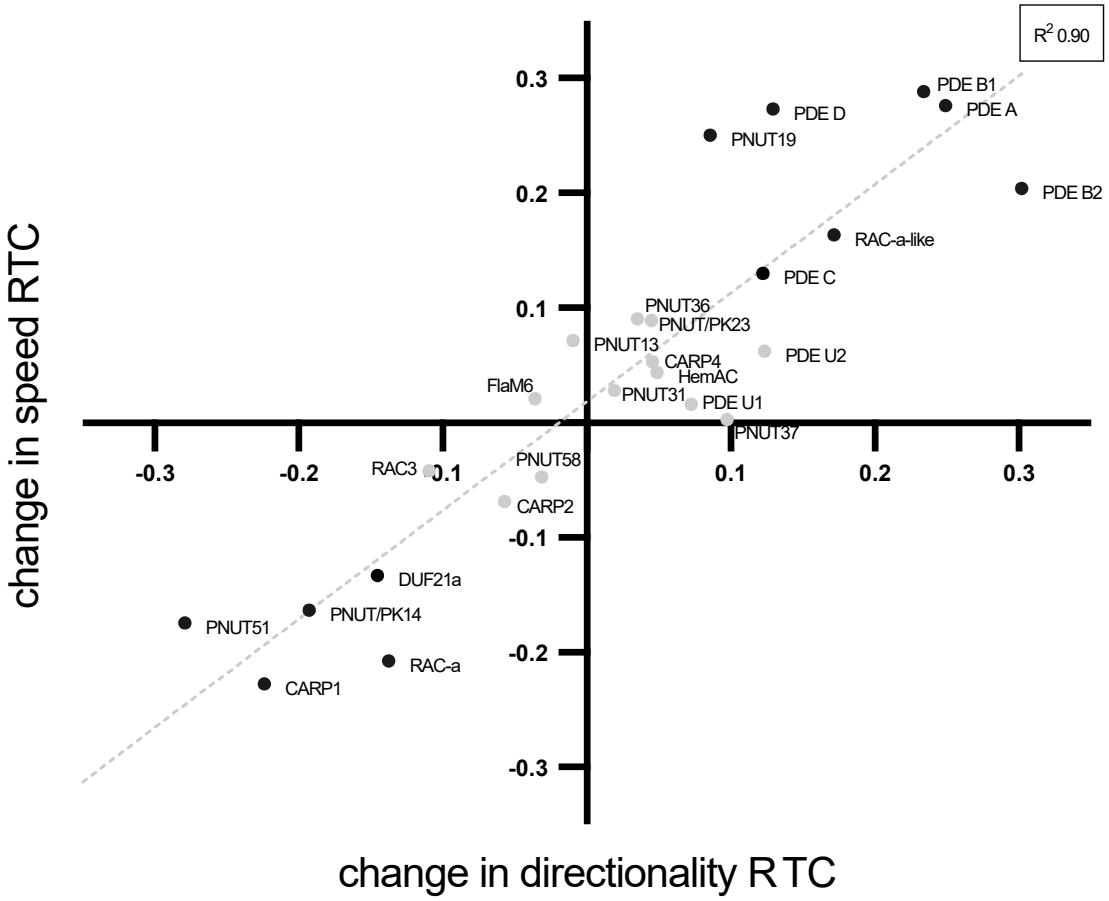


Figure 2-19: Null mutant swimming behaviour.

Population motility assay results for null mutants where population speed and directionality (velocity/speed) relative to control (RTC) are plotted. Dotted line represents a simple linear regression analysis of speed RTC and directionality RTC with associated $R^2 = 0.9$, indicating a tight correlation. Statistically significant speeds RTC are indicated by black dots, the remaining data points in grey. Unpaired student t-test assuming equal variance of each mutant motility measurement in triplicate against the dataset of parental control motility data obtained in the Sir William Dunn School of Pathology lab between 2018-20. Raw data for speed and directionality along with the respective p-values are summarised in Table 2-2 and the parental control motility dataset summarised in Table 2-3.

In addition to these, we observed that *ΔPNUT19* and *ΔRAC-a-like* were also among the significantly faster swimmers. On the other end of the spectrum, we found that *ΔCARP1* was the most motility defective mutant, alongside *ΔPNUT/PK14, ΔPNUT51, ΔRAC-a, and ΔDUF21a*. It is reported that the speed and directionality measurements tightly correlate for the majority of flagellar mutants in *L. mexicana* (77), asides from a cohort of mutants associated with loss of N-DRC and ODA which display an uncoordinated swimming phenotype defined as a disproportionately lower directionality relative to population swim speed (77). Here, we saw that our cohort of mutants conformed to the former motility relationship, with a correlation between change in speed RTC and change in directionality RTC with an R^2 of 0.9003 (Simple linear regression, Figure 2-19A).

Table 2-2: Population motility measurements for Leishmania null mutants.

Columns 1 and 2 indicate the gene ID and mutant name respectively, where the knockout status is indicated to the left as detailed in Table 2-1. Columns 3 shows the average swim speed tracks of up to 10,000 cell traces obtained in triplicate from each mutant. Column 4 summarises the significance (underlined, significance cut-off p < 0.5) of the motility measurements against the parental control motility dataset (Table 2-3) using an unpaired two-tailed student t-test assuming equal variance. Column 5 displays the directionality in triplicate with the p-values as determined before in column 6. It is indicated in column 7 which control dataset (a – j, column 1 in Table 2-3) was measured in parallel to each respective mutant. In cases where more than three replicates were measured, the measurements are separated by a semicolon. Grey shading indicates that no motility assay was performed for that mutant, or the mutant knockout line was not generated. The data from this table is graphically represented in Figure 2-19 as change relative to the parental control (RTC) dataset.

Table legend on previous page.

Δ	Gene ID	Given Name	Population speed (µm/s)			Speed P-value	Population directionality (velocity/speed)			Direction P-value	Batch ref
Putative Nucleotide/Nucleoside Transducer (PNUT)	LmxM.08_29.1040	FlaM6	7.98	7.51	7.32	0.72643	0.30	0.24	0.28	0.59824	c
	LmxM.09.0780	DUF4464/ CARP2	7.02	6.95	6.84	0.25460	0.27	0.28	0.25	0.39475	j
	LmxM.14.0050	PNUT51	6.47	6.14	5.84	0.00542	0.20	0.23	0.18	0.00015	g
	LmxM.15.1190	PNUT13	8.22	8.06	7.66	0.23575	0.29	0.28	0.27	0.88348	c
	LmxM.15.1200	PNUT/PK14	6.19	5.76	6.74	0.00909	0.24	0.21	0.23	0.00581	c
	LmxM.18.0130	DUF21a	6.40	6.19	6.78	0.03063	0.24	0.22	0.26	0.03406	g
	LmxM.18.0140	DUF21b									
	LmxM.20.0770	PNUT/PK23	8.13	8.41	7.79	0.14215	0.29	0.31	0.28	0.49863	c
	LmxM.22.0400	PNUT75									
	LmxM.23.0160	PNUT58	7.49	7.25	6.54	0.43241	0.29	0.28	0.25	0.64047	g
	LmxM.25.1460	CARP4	8.08	7.85	7.60	0.37580	0.32	0.29	0.27	0.49674	d
	LmxM.27.1480	PNUT31	7.21	7.47	8.29	0.64178	0.27	0.28	0.31	0.77496	d
	LmxM.30.0490	PNUT76									
	LmxM.31.1990	PNUT36	7.39	8.28	8.69	0.14165	0.27	0.30	0.30	0.59714	b
	LmxM.31.2530	PNUT37	6.95	7.92	7.54	0.95908	0.28	0.31	0.34	0.15497	d
	LmxM.31.3970	CARP1	5.96	5.69	5.61	0.00040	0.23	0.21	0.22	0.00150	e
	LmxM.33.2650	DUF21c									
	LmxM.33.4620	PNUT45									
	LmxM.36.0830	PNUT19	8.52; 10.3	10.20; 8.28	7.76; 10.8	<0.00001	0.28; 0.33	0.33; 0.24	0.28; 0.35	0.32630	c
adenylate cyclase	LmxM.05.0050	hypotAC									
	LmxM.17.0190	RAC3	7.04	6.91	7.46	0.48778	0.26	0.24	0.26	0.10434	e
	LmxM.17.0191	RAC4									
	LmxM.17.0200	RACa	5.92	5.73	6.06	0.00110	0.24	0.23	0.25	0.04283	i
	LmxM.17.0235	RAC1									
	LmxM.17.0236	truncRAC									
	LmxM.17.0237	RAC2									
	LmxM.28.0090	HemAC	8.56	7.85	6.91	0.47610	0.33	0.30	0.25	0.47766	d
	LmxM.36.3180	RAC-a-like	8.39	8.57	9.04	0.00863	0.32	0.32	0.35	0.01317	c
phosphodiesterase	LmxM.04.0030	PDE U1	7.43	6.97	8.31	0.79159	0.30	0.28	0.33	0.28421	c
	LmxM.08_29.2440	PDE D	9.43	9.34	9.67	0.00003	0.33	0.32	0.30	0.05743	b
	LmxM.08_29.2680	PDE C	7.78	8.34	9.13	0.03687	0.32	0.32	0.31	0.06962	c
	LmxM.15.1480	PDE B2	8.42;10.20	8.71; 9.13	8.46; 8.88	0.01835	0.26; 0.36	0.25; 0.31	0.32; 0.30	0.15812	j
	LmxM.15.1481	PDE B1	9.76	10.26	8.77	0.00002	0.36	0.34	0.33	0.00101	f
	LmxM.17.0950	PDE U2	8.91	7.25	7.57	0.31506	0.34	0.30	0.31	0.07092	c
	LmxM.18.1090	PDE A	9.25	9.20	10.06	0.00003	0.36	0.33	0.36	0.00052	c

Table 2-3: Motility measurements for parental controls.

Column 1 contains reference letters to indicate which control measurement is relevant for each null mutant listed in Table 2-2. Column 2-4 contain the triplicate population speed measurements, and columns 5-7 the respective directionality measurements from motility assays performed on the same day in the same M199 culture medium batch as motility measurements performed on null mutants. Below the table is the averaged speed and directionality for the whole control population dataset, in agreement with previous control measurements (77). The parental control used throughout this thesis is the C9T7 expressing cell line made previously in the lab (221).

Batch ref	Population speed (µm/s)			Population directionality (velocity/speed)		
a	6.59	7.24	7.75	0.25	0.27	0.29
b	7.39	7.58	6.50	0.31	0.29	0.25
c	7.28	8.16	6.12	0.30	0.30	0.23
d	7.80	8.19	7.68	0.27	0.28	0.26
e	8.68	7.58	7.97	0.29	0.28	0.29
f	6.89	7.91	8.38	0.27	0.29	0.31
g	7.29	6.79	5.89	0.28	0.26	0.22
h	6.37	6.53	6.41	0.24	0.25	0.25
i	7.43	6.66	7.23	0.29	0.28	0.30
j	9.05	7.60	7.56	0.38	0.33	0.34
	Mean speed	7.45 µm/s		Mean direction	0.28	

Since the motility assay only reports average speed for all cells in a population, we asked what factors determined this average speed. We looked at three levels of resolution, first plotting the speed for individual cells within the population. Then we assessed the flagellar waveform of individual cells to determine if the proportion of cells propagating the symmetric tip-to-base beat which drives forward motility was altered (Population Overview Waveform Analysis (POWA)). Finally, we used high speed video microscopy to measure the parameters of flagellar beats (*e.g.,* beat frequency and amplitude).

2.2.3.2. Change in population swim speed is attributable to altered proportions of cells propagating forward motility and changes in beat frequency

The faster swimming phosphodiesterase mutants:

Firstly, we analysed *ΔPDE A, ΔPDE B1, ΔPDE B2 and ΔPDE D*, which all showed elevated population swim speeds (Figure 2-20A). In addition to these single-gene mutants, we created a double null mutant by deleting *PDE B2* and *PDE D* with one drug resistance cassette, on top of the *ΔPDE B1* and *ΔPDE A* mutant backgrounds respectively, then using limiting dilution, we obtained a complete double null genotype (Figure 2-20C, 20D). We assessed the motility of double mutants *ΔPDE A/ΔPDE D* and *ΔPDE B1/ΔPDE B2* to understand whether the faster swimming behaviour is phenotypically additive, and found it was not. Figure 2-20B summarises the POWA outcome, where low magnification (X20), high speed (200 Hz) short videos (0.5 seconds) are taken of a small sample of each population to determine the proportions of cells using; forward motility, a rapid tip-to-base symmetric wave which may be continuous (dark blue) or interrupted (light blue) during the short time observed; tumbling motility (red), an asymmetric base-to-tip whipping motion which mediates an on the spot rotation of the cell used to change direction, and uncoordinated (orange), which are neither of the previous two categories with undefined beat direction and movement. In addition to these, we also include a category which captures the cells switching (green) from tumbling motility to forward motility (or vice versa).

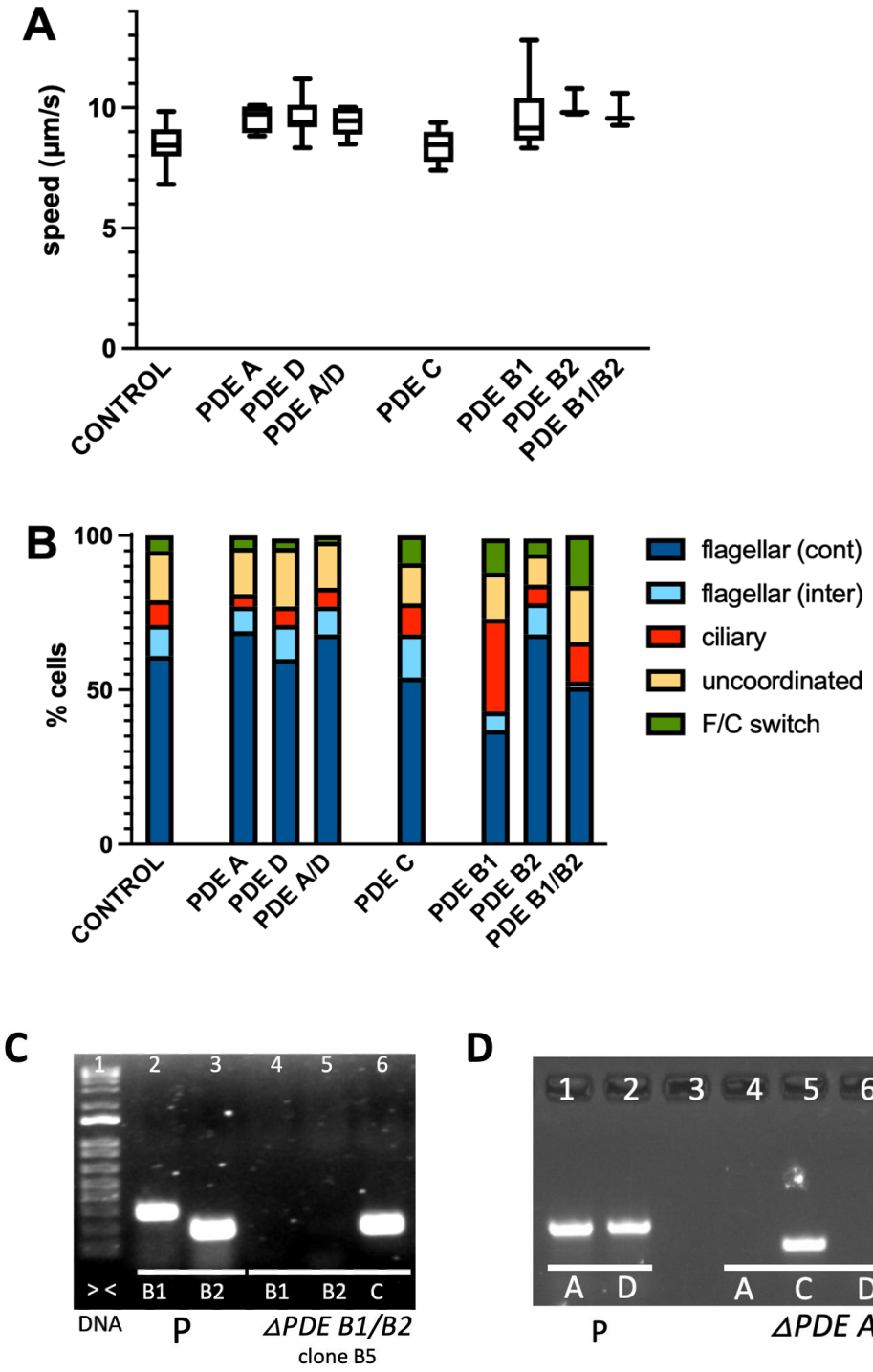


Figure 2-20: Motility behaviour of PDE null mutants.

Deletion of flagellar localised phosphodiesterase (cyclic nucleotide negative regulators) changes the proportion of forward motility (A) mutant population swim speed of ΔPDE A, ΔB1, ΔB2, ΔC and ΔD alongside double mutants generated for A/D and B1/B2. (B) Population overview waveform analysis (POWA) of PDE isoforms A-D including double gene

deletions of PDE A/D and PDE B1/B2. Dark and light blue represent the symmetric tip-to-base wave for forward motility, the red is the reverse asymmetric base-to-tip wave, green is a switch between flagellar/ciliary, and orange is uncoordinated wave movement. Manual categorisation of waveforms performed in ImageJ from video snapshots of 0.5 seconds. (C) PCR based verification of PDE B1/B2 double KO genotype. Primers targeting the ORF of PDE B1 and B2 are tested on the parental genomic DNA (lanes 2-3), followed by the same primers used on the mutant genomic DNA isolated from clone B5 (lanes 3-4) and finally a PCR targeting a housekeeping gene PF16 is used to check the DNA quality (lane 6). Limiting dilution yielded clone B5 with a homozygous gene replacement of PDE B2 with just G418 drug resistance cassette. DNA ladder represents Invitrogen 1 KB + (lane 1). (D) PCR based verification of PDE A/D double KO genotype. Lanes 1-2 contains the PCR products from primers targeting PDE A and PDE D ORFs amplified on the genomic DNA of parental controls. Lane 3 is empty. Lanes 4-5 and 6-7 show the alternating amplification of a fragment within the ORF of the deleted gene (indicated in Figure) with the positive control PCR targeting a housekeeping gene (PF16) denoted as 'C' for control. Lane 8 contains the Invitrogen 1 KB DNA ladder.

In the parental control population, 60% of cells performed a continuous flagellar beat, 10% a flagellar beat with interruptions (dark and light blue respectively in Figure 2-20B). 10% performed a ciliary beat and a small proportion were observed to switch between these modes (red and green respectively in Figure 2-20B). The remainder performed uncoordinated flagellar movements that could not be classified as flagellar or ciliary (orange in Figure 2-20B).

By comparison, we saw that *ΔPDE A, ΔPDE A/D* and *ΔPDE B2* displayed elevated proportions of cells using continuous forward motility (flagellar wave dark blue, > 68%). *ΔPDE D* and *ΔPDE C* displayed the most comparable waveform proportions to parental controls, where at the other end of the scale, the *PDE B1* mutant displayed a striking

decrease in forward motility (down to 43%) and increase in ciliary (up to 30% tumbling and F/C switching combined) and switching behaviour. This is in contrast to its closely related *PDE B2* mutant which localises to the same distal flagellar region and displayed no obvious change in tumbling or switching motility (Figure 2-20B). Together the POWA demonstrates that these cell lines, which all show increased average population swim speeds, differ in their propensity for different waveforms.

This brings about an intriguing question of how the *PDE B1* mutant on a population level, is still able to swim faster than parental controls if the tumbling behaviour is so increased. It is observed that ciliary beating is a momentary, as opposed to persistent, behaviour, and thus it could be that the forward motility performed by cells in-between ciliary beats is much faster than that of a normal parental control cell.

Slower swimming mutants and faster swimming ΔPNUT19:

We found in the POWA that although the faster swimming *ΔPNUT19* had comparable proportion of forward swimming cells to controls (~75%) (Figure 2-21A), the proportion of cell traces in "slow" (< 5 μm/s), "medium" (5-10 μm/s) and "fast" (> 10 μm/s) swimming categories showed it had a larger proportion of cells swimming with fast motility (>10 μm/s) (Figure 2-21B), and moreover, we observed a diminished propensity for tumbling motility in *ΔPNUT19* (< 5%) (Figure 2-21A).

On the other hand, we found that our slower swimming *ΔCARP1* and *ΔRAC-a* populations had an obvious decrease in cells swimming forward (< 50%) (Figure 2-21A), however the latter also displayed a decrease in tumbling motility. Most striking, was the increase in proportion of cells showing flagellar/ciliary switching and ciliary beats in *ΔCARP1* cells, made evident by the POWA (Figure 2-21A). Assessing the individual cell track speeds of *ΔCARP1*

showed that the majority of cells had shifted towards swimming in the slow (< 5 μm/s) to medium (5-10 μm/s) range of speeds compared to the control which demonstrates about

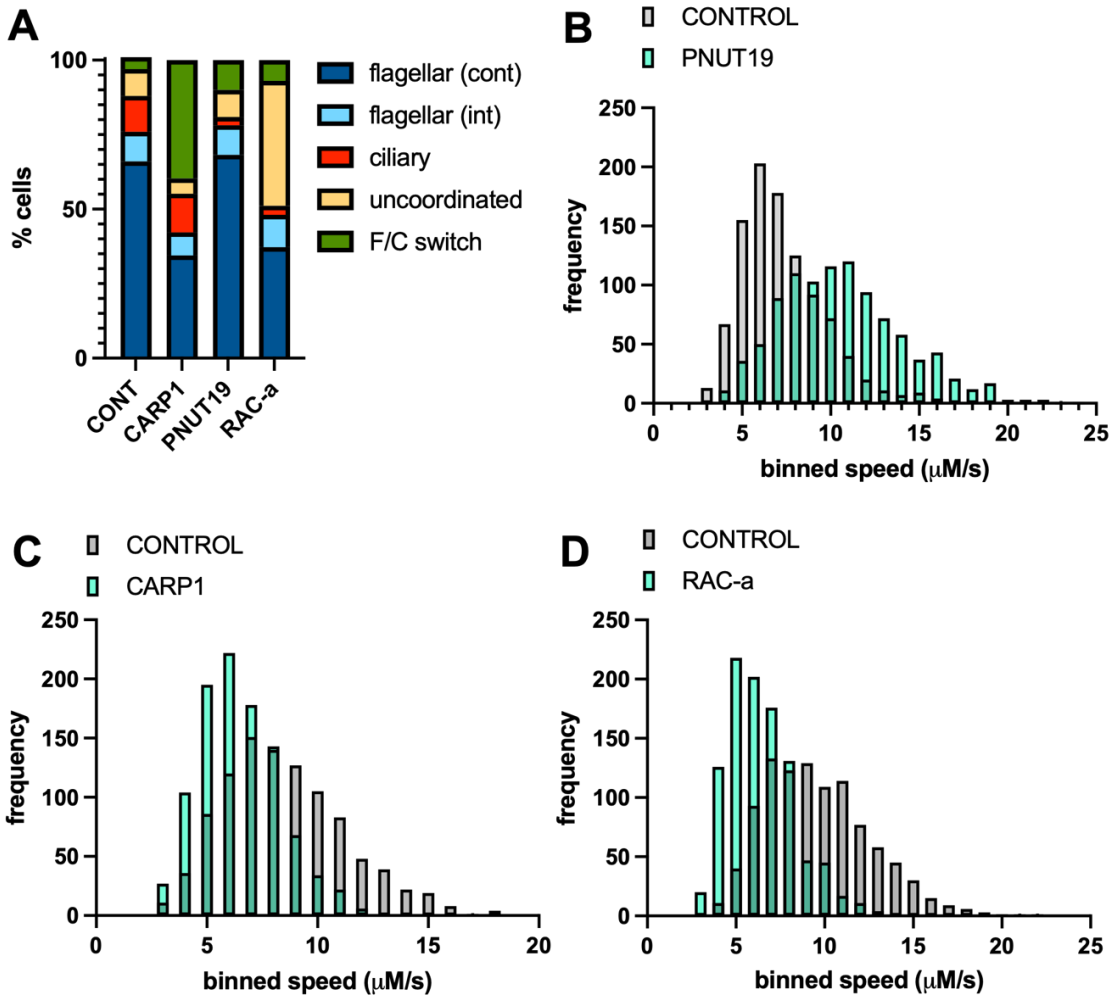


Figure 2-21: Flagellar waveform and cell track analysis.

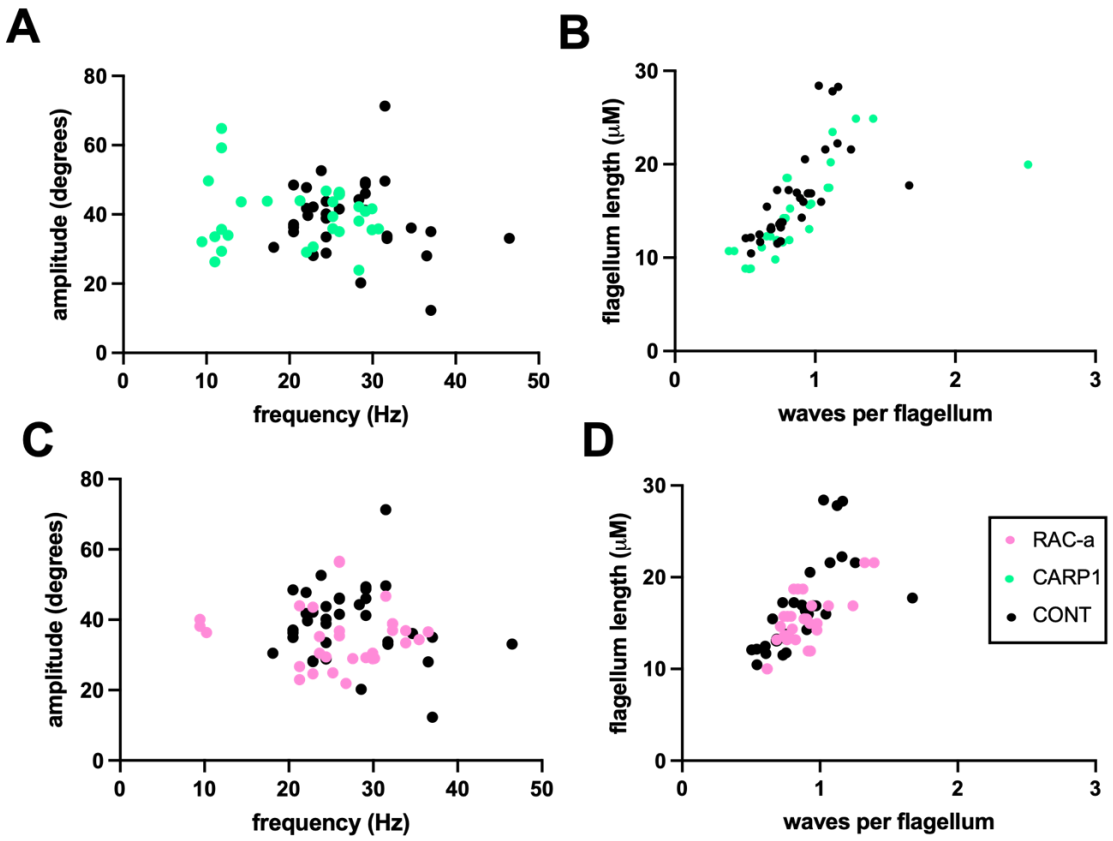
(A) Population Overview Waveform Analysis (POWA) of selected mutants ΔCARP1, ΔPNUT19, ΔRAC-a and parental controls. (B-D) Proportion of first 1000 cell tracks from triplicate motility assay measurements of each mutant cell line (total 3000 tracks for each cell line combined in histogram) demonstrating the proportions of 'fast' (> 10 μm/s), 'medium' (5-10 μm/s) and 'slow' (< 5 μm/s) cell displacement from each motility, plotted as binned speeds (μm/s) against frequency of tracks. Grey bars represent control measured in parallel to the mutant in mint.

one third of the population swimming above 10 μm/s (Figure 2-21C). We saw a similar shift of the *ΔRAC-a* population towards slow motility relative to the control (Figure 2-21D). Taken together, these analyses indicate that the faster average speed of the *ΔPNUT19* population is attributable to more cells reaching the fastest swim speeds (>10 μm/s) with fewer tumbling events. As *ΔCARP1* and *ΔRAC-a* display similar diminished proportions of cells propagating the tip-to-base flagellar beat, this may be the determining factor of population speed. Although the POWA demonstrates an interesting difference between the two, *ΔCARP1* appear to be switching between ciliary and flagellar waveforms much more frequently. By contrast, close to half the observed *ΔRAC-a* cells struggled to generate a recognizable waveform at all.

2.2.3.3. Dissection of flagellar beating parameters suggests cAMP contributes to beat frequency but not amplitude

The motility analysis alongside protein sequence scrutiny so far suggested that there is at least one likely cAMP transducers downstream of RAC-a at the flagellar tip, CARP1, which is required to reach normal population swim speeds. We chose to assess the waveform parameters of a targeted set of mutants, to better understand whether for the swimming cells, it was only a change in the proportion of cells propagating a flagellar waveform that caused the change in population swim speed, or whether there were also changes to the beat amplitude, frequency, wavelength, and/or number of waves per flagellum affected how the mutants were able to displace themselves. We captured high speed videos with high magnification (100x) of cells propagating the tip-to-base flagellar waves and used Fourier wave decomposition to assess changes in waveform parameters against parental

controls (see Chapter 5: Materials and methods, Section 2.2.4, 2.3). We saw that flagellar movement in *ΔCARP1* cells had similar beat amplitudes to controls (mean 39 degrees) (Figure 2-22A), however the beat frequency was significantly diminished from the normal average of 27Hz to 21Hz (Mann-Whitney test, p = 0.0153) (Figure 2-23A).



E

	n cells	total t (s)	ampl (deg)	Hz	w/f	beat wl (μM)	F-length (μM)
CARP1	20	38	39.58	21.07*	0.88	17.72*	14.89
RAC-a	14	37.4	35.10	26.03	0.88	17.41*	15.02
CONTROL	21	33	39.11	27.15	0.85	19.35	17.04

Figure 2-22: Waveform parameters for slow swimming mutants.

Fourier decomposition of tip-to-base flagellar waveform of ΔCARP1 and ΔRAC-a. Beat frequency (Hz) plotted against amplitude (degrees) and waves per flagellum plotted against flagellum length (μm) for (A-B) ΔCARP1 cells (mint) and (C-D) ΔRAC-a cells (pink). (E) Summary table of number of cells observed (n cells), total time observed in seconds (total t

(s)) in addition to the average amplitude, frequency, waves per flagellum (w/f), beat wavelength (beat wl) and flagellum length (F-length) for each mutant and the parental control cells. Statistical significance tested by performing a Mann Whitney non-parametric test. Asterisk indicates p-values < 0.5.

Intriguingly also, the flagella appeared shorter (mean 14.89 µm) than control flagella (17.04 µm) with a significantly lower beat wavelength of 17.72 µm compared to 19.35 µm in parental controls (Figure 2-22E). The flagellar length and number of waves per flagellum appeared to be positively correlating, as seen in controls cells (Figure 2-22B).

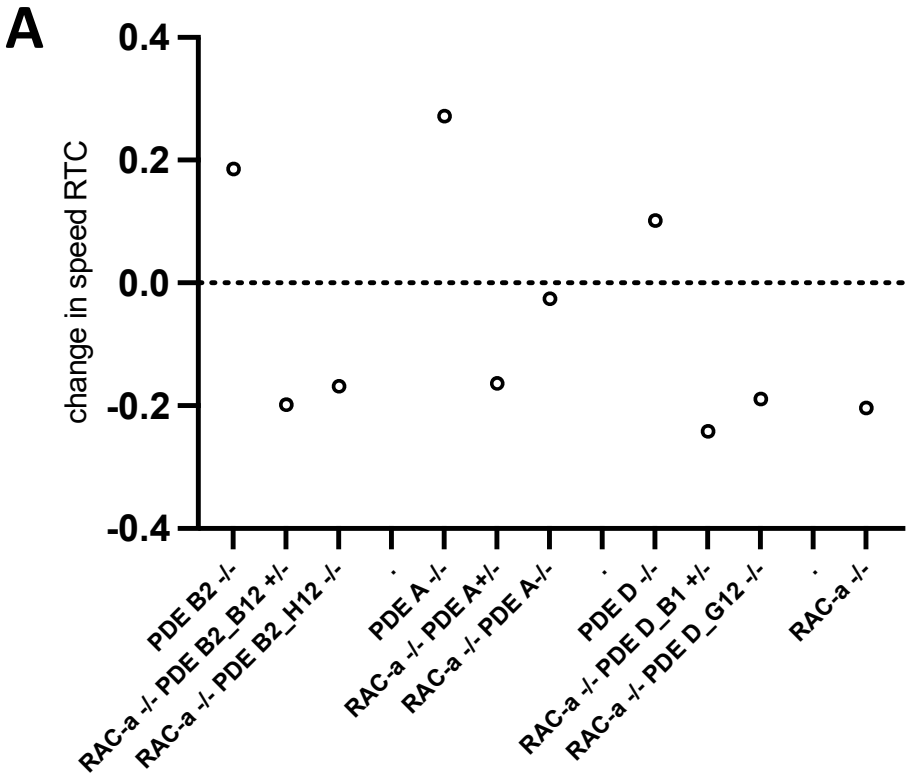
Beating parameters of *ΔRAC-a* cells were assessed by the same methods. The results show that asides from a significantly diminished beat wavelength (17.41 µm), which is likely attributable to the shorter flagella (15.02 µm) seen in the cohort of cells captured, the beat frequency, amplitude and waves/flagellum were comparable to parental control cells (Figure 2-22C, 22D, 22E).

From this analysis, we see that RAC-a and CARP1 are potentially required to reach normal flagellar lengths, and that upon loss of CARP1, cells are unable to reach higher beat frequencies above 30 Hz. Otherwise, the *ΔRAC-a* cells are able to beat flagella with normal wave parameters.

2.2.3.4. Deletion of flagellar localised PDE A, but not PDE D or B2, can rescue the slow swimming phenotype of ΔRAC-a

Our data demonstrates that deleting flagellar localised PDEs in *Leishmania* increases the population swim speed (Figure 2-20A / Section 2.4.2), presumably as a consequence of

increased levels of their substrate in the flagellum, be it cAMP, a different cyclic nucleotide or a novel endogenous ligand. On the other hand, we identified also a flagellar tip localised adenylate cyclase, RAC-a, for which null mutant swam measurably slower than parental controls (Figure 2-19 / Section 2.4.1). This brought about the question, if this RAC-a is acting upstream of the any of these PDE isoforms within the flagellum, could deletion of a PDE



B

cell line	*speed 1*	*speed 2*	*speed 3*		*mean speed*	*change RTC*
Batch 1						
control	8.12	8.66	8.8		8.53	n/a
PDE B2 -/-	10.8	9.73	9.8		10.11	18.57
RAC-a -/- PDE B2_B12 +/-	6.84	6.59	7.08		6.84	-19.82
RAC-a -/- PDE B2_H12 -/-	7.64	7.08	6.56		7.09	-16.81
Batch 2						
control	8.49	8.86	8.29		8.55	n/a
RAC-a -/-	6.68		6.93		6.8	-20.38
PDE A -/-	10.8	11.3	10.5		10.87	27.15
RAC-a -/- PDE A+/-	7.56	7.28	6.6		7.15	-16.38
RAC-a -/- PDE A-/-	8.97	7.52	8.49		8.33	-2.57
Batch 3						
control	10.6	9.68	9.53		9.94	n/a
RAC-a -/- PDE D_B1 +/-	6.41	7.21	6.17		6.60	-33.61

RAC-a -/- *PDE D_G12 -/-*	7.43	7.32	7.12		7.29	-26.64
Batch 4						
control	9.62	8.67	9.57		9.29	n/a
PDE D -/-	10.3	10.4	10		10.23	10.19

Figure 2-23: Genetic rescue of ΔRAC-a mutant slow motility.

(A) Hetero- and homozygous deletion of phosphodiesterase isoforms B2, A and D in the ΔRAC-a cell line shows that only a homozygous deletion of PDE A can rescue the slow swimming ΔRAC-a phenotype back to parental control speeds (dotted line). Change in population swim speed relative to control (RTC). Each point represents the average of at least three replicates. Dashed line represents zero change from parental control measurements. (B) Raw population swim speed measurements from three replicates (speed 1, -2 and -3) and calculated mean speed that were used to calculate the change RTC shown in (A). Motility assays were done in four batches, as indicated and a parental control cell line was assessed for motility in parallel with each batch. The change of mean speed of each mutant relative to control was calculated separately for each batch.

rescue the slow swimming motility of *ΔRAC-a*. This is based on the assumption that other ACs in the flagellum (such as the HemAC or RAC1-3 which are all present in the flagellum (refer to Figure 2-10B)) provide a base level of cAMP in the absence of RAC-a, which may be augmented by PDE deletion. Figure 2-23 shows the motility data from the *ΔRAC-a* cells in combination with heterozygous and homozygous deletions of the negative regulators of swim speed, PDE isoforms A, D and B2, which all negatively regulate swim speed. For reference, the speed of *ΔPDE A, B2* and *D* cells are also plotted, which sit above the dashed line demonstrating their faster motility relative to parental controls. Following deletion of PDE B2 or PDE D in the *ΔRAC-a* background, the cells still swam as slowly as the *ΔRAC-a*. By contrast, upon deletion of PDE A, the swim speed reverted to the level of the parental control line. This effect was only seen when both alleles of PDE A were deleted (Figure 2-23,

compare RAC-a -/- PDE A +/- with RAC-a -/- PDE A -/-). This certainly suggests that either RAC-a and PDE A are modulating the same substrate, which is potentially cAMP, or the consequence of removing PDE A is dominant over the slower motility phenotype of RAC-a. Or indeed, it could mean that PDE B2 or PDE D are not located in the correct subcellular microdomain to compensate the loss of substrate synthesised by RAC-a at the flagellar tip. These data ultimately demonstrate that the loss of RAC-a is phenotypically dominant over that of the loss of PDE B2 and PDE D. As stated previously, this model is consistent with there being other producers of the cyclic nucleotide signal within *Leishmania* flagella. If RAC-a was the only cAMP producer, then we would not have expected any additional deletion of PDEs to rescue the cAMP deficiency.

2.2.4. Pharmacological manipulation and genetic rescue of *ΔRAC-a* slow swimming phenotype corroborates a role in speed modulation

Having explored in depth the consequence of removing components of the putative cyclic nucleotide signalling pathway with a genetic approach, we attempted to modulate flagellar motility directly, by exposing cells to pharmacological inhibitors or activators, or membrane permeable cAMP analogues.

8-Bromo-cAMP, a cell permeable cAMP analogue, had no obvious dose dependent effect on cell motility across a concentration range from 10 nM up to 100 µM (Figure 2-24A).

Next, we used toyocamycin, a secondary metabolite of the *Streptomyces* fungi which was identified in a nucleoside analogue screen for activators of the divergent kinetoplastid PKAR1 (142). Interestingly at 500 nM, toyocamycin caused a measurable increase in population swim speed, however it had a dose dependent inhibitory effect at higher

concentrations (10 and 100 µM) (Figure 2-24B). We questioned whether this inhibitory effect on motility was a side effect of potential toyocamycin toxicity. This was tested by growing the cells in the presence of 500 nM - 50 µM toyocamycin alongside an untreated control population for 48h and plotting a growth curve (Figure 2-24A).

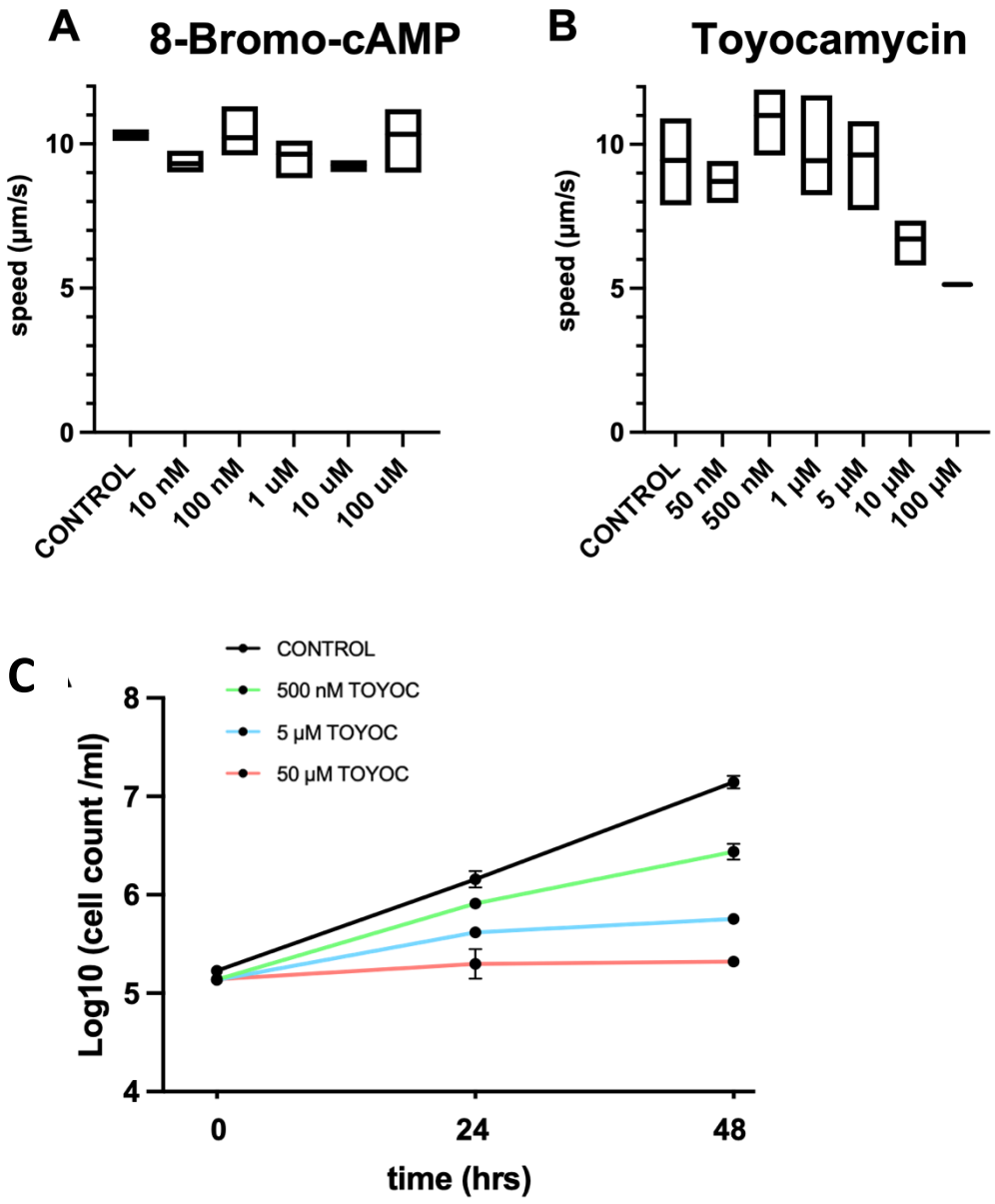


Figure 2-24: Pharmacological manipulation of parental control swim speed.

(A) Speed measurements of L. mexicana Cas9 T7 treated with 8-Bromo-cAMP (cell permeable cAMP analogue) concentrations from ranging from 10 nM to 100 µM and an untreated

control incubated with 0.1% water. (B) Speed measurements of L. mexicana Cas9 T7 treated with a range of toyocamycin concentrations from 50 nM – 100 µM. Increased cell swim speed was observed with 500 nM toyocamycin, however a dose-dependent inhibition of motility was seen at micromolar concentrations. An untreated control was incubated with 0.1% DMSO. For motility assays, measurements were done in triplicate and the incubation period was kept between 30 min - 1 hr. (C) Prolonged growth in the presence 500 nM to 50 µM toyocamycin demonstrates a dose-dependent inhibitory effect on growth over 48 hrs. Controls represent parental control cells grown in the presence of 0.1% DMSO. Each condition tested in triplicate parallel flasks. Drug stocks were made at 1000x the desired concentration so that the drug solution is always added in a 1:1000 v/v ratio.

A dose-dependent inhibitory effect on growth was observed on treated parental control populations (Figure 2-24C), suggesting this compound has targets outside of the divergent parasite PKAR subunits which themselves are not essential for promastigote viability (see Chapter 3, Figure 3-11B). It is interesting that although 500 nM, toyocamycin appears to have a stimulatory effect on flagellar motility (Figure 2-24B), it also has a negative effect on population growth (Figure 2-24C).

Lastly, we found that two compounds designed to bind and inhibit PDE B1 and PDE B2 had been synthesised, named Compound (Cpd) A and CpdB. As there was limited stock of CpdA, we were kindly gifted the CpdB compound by Harry De Koning (144,186). We asked whether CpdB inhibition of PDE B1 and B2 enzymes would phenocopy the fast-swimming phenotype of the null mutants (Figure 2-20A). As the IC50 of CpdB was reported to be 50 nM on recombinant PDE B1 (186), we tested a range from 100 pM to 100 µM in DMSO, although it must be noted that higher concentrations were observed to precipitate when added to water-based solutions such as culture medium. To our surprise, CpdB had a dose

dependent inhibitory effect at higher concentrations (µM range) on the forward flagellar wave, where the flagellar/ciliary switching behaviour as well as the tumbling ciliary

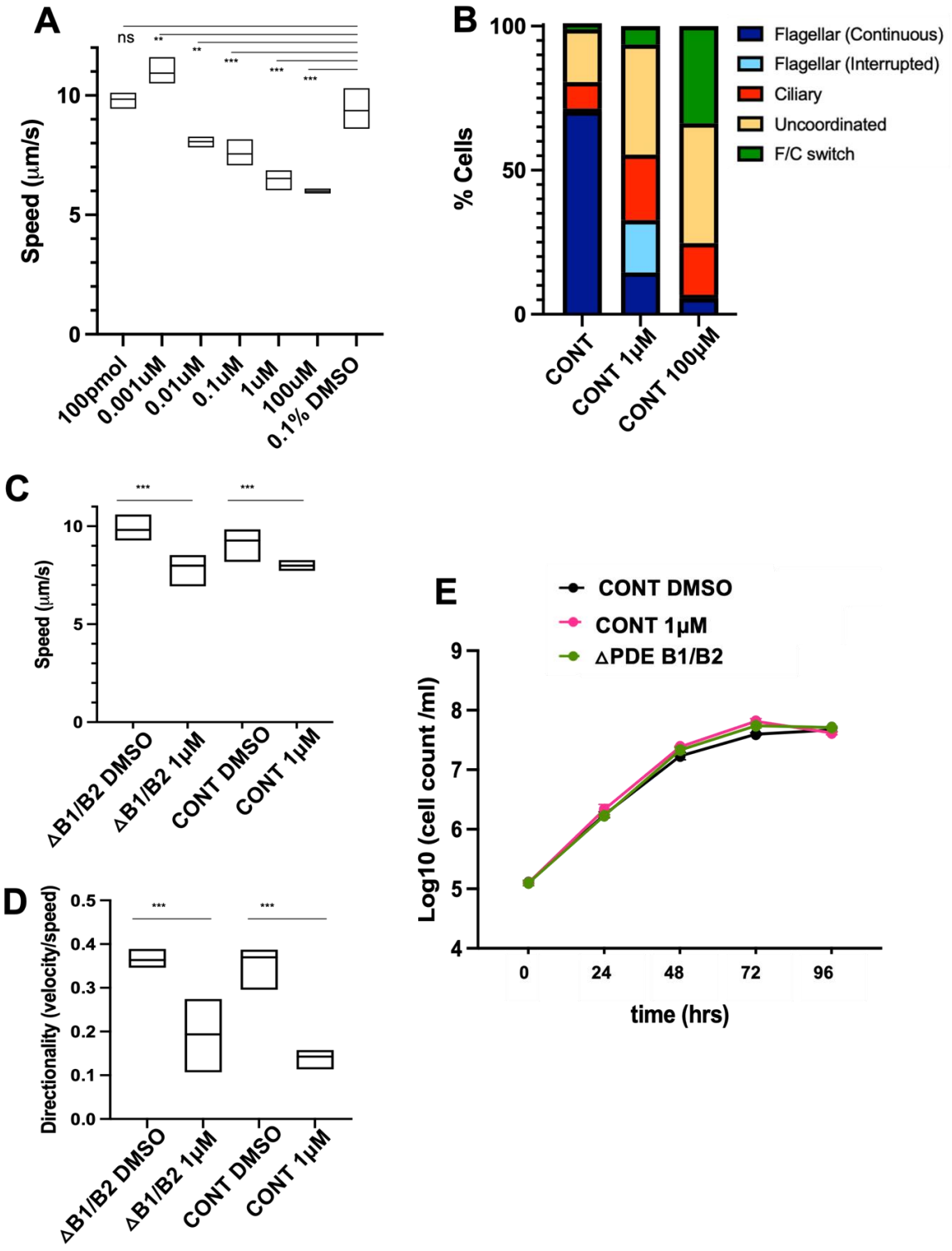


Figure legend on following page.

Figure 2-25: CpdB likely has targets outside of PDE B1/B2.

(A) Speed measurements of L. mex Cas9 T7 treated with a range of Compound B (CpdB) concentrations from 100 pM to 100 µM. Controls were assayed with 0.1% DMSO. (B) Comparing the effect of 1 and 100 µM CpdB on the proportion of waveform types propagated compared to untreated parental control populations (Cas9 T7). (C) Changes in population speed and (D) directionality of parental control cells (Cas9 T7) and PDE B1/B2 double null mutant with 1 µM CpdB treatment or 0.1% DMSO as a control. Unpaired students t-test assuming equal variance was used to test for significance. (E) Growth curve comparing 1 µM CpdB treatment with the growth of parental controls (CONTROL) and the PDE B1/B2 double null mutant over 96 hours. Measurements ran in triplicate parallel flasks.

beat became more dominant with higher concentrations (Figure 2-25A, 25B). This is reminiscent of the PDE B1 mutant which showed an increased tumbling and switching phenotype, however, CpdB treatment did not phenocopy the flagellar waveform proportions described in the PDE B1/B2 double mutant shown previously in Figure 2-20B. However, we did indeed see that at lower concentrations, we saw a stimulatory effect on population speed (Figure 2-25A).

If the CpdB was exclusively targeting PDE B1 and B2, as it was designed, we would expect to find that CpdB incubation would have little or no effect on the genetic double null mutant of PDE B1/B2 (Figure 2-20C). Figures 2-25C, 25D show that CpdB at 1 µM had a similar effect of motility inhibition to parental controls, suggesting that CpdB in the micromolar range is targeting other components asides from these two PDEs.

Literature points to these two PDE B proteins being together essential, at least from evidence in bloodstream form *T. brucei,* where it is thought they compensate for one another in single null mutants (164). As we showed previously that the motility inhibition of toyocamycin was biologically linked to cell lethality (Figure 2-24C), we tested whether

motility inhibition from CpdB treatment could also be a result of compound toxicity. Figure 2-25E demonstrates clearly that neither parental control populations, nor genetic double mutants of PDE B1/B2 showed growth defects over a 96-hour period of exposure to 1 µM CpdB.

2.2.4.1. Pharmacological rescue of slow swimming ΔRAC-a

We have established so far that in *Leishmania*, CpdB likely has targets outside of PDE B1 and B2, where nanomolar concentrations are able to elevate, and micromolar concentrations inhibit population motility in parental controls. We next asked whether the former stimulatory effect was able to rescue, to any extent, the slow swimming phenotype of *ΔRAC-a* cells. In parallel, we tested the effect of 100 nM CpdB on *ΔRAC-a* next to the *ΔRAC-a/ΔPDE A* double mutant which we previously showed had comparable population speed to controls (Figure 2-23, Section 2.4.2). We saw that CpdB had a similar rescue capability on *ΔRAC-a* population speed and directionality (Figure 2-26A), suggesting the downstream targets of CpdB may include PDE A.

Lastly, we decided to explore the inhibitory effect of higher micromolar concentrations of CpdB on *ΔCARP1* and *ΔRAC-a* cells. We saw that even up to 100 µM, no significant change in swimming behaviour was seen in *ΔCARP1* (Students unpaired t-test, Figure 2-26B). Contrastingly, we observed that, where 1 µM of CpdB diminishes the swim speed of parental control populations, 1 µM CpdB had the opposite effect on *ΔRAC-a* motility, increasing it slightly. We did, however, observe an inhibitory effect on population motility of *ΔRAC-a* at 100 µM (Figure 2-26B).

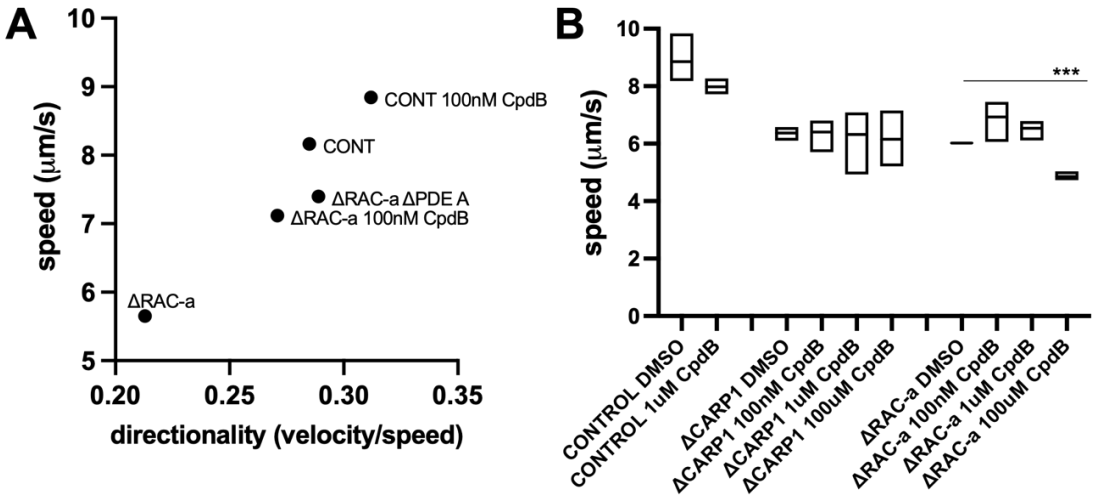


Figure 2-26: CpdB treatment can rescue slow swimming motility of ΔRAC-a.

(A) Directionality (velocity/speed) plotted against speed (μm/s) of the slow swimming ΔRAC-a compared with ΔRAC-a treated with 100 nM CpdB. Measured in parallel were the parental control populations with and without 100 nM treatment in addition to ΔRAC-a/PDE A double null mutant which was previously shown (Figure 2-23) to rescue the slow motility phenotype. (B) The motility measurements of ΔCARP1 and ΔRAC-a treated with a range of CpdB concentrations from 100 nM to 100 μM, highlighting that ΔCARP1 does not have any net change in population speed, however ΔRAC-a requires the highest CpdB concentration (100 μM) to inhibit the population motility. The controls are incubated with 0.1% DMSO.

2.3. Discussion

2.3.1. Limitations of techniques and proposed next experiments

2.3.1.1. Only one to four predicted cAMP transducers encoded in the L. mexicana genome

A combination of literature searches as well as canonical PFAM and Superfamily domain searches on the TriTrypDB yielded a list of 35 putative cyclic nucleotide signalling components in *L. mexicana* (excluding the published divergent parasite PKAR). As the cAMP binding domain sequence of the phosphate binding cassette is well described (125), we used the presence of canonical glycine/glutamate and arginine residues to determine whether our PNUTs contained classical or divergent (likely cAMP insensitive) cyclic nucleotide binding domains (CNBDs) (Figure 2-4). This revealed that only four CNBDs from four PNUTs contained the canonical residues in the expected positions according to our reference panel (Figures 2-2, 2-3). One PNUT (PNUT/PK23) contained a documented alanine/glutamate switch which is observed to result in cAMP repulsion from the binding pocket of PKAR1, as reported in *T. cruzi* (142), and similarly we saw that the glutamate present in position 3 of the PNUT19 PBC had a similar repulsion to the cAMP molecule (Figure 2-7B). Another PNUT (FlaM6) had poor predicted cAMP binding position from SWISS-MODEL and Swiss Dock *in silico* output (Figure 2-6B). As this analysis is purely predictive, we decided it was not robust enough evidence to exclude the other divergent 14 PNUTs (with 'classical-like' and 'non-classical' PBCs) from the projects' protein tagging and motility analysis. These early diverging eukaryotes are documented to have repurposed canonical signalling components in unexpected ways (142), which may mean that they have also evolved novel mechanisms of responding to a cyclic nucleotide signal outside of the conserved CNBD. If our predictions

are correct, the *L. mexicana* genome truly encodes only one classical (with three more PNUTs a at a lower confidence) cAMP transducer protein. If more time were available, it would be worthwhile optimising experimental techniques to assess *in vivo/in vitro* cAMP fluctuations as well as protein binding of cAMP in *Leishmania*. Several *in vitro* experiments on purified recombinant proteins have been used to assess cAMP binding or hydrolytic activity (144,186,190). For example, the use of cAMP-coupled agarose beads, whereby the bound target protein is displaced by either 1 or 10 mM of free cAMP (190). This could prove a valuable indicator on whether a protein of interest is able to bind the ligand, however, is not physiologically relevant in terms of concentration (millimolar range) and is only meaningful if assays are conducted with the correct ligand because even PKAG will bind cAMP within the micromolar range, however it is not the physiological activator. Of course, obtaining a co-crystal structure of protein and ligand would add confidence to our predictions, answering what our classical PNUTs can bind, but that said, many PKG proteins have been co-crystalised with cAMP rather than cAMP (see Chapter 2 reference panel for cAMP bound proteins) and so it is imperative to recognise the limitations of whatever technique is used.

Previous publications have used whole cell lysate and ELISA, in combination with cell treatments such as pharmacological inhibition of PDEs, to interpret drug efficacy (144,164). This techniques main limitation is that it measures whole cells, thus measuring global cAMP changes, and moreover, it is not known whether the anti-cAMP-Ab is cross-reactive to novel nucleoside molecules which are likely present in the cell lysate. Our protein localisation screen indicates that the cAMP synthesisers are confined to precise domains such as the flagellar tip and CVC. Thus, the resolution of this ELISA technique is likely not enough to

detect the loss of one AC from the tip of the flagellum, and that is assuming it is cAMP being produced.

A recent publication utilises a cell reporter which infers PKA activation by the phosphorylation of exogenous VASP (a target of mammalian canonical PKA phosphorylation) expressed within the parasites (142). This indirectly infers cellular levels of the PKA activator, however again, whole cell lysate is needed here to quantify phosphoprotein abundance and thus the technique lacks the resolution needed to detect fluctuations within micro/nanodomains. To adapt this technique to answer our questions, we could consider fusing a localisation sequence to chaperone the reporter protein to the desired domain (*i.e.,* the axoneme or flagellar tip membrane). Furthermore, instead of lysing the cells to infer phosphorylation levels, it would be more useful if a visual signal could be quantified *e.g.* luciferase (228), fluorescence or FRET signal was emitted upon reporter protein phosphorylation. Ultimately, techniques which act within an intact biological environment where outcomes maybe visualised in real time would be most ideal to understanding the dynamics of cAMP production and degradation within specific microdomains. FRET between cAMP and specific target transducer proteins could provide some visual proof of dynamic binding. A multitude of genetically encoded FRET sensors, where small molecules such as cAMP cause a change in proximity of reporter proteins (FRET on and off sensors), have been developed for use in mammalian cells (42). Bioluminescent based cAMP sensing has also been developed, for example cADDis assay kits by Molecular Montana, however these are also designed for mammalian-based experiments using viral expression vectors and so would need heavy adaptations to be useable in kinetoplastid species. The establishment of these types of reporter assays are often not trivial, likely taking a large amount of work and time to be reproducible, robust and sensitive enough,

however, the outcome product would be useful to conjoin our observations of flagellar waveform behaviour in certain mutants, and the internal signal dynamics which correlate.

2.3.1.2. Residues of the phosphate binding cassette are (almost) invariable throughout diverse CNBD containing proteins

Within our reference panel from proteins co-crystalised with cAMP from the Protein Database (PDB) we noted that there was almost a consensus of two glycine spaced 11 amino acids apart nearer the N-terminus of the CNBD, and a GE and R residue in positions 1, 2 and 11 of the PBC. There were, however, three cases of prokaryotic sequences, *i.e.* cAMP Response Protein (CRP) of *E. coli* and *Y. pestis*, and the virulence factor regulator (Vfr) of *P. aeruginosa* (a homolog of the CRP (230)), where the PBC contained a 1-4aa insertion. When we inspected these co-crystal structures more closely, we see that whist they appear to have canonical cAMP binding position and hydrogen bond formation despite the longer PBC sequence, the *E. coli* and *P. aeruginosa* proteins are noted to have a predicted second cAMP bound outside of the CNBD, hydrogen bonding with ARG-180 and GLU-58 (Figure 2-27A, 27B). Whether this reflects the biologically relevant binding position is debatable, as cAMP is vulnerable to degradation by PDE enzymes if not protected by an appropriate binding pocket. We cannot discard the possibility completely that kinetoplastids have evolved a novel mechanism of binding and responding to cyclic nucleotide second messengers, which may not involve a classical PBC or CNBD. In this scenario, we do not have an established set of reference proteins which exhibit alternative cAMP docking with which to compare our divergent PNUT proteins. It may be that, as the DUF21 proteins which have repurposed their

CNBD for protein dimerization (217), the cohort of PNUTs included in this study may have equally diverged to fit niche roles within the *Leishmania* lifecycle.

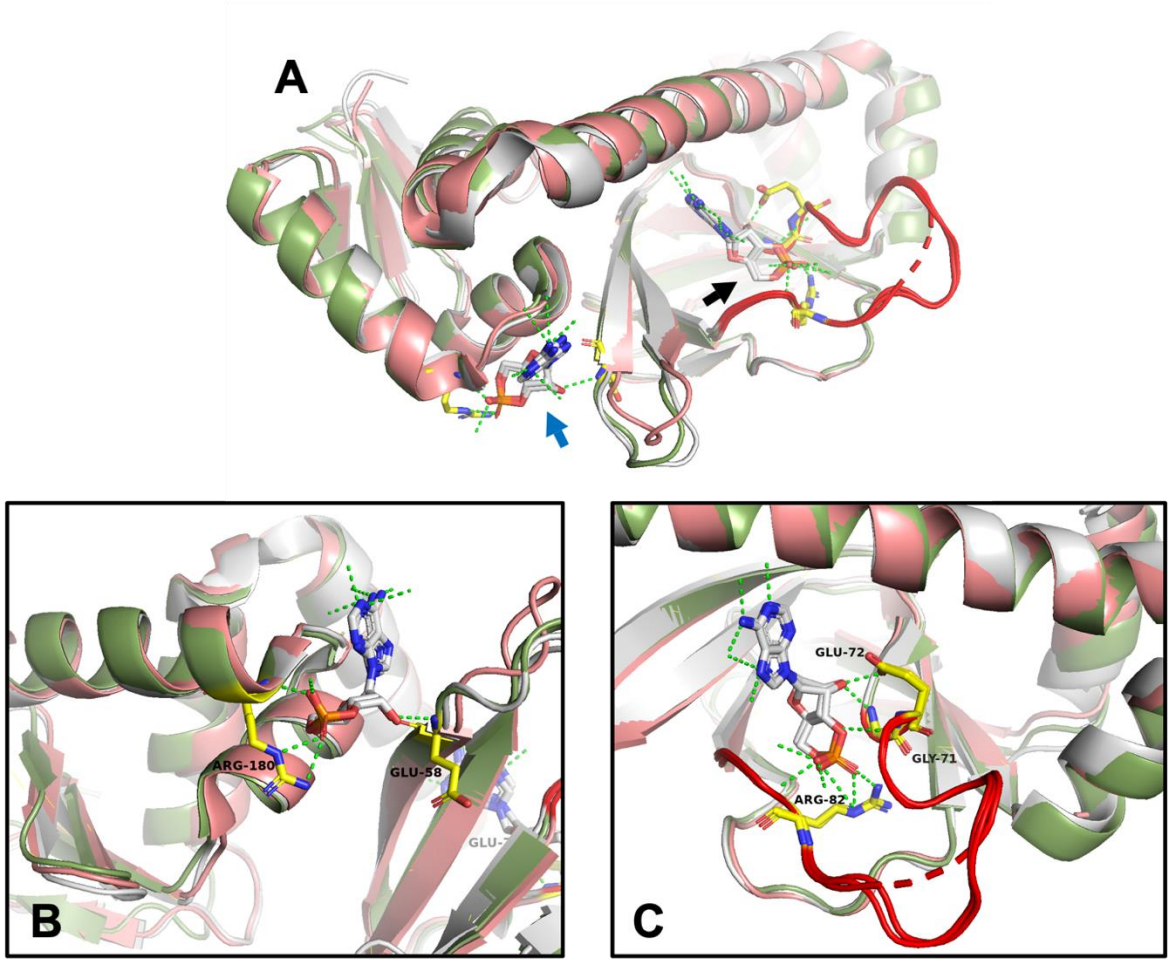


Figure 2-27: Unconventional cAMP binding positions.

(A) Overlay of the three cAMP receptor protein (CRP) from E. coli (pea green), P. aeruginosa (grey) and Y. Pestis (salmon) (PDB codes 3KCC, 2OZ6 and 6DT4 respectively sourced from PDB) co-crystallised with cAMP molecules. Highlighted are the primary canonical binding position of cAMP in the PBC (black arrow) and a potential secondary binding position for cAMP for E. coli and P. aeruginosa (blue arrow). (B) close up visual of the hydrogen bond formation of cAMP with GLU-58 and ARG-180 of the unconventional cAMP binding position and (C) close up of the canonical binding interactions of cAMP with the PBC. PyMOL used to visualise structures and create figures.

2.3.1.3. Endogenous fluorescent tagging of putative cyclic nucleotide signalling components was successful in establishing likely signalling microdomains

Our approach to endogenously fuse mNG to our target proteins yielded clear protein localisations for 29 of the 32 tagged components. There were three proteins which yielded unclear localisations and three proteins which were not possible to tag due to incomplete genome sequence availability. We ultimately identified at least nine subcellular domains for our cohort of proteins, namely, the flagellar axoneme, distal flagellum, proximal flagellum, flagellar pocket, flagellar collar/FAZ, contractile vacuole complex, basal body, small cytoplasmic organelles and the nucleus. Firstly, four PDEs, four ACs and 11 PNUTs were enriched within the flagellum.

Flagellar domains

Of the flagellar localised PDEs we observed isoforms B1 and B2 to have a distal to proximal gradient only with the C-terminal tag, and a more homogenous distribution along the entire axoneme with the N-terminal tag. This makes sense in context of previous work (159) which described how the N-terminus sequence of PDE B1 contained the signal for axonemal localisation (231), thus blocking this end has potentially caused an aberrant protein distribution along the flagellum. As *ΔPDE B1* and *ΔPDE B2* both show increased population swim speed, with the *ΔPDE B1* population propagating the reverse ciliary wave in a significant proportion of cells (Figure 2-20B), it would be intriguing to investigate and compare the waveforms of PDE B1 and PDE B2 N- and C-terminal tag expressing mutants. This would answer whether the different distributions of protein along the flagellum have

an effect on the proportions of forward and reverse beats propagated, in context of the null mutant phenotypes that we described.

Although PDE A and D are both predicted by DeepTMHMM to be cytoplasmic globular proteins, this is in disagreement with TriTrypDB where PDE D is predicted to have a TMD at the C-terminus. Both C-terminal tags appeared enriched towards the distal flagellum, a microdomains we know receptor type adenylate cyclase are embedded in the membrane. Consistent with previous findings in *Leishmania* (77), we find these localisations in combination with faster swimming null mutant phenotypes point towards cAMP being a negative regulator of swim speed, where cAMP specifically takes effect in the distal flagellar fraction. It has been shown that all of these flagellar localised PDEs, asides from PDE D, are able to complement PDE deficient yeast (181). As there is a novel parasite specific signalling pathway now described, it still remains to be found what is synthesising and degrading these novel signals. Also, flagellar localised were RAC-a and RAC1/RAC3, all showing similar tip enriched signals tapering off towards the mid-flagellum (Figure 2-10C). Interestingly, we saw the HemAC enriched throughout the entire flagellum, where it was recently published to be also enriched towards the tip (158). Once we established the localisation of cyclic nucleotide synthesisers and degraders to the distal flagellum, it would have been plausible to hypothesise that the signals transducer protein/s would also be localised in the distal flagellar portion. However instead, we saw instead that 10 of our PNUTs were detectable along the entire flagellar length, with an additional two which were localised to the proximal flagellum (FlaM6 and PNUT37) and one (PNUT19) which localised occasionally to the very flagellar tip as a dot, alongside a flagellar collar/pocket/FAZ localisation. Of the 10 axonemal PNUTs, two did not contain any predicted cAMP binding domains (CARP2 and CARP4), and CARP1 was the only protein to contain a classical PBC sequence described to bind cAMP.

This alludes to only one transducer downstream of the four ACs and PDEs which localise to the (distal) flagellum.

Potential protein localisations to the Contractile Vacuole Complex

We saw that PDE C, previously hypothesised to be involved in the osmoregulatory function of the contractile vacuole complex (CVC) in *T. cruzi (145,179)*, localised to several bright dots near the flagellar pocket/collar. We found that one hypothetical adenylate cyclase (hypothAC) and two PNUTs were also found in this region, the hypothAC as one bright dot, and PNUT76 with DUF21a with more diffuse enrichments just below the kinetoplast. We may, given more time, have explored these as potentially involved signalling components in the proposed osmoregulatory function of the CVC. Exposure of the null mutants to adjusted culture medium conditions may have confirmed (or not) this involvement. There are, however, more structures to consider around this region of the cell. For example the basal body, flagellar pocket membrane and exo- and endocytic secretion systems from the flagellar pocket (232). To find precisely which organelle or structure these components are localised to, we could perform tagging of marker proteins (79) and perform super-resolution microscopy.

2.3.1.4. The unknown localisation of axonemal CARP1

The CARP1 knockout line was the slowest swimming mutant in our motility screen (Figure 2-19). Tagged CARP1 appeared firmly embedded in the flagellar axoneme, still visible in detergent extracted cytoskeletons in promastigote parasites (Figure 2-14). Therefore, we hypothesised that CARP1, containing the canonical residues for cAMP binding, acts to

transduce a cAMP signal to axonemal protein complexes that cause flagellar bending. Thus, we saw fit to investigate what axonemal structure it may be interacting with to ultimately tune the flagellum movement. Our approach was to utilise a cell line expressing tagged CARP1 as a reporter line, in which we deleted core axonemal structures to see if the CARP1 localisation would change or disappear from the flagellum. Although we gained null mutants for many of the structures targeted (Figure 2-14), generation of null mutants was noted to be particularly inefficient where many targeted proteins yielded no stable mutant despite many attempts of transfecting. To our surprise, we observed that the CARP1 protein was still present after deletion of components within the distal outer dynein arm docking complex, N-DRC, radial spokes, central pair, and some parts of the IDA. All we may conclude from this is that the localisation of CARP1 is not dependent any of the nine proteins investigated. The additional structures that we targeted for disruption included the microtubule lumen, which is documented to contain numerous protein structures (Microtubule Inner Proteins (MIPs)) which have been well described in recent cryo-EM work (34,109). We attempted deletion of several of the *Leishmania* RIB72 paralogues documented to cause loss of several other MIP structures in *Tetrahymena* null mutants (34). We additionally targeted the CCDC39/40 structure which holds in place the entire inner dynein apparatus and basalin, required for the central pair nucleation (233). The flagellum itself is not essential for promastigote survival (77), and thus these technical issues of gene deletion are unlikely due to gene essentiality. We cannot rule out, however, that CARP1 isn't tethered directly to the tubulin protofilaments of the axonemal cytoskeleton, a localisation we are limited in exploring due to the essentially of tubulin to cell viability and indeed the essentiality of tubulin for building a flagellum.

Given more time, I would revisit this technique of targeted gene deletion and create a new mNG::CARP1 parental cell line to work with, in case there is some technical issue with the previous clone picked. As well as this, I would spend efforts to try and identify CARP1 binding partners to determine its precise localisation within the axoneme, exploring techniques like Bio-ID, immunogold-EM, or even to utilise the salt extraction of CARP1 at 5 M NaCl alongside mass spectroscopy to identify what other proteins may be solubilised with CARP1. This technique has been fruitful before in identifying axonemal localisations (223), and works on the basis of some axonemal proteins being loosely bound, whilst others are embedded in the core structure of microtubules and radial spokes. This technique would potentially highlight the proteins anchored alongside CARP1 and provide us with new target domains to test localisation dependencies with. Determining the interaction partners of CARP1 would significantly increase our understanding of how cAMP may be modulating the flagellar beating.

2.3.1.5. Motility phenotypes in the null mutant library

The CRISPR-Cas9 technique was successful in making a knockout library of 25 mutants, three of which still contained detectable fragments of the ORF by our diagnostic PCR method of genotype verification (Figure 2-17). The population motility assessment of these 25 mutants revealed that *⊿CARP1*, *⊿RAC-a*, *⊿DUF21a* and two PNUTs *(⊿PNUT/PK14* and *⊿PNUT51*) had the lowest population swim speed. This highlights several curious points. Our localisation study pointed out that four adenylate cyclase were flagellar enriched, mostly towards the distal tip. However, our motility assay showed that, of these, only *⊿RAC-a* presented a reduced motility and *⊿RAC-a-like* presented an increased population motility.

As the RACs have been hypothesised to dimerise as a possible mechanism of catalytic activity modulation (169), it may mean that the RAC-a deletion has dominant negative effect on the RACs localised to the tip membrane, acting effectively as the main modulator of RAC activity in that domain. Alternatively, it may be that the other flagellar tip RACs are not active in the standard M199 culture conditions, and thus the null mutants do not present a change in motility. This is plausible as it is not known yet what activates kinetoplastid ACs. As for the faster swimming *⊿RAC-a-like* population, it is hard for us to hypothesise why or how *⊿RAC-a-like* presents a faster population motility without a clear protein localisation (Figure 2-10B). Among the slow swimming mutants, was DUF21a which localised to a domain around the flagellar pocket/kinetoplast (Figure 2-11F). As previously noted in Figure 2-1B', these *Leishmania* DUF21 containing proteins share significant domain similarity to the CNNM proteins described in mammals to be magnesium or metal ion transporters (217). As a broad range of enzymes require magnesium for catalytic function, removing means of magnesium transport would likely have a global effect on cell biology. Thus, the slow swimming phenotype of the DUF21a null mutant is potentially an indirect effect of magnesium dysregulation.

We also observed the ΔPNUT/PK14 cells to swim significantly slower. For PNUT/PK14, our protein sequence analysis showed similar patterns of amino acid divergence within the phosphate binding cassette, to the recently described divergent PKAR1 of *T. cruzi* (142) (Figure 2-4B). If the divergent CNBD sequence of PNUT/PK14 is truly indicative of its ligand, this finding may present the first signalling component outside of the divergent PKA (Chapter 3) to transduce this novel ligand. Lastly, we saw that CARP1 was the slowest swimming mutant in our dataset, and in combination with its localisation to the flagellar axoneme, and its classical PBC sequence for cAMP binding, we predict this is the only

canonical downstream transducer of the cAMP signal within the flagellum. The POWA from CARP1, with a large proportion of tumbling motility, indicates it plays a role in the balance between forward flagellar motility and reverse ciliary beats (see section 2.6.1 for proposed model).

On the other end of the spectrum, we observed that seven null mutants in our mutant library that swam significantly faster than controls, among which flagellar localised PDEs are enriched alongside PNUT19. Our sequence analysis of PNUT19 shows that although it contains the canonical GE and R residues necessary for cyclic nucleotide binding (125), a residue switch at position 3 appears to have introduced a negative glutamate which is predicted by Swiss Dock to repel the cAMP molecule out of the PBC (Figure 2-7B). Although we categorise the PNUT19 PBC 'classical', we have low confidence of cAMP being its biological ligand and only experimental investigation such as those discussed in section 2.6.1.1, will bring clarity as to what it binds. The localisation data indicates PNUT19 presence in several domains, *i.e.,* flagellar attachment zone (FAZ), collar, pocket area, as well as the flagellar tip. PNUT19 protein is a very large protein with a C2 domains in addition to the CNBDs (Figure 2-28). The EF-hand and C2 domains are both equally prevalent calcium sensors in eukaryotic organisms, where the latter domain coordinates protein membrane trafficking in a calcium dependent manner (234). Based on this, it would be worth investigating whether the localisations of PNUT19 change under various calcium conditions (*e.g.,* chelation). This protein is not the first calcium sensing negative regulator of forward motility in kinetoplastids. LC4-like localises to the distal outer dynein arm complex and negatively regulates swim speed by decreasing the chance of cells propagation a tip-to-base symmetric flagellar beat (227). We may postulate that the calcium sensing PNUT19, when

localised at the flagellar tip, works in combination with LC4-like to negatively regulate swim speed.

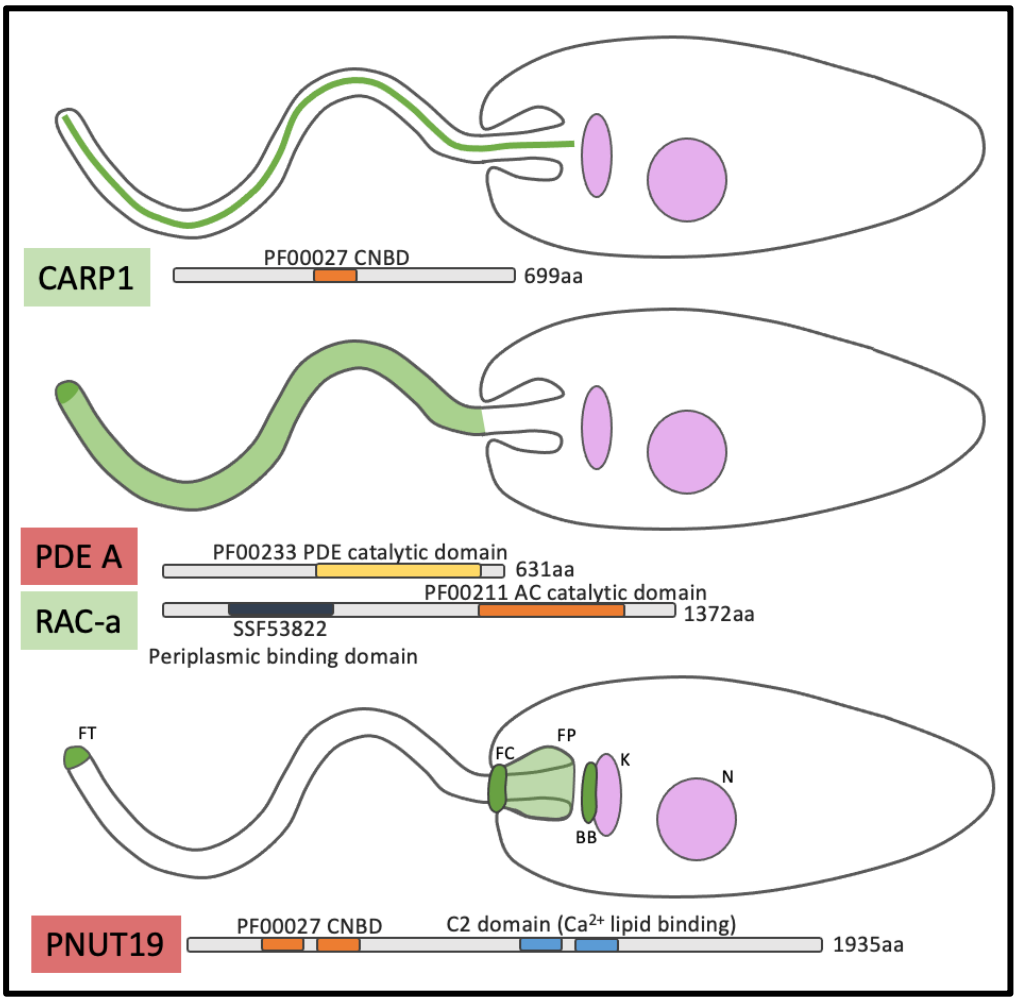


Figure 2-28: Microdomains involved in flagellar motility.

Cartoons of promastigote cells with the summarised sub-cellular microdomains involved Leishmania flagellar motility. CARP1 and RAC-a in the flagellar axoneme and distal flagellar tip respectively, are required for normal population swim speed. The negative regulators of swim speed are shaded in red, where PDE A is enriched at the distal flagellar half and PNUT19 localises to both regions within the flagellar pocket/collar and is observed often as a dot at the flagellar tip. Protein domain architecture is depicted along with the protein length. proteins Abbreviations: BB – basal body, K – kinetoplast, N – nucleus, FC – flagellar collar, FT – flagellar tip.

2.3.2. Proposing a model for cAMP modulation of flagellar motility

Ultimately, the experiments reported in Chapter 2 were designed towards gaining a testable hypothesis of how cAMP may be acting within the motile flagellum. Piecing the findings together, it was evident by the POWA outcome that both CARP1 and PDE B1 mutants displayed a disproportionally increased reverse beat (cilairy and flagellar/ciliary switching behaviours) and decreased proportions of forward swimming cells (flagellar waves) (Figures 2-20B, 2-21A). Intriguingly, the closely related PDE B2 enzyme (previously assumed to work similarly to PDE B1 as they can compensate for eachothers loss in *T. brucei* bloodstream forms (164)), appeared to have a different null mutant phenotype to *ΔPDE B1* with only a marginal increase in forward motility compared with control populations. If these enzymes compensated for eachother within the flagellar organelle of *Leishmania*, we would expect the null mutant phenotype to present itself only when both were isoforms were deleted. However this was not the case. The dual knockout of both PDE B1 and B2 isoforms presented an intermediate phenotype, with a marginal increase in tumbling motility and a marginal decrease in forward motility. However this mutant still maintained an increased population swim speed overall (Figure 2-20C). These data suggest distinct functions of the two isoforms, perhaps attibutable to different affinities for cAMP hydrolysis.

Considering that *ΔCARP1* and *ΔPDE B1* are the only mutants from our entire screen that show similar degrees of increased ciliary waveforms, it is tempting to speculate that they may be part of the same signalling pathway, perhaps even associating with the same axonemal structure to modulate the balance between flagellar and ciliary beats (forward and tumbling motility respectively). As CARP1 is localised along the entire flagellar axoneme cytoskeleton, and PDE B1 (which we assume hydrolyses cAMP based on prior evidence

(144,164)) localises most strongly to the distal flagellar cytoskeleton and tapers off towards the proximal end, it may follow that under normal *in vitro* media culture conditions, PDE B1 creates a low cAMP environment in the distal flagellum around CARP1, with increasing cAMP abundance towards the proximal base region (as PDE B1 abundance tapers off). This normal balance results in a dominant (75% population) forward motility behaviour with a minority (1-10%) of cells propagating a ciliary beat, is observed in our parental controls. When this proximal/distal cAMP balance is removed/disrupted (by means of removing the cAMP transducer *i.e. ΔCARP1*), the waveform proportions becomes dominated by base-to-tip ciliary waves, but notably does not abolish completely the forward motility. In *ΔCARP1* cells which are still found to propagate the tip-to-base wave for forward motility, the beat amplitude remains normal whilst the beat frequency and wavelength are significantly diminished. Interestingly, when we create conditions of high cAMP abundance by deletion of the distal flagellar PDE B1, or incubating cells with the CpdB kinetoplastid PDE inhibitor (in the micromolar range) which has been shown to cause elevated cAMP (144), we also see an increase in reverse ciliary waves (although not seen with cell permeable cAMP analogues). Together these observations suggest that either no cAMP or too much cAMP in the wrong place (*i.e.* proximal vs distal flagellum) has a similar effect on increasing the proportion of reverse waves (Figure 2-30). Note that the CpdB intervention increases the population swim speed at lower concentrations (~100 nM), however inhibits motility at higher concentrations (>1 µM) by increasing the tumbling motility, but importantly, has no effect on the population swim speed of CARP1 null mutants from 100 nM even up to 100 µM (Figure 2-25B). This could suggest that CARP1 within the axoneme is modulating the population swim speed as well as wave direction, whereby slight increases of cAMP

increases population swim speed, however at high cAMP levels, the reverse wave is propagated.

Proposed axonemal domain for CARP1

Facinatingly, it has previously been described that removal of the distal outer dynein arm-docking complex (dDC) results in an increased proportion of ciliary waveforms in *Leishmania* (227), reminiscent of the *ΔCARP1* and *ΔPDE B1* phenotypes we describe. We already established in Chapter 2, Figure 2-14B, that CARP1 is not localised within the distal ODA DC itself, however, taken together all these findings, it could be that CARP1 is situated close to the ODA, perhaps within the MIP which have been shown (for FAP85, FAP129 and FAP182 (235)) to interact with the ODA-DC through the microtubule protofilaments. In fact, recent cryo-EM of mammalian cilia demonstrate the ODA periodicity and docking is dependent on two paralogues of *Chlamydomonas* FAP182 (Pierce1 and Pierce2), which link the 48nm MIP periodicity to the ODA 24nm periodicity by binding to CFAP53 and 'piercing' through the microtubule protofilaments (63). As the original screen which identified CARP1 as a downstream effector of PDE inhibition (186) also identified the calcium sensing CARP4 which is part of a family of MIPs (including Rib72) within the microtubule lumen, it is a promising axonemal region to pursue in context of second messenger modulation of dynein activity and and so it is a plausible domain for cAMP to act through CARP1. It could be that PDE B1 is also found within this microdomain to maintain the proximal-distal gradient of cAMP around CARP1 transducer protein, likely acting to maintaining the signalling boundary and resetting the signal.

Our localisation and motility data also point to RAC-a localising to the distal flagellar tip and being required for reaching normal population swim speeds. This, combined with CARP1

localising along the entire axoneme and PDE B1 demonstrating a distal flagellar enrichment suggests that CARP1 acts in three different flagellar fractions to transduce a cAMP signal, the proximal half, the distal half and the flagellar tip (Figure 2-29A). Assuming that the RAC-a is actively producing cAMP at the tip domain (Figure 2-29B), these localisations suggests that; (a) at the flagellar tip downstream of RAC-a activity, CARP1 acts to increase chance of flagellar wave propagation (Figure 2-29B); (b) in the distal half with low levles of cAMP binding it promotes the tip-to-base wave propagation (Figure 2-29C, 29D); and (c) CARP1 bound to cAMP in the proximal flagellum forms part of the machinery to suppress the reverse wave from propagating (Figure 2-29E).

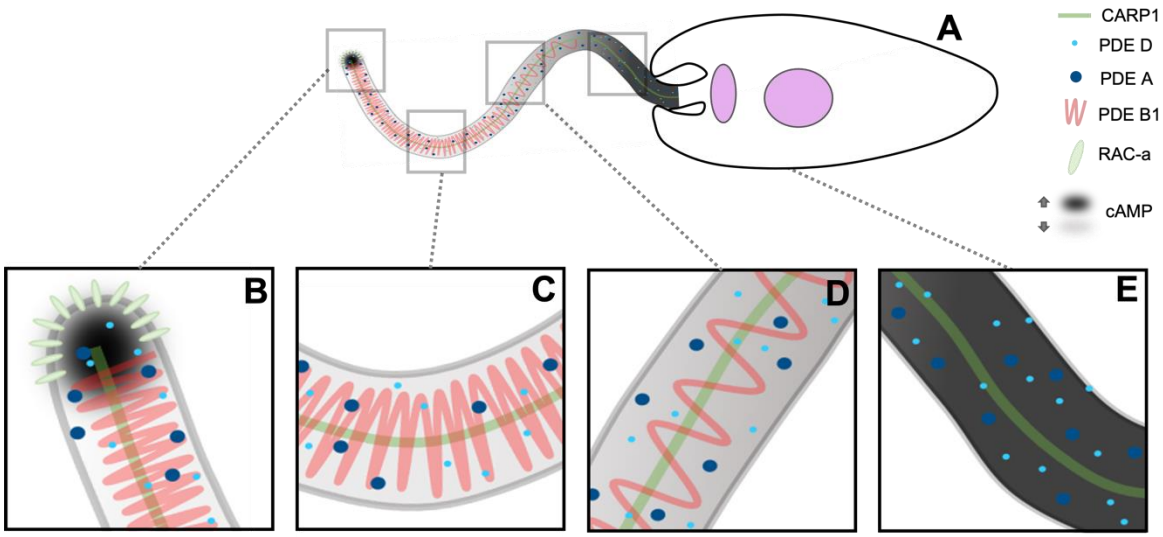


Figure 2-29: Model for cAMP modulation of flagellar movement.

Cartoon depicting proposed model for cAMP gradient mediating the balance between forward (symmetric beat) and (asymmetric beat) tumbling motility. (A) whole cell plus diagram key, (B) flagellar tip with cAMP production by RAC-a contacting CARP1 whose axonemal localisation is unknown, (C) PDE B1 localises around CARP1 to create an area of low cAMP binding in the distal flagellar portion (D) PDE B1 abundance tapers off and cAMP binding to CARP1 at low levels (E) CARP1 binding to cAMP at a maximum whilst PDE B1 is at very low abundance. PDE A and PDE D soluble throughout the flagellar cytoplasm.

Our experimental data demonstrates we are able rescue the RAC-a deficiency with a homozygous deletion of PDE A as well as 100 nmol CpdB which both likely increase the flagellar cAMP levels. If RAC-a was the only cAMP producer, we would expect the RAC-a null mutant to phenocopy the CARP1 null mutant. However our localisation data showed that RAC1-3 and the HemAC all are detectable in the flagellum and thus there are likely other producers of the cAMP signal. Ultimately, given more time, we would explore the consequence of deleting PDE B1 on top of *ΔRAC-a*, hypothesising that the slow motility would not be rescued as the proximal-distal/flagellar tip cAMP gradient levels will have been disrupted and would result in an increased reverse beat. This proposed model fits with the findings in *T. brucei* where PDE B1 are incapable of SoMo or successful translocation through the tsetse fly vector (57), suggesting this proximal/distal gradient of cAMP along the flagellum may be the communicator of chemotaxis behaviours such as pH taxis exhibited by early procyclic trypanosomes (162).

We propose the CARP1 and PDE B1 form a unique pathway influencing or forming part of the ciliary inhibition machinery along the axoneme and associates with (but is not located within) the outer dynein arm apparatus. Cryo-EM of CARP1 *in situ* or obtaining co-crystal structures for both cAMP bound and apo forms could shed light on the function and conformation of the protein. As the models proposed for flagellar beat machanics involve spatially restricted inhibition of dynein binding (3), it may prevale that CARP1 in bound and unbound states (possibly located within the microtubule lumen) result in changes in the proximity of the ODA to the adjacent microtubules, thus modulating the likelihood of a binding event occuring.

Ultimately, second messenger modulation of the flagellum is likely far more complex than the model proposed because of the mutlitude of calcium responsive protein speckled

throughout the axoneme. Not only this, but the intriguing hint of a novel nuceloside messenger activating divergent parasite PKAR in the flagellar axoneme, of which PDE B1, ODA distal docking complex and PNUT19 have been shown to be downstream phosphorylation targets during synthetic activation in *T. brucei* (142).

It is probable that they all work together to maintain the balance of symmetric/asymmetric wave propagation, and some protein transducers will serve as a cross road between them, such as the PNUT19 messenger which appears to have both a CNBD and a C2 domain.

Although, from our assessment, it appears that CARP1 is the only canonical downstream effector of cAMP within *L. mexicana* flagellar axoneme.

CHAPTER 3

An essential role for divergent

PKA in forward motility

3. An essential role for divergent PKA in forward motility

3.1. Introduction

It has been established recently that kinetoplastids like *T. brucei* and *T. cruzi* have diverged from the well-studied eukaryotic PKA signalling paradigm relevant from slime moulds to yeast to mammals, forming instead a heterodimer of PKAR-PKAC, which is non-responsive to cAMP (Figure 3-1A, 1B) (142). The targeted phosphorylation of proteins is a way by which flagellar beat mechanics can be altered, and additionally has been shown to be an intrinsic part of the mechanism by which second messenger signals are transduced *i.e.,* PKA and PKG. Both second messengers calcium and cAMP have been linked to changes in flagellar beating behaviours in mammalian bull sperm (207), hamster sperm (208,236), *Chlamydomonas* (237)(50), sea urchin sperm and *Leishmania* (59,104), as well as several more ciliated model organisms like *Paramecium* (238) and *Tetrahymena* (239). In the context of studying flagellar beating, many studies reported a correlation of phosphoprotein repertoires with kinase/phosphatase activation and inhibition, often the phosphoproteins were identified with gel immunoblotting techniques, without identification of the specific phosphorylation target (104,240–244). Several targets for serine/threonine protein kinases, such as casein kinase 1 (CK1), have been identified, including structural and enzymatic substrates within the flagellum (240). A study comparing phosphoproteomes of CK1 inhibited versus non-inhibited cells highlighted 18 differentially phosphorylated proteins within the central pair (PF6 and HYD3), intra-flagellar transport (IFT43), radial spokes (RSP11 and RSP17), ODA-docking complex (DC1 and DC2), glycogen synthase kinase 3 and many flagellar associated proteins (FAP) (245). Most studied, is the direct phosphorylation of the inner-dynein arm

component IC138, described to have six phosphosites at the N-terminus and hypothesised to be phosphorylated by both CK1 and PKA in *Chlamydomonas* (240).

Mammalian PKA, is known to be essential in sperm capacitation events during fertility (53,207). Here, soluble adenylate cyclase (sAC) responds to high external HCO_3^-, causing a spike in cAMP synthesis (246,247). This consequential increase in PKA activity correlates tightly with increased protein tyrosine phosphorylation linked with the hyperactivation behaviour characteristic of sperm capacitation events (207). Several phosphosites within A-kinase anchoring proteins (AKAPs) (241,242), fibrous sheath (243) and outer dense fibres proteins (Odf2) (248,249) and also the central pair protein SPAG16L (homolog of *Chlamydomonas* PF20) (244) have been shown to correlate with capacitation. PKA is part of the AGC kinase subgroup, owing to its similarities to cGMP-dependent protein kinase (PKG) and protein kinase C (PKC) (16). In its inactive state unbound to cAMP, the autoinhibitory domain (AI) of the PKAR subunit occupies and inhibit the catalytic core of the PKA-catalytic (PKAC) subunit (251). AI domain sequences differ, in that Type I PKAR have an inhibitory pseudo-substrate motif, and Type II PKAR have an auto-phosphorylatable sequence typically involving a serine residue (252,253). In higher eukaryotes, the PKA heterotetrameric holoenzyme is compartmentalized to sub-cellular micro-domains by AKAPs, which act also to dock other signalling molecules, creating in essence local micro-signalosomes (254) (Figure 3-1). The anchoring mechanism of mammalian AKAPs to PKAR subunits (Figure 3-1A) through an amphipathic helix and the dimerization docking (D/D) domain has been well studied (255,256).

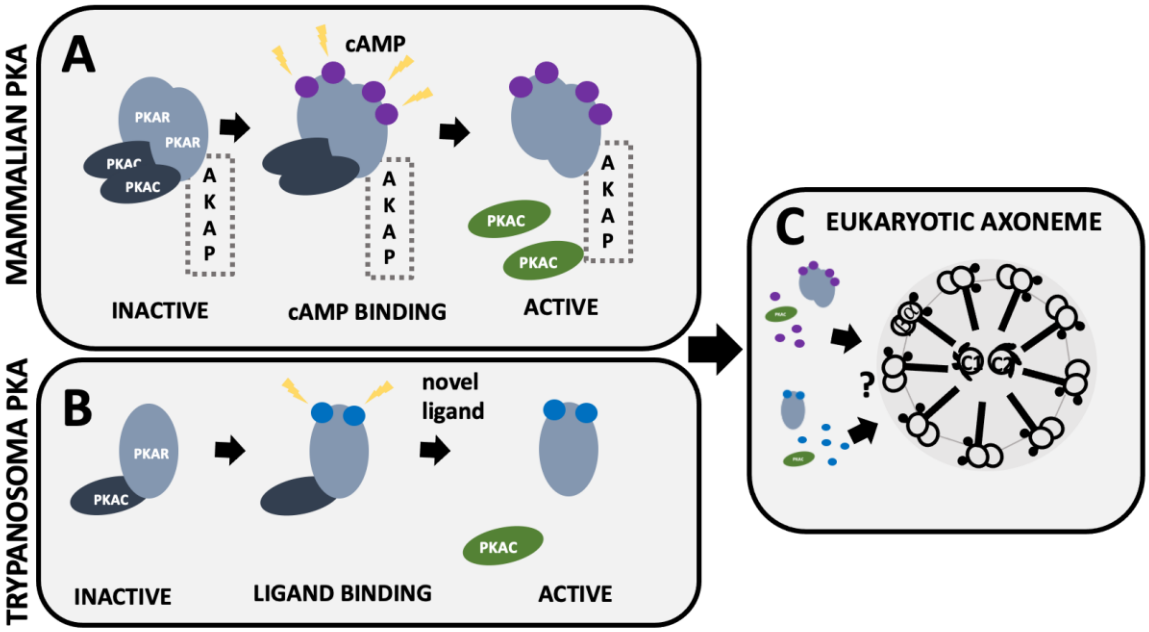


Figure 3-1: Classical and divergent PKA signalling.

Graphical representation of the differences between (A) canonical eukaryotic PKA signalling paradigm and (B) early diverging kinetoplastid parasite PKA described by(142). cAMP molecule represented by a purple circle, the novel endogenous ligand represented by a blue circle. PKA - protein kinase A. PKAR –regulatory subunit. PKAC – catalytic subunit. AKAP – A-kinase anchoring protein. (C) cartoon of a canonical 9 + 2 eukaryotic motile flagellar axoneme highlighting the open question of how second messengers and novel endogenous ligands may be transduced within the structure to modulate flagellar motility.

Several classical AKAPs have been identified in *Chlamydomonas*, namely AKAP240 and AKAP97 (RSP3) (257). In other unicellular organisms like *Plasmodium,* studies indicate that instead of direct binding to AKAP (PfAKAL), an adaptor protein called Pf14-3-3 mediates PKAR anchoring (258).

Chapter 1, Section 1.2.2 discusses the identification and characterisation of a divergent PKAR subunit in *T. brucei* and *T. cruzi*. Although kinetoplastid homologues for AKAPs are recognisable by protein BLAST from *Chlamydomonas* AKAP97 (RSP3) (257), no evidence has

yet demonstrated direct *in vivo* or *in vitro* interaction between AKAP and PKAR, and so it remains an open question how and where the parasite PKA subunits are docked.

There have already been studies on the two PKAR and three PKAC subunits of *Leishmania* and *Trypanosoma* species (77,142,199,204,259–261). Previous studies in the Gluenz lab showed that *L. mexicana* PKAR1, for example, seems to be required to reach normal parasite swim speeds *in vitro*, but isn't essential for sand-fly colonization and infection (77). *T. brucei* PKAR1 (a.k.a. FM458) was identified as part of the flagellar matrix proteome of mammalian infectious form parasites (262). FM458 knockdown mutants presented a reduced cell displacement ability, however unusually, knockdown was not lethal in bloodstream forms (BSF), contrasting what is typically seen when flagellar structure is compromised in BSF trypanosomes (41,262). A second, less studied PKAR subunit has been highlighted; firstly in an *in silico* search for predicted cyclic nucleotide binding domains containing proteins encoded in the *T. cruzi* genome (190), and secondly, in a screen to establish the phophoproteome profiles during promastigote to amastigote differentiation. Called PKAR' in *L. donovani*, it was shown to contain four phosphorylation sites which are dephosphorylated during promastigote to amastigote differentiation stages (263). Most recently, this subunit was shown to pair with PKAR3, leading to its renaming as 'PKAR3'. PKAR3 and PKAC3 deletion correlated with cell rounding, linking their functions to promastigote cell body morphology (204). The *L. major* PKAC subunits appear to be temperature sensitive, where rapid dephosphorylation of target motifs (RRXS/T) is observed after only 10 minutes at 35 °C, suggesting PKA signalling is promastigote specific (operating at a temperature of 27°C) and post-translationally regulated (199,259). Interestingly, the known mammalian PKA phosphorylation substrate vasodilator-stimulated protein (VASP), when exogenously expressed in *T. brucei*, was phosphorylated on serine-157 by endogenous

parasite PKA (142). Suggesting that although *Trypanosoma* PKA homologues have diverged away from cAMP sensitivity, the downstream biological activity may still share significant homology across eukaryotic species especially where highly conserved specialised organelles exist, like the flagellum.

Given the established links between PKA signalling and flagellar motility in several distinct species, and the divergent nature of PKA signalling in kinetoplastids, I wanted to understand in detail how *Leishmania* PKA mechanistically influences flagellar beating (Figure 3-1C). From this, we could potentially learn how divergent parasite signalling pathways influence the highly conserved eukaryotic machinery, the flagellar axoneme. This information may also be relevant for understanding better how canonical PKA modulates flagellar beating in other eukaryotes.

Firstly, we confirmed that the genome of *Leishmania* spp encode two regulatory and three catalytic subunits for PKA. Secondly, endogenous fluorescent tagging and targeted gene deletion showed that these subunits have specific and distinct localisations, within the axoneme, the nucleolus and the cell body cortex, respectively, and we used tagging and deletion phenotypes to define the heterodimer pairing preferences between PKAR and PKAC subunits. Lastly, by examining the effect of gene deletion on the resultant flagellar waveforms, we provide evidence that all catalytic subunits contribute differently to flagellar beat dynamics: PKAC1 is essential for the formation of a rhythmic symmetric beat for forward motility, and PKAC2 and PKAC3 mutants show aberrant beat frequencies.

3.2. Results

3.2.1. The genome of *Leishmania* spp encode two divergent regulatory and three catalytic PKA subunits

BLAST searches with the three PKAC and the single PKAR sequences from *Trypanosoma brucei* (142) identified syntenic *Leishmania mexicana* orthologues for all four genes. Table 3-1 summarises the gene accession numbers and annotations as found in TriTrypDB, where each row represents genes found in a syntenic locus across kinetoplastid species, as illustrated in Figure 3-2. Note that Tb-/TcPKAC1 are in a syntenic locus with *Leishmania* PKAC2, and Tb-/TcPKAC2 are in a syntenic locus with *Leishmania* PKAC1 homologues. Additional searches for *L. mexicana* proteins with a cyclic-nucleotide binding domain (CNBD) (PFAM ID: PF00027) revealed one additional protein with similar protein architecture to PKARs, including an autoinhibitory (AI) domain followed by two CNBDs. This additional PKAR (LmxM.33.2820) is a homologue of the recently named PKAR3 subunit, published in a pre-print (204) and we will be consistent with this nomenclature (204). Syntenic orthologues of LmxPKAR3 were found in *L. major*, *L. donovani,* and *T. cruzi* but not in *T. brucei* genomes (Table 3-1) (Figure 3-2D).

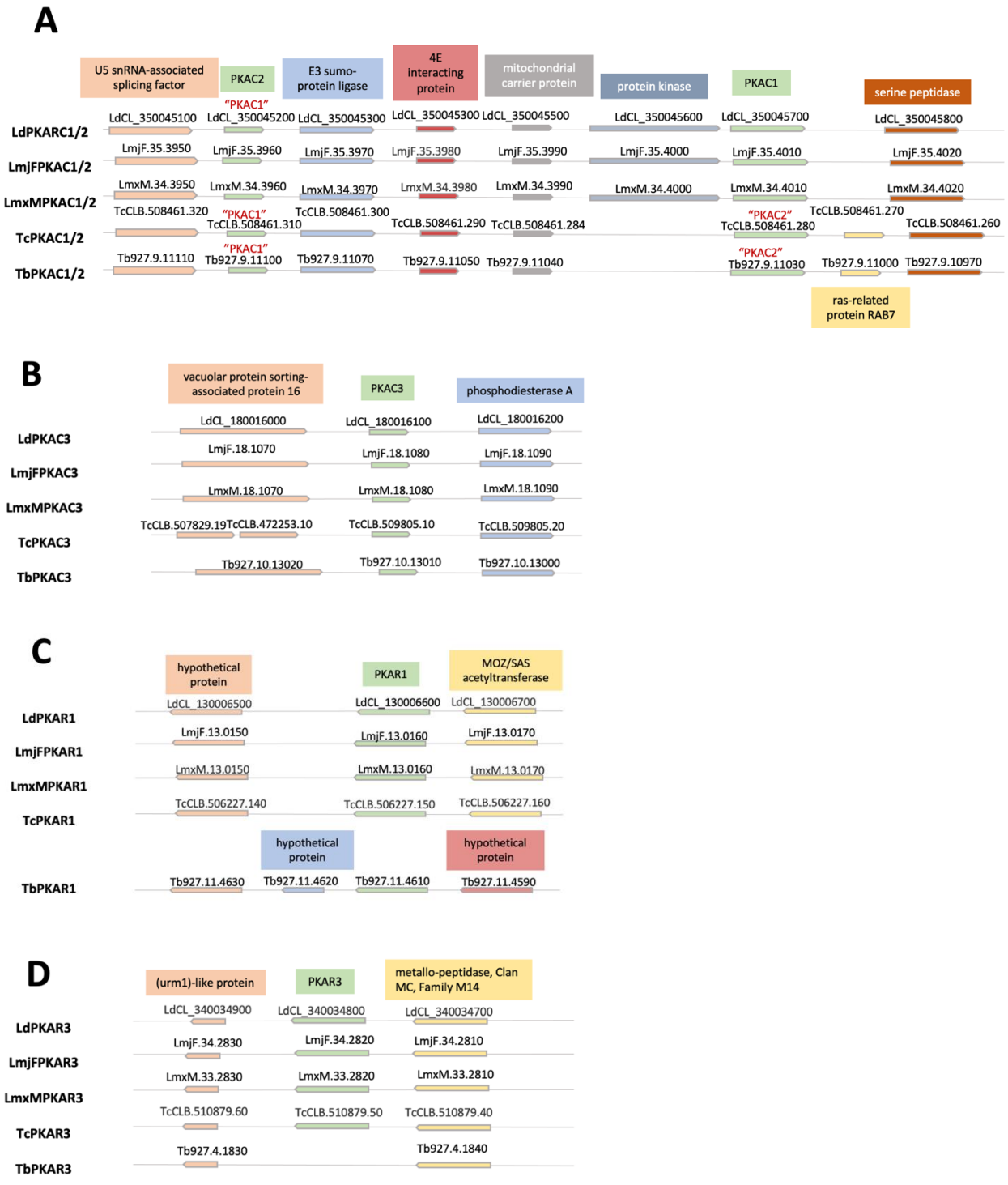


Figure 3-2: PKAC and PKAR synteny.

Cartoon representation of genomic regions for PKAC1, PKAC2, PKAC3, PKAR1 and PKAR3 in representative kinetoplastida species L. donovani, L. major, L. mexicana, T. cruzi and T. brucei. Genes encoding the PKA subunits of interest shaded in green. Gene annotations

taken from TriTrypDB release 56. (A) PKAC1 and PKAC2, (B) PKAC3, (C) PKAR1 and (D) PKAR3.

Table 3-1: Kinetoplastid PKAR and PKAC genes.

Accession numbers for all PKAR and PKAC orthologues found encoded in the genomes of L. mexicana, L. major, L. donovani, T. brucei and T. cruzi. Each row represents genes found in a syntenic locus across kinetoplastid species, as illustrated in Figure 3-2. Gene synteny determined using the TriTrypDB gene browser.

	Leishmania spp.				*Trypanosoma spp*	
	L. mexicana (Lmx)	*L. major (Lmj)*	*L. donovani (Ld)*		*T. brucei (Tb)*	*T. cruzi (Tc)*
PKAR1	LmxM.13.0160	LmjF.13.0160	LdCL_130006600	**PKAR1**	Tb927.11.4610	TcCLB.506227.150
PKAR3	LmxM.33.2820	LmjF.34.2820	LdCL_340034800	**PKAR3**	n/a	TcCLB.510879.50
PKAC1	LmxM.34.4010	LmjF.35.4010	LdCL_350045700	**PKAC2**	Tb927.9.11100	TcCLB.508461.310
PKAC2	LmxM.34.3960	LmjF.35.3960	LdCL_350045200	**PKAC1**	Tb927.9.11030	TcCLB.508461.280
PKAC3	LmxM.18.1080	LmjF.18.1080	LdCL_180016100	**PKAC3**	Tb927.10.13010	TcCLB.509805.10

To determine whether LmxPKAR1 and LmxPKAR3 follow the same residue substitutions documented to be responsible for a ligand switch in *T. brucei* (142), amino acid sequence alignments were analysed using *Homo sapiens* PKARI-a and PKARII-a (accession: P10644 and P13861 respectively) as references for canonical PKAR with further cross reference to the panel of cAMP binding domains in Chapter 2.2.1, Figure 2-3, which highlight the invariable residues within classical CNBD.

N-terminal domain. Typically, the N-terminus of eukaryotic PKARs contains a conserved dimerization/docking domain (DD), necessary to hold the heterotetramer together and

anchor it typically to the amphipathic helix region of an AKAP (256). *Trypanosoma* PKAR1s have been shown to lack the DD domain and instead contain a leucine rich repeat (LRR) (IPR032675), which is also conserved in *Leishmania* spp (Figure 3-3A). PKAR3 sequences, lack a DD domain or an LRR. Instead, there is a short coil domain predicted near the N-terminus of all examined *Leishmania* sequences, but not TcPKAR (Figure 3-4A).

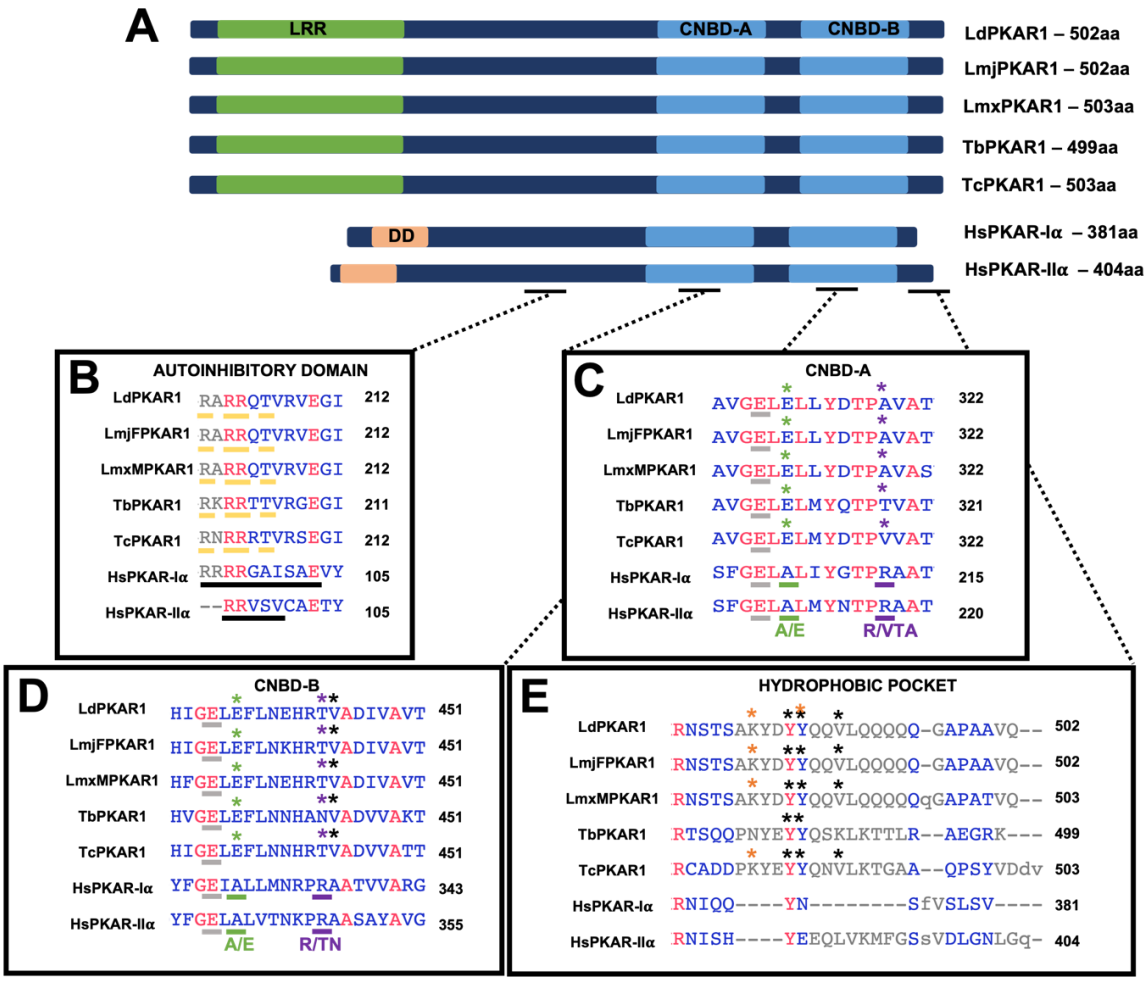


Figure 3-3: Sequence analysis of PKAR1.

Cartoon representation of trypanosomatid PKAR proteins LdPKAR1 (LdBPK.13.2.000160), LmjPKAR1 (LmjF.13.0160), LmxPKAR1 (LmxM.13.0160), TbPKAR1 (Tb927.11.4610), TcPKAR1 (TcCLB.506227.150), and Homo sapiens cAMP-dependent protein kinase type I-alpha regulatory subunit PKAR-Iα (P10644, KAP0_HUMAN) and type II-alpha regulatory subunit PKAR-IIα (P13861|KAP2_HUMAN). LRR, leucine rich repeat; DD, dimerization docking domain; CNBD, cyclic nucleotide binding domains (PFAM ID: PF00027); AI, autoinhibitory

domain sequence (Poteet-Smith et al., 1997). (B) AI sequence alignment. Underlined residues highlight the RRxT motif in trypanosomatid PKAR1 sequences of which the threonine has the potential to be autophosphorylated by docked catalytic subunits and the RRxA residues reported to form a pseudo-substrate for PKAC catalytic sites in mammalian PKA heterotetramers. The universally conserved arginine residues are highlighted in red. (C-D) CNBD: CNBD: The canonical phosphate binding cassette (PBC) motif FGELAL[ILVM]xxxPRAA (Peng et al., 2015) demonstrated by the two H. sapiens PKAR reference sequences. Residues in red are shared across all sequences aligned, where residues underlined in grey highlight a universally conserved glutamate, residues underlined in green highlight an alanine to glutamate switch, and residues underlined in purple demonstrate the arginine switch to V, T, A or N. (E) Hydrophobic pocket: black asterisk indicates the residues reported to form part of the Trypanosoma specific hydrophobic pocket. Indicated by orange asterisks are K and Y residues reported to increase affinity to binding synthetic nucleoside analogue 7-cyano-7-deazainosine (a.k.a. Jaspamycin). Residue switched in all these positions have been shown to correlate with divergence away from cAMP sensitivity (142).

Autoinhibitory domain. A so-called autoinhibitory domain (AI) mimics the phosphorylation targets of PKAC and functions to inhibit the catalytic kinase subunits. This short sequence, typically RRXA(G) in Type I PKARs (PKAR-I) and RRXS(T) in Type II PKARs (PKAR-II), is positioned towards the N-terminus, where in the former, the alanine (A) or glycine (G) replaces the phosphorylatable serine (S) or threonine (T) residues found in true downstream substrate sites (253)(252) (Figures 3-3B, 4B). Putative AI sequences were detected in most trypanosomatid PKARs: PKAR1 alignments show an RRXT sequence, similar to the auto-phosphorylatable AI domains found in mammalian PKAR-II. The AI sequences of *Leishmania* PKAR3 share the core 5 residues (RGAIS) of the canonical mammalian RRRRGAISAE sequence of PKAR-I α AI, but notably are missing one of the two initial arginine residues to conform to the RRXA category of AI (Figure 3-3B). The TcPKAR3 AI sequence similarly

deviates with an XRXG sequence, where neither conform to any AI sequences described across eukaryotes (Figure 3-4B) (264).

Cyclic-nucleotide binding domain. Chapter 2.2.1 details the conserved residues of canonical CNBD required for hydrogen bonding to cyclic nucleotides (125), as well as patterns of divergence described in divergent *Trypanosoma* PKAR CNBDs.

Both CNBD-A and CNBD-B in *Leishmania* PKAR1 sequences show the residue switches at the mammalian alanine (A/E) in position four of the PBC, and arginine (R/(VTAN)) at position eleven (green and purple asterisks respectively in Figure 3-3C, 3D). This negatively charged glutamate (E) residue is predicted to clash with the phosphate group and repel the cAMP molecule out of the binding pocket. Moreover, there is no positively charged arginine (R) residue to dock the exocyclic phosphate either, strongly suggesting that LmxPKAR1, similarly to *T. cruzi* and *T. brucei* (142), no longer responds to cAMP signals. Notably, the arginine has been switched to polar uncharged (R/TN) or aliphatic (R/AV) residue.

The residue switches evident in the parasite LmxPKAR3 CNBDs are less definitive (Figure 3-4C, 4D). The first alanine (A) in CNBD-A has been switched to a glycine (G), which depending on pH of the environment, can exist as net positive, neutral or negative from low to high pH respectively. Thus, it is unknown if this residue would clash with cAMP docking in the same manner as a glutamate defined by (142). The alanine on CNBD-B of LmxPKAR3 displays an A/E, identical to PKAR1 sequence divergence at this position. The PBC sequence in LmxPKAR3 CNBD-A and CNBD-B demonstrate an arginine residue switch towards residues with polar uncharged (R/STN) or hydrophobic side chains (R/A) (purple asterisk, Figure 3-4C, 4D). Most surprisingly is that the conserved glutamate within the PBC of some PKAR3 sequences (underlined in grey in Figures 3-3C, 3D and 3-4C, 4D), which interact with the hydroxyl group on cAMP, has been switched to an aspartic acid (D) in CNBD-A and aspartic

acid or glutamine (D/Q) in CNBD-B (grey asterisks, Figure 3-4C, 4D). This points towards LmxPKAR3 having also diverged away from cAMP binding, but the residue substitutions are different from those seen in Tb-/TcPKAR1.

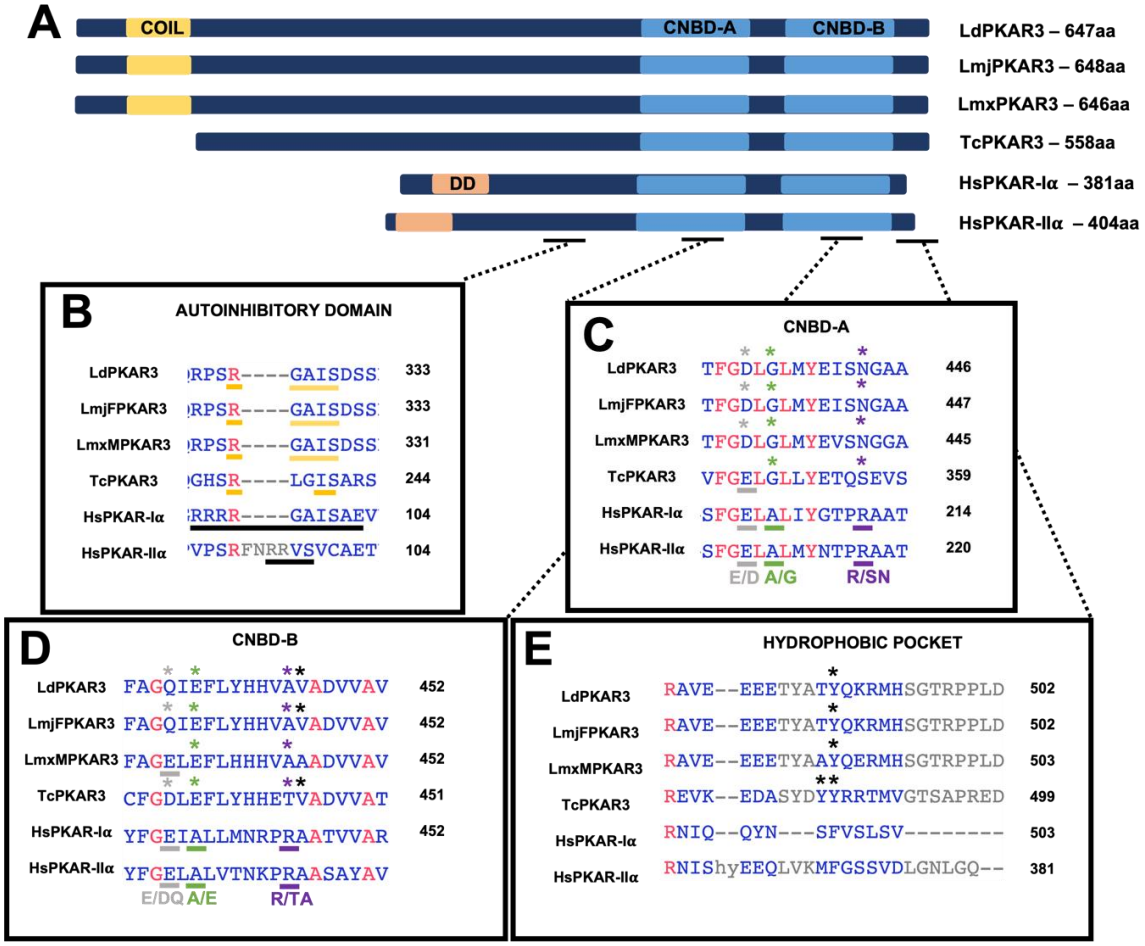


Figure 3-4: Sequence analysis of PKAR3.

Cartoon representation of trypanosomatid PKAR proteins LdPKAR3 (LdBPK.34.2.002680), LmjPKAR3 (LmjF.34.2820), LmxPKAR3 (LmxM.33.2820), TcPKAR3 (TcCLB.510879.50), and Homo sapiens cAMP-dependent protein kinase type I-alpha regulatory subunit PKAR-Iα (P10644, KAP0_HUMAN) and type II-alpha regulatory subunit PKAR-IIα (P13861|KAP2_HUMAN). LRR, leucine rich repeat; DD, dimerization docking domain; CNBD, cyclic nucleotide binding domains (PFAM ID: PF00027); AI, autoinhibitory domain sequence (Poteet-Smith et al., 1997). (B) AI sequence alignment. Underlined letters highlight shared residues between the RGAIS motif of H. sapiens PKAR-Iα and residues in Leishmania PKAR3

proteins. (C-D) CNBD: The canonical phosphate binding cassette (PBC) motif FGELAL[ILVM]xxxPRAA (Peng et al., 2015) demonstrated by the two H. sapiens PKAR reference sequences. Residues in red are shared across all sequences aligned, where residues underlined in grey highlight a glutamate switch to D or Q, and residues underlined in green highlight an alanine switch to G or E for CNBD-A and -B respectively. Purple asterisks demonstrate the arginine switch to S, N, T or A. (E) Hydrophobic pocket: black asterisk indicates residues reported to form part of the Trypanosoma specific hydrophobic pocket (142).

Hydrophobic pocket. All parasite sequences for PKAR1 and PKAR3 show an extended C-terminus end relative to the mammalian sequence (Figures 3-3E, 3-4E). Two tyrosine (Y) and two valine (V) residues were implicated in forming a parasite specific hydrophobic pocket documented in TcPKAR1 (denoted by black asterisks in Figures 3-3D, 3E and 3-4D, 4E) (142). Parasite PKAR1 sequences, for all but TbPKAR1, contain all four of these YV residues. Contrastingly in PKAR3 sequences, *Leishmania* only have one Y and one V, where TcPKAR3 has three of the four hydrophobic residues, indicating the LmxPKAR3 orthologues, again, do not follow exactly the same patterns of sequence divergence as Tb-/TcPKAR1.

Taken together these data indicate that a divergent PKAR1 is conserved in all trypanosomatids, and an additional PKAR3 is found in *Leishmania* spp. and *T. cruzi*, with an unknown ligand specificity.

Catalytic subunits. All kinetoplastid genomes encode three highly conserved PKAC subunits, PKAC1-3. PKAC3 was identified first in 1996 and named c-lpk2 in *L. major* (260), where it was noted to have an unusual 8 amino acid C-terminal extension, common to all trypanosomatid PKAC3 homologues (Figure 3-5F). All trypanosomatid PKAC sequences, except LmxPKAC2, have an essential C-terminal FXXF sequence, where mutating either phenylalanine consistently diminishes catalytic activity (265)(266).

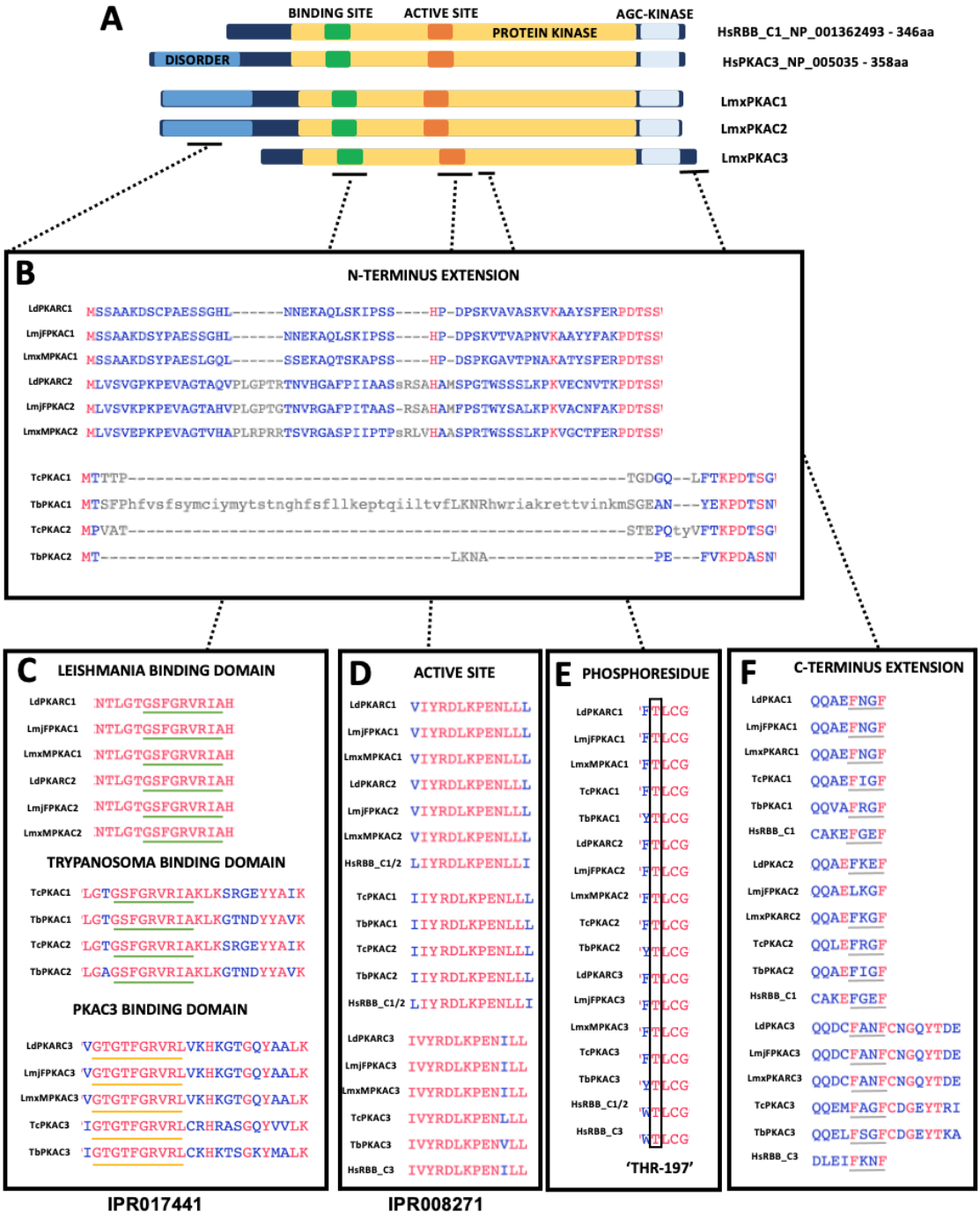


Figure 3-5: Sequence analysis of PKAC.

Cartoon representation of the classical protein architecture of L. mexicana PKAC subunits compared to the Homo sapiens reciprocal best blasts (RBB) of LmxPKAC1 and LmxPKAC3 (accessions NP_001362493 and NP_005035 respectively). Protein domains are colour coded and information was sourced by using InterProScan. Binding site: IPR017441, active site: IPR008271, protein kinase domain: IPR000719, AGC-kinase: IPR000961. Protein sequence

alignments of the (B) N-terminus extension, (C) binding domain, and (D) catalytic core across representative kinetospastid species. (E) Universally conserved threonine positioned within the activation loop, described to be a phospho-target for the modulation of kinase activity (Steichen et al., 2012). (F) C-terminus extension of PKAC3 homologues in comparison to LmxPKAC1 and -C2 sequences. Underlined sequences in green indicated conservation across PKAC1 and -C2 in all representative species. Underlined residues in yellow indicates conservation across all PKAC3 sequences. Underlined residues in light blue indicates the FXXF feature in the AGC-kinase family (Etchebehere et al., 1997).

The highly similar LmxPKAC1 and -C2 are located on chromosome 34 but are not in an array (Figure 3-2A). Sequence alignments of LmxPKAC1 and LmxPKAC3 against the reciprocal best blast hit found in *H. sapiens* (NP_001362493 and NP_005035, respectively) were used where appropriate, to determine whether conserved residues of the kinases were apparent. Both the active sites and peptide binding sites within all *Leishmania* PKAC1 and -C2 are identical (Figure 3-5C, 5D). LmxPKAC1 and -C2, but not -C3, have variable N-terminal extensions which harbour a predicted disorder domain (Figure 3-5A, 5B). The catalytic activity of eukaryotic PKAC have been shown to be modulated by phosphorylation of several residues, of which Threonine-197 in the activation loop is particularly involved in biological activity (267)(268). The phosphorylated Thr-197 is shown to form a hydrogen bonding network which brings together several regions of the PKAC structure to stabilise an active tertiary structure (268). This residue is indeed conserved across trypanosomatid PKAC (Figure 3-5E), suggesting phosphorylation as a mechanism for modulation of kinases activity may be used by these parasites too.

3.2.2. *L. mexicana* PKACs and PKARs show distinct localisation patterns in the flagellar axoneme, nucleus and cell body cortex

To establish the subcellular localisation of the different PKAC and PKAR subunits in *L. mexicana*, we inserted fluorescent protein fusion tags (mNeonGreen, mNG) at the endogenous gene loci to image protein localisations in different cell- and lifecycle stages. Cell cycle was assessed by using the number of flagella (F), kinetoplasts (K) and nuclei (N) as markers (222). Protein localisation was observed three days post induction of axenic amastigote differentiation conditions (Schneider's Medium, pH 5.5 and 34 °C).

PKAC1. mNG::LmxPKAC1 localised to the flagellar axoneme in 1K1N1F cells, where a signal was still observable in NP-40 detergent-extracted cytoskeletons (Figure 3-6A). Through the cell division cycle, the signal abundance diminished in the axoneme and increased within the nucleus, corroborating recently reported data (261). Strikingly, within the nucleus, LmxPKAC1 signal intensity was consistently strongest in areas of low Hoechst staining (Figure 3-7A, A'), suggesting association with the nucleolus specifically. The LmxPKAC1 signal re-appeared in the axoneme again at cytokinesis. In axenic amastigotes, the mNG::LmxPKAC1 signal appeared greatly diminished, with weak variable cytoplasmic signal (Figure 3-6A). Fusion of mNG to LmxPKAC1 at the C-terminus disrupted the localisation to the axoneme (Figure 3-6F) as previously reported (77).

PKAC2. mNG::LmxPKAC2 signal was partitioned between the flagellum and the cell body cortex in non-dividing cells (Figure 3-6B) and throughout the promastigote cell division cycle (Figure 3-7B). Notably, in early promastigote division (2F1N1K), LmxPKAC2 often appeared increased in the new growing flagellum. The axonemal signal was no longer visible in detergent-extracted cytoskeletons, and a weak variable cytoplasmic signal was seen in

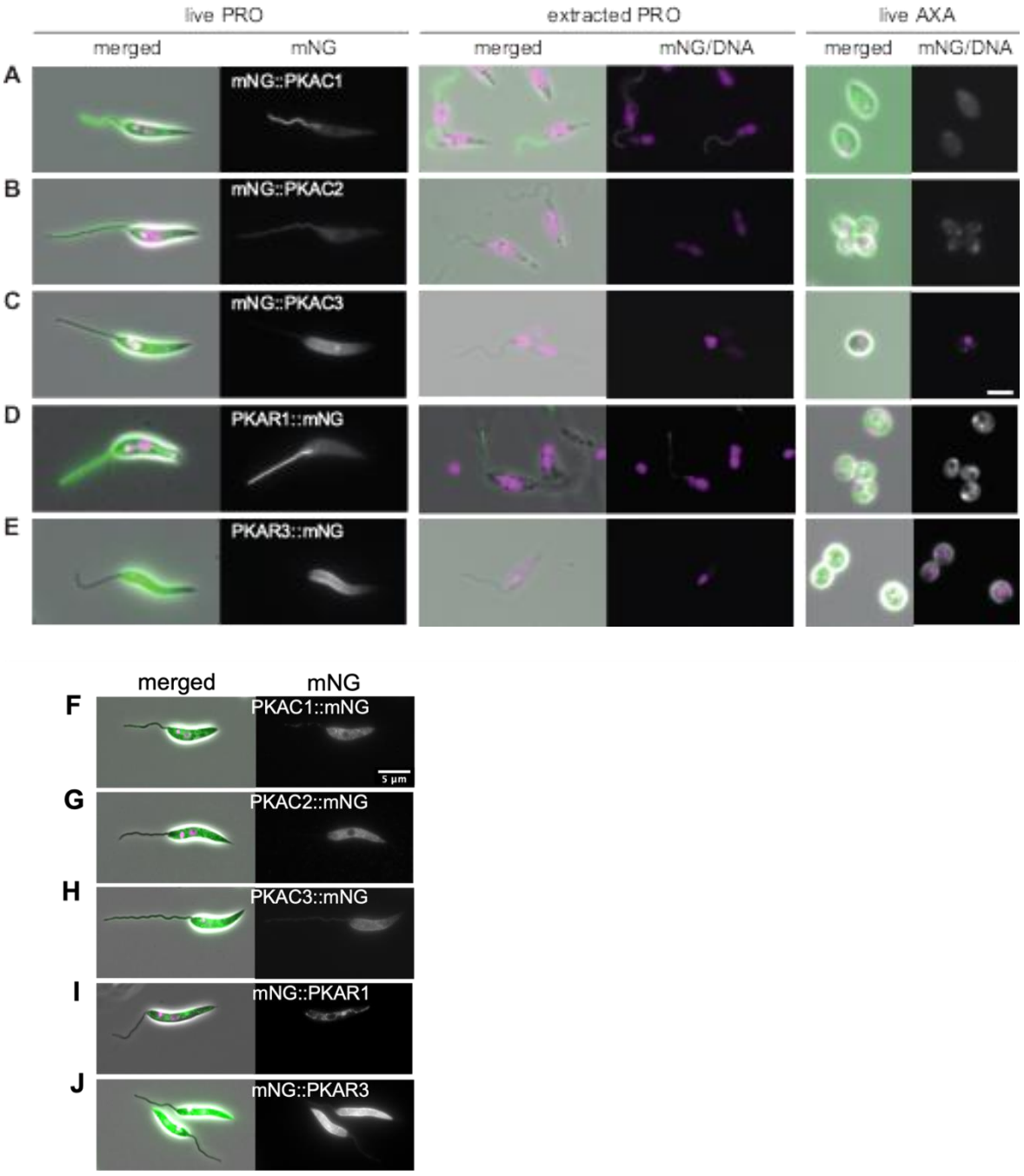


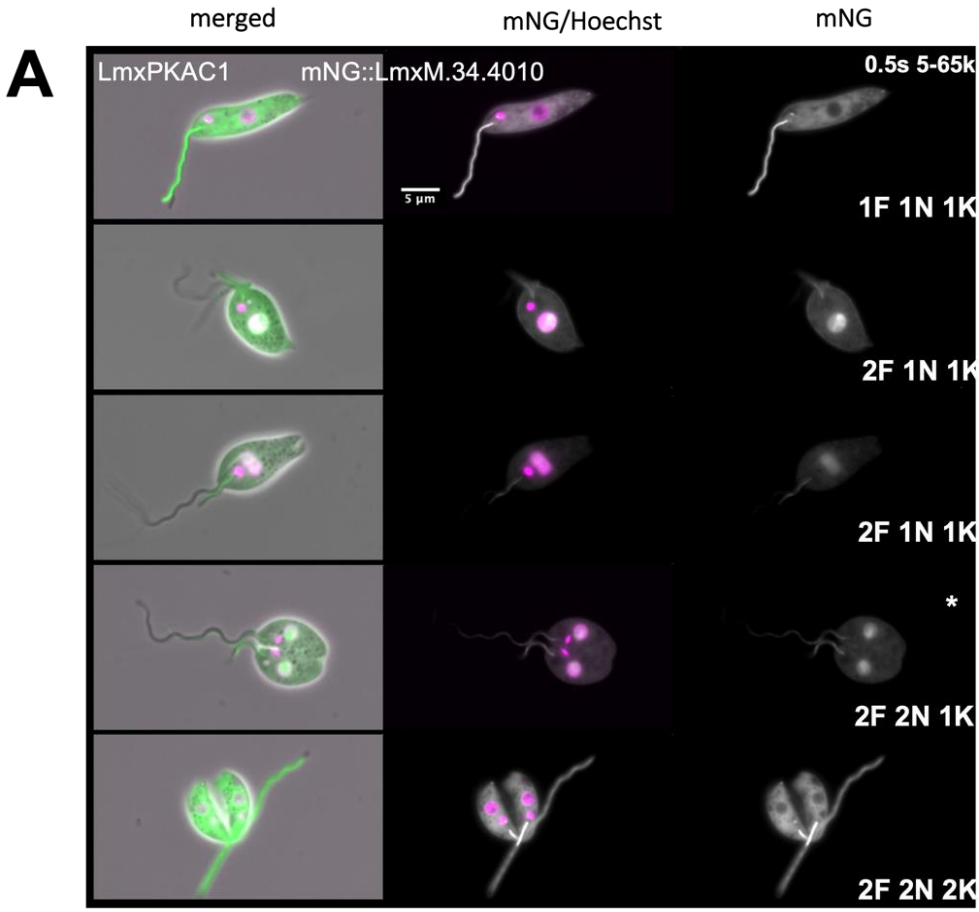
Figure 3-6: Localisations of tagged L. mexicana PKAC and PKAR subunits.

Micrographs of cells expressing endogenously mNG-tagged PKAC or PKAR subunits. (A) mNG::PKAC1 (LmxM.34.4010), (B) mNG::PKAC2 (LmxM.34.3960), (C) mNG:: PKAC3 (LmxM.18.1080), (D) LmxPKAR1::mNG (LmxM.13.0160), (E) PKAR3::mNG (LmxM.33.2820). Panels in A-E show live promastigotes (PRO, left), detergent (0.1% NP-40/PEME) extracted promastigote cytoskeletons (middle) and live axenic amastigotes (AXA, right). For each sample type a merged fluorescence with phase contrast image is shown, and the combined mNG and Hoechst fluorescence. (F-J) Tag localisation of the opposing terminus.

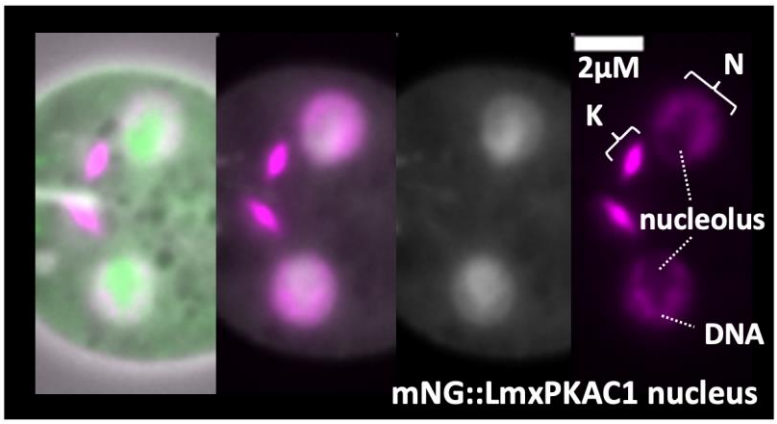
Demonstrating that the axonemal localisation is absent in PKAC1, -C2 tagged on the N-termini and PKAR1 tagged on the C-termini. Scale bar indicates 5 µm.

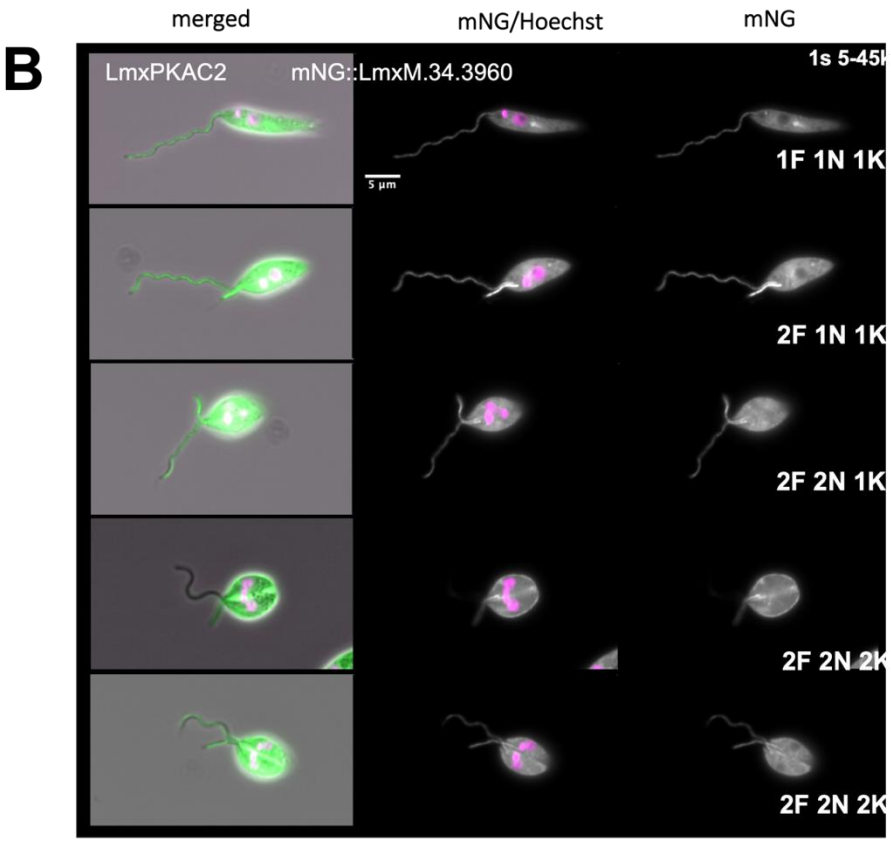
axenic amastigotes (Figure 3-6B). Fusion of mNG to the C-terminus hindered protein localisation to the axoneme (Figure 3-6G).

PKAC3. The pattern of mNG::LmxPKAC3 localisation appeared similar to that of LmxPKAR3 (Figures 3-6C, 6E). In non-dividing cells, there was a cortical cell body signal that was strongest in the mid-zone and tapered off towards the posterior pole (Figure 3-6C). In 95% of non-dividing cells, a distinctive edge effect was evident (quantified in Figure 3-8A, 8F).


merged
mNG/Hoechst
mNG
A
LmxPKAC1
mNG::LmxM.34.4010
0.5s 5-65k
5 µm
1F 1N 1K
2F 1N 1K
2F 1N 1K
*
2F 2N 1K
2F 2N 2K

A’


2µM
N
K
nucleolus
DNA
mNG::LmxPKAC1 nucleus



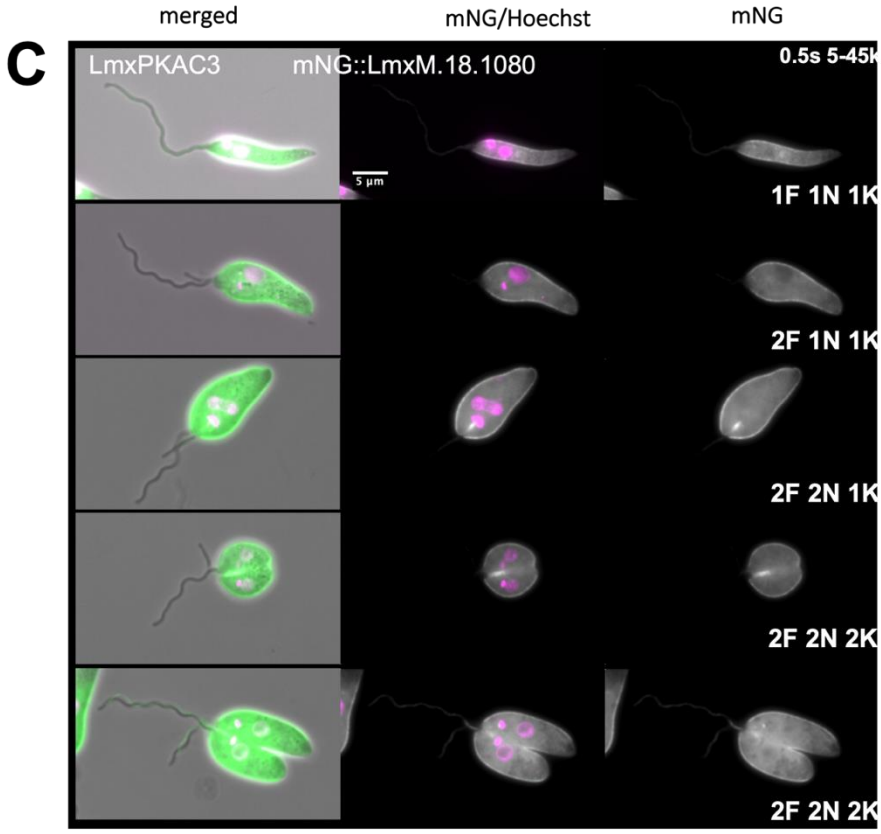


Figure legend on following page.

Figure 3-7: Cell cycle localisation of PKAC.

Promastigotes in different stages of the cell cycle, expressing (A) mNG::PKAC1, where (A') displays a magnified view of the PKAC1 in the nucleolus (scale bar of 2 µm), (B) mNG::PKAC2, and (C) mNG::PKAC3. F, flagella; N, nuclei; N, dividing nucleus, K, kinetoplasts; nol, nucleolus. Scale bar represents 5 µm. In the top right-hand corner of all panels, the fluorescence excitation time is indicated alongside the minimum and maximum greys values (e.g., 5 - 45k indicates 5000 - 45000) set on ImageJ for standardisation of the mNG fluorescent intensity.*

A faint soluble signal was also present in the flagellum, with an intensity gradient decreasing towards the distal flagellum (Figure 3-8F). In dividing promastigotes, LmxPKAC3 appeared more uniform across the cell body cortex, with reduced flagellum signal (Figure 3-7C). The promastigote cortex signal disappeared in membrane-extracted cells and showed a weak variable cytoplasmic signal in the cell body of axenic amastigotes (Figure 3-6C).

PKAR1. PKAR1::mNG localised to the flagellar axoneme in promastigote forms, with a fainter soluble cell body signal, throughout all stages of promastigote cell division (Figures 3-6D and 3-8A). Upon membrane extraction with 0.1% NP-40, the fluorescent signal remained in the axonemal cytoskeleton (Figure 3-6D). In amastigotes, a strong LmxPKAR1::mNG signal was observed in the cytoplasm of axenic amastigotes (Figure 3-6D). Fusion of mNG to the N-terminus of LmxPKAR1 resulted in a reticulated cell body signal, suggesting that blocking the LRR domain affects protein localisation (Figure 3-6I).

PKAR3. LmxPKAR3 was successfully tagged at both ends, and both mNG::LmxPKAR3 and LmxPKAR3::mNG localised exclusively to the cell body cortex in live promastigotes (Figures 3-6E, 6J). This signal was detergent extractable, suggesting LmxPKA3 is anchored weakly to the cortical cytoskeleton, or is associated with the plasma membrane (Figure 3-6E).

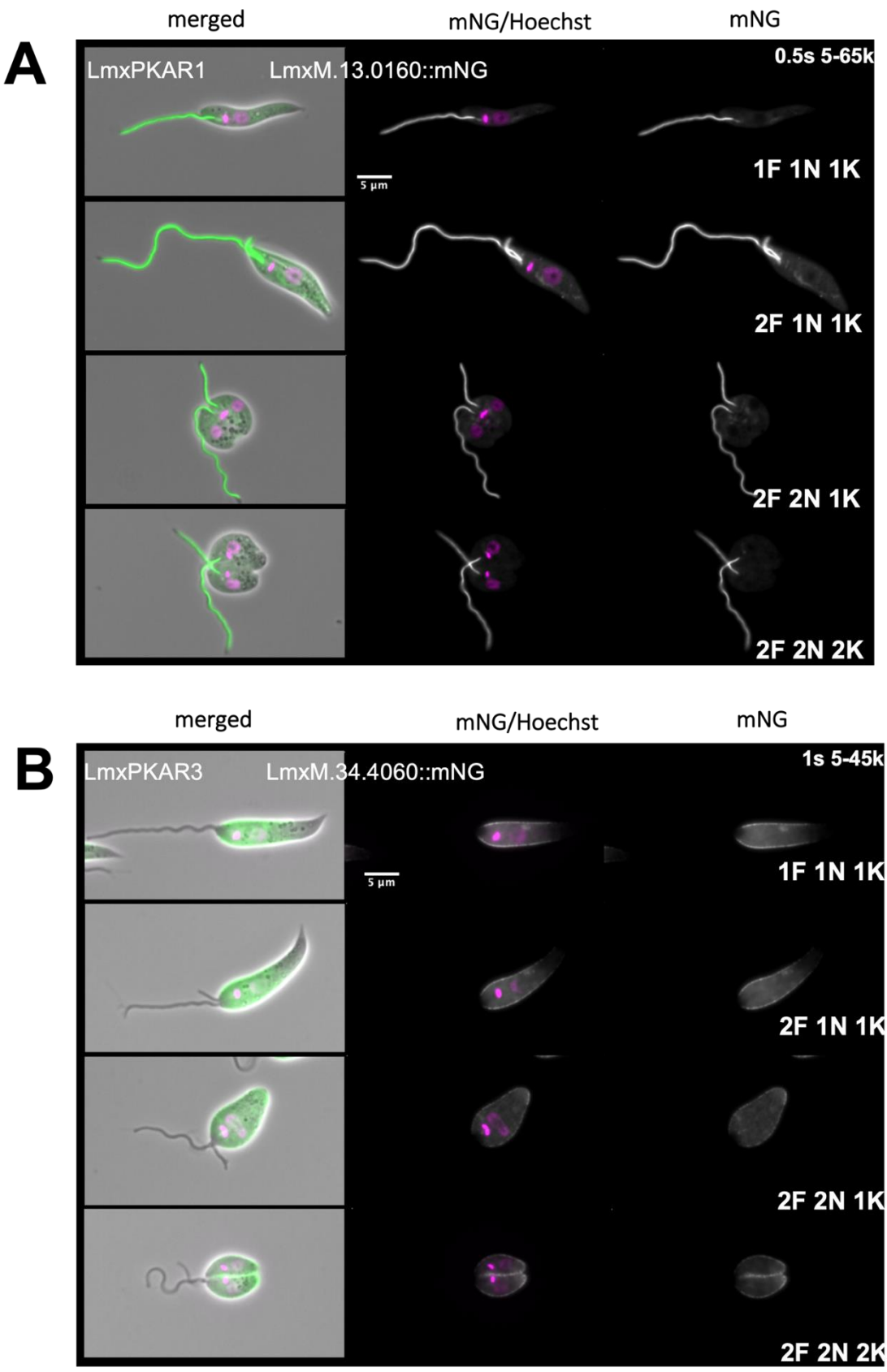


Figure legend on following page.

Figure 3-8: Cell cycle localisation of PKAR.

Promastigotes in different stages of the cell cycle, expressing (A)PKAR1::mNG (scale bar of 5 µm), (B) PKAR3::mNG. F, flagella; N, nuclei; N, dividing nucleus, K, kinetoplasts. Scale bar represents 5 µm. In the top right-hand corner of all panels, the fluorescence time is indicated excitation for mNG capture alongside the minimum and maximum greys values (e.g., 5 - 45k indicates 5000 - 45000) set on ImageJ for standardisation of the mNG fluorescent intensity.*

Closer examination of the different cell cycle stages showed that in non-dividing (1F1N1K), and early dividing (2F1N1K) promastigote cells (Figure 3-8B), the cortical LmxPKAR3 signal was most intense in the cell body mid-zone and tapered off towards the posterior pole (quantified in Figure 3-8A, 8F). In late division (2F2K1N/ 2F2K2N), the LmxPKAR3 signal intensity became more uniform along the cortex, occasionally even appearing enriched at the posterior pole (Figure 3-8B). In axenic amastigotes, the LmxPKAR3 signal persisted at the cell body cortex (Figure 3-6E).

3.2.3. Localisation dependencies

Given the striking similarities in the localisation of LmxPKAC3 and LmxPKAR3 at the cell cortex, and the strong axonemal localisation of LmxPKAC1 and LmxPKAR1, the question arose whether there were specific LmxPKAC/PKAR pairings in different cellular compartments. To test whether the localisation of any LmxPKAC subunit was dependent on

the expression of specific PKARs, we deleted the LmxPKAR1 or LmxPKAR3 genes in cells expressing tagged LmxPKAC1, -C2 or -C3.

Following deletion of LmxPKAR1, promastigotes no longer showed the strong axonemal LmxPKAC1 and LmxPKAC2 signal that was seen in the parental cell line (compare Figure 3-

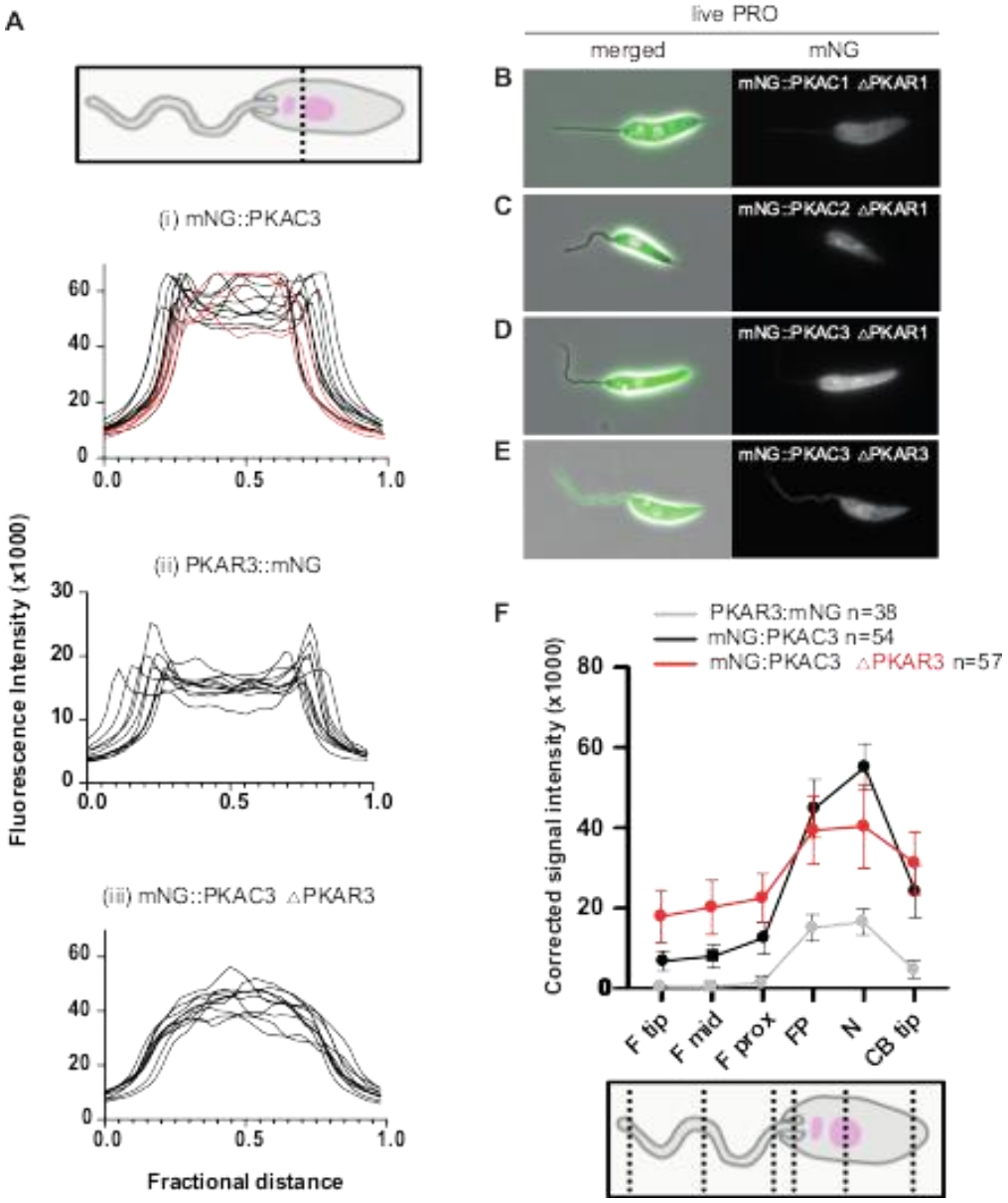


Figure 3-9: Localisation dependencies of L. mexicana PKAC and PKAR subunits.

(A) Measurement of the mNG signal intensity across a line though the cell body (cartoon) show a clear edge effect for the majority of mNG:: PKAC3 cells (i) (black lines, n=11; red lines show a minority of cells (n=3) with a diffuse cell body signal. An edge effect was detected for all measured PKAR3::mNG cells (ii) (n=12). The edge effect for mNG:: PKAC3 was lost

following PKAR3 deletion (iii) (n=10). (B-E) Micrographs showing the localisation of mNG-tagged PKAC subunits following deletion of PKAR subunits: (B) mNG::PKAC1 ⊿PKAR1; (C) mNG::PKAC2 ⊿PKAR1; (D) mNG::PKAC3 ⊿PKAR1; (E) mNG::PKAC3 ⊿PKAR3. (F) Quantitation of fluorescence signal intensity in cells expressing PKAR3::mNG, mNG::PKAC3 and in cells expressing mNG::PKAC3 following PKAR3 deletion. Measurements were taken at six points along the flagellum and cell body as shown in the cartoon. Measurements all performed in ImageJ.

6A, 6B with Figure 3-9B, 9C). By contrast, deletion of LmxPKAR1 had no visible effect on LmxPKAC3 localisation at the cell cortex (Figure 3-9D). We then tested whether loss of LmxPKAR3 would affect LmxPKAC3 localisation and found that the distinct cortical signal of LmxPKAC3 appeared diminished and the signal appeared to become more widely distributed throughout the cell body (Figure 3-9E). To quantify this change in signal distribution, two fluorescent quantification methods were used. Fluorescently tagged proteins that localise to the cortical cytoskeleton or plasma membrane typically display an edge effect in the intensity plot (79), thus analysis of the cross section spanning the cell between the kinetoplast and the nucleus (Figure 3-9A) was used to confirm a complete loss of the edge effect for LmxPKAC3 signal after LmxPKAR3 was deleted (Figure 3-9A). Secondly, as LmxPKAR3 and LmxPKAC3 both have very distinct signal profiles which vary along the length of the cell, a 6-point quantitation technique for fluorescent intensity was used to assess precise changes in signal distribution of LmxPKAC3 post deletion of LmxPKAR3. Typically, the signal profile of LmxPKAC3 is at its lowest at the distal flagellum, gradually increasing in intensity towards the pocket region (Figure 3-9F). There was a clear alteration in LmxPKAC3 signal after LmxPKAR3 deletion, most notably, an increasing intensity in the

flagellum and a less evident cell body gradient, appearing clearly to be soluble in the cytosol and no longer docked in the plasma membrane or cortex (Figure 3-9E).

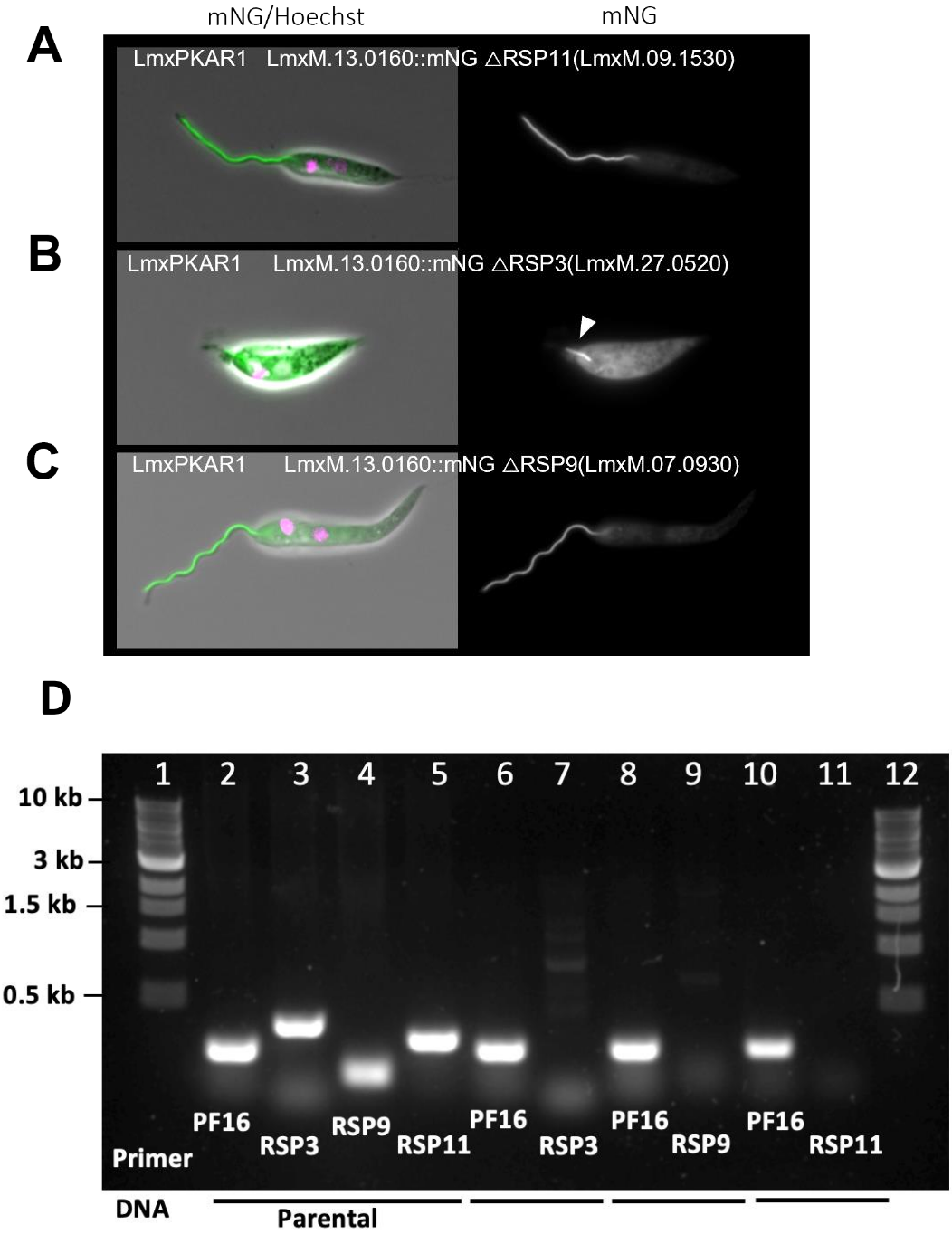


Figure 3-10: PKAR1 is not anchored in the radial spokes.

Demonstration of mNG::PKAR1 signal still visible in the flagellar axoneme after deletion of proposed radial spoke AKAPs (A) RSP11 (LmxM.09.1530) (B) RSP3 (LmxM.27.0520) and (C) RSP9 (LmxM.07.0930). (D) Diagnostic PCR to test for loss of the respective RSP gene in the

mutant cell lines. Lanes 1 and 12, DNA ladder; Lanes 2-5, genomic DNA from the parental cell line amplified with primers specific to the indicated ORFs; Lanes 6, 8 and 10, amplification of the PF16 ORF from the genomic DNA of the RSP mutants (PCR positive control); Lanes 7, 9 and 11, diagnostic PCR using genomic DNA from the respective RSP mutant cell line.

Lastly, as several publications point to PKA being associated with the radial spokes of the flagellar axoneme via AKAPs, specifically those proteins which contain an RII domains such as AKAP97 (RSP3) and RSP11 identified in *Chlamydomonas* (257,269). We deleted radial spoke proteins of the head (RSP) 9, and stalk RSP3 and RSP11 (270) on top of LmxPKAR1::mNG to see if the axonemal signal disappeared. LmxPKAR1::mNG signal was still observed in the axoneme (Figure 3-10), after confirming deletion (Figure 3-10D), suggesting that PKA is not associated with radial spokes in *Leishmania* spp.

Taken together, these data suggest that in non-dividing promastigotes, LmxPKAR1 is required for docking LmxPKAC1 and LmxPKAC2 in the flagellar axoneme, whilst LmxPKAR3 docks LmxPKAC3 at the cell body cortex. All LmxPKA subunits apart from LmxPKAR1 show subtle localisation differences during the cell cycle, indicating pleiotropic function or mechanisms of sequestration during division events.

3.2.4. Toyocamycin and inosine exposure dissociates PKAC1 signal from the axonemal cytoskeleton

Trypanosoma PKA is pharmacologically activated by toyocamycin (142). We hypothesised that LmxPKAR1 activation would involve LmxPKAC1 dissociation from LmxPKAR1, and consequently be solubilised from the flagellar axoneme where they both localise. We tested

this potential dissociation by incubating cytoskeletons from mNG::LmxPKAC1 expressing cells (Figure 3-11A) with cAMP, or toyocamycin prior to imaging. In addition to these, we tested the effect of inosine, considering that it is both similar in structure and arguably more biologically relevant as part of eukaryotic purine metabolism pathways (271), relative to toyocamycin which derives from *Streptomyces*.

The axonemal mNG::LmxPKAC1 signal remained visible in all flagellar cytoskeletons after treatment with cAMP, up to 100 µM (Figure 3-11B), however quantification suggested a small but significant decrease in fluorescent signal relative to untreated cytoskeleton controls (Figure 3-11E). Interestingly, we observed that 1 µM inosine had a very similar effect of dissociating the flagellar cytoskeleton mNG::LmxPKAC1 signal than 100 µM toyocamycin (Figure 3-11C, 11D, 11E). The mNG::LmxPKAC1 was visibly diminished to a small extent after treatment with 1 µM toyocamycin and lost in most cells upon addition of 100 µM toyocamycin (Figure 3-11D, 11E), consistent with a model where ligand binding causes conformational change in axonemal LmxPKAR1 and release LmxPKAC1 into the soluble fraction. These data together support the hypothesis that the ligand for divergent kinetoplastid PKA is likely not a cyclic nucleotide, but instead a nucleoside analogue either endogenously produced or exogenously sourced.

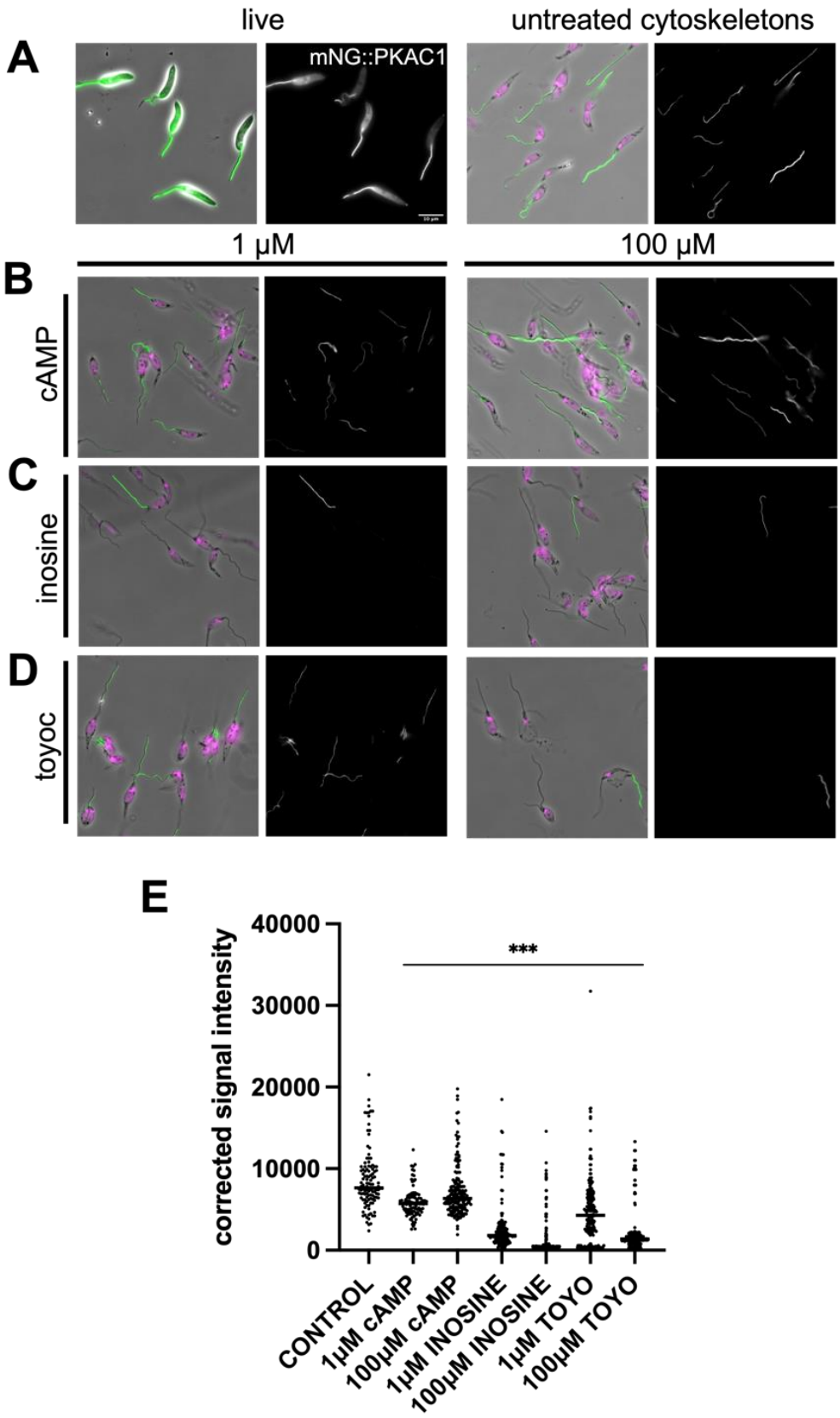


Figure legend on following page.

Figure 3-11: Pharmacological displacement of PKAC1 signal from the axoneme.

*Detergent-extracted promastigote cytoskeletons imaged by fluorescence microscopy: (A) from untagged L. mexicana live (left) and untreated detergent extracted (right). From mNG::PKAC1-expressing cells after treatment with (B) cAMP, (C) inosine or (D) toyocamycin, as indicated. (E) Quantification of the cytoskeleton-associated mNG::PKAC1 signals. Background fluorescence was subtracted from maximum intensity values taken from the middle of the flagellar axoneme. Each data point represents one cell. Significance was determined using an unpaired t-test assuming equal variance *** indicates all treated cytoskeleton conditions were highly significant compared to untreated cytoskeleton control (p<0.001). n > 50 cell measured for each condition.*

3.2.5. PKAC1 is essential for forward motility of parasites

It was previously shown that partial deletion of LmxPKAC1 (Δ*LmxM.34.4010*) reduced promastigote swim speed (77). Here we employed the same CRISPR-Cas9 knockout strategy to generate full knockout cell lines for LmxPKAC1, LmxPKAC2 and LmxPKAC3 as well as LmxPKAR1 and LmxPKAR3 (knockout validation in Figure 3-14A) to measure precisely how the loss of each of these proteins affected flagellar motility. The swimming behaviour of null mutant populations was measured with the same method used in (77) (Chapter 5: Methods) and the results (Figure 3-12A) confirmed that promastigotes lacking LmxPKAC1 swam slower (4.9 μm/s) than the parental cell line (7.4 μm/s). A reduced mean population swim speed was also observed for *ΔLmxPKAC3* and *ΔLmxPKAR1* populations (5.7 μm/s and 5.4 μm/s, respectively); deletion of LmxPKAR3 had the opposite effect and resulted in an elevated swim speed (8.4 μm/s). By contrast, deletion of axonemal LmxPKAC2 did not significantly alter parasite swim speed. All null mutants were all viable as promastigotes, with the same *in vitro* growth rates as the parental cell line (Figure 3-12B).

To test what the combined effect was of deleting LmxPKAC1 and either LmxPKAR3 or LmxPKAC2 in the same cells, the respective double null mutants were generated (genotype validated in Figure 3-15B). These showed the same reduced swim speed as the *ΔLmxPKAC1* line (Figure 3-11A), indicating that loss of LmxPKAC1 was the dominant cause of the observed motility phenotype, which could not be rescued or further compounded by secondary gene deletion of LmxPKAR3 or LmxPKAC2.

Since swim speed measurements report the average for a whole population, we next used high speed video microscopy, alongside semi-automated tracing scripts (60,80) (Chapter 5: Methods, Section 5.3) to further dissect how deficiency of each PKA subunit was affecting the flagellar beat of individual cells. First we used population overview waveform analysis (POWA), described in (227) (Chapter 5: Methods), capturing 0.5 s of high speed (200 Hz) low magnification (X20) videos to assess the relative proportions of the different waveforms that *L. mexicana* are known to generate (Section 1.1.1.2): the tip-to-base symmetric flagellar waveform, the base-to-tip asymmetrical ciliary waveform, or, in an undefined chaotic manner referred to as uncoordinated movement.

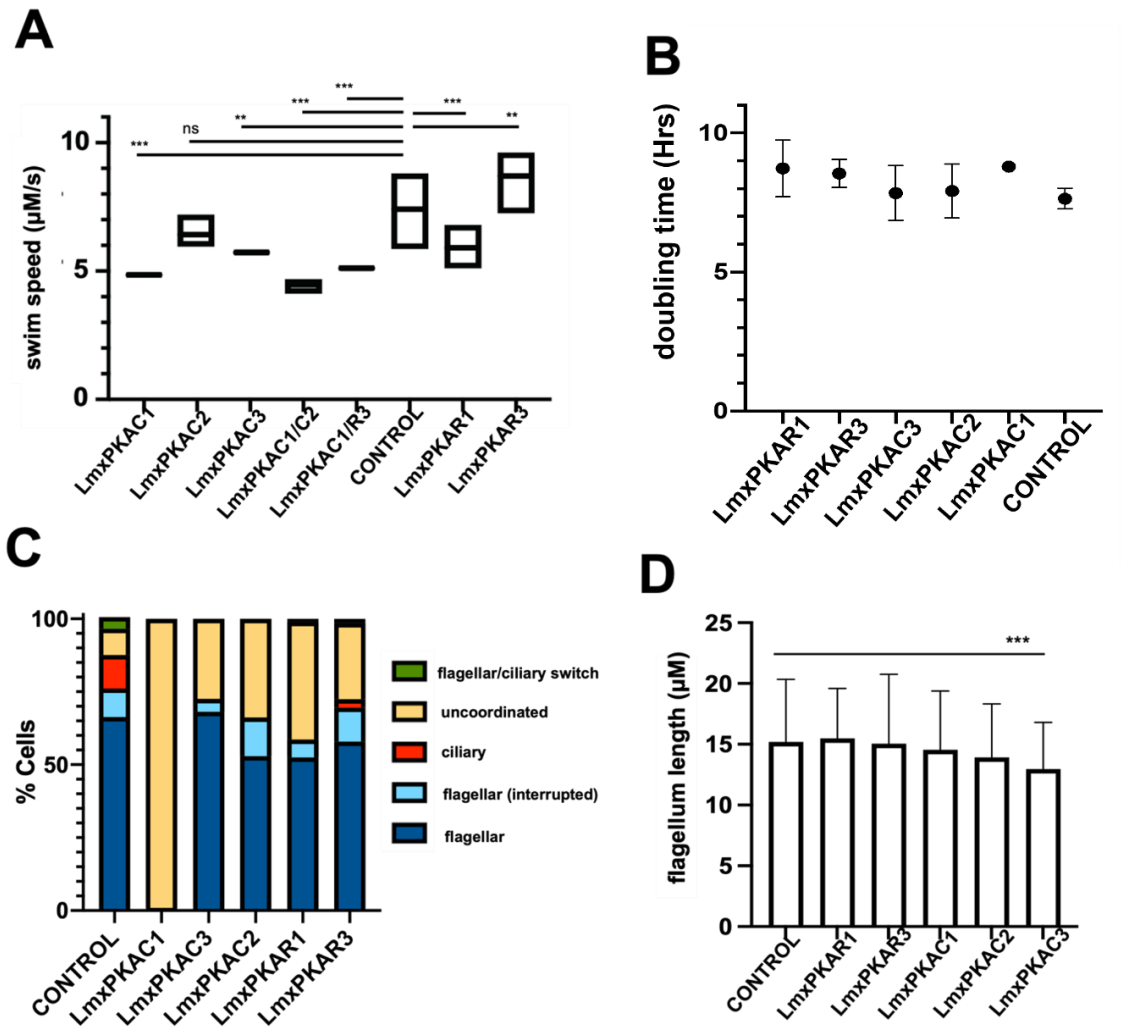


Figure 3-12: Population motility of PKAR and PKAC mutants.

(A) Mean population swim speed of parental controls and null mutants for PKAC and PKAR subunits and of dual knock outs of PKAC1/PKAC2 and PKAC1/PRAR2. Swim speed measurement data from at least three replicates per population. Unpaired t-test against parental control (p<0.05, ** p<0.05, *** p<0.001) (B) PKAR and PKAC null mutants and parental controls were grown in triplicate flasks from densities 1x10^5 to 1x10^{7}cells/ml. We calculated the doubling time for 0 - 24hrs and 24 - 48hrs then took the average, equating in six doubling times for each null mutant population. (C) Population overview waveform analysis and (D) quantification of flagellar length for PKAR and PKAC mutants. (n > 70 for each population).*

ΔLmxPKAC3 and *ΔLmxPKAR3* mutants showed similar proportions of cells propagating flagellar beats as the parental cells (~75%), but all the mutants appeared to display fewer instances of ciliary beats and a greater proportion of cells (> 25%) beating in an uncoordinated manner (Figure 3-12C). *ΔLmxPKAC2* and *ΔLmxPKAR1* populations both displayed a lesser proportion of cells using forward motility. Strikingly, *ΔLmxPKAC1* mutants were completely unable to propagate the typical tip-to base symmetrical flagellar wave for forward swimming and instead showed completely uncoordinated beating patterns (Figure 3-12C). Lastly, we quantified the flagellar length of PKA null mutants and saw that there was a slight, but significant reduction in flagellar length in the *ΔLmxPKAC3* population (Mann-Whitney test for significance against parental control) (Figure 3-12D and Table 3-2i)

3.2.6. All PKAC subunits contribute in different ways to beat amplitude and frequency

In order to dissect how the loss or dysregulation of PKAC kinases contribute to the overall waveform, the dominant beat frequency, and amplitude comprising the tip-to-base flagellar waves. *L. mexicana* cells usually beat the flagellum 20-35 times per second (Hz) and the shear amplitude varies between 40-60 degrees along the flagellum (80). This was confirmed here for the parental cell line (Figure 3-13).

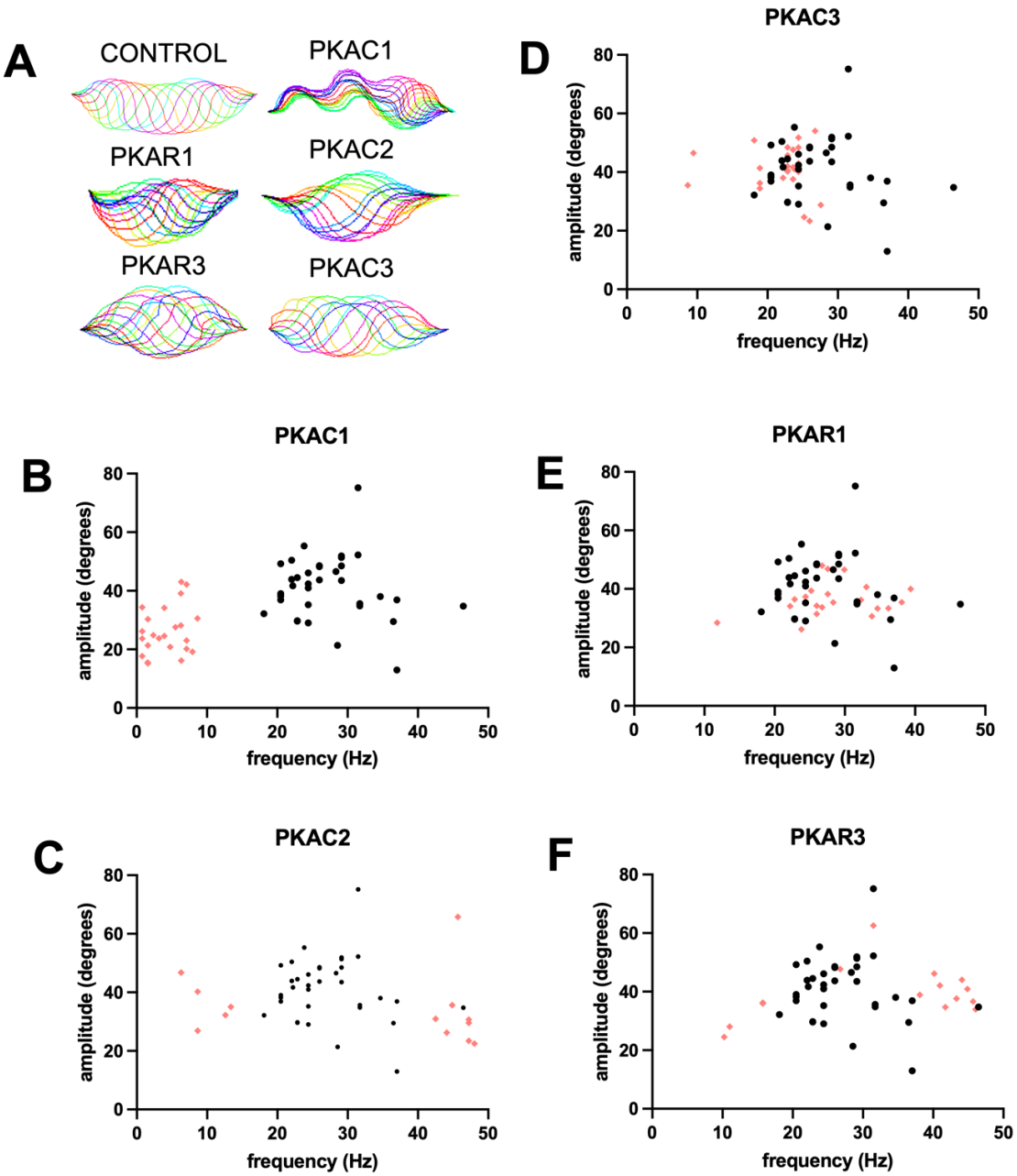


Figure 3-13: Fourier decomposition of the flagellar waveform in PKA mutants.

(A) computer generated flagellar traces of one exemplary phase cycle for each PKA mutant and parental control, highlighting the striking loss of symmetry in ΔLmxPKAC1 mutant flagella. (C-G) Beat amplitude (degrees) plotted against frequency (Hz) for PKAR and PKAC mutants (salmon coloured diamonds) overlaid on parental control parameters (black circles). The p-values ascertained from performing appropriate Mann-Whitney tests can be found in Table 3-2(ii).

ΔLmxPKAC1 mutants were never observed propagating a rhythmic symmetric flagellar wave (Figure 3-13B), however we still extracted the dominant beat frequency of attempted tip-to-base movements, which were greatly diminished (< 10 Hz) (Figure 3-13C), indicating that LmxPKAC1 is required for the generation of a normal flagellar beat. Null mutants of LmxPKAC1 and LmxPKAC2 displayed significantly diminished beat amplitudes (Figures 3-13C, 13D), but *ΔLmxPKAR1* cells retained a comparable beat frequency and amplitude, relative to parental control cells (Figure 3-13F). We observed that *ΔLmxPKAC3* cells had significantly diminished beat frequencies (22 Hz), but otherwise displayed normal beat parameters (Figure 3-13E). Lastly, although the *ΔLmxPKAR3* mutant showed a statistically normal beat frequency for flagellar waves, the flagella appeared to beat bimodally, that is, a sub-population with low beat frequency (~15Hz) and one with an abnormally high beat frequency (> 40Hz) (Figure 3-13F). The same bimodal frequency distribution was observed for the *ΔLmxPKAC2* cells (Figure 3-13C). More cells would need to be captured to ascertain the true relative proportions of the mutant populations beating with abnormally low and high frequencies and whether this alone explains the normal average population speed for *ΔLmxPKAC2* and elevated population swim speed for *ΔLmxPKAR3*.

Table 3-2: Summary numbers for the flagellar waveform of PKA null mutants.

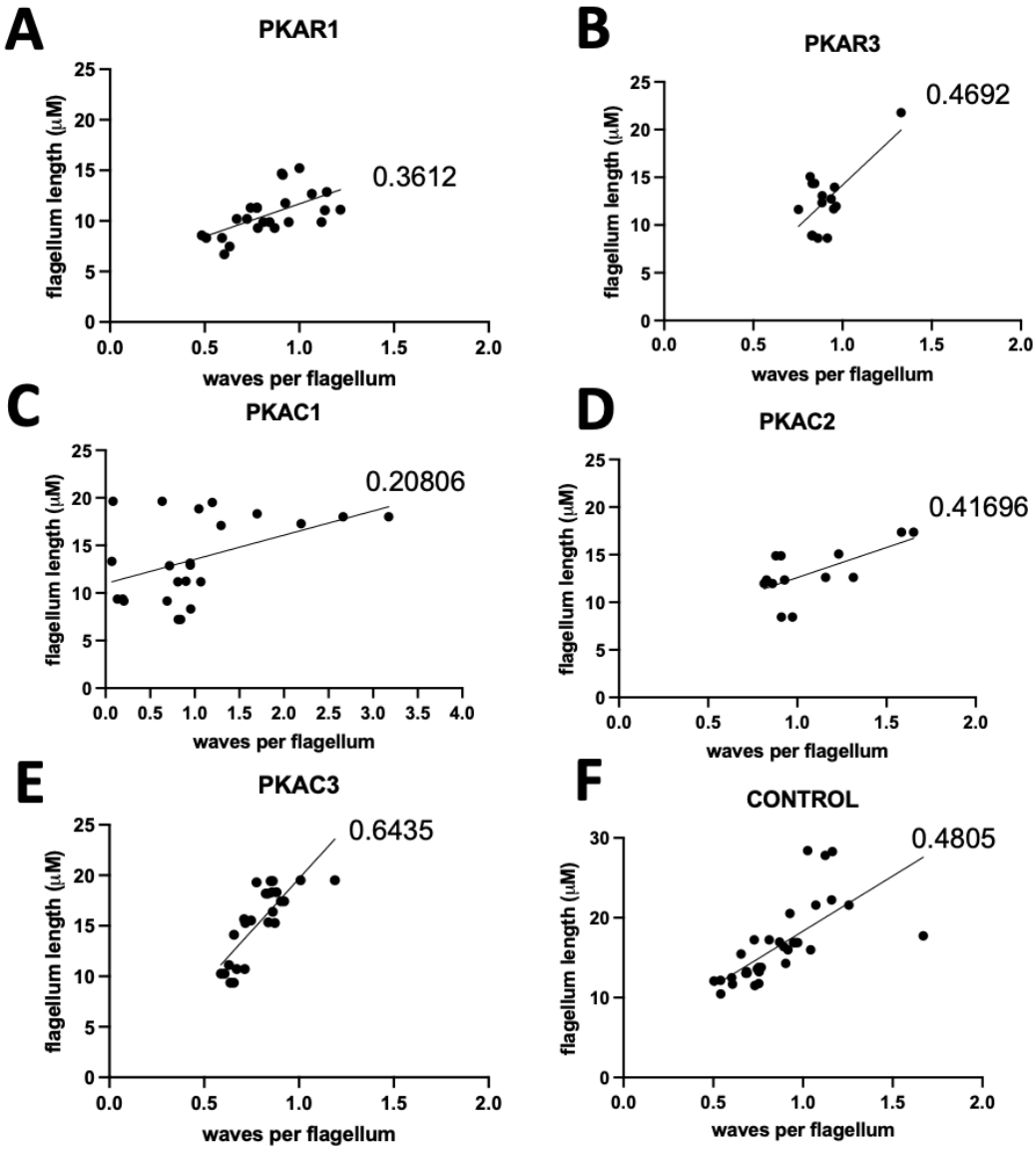
(ii) For each null mutant cell line the following numbers are shown: Number (n) of timepoints captured by high-speed video microscopy, where each timepoint represents 256 video frames, and n cells captured in total; the total time observed for each mutant dataset in seconds. The mean amplitude (amp) in degrees (deg); mean beat frequency (beats per second, bps; Hz); number of waves per flagellum (w/f); flagellum length in µm and n of cells for which length was measured. ***(ii)*** *Mann-Whitney test was used to test for significance of each dataset against that of the parental control (CONT) measurements. P-values are indicated, *** = p < 0.001, ** = p < 0.005, * = p < 0.05.*

(i)	n timepoints (n cells)	total time observed (s)	mean amp (deg)	mean Hz (bps)	Waves per flagellum (*w/f*)	flagellum length (µm) (n cells)
PKAR1	24 (17)	32.6	37	28	0.84	15.5 (57)
PKAR3	15 (10)	20.4	39	33	0.91	15 (88)
PKAC1	25 (17)	34	26***	4***	1.01	14.6 (93)
PKAC2	13 (7)	17.7	34*	32	1.08**	13.9 (97)
PKAC3	25 (15)	34	41	22***	0.79	13** (143)
CONT	35 (21)	48	41	27	0.85	15.2 (75)

(ii)	*p -values Mann-Whitney test*				
	PKAR1	PKAR3	PKAC1	PKAC2	PKAC3
amp	0.0538	0.3556	*** <0.0001	* 0.0178	0.9881
Hz	0.2564	0.0551	*** <0.0001	0.2659	*** 0.0035
w/f	0.9664	0.2048	0.5357	** 0.0093	0.3456
F-length	0.4636	0.7211	0.4434	0.1858	** 0.0089

Lastly, as it is reported that flagellum length and waves per flagellum positively correlate (58), so that the longer the flagellum, the more waves/flagellum, we assessed this parameter in our PKA mutants. Our parental control cells did indeed show a positive

correlation with R_2 of 0.4805 (Spearman's correlation) and so did *ΔLmxPKAC2*, *ΔLmxPKAC3*, *ΔLmxPKAR1* (see Figure 3-14). *ΔLmxPKAR3* showed an even tighter correlation between flagellar length and waves/flagellum with an R_2 of 0.6435 Figure 3-14E. Finally, it was clear that these parameters appeared decoupled in the *ΔLmxPKAC1* null mutant population with R_2 of 0.208 (Figure 3-14C).



G

Mann-Whitney test wavelength/flag				
PKAR1	PKAR3	PKAC1	PKAC2	PKAC3
ns 0.9664	ns 0.2048	ns 0.5357	sig 0.0093	ns 0.3456

Figure 3-14: Correlations between flagellum length and waves/flagellum in PKA mutants.

(A-F) Scatter plots of flagellum length (μm) against waves per flagellum with associated linear regression R^2 value. Each point represents one cell. (G) Summary of p-values from Mann-Whitney non-parametric test for significance against parental control measurements.

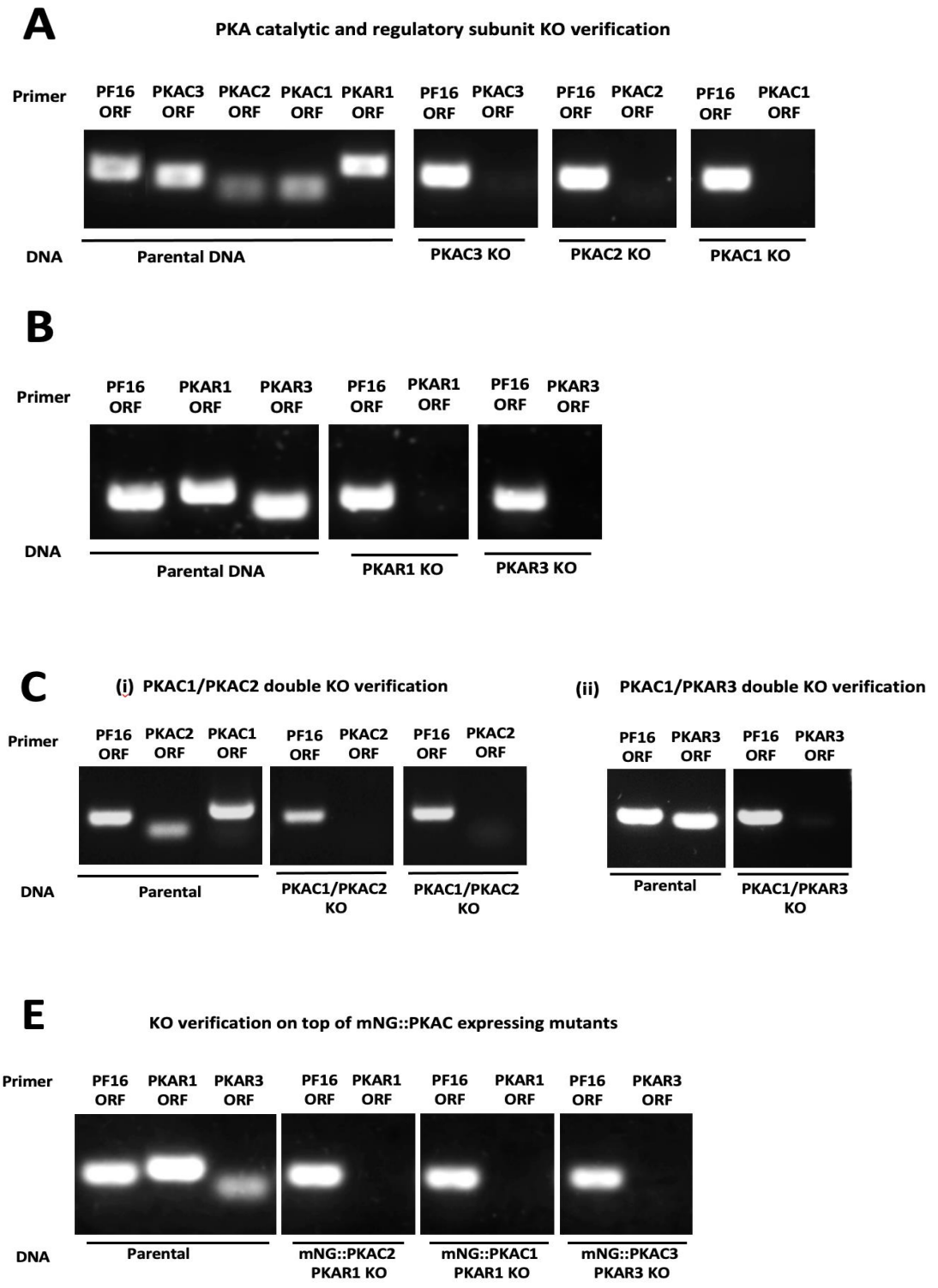


Figure 3-15: PCR validation of knock out mutants.

For all gel layouts, the first panel represents a quality control of the primer pairs, whereby PCR amplification using ORF primers listed in figure were used on the parental control genomic DNA template. Following this, the alternation of PCR amplification of a fragment

within PF16 locus (LmxM.20.1400) was used as positive control and within the ORF of the target gene of deletion for (A) ΔLmxPKAC3, -C2, -C1, (B) ΔLmxPKAR1, -R3. (C) double null mutants (i) ΔPKAC1/PKAC2 and (ii) ΔPKAC1/PKAR3 and (D) ΔPKAR1 and ΔPKAR3 on parental cell lines expressing mNG C-terminally fused PKAC subunits listed in figure. The diagnostic primer sequences were taken from LeishGEdit for all but PKAC1, where a bespoke primer design was required due to sequence similarity. The sequence for PKAC1 diagnostic primers are listed in Chapter 5: Methods, Table 5-1.

3.3. Discussion

Taken together, we found that LmxPKAC1 is concentrated in the flagellar axoneme, dependent on the presence of LmxPKAR1 for its localisation, and is required for the generation of a normal symmetric flagellar beat. In its absence, flagella beat totally uncoordinated, and the parameters extracted from the dominant beat frequency of flagellar movement demonstrated extremely reduced beat frequency and amplitude, and a decoupling of flagellum length and waves per flagella (Figures 3-13 and 3-14).

We saw that LmxPKAC2 localises to the axoneme and cell body, where loss of LmxPKAC2 does not have a significant effect on population swim speed but slightly increases (up ~10%) the proportion of uncoordinated beating, much less dramatic than loss of LmxPKAC1. Fourier decomposition of the flagellar wave from *ΔLmxPKAC2* cells demonstrated a significant reduction in wave amplitude and a bimodal beat frequency. We showed that although LmxPKAR1 docks LmxPKAC1 and LmxPKAC2 in the flagellar axoneme (Figure 3-9B, 9C), the loss of LmxPKAR1 does not phenocopy *ΔLmxPKAC1* and *ΔLmxPKAC2* mutant motility (Figure 3-12A). Instead *ΔLmxPKAR1* mutants displayed a slight but significant reduction in population swim speed, with an increased proportion of uncoordinated waves similar to that of *ΔLmxPKAC2* mutants. The waveforms from flagellar beats were comparable to parental controls, asides from a slight but significant reduction in beat amplitude. We hypothesise that in the absence of LmxPKAR1 to dock LmxPKAC1 in the axoneme, there is sufficient residual soluble LmxPKAC1 to act on its putative axonemal targets to mediate a rhythmic symmetric flagellar beat, and thus loss of LmxPKAR1 from the axoneme does not equate to total loss of LmxPKAC1 from the flagellum environment.

Additionally, we described the docking of LmxPKAC3 to the cell body cortex by LmxPKAR3. Loss of LmxPKAC3 leads to a moderate but significant reduction in population swim speed, however loss of its regulator LmxPKAR3 caused a significant elevation in population speed (Figure 3-12A). Both of these mutants had comparable levels of forward motility to parental controls (Figure 3-12C), however wave decomposition indicated that LmxPKAC3 contributed specifically to beat frequency, with cells unable to reach the higher beat frequencies above 30 Hz (Figure 3-13D). This alone appears to explain the reduction in population swim speed. Although none of the wave parameters of *ΔLmxPKAR3* mutant flagellar beats were statistically different to parental controls, when averages were compared, we observed a bimodal beat frequency with more cells exceeding 40 Hz compared to parental control (Figure 3-13E, 13F). This observation was similar to that seen in *ΔLmxPKAC2* mutants. Interestingly, we saw that all five PKA mutants had apparent reductions in the proportion of tumbling motility (Figure 3-12C), which may indicate additional contributions of these kinases to the balance between the forward and reverse beat propagation.

We conclude that all the PKA subunits studied here contribute in some way to the fine tuning of flagellar movement. LmxPKAC1 is essential for the propagation of a symmetric flagellar beat and the localisation dependency results (Figure 3-9) suggest it is regulated by LmxPKAR1. As the null mutant phenotypes from each mutant appear distinct with regards to their specific effects on amplitude, beat frequency and number of waves per flagellum, it is tempting to hypothesise that the downstream protein targets are also distinct between these subunits. The distinct localisation of each subunit may also allude to their functions. The dual localisation of LmxPKAC1 to the nucleolus as well as the flagellar axoneme in dividing cells may hint at cell-cycle stage-specific phosphorylation substrates. The dual localisation of LmxPKAC2 to the flagellar axoneme and cell body cortex suggests it is

regulated by both LmxPKAR and potentially plays a signalling role in both domains. Lastly the localisation of LmxPKAC3 predominantly to the cell body cortex with a faint soluble flagellar signal, combined with a null mutant phenotype of slow motility and a diminished beat frequency begs the question of whether its docking away from the flagellar axoneme is a purposeful spatial sequestration as a means to modulate catalytic activity in the flagellum, or its activity in the flagellum is secondary to a more central biological role within the cell body. Recent work in *L. donovani* described that PKAR3 and PKAC3 null mutants had more rounded cell bodies, leading to their proposed function in modulating cell body morphology (204). Although a mechanism is yet to be described for this.

The experiments reported in this chapter were designed to probe all PKA regulatory and catalytic subunits of *L. mexicana* under the same conditions and the results allow me to propose some tentative functions for these divergent PKA subunits in modulating the behaviour of a conserved motile flagellum. However, there are limitations. The small sample size for waveform decomposition ultimately limits the scope of what we can claim, especially in the case of the bimodal beat frequency phenotypes of *ΔLmxPKAC2* and *ΔLmxPKAR3* mutants where the number of cells observed was under 10. The limiting factor with the given experimental setup was the ability to capture fast swimming cells for the required length of time in videos and of the required quality for extraction of waveform parameters. Optimising the high-speed video capture of beating flagella and automated flagellar tracing pipeline for a lower magnification (*e.g.,* X40 instead of X100) would increase our ability to capture a larger population of cells.

In follow up to this work, it would be informative to (a) investigate the phosphoproteome of some of the mutant cell lines created in this study, and (b) identify where precisely LmxPKAR1 is in the axoneme, having already established it does not require radial spokes

for localisation to the axoneme (Figure 3-10). We may already gain insight into the phosphorylation targets of *L. mexicana* PKA by looking at the phosphopeptides upregulated after treatment of *T. brucei* with 8 µM Jaspamycin for 15 minutes (142). This published dataset lists upregulated phosphsites within several axonemal dynein light intermediate chains (DLICs), the distal ODA-docking complex dDC2, the inner dynein arm regulator IC138, and interestingly, several putative cyclic nucleotide signalling components studied in Chapter 2, namely PNUT/PK23 (containing two upregulated phosphosites), PNUT19, PNUT31, PDE B1 and PKAR1 itself (Table 2-1). As the same publication identified toyocamycin as a synthetic activator of divergent PKAR, albeit less efficacious, it may follow that the motility effect of toyocamycin treatment, that we described in Chapter 2, Section 2.5, is caused by similar phosphorylation activity to that mediated by Jaspamycin in *T. brucei*. We saw that even at low nanomolar concentrations of toyocamycin, a dual effect was observed. Both a dose dependent inhibition of cell division, and a positive effect on promastigote motility was evident (Figure 2-24C, 24D). Intriguing also, was that *Leishmania* null mutants of PDE B1 and PNUT19 presented with increased population motility (Figure 2-19). This suggests that targets downstream of PKAR activation (see above) may include axonemal dynein complexes as well as other putative components of the cyclic nucleotide signalling pathway that modulate flagellar beating to increase cell displacement. Taken these findings together, and assuming that PKAC substrates are likely to be located close to the regulating PKAR, we may hypothesise that LmxPKAR1 is likely localised near the inner and outer dynein arm region, perhaps between them both in the nexin-dynein regulatory complex (N-DRC).

To bring this manipulation of the motile flagellum into the context of sandfly transmission of parasites, would allow us to understand whether a faster swimming parasite population

(*i.e.,* LmxPKAR3 mutants or introducing nanomolar concentrations of toyocamycin into the feed of sandfly infected with promastigote parasites) would confer a fitness benefit or whether other biological mechanisms are compromised in such populations, such as the loss of chemotaxis. Examples of this have previously been alluded to, where the loss of PDE B1 in *Leishmania* results in faster motility, however *ΔPDE B1* in *T. brucei* lose the capacity for Social Motility and pH taxis (57,162). Interestingly, it has already been shown that the slower swimming *ΔLmxPKAR1* mutant maintains a comparable colonisation fitness to control cells in sandfly (77). This may be explained by our finding that the waveform parameters of *ΔLmxPKAR1* mutants are largely unchanged. What is interesting, is the apparent toxicity of toyocamycin to *Leishmania*, in combination with our clear finding that none of the PKA subunits are essential for promastigote viability or growth (Figure 3-12B), suggesting that toyocamycin has targets outside of the LmxPKAR subunits. What is lacking in our experiments, is an assay to measure kinase activity, either by *in vitro* assays which quantifying conversion of given ATP to ADP or phosphorylation of a generic given substrate (*e.g.,* VASP) (142). Ultimately, establishing a FRET system between PKAR and PKAC pairs would be most informative to infer real time dynamic release of PKAC in various conditions (*i.e*., toyocamycin) especially combined with our observations of faster and slower mutant motility or waveform reversal. Many open questions remain to be explored in this intriguing new field of novel divergent kinetoplastid signalling pathways. However, techniques used thus far in Chapter 3 have succeeded in bringing to light some of the biological roles of divergent PKA to the motile flagellum.

CHAPTER 4

The outer dynein arms are needed for directional cell motility

4. The outer dynein arms are needed for directional cell motility

Work within this chapter was done in collaboration with Dr Richard J Wheeler and Dr Benjamin J Walker who provided the automated cell tracing scripts and Fourier decomposition of the wave. Many of the cell lines included in this chapter were previously generated in house for previous projects (77) by James Smith and Dr Tom Beneke. Where indicated, cell lines were kindly generated and donated by Cecile Fort (Wheeler Lab).

4.1. Introduction

Dynein motor proteins studded along axonemal microtubules transduce the chemical energy of ATP into motion by driving the relative sliding of adjacent microtubules (1,2). The motile flagellum is typically equipped with a set of outer dynein arms (ODA), among which either two or three dynein heavy chains (DHC) are anchored depending on the species, and inner dynein arms (IDA) which comprise of around 7 DHC (IDA-α, -β, -a, -b, -c, -d, -e, -f, and -g) (see Chapter 1, Figure 1-1 and 1-2). Understanding how motile cilia convert chemical energy to movement becomes important when inherited defects in certain components result in human disease. Primary ciliary dyskinesia (PCD) is the term given when an autosomal recessive mutation is inherited which manifests in malfunctioning motile cilia (272). Successful diagnosis often relies on microscopy to quantify ciliary beat frequency (CBF), beat pattern (CBP) or structural abnormalities from patient brush biopsies (273). To date around 45 genes have been aetiologically linked to the disease, which presents with

various symptoms, from increased pulmonary infection, subfertility, ear inflammation or even mirror imaged organ arrangement (*situs invertus*), ultimately depending on which downstream defect within the cilium is caused by the inherited mutation (273). Among the most commonly reported mutations are those within DNA1I (intermediate chain 1 (IC1)) and DNAH5 (ODAα), together accounting for just under a third of all PCD cases and both of which form part of the outer dynein apparatus (32,274). At a reduced prevalence among PCD patients, mutations involving components of the Dynein Axonemal Assembly Factors (275), inner dynein arms (IDA), radial spokes (RSP) (224), dynein regulatory complex (DRC) and central pair (CP) have also been documented (272,274). Usefully, the collation and publication of patient genotype and associated phenotype allows us to start dissecting the contributions of component of the ODA and IDA to wave formation in different cell types (276).

It is a long-standing consensus that the ODA are dispensable for flagellar wave formation, mainly contributing to the power behind the beat, whereas the IDA are mainly responsible for wave propagation and shape (Chapter 1, Section 1.1.2) (69,81). However, several lines of evidence suggest that these IDA ODA contributions may not apply to every organism, waveform or cell type. Two independent studies in kinetoplastids and one in *Tetrahymena* have indicated a potentially essential role for the ODA in forward motility (85,86,277). Interestingly, mutations in DNAH11 (ODAα in *C. reinhardtii*, ODAβ in *H. sapiens and L. mexicana*) have been associated with both immotile tracheal cilia and reduce sperm motility in mice (87), and hyperkinetic CBF with aberrant CBP in human tracheal cilia (276). Intriguingly, eel sperm naturally occur without the ODA apparatus with reportedly identical IDA morphology to *Chlamydomonas* and *Tetrahymena*, however they are still able to beat at high frequencies exceeding 60 Hz (278), where ODA deficient *Chlamydomonas* and sea

urchin sperm report severely diminished beat frequencies (69,81). Additionally, it has been reported that the majority of ODA mutants generated in *Chlamydomonas* have been immotile or unable to propagate a symmetric wave (84), with only a few isolated cases of ODA mutants which can swim with both flagellar and ciliary beats (69).

Ultimately it is widely accepted that the contributions of the axonemal dyneins to the movement of motile cilia and flagella are modulated by second messengers, namely calcium and cAMP. A robust body of evidence in diverse eukaryotic species and cell types demonstrate that calcium and cAMP modulate the wave direction and shape (see Chapter 1, Section 1.1.4). In *Leishmania*, we found the flagellar protein PNUT19 contains a cyclic nucleotide binding domain in addition to a calcium lipid binding protein (C2 domain), localises to the flagellar collar/pocket and occasionally to the very flagellar tip, and negatively regulates swim speed (Chapter 2, Figure 2-11 and 2-19). Not only this, but we found CARP1 mutants show an elevated reverse beat and flagellar-to-ciliary switching behaviour, suggesting this predicted axonemal transducer of cAMP in the *Leishmania* axonemes is important for wave direction (Chapter 2, Sections 2.21, 2.2.3 and 2.4). Conversely, Mukhopadhyay and Dey demonstrated that a high cAMP environment in reactivated *Leishmania* cytoskeletons triggers asymmetric ciliary wave propagation (59). On the other hand, they showed that inhibiting the calcium sensing machinery, calmodulin and calcineurin, also resulted an increased ciliary beating (104), together suggesting that a high cAMP combined with a low calcium signal both work to mediate the cell tumbling/turning events in *Leishmania* species. As it is reported that mutants of the distal docking complex (dDC) also show an increased propensity for propagating a ciliary wave in *Leishmania* (227), our model for cAMP transduction through axonemal CARP1 (Chapter 2, Section 2.5.3, Figure 2-29) proposes an association with the ODA and its activity, where a gradient of cAMP along

the axoneme is maintained by distal localised PDEs and RACs. We hypothesise that this balance works to suppress the reverse wave and/or facilitate the dominant flagellar wave for forward motility.

It is currently not fully documented how the ODA and IDA contribute to *Leishmania* motility. And so, in order to understand better how CARP1 transduction of cAMP may be acting, and moreover whether our proposed model is plausible, we must fill this knowledge gap.

In this study, we interrogated the contributions of individual axonemal DHCs and other axonemal components to flagellar wave formation by combining gene deletion with CRISPR and applying tools for automated cell tracing and waveform shape quantitation, which have previously been used for the description of *Leishmania* waveforms (60,61,80). We compared the beating parameters of DHC null mutants to those of the control flagellar beat and ask how forward motility is affected across our panel of mutants. As a reference point for comparison with *Chlamydomonas* outside of the dyneins, we also assessed the waveforms produced in deletion mutants of radial spoke protein RSP4/6, NDRC4 and MBO2. These were chosen because in *Chlamydomonas* the respective mutants present with characteristic flagellar beat phenotypes (47,70,279).

We demonstrate that *L. mexicana* forward motility cannot tolerate the complete loss of ODA dynein heavy chains along the entire axoneme, a finding that has previously been alluded to in work from *T. brucei* (85,86), however *Leishmania* mutants with partial ODA deficiency demonstrate similar reductions in beat frequency (< 50%) to those describes in KCl treated sea urchin sperm (81) and *Chlamydomonas* mutants (69). This, broadly speaking, indicates that the principles established in *Chlamydomonas* and sea urchin also hold true for *Leishmania,* where the ODA are indeed needed to reach normal high beat frequencies. We

describe the contributions of individual dyneins to flagellar beat shape, and see that mutants lacking the single IDA DHCs are still able to propagate a flagellar wave with slight reductions in either beat frequency or amplitude, however mutants lacking either of the IDA double headed DHCs (alpha and beta) demonstrate a unique form of flagellar immobility imposed by the proximal flagellar curl, perhaps suggesting an imbalance of dynein activity. From the lack of free moving flagella to extract waveform parameters for cross-comparison, we are unable to unpick whether the same universal principles of IDA contributions apply to *Leishmania* flagella, as they do in *Chlamydomonas* (69). These findings do however suggest that the IDA double headed DHCs contribute in a unique way to the axonemal beat iteration, which introduces a curious structural phenomenon to be explored with techniques such as cryo-EM.

4.2. Results

4.2.1. Selection of proteins for functional interrogation

4.2.1.1. Identification of axonemal dyneins in L. mexicana

To curate our list of axonemal dyneins in *Leishmania*, we first used a PFAM search for dynein heavy chain PF03028 (Dynein heavy chain region D6 P-loop domain) in TriTrypDB, which identified 14 genes (listed in column 3 of Table 3-1). One was immediately excluded (LmxM.29.3410), as its protein architecture lacked the canonical 6 AAA domains and was much smaller (~600 aa) than expected for dynein proteins (>3000 aa), leaving 13 dynein heavy chains. Next, we cross-checked our list with a phylogenetic study of eukaryotic dyneins by Wickstead and Gull (22). This study revealed the *Homo sapiens* genome to encode 14, *Chlamydomonas* genome to encode 15, and *Leishmania major* and *Trypanosoma brucei* genomes to encode 12 DHCs (see Table 3-1, column 6), indicating that we identified one extra dynein heavy chain (LmxM.27.2590) which may have come to light as a result of more recent *L. mexicana* genome annotation updates. Even though LmxM.27.2590 was annotated as a having a point mutation on TriTrypDB, we included this as a legitimate dynein heavy chain for several reasons: Firstly, it comprises a full uninterrupted coding sequence for a protein of the expected size (4337aa) and domain architecture, including the canonical AAA domains of a dynein heavy chain (187). And secondly, the localisation of the *T. brucei* syntenic ortholog on TrypTag database, localises to the flagellar axoneme (Figure 4-3), demonstrating at least protein expression, and expected localisation (187). Next we identified and removed from our list the cytoplasmic heavy chain dyneins responsible for cytoplasmic and intraflagellar transport (IFT) cargo

transport, of which three were found to be encoded in the *L. mexicana* genome (DYNC1H1: LmxM.22.1110, DYNC2H1: LmxM.33.4160, DYNC2H2: LmxM.27.1750) (280). To be clear which of the *Leishmania* dyneins corresponds to which orthologues in *Chlamydomonas* and *Homo sapiens*, we used COBALT (281) to make a multiple sequence alignment of full-length dynein sequences and construct a Fast minimum evolution phylogenetic tree. We included a total of 16 DHCs for *C. reinhardtii* (Table 5-2) and 15 DHCs for *H. sapiens* (Table 5-3) (details in Chapter 5: Methods, Section 5.6.). This tree (Figure 4-1) was in agreement to the published work on eukaryotic dynein phylogeny based only on the sequence within the PF03028 dynein heavy chain domain (22). As the nomenclature of axonemal dyneins across eukaryotic organisms is somewhat convoluted, we used where relevant the recently unified nomenclature for axonemal dyneins in *Chalmydomonas* (282) and *Homo sapiens* (283) and for *Leishmania*, consulted with the identified phylogenetic dynein families outlined by Wickstead *et al* (22), naming our *Leishmania* dyneins according to the family that they belong to (*e.g.,* IDA5). Note that where more than one DHC belong to the same family, we annotate as IDA5a, -b, -c according to the lowest to highest gene ID chromosome number

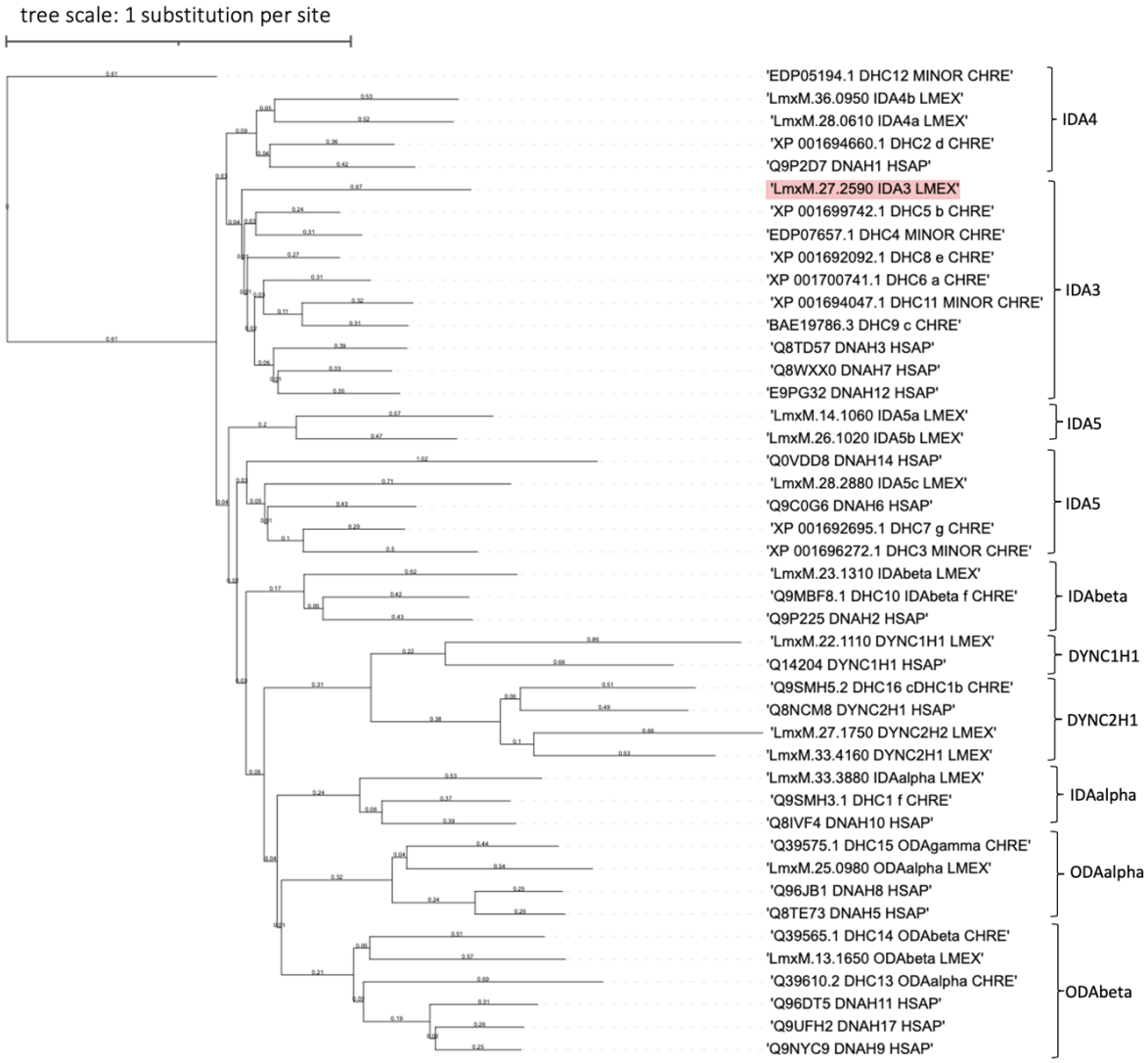


Figure 4-1: Phylogeny of dynein heavy chains (DHC) encoded in H. sapiens, L. mexicana and C. reinhardtti.

Fast minimum evolution phylogenetic tree (distance, Kimura. Max seq difference, 0.85) of full length DHC protein sequences calculated by Cobalt (284) and figure adapted using iTOL (285). Right are the dynein family clusters as named in (22). Scale represents 1 amino acid substitution per site. Genbank accession number for each dynein as well as other names (DNAH for H. sapiens (283), DHC for C. reinhardtti (282)) established by the literature. Highlighted in red is the novel IDA dynein heavy chain (LmxM.27.2590) which is shown to cluster with the IDA3 family.

respectively. This strategy allowed us to pinpoint the evolutionary positioning of our novel DHC (LmM.27.2590) alongside the IDA3 family (highlighted in red in Figure 4-1).

We obtained a final list of 10 *L. mexicana* axonemal DHC proteins (Table 4-1), for which we interrogated their individual contributions to flagellar wave form and beat pattern.

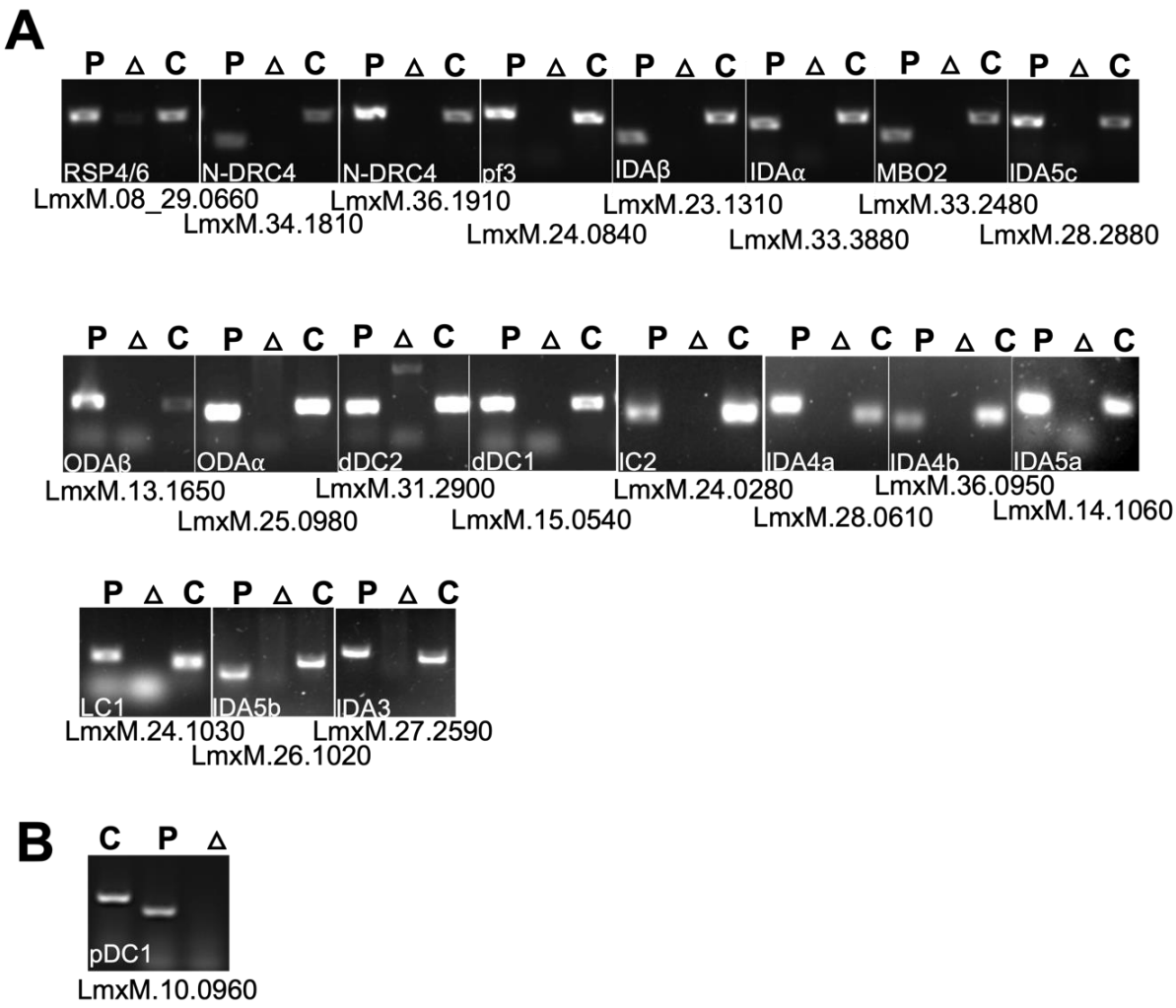


Figure 4-2: Gene knockout validation.

*(A) Represent batches of knockout verifications performed in parallel with the same PCR master-mix and run within the same thermocycler. (B) knockout validation of the pDC1 gene kindly generated and gifted by our collaborator Cecile Fort, Wheeler Lab. Knockout verification for ΔpDC1/dDC2 genotype is available upon request from Ceclile Fort. (**P**) represents the ORF primers from the target gene amplifying a fragment from genomic DNA*

*of the mutant cell line, (Δ) represents the ORF primers from the target gene amplifying a fragment from genomic DNA of the mutant cell line, (**C**) represents a positive control PCR reaction where primers targeting the ORF of a housekeeping gene (PF16) is used to verify the quality of the genomic DNA for the mutant cell line. The protein names and gene IDs are indicated in figure for each target gene.*

Table 4-1: Dynein heavy chains encoded in the T. brucei, L. major, L. mexicana genomes.

Axonemal dynein genes in T. brucei (column 1), L. major (column 2) and L. mexicana (column 3), identified by searching TriTrypDB for DHC D6 P-loop domain (PF03028). Genes printed in bold were included in this study. Protein length is shown for the L. mexicana gene products (column 4); hypothetical protein (LmxM.29.3410) was excluded from our study due to it small size column 4. L. mexicana protein names given in column 5. Human and Chlamydomonas orthologues are indicated in columns 6 and 7 respectively.

T. brucei	*L. major*	*L. mexicana* (PF03028)	protein length (aa)	*L. mexicana* name	*H. sapiens (Braschi et al. 2021)*	*C. reinhardtii (Hom et al. 2011)*
Tb927.11.3250	LmjF13.1650	**LmxM.13.1650**	4667	ODAβ	DNAH9 / DNAH11 / DNAH17	DHC13/DHC14
n/a	LmjF14.1060	**LmxM.14.1060**	4268	IDA5a	n/a	n/a
Tb927.7.3160	LmjF22.1110	LmxM.22.1110	5670	DYNC1H1 (cytoplasmic)	DYNC1H1	n/a
Tb927.8.3250	LmjF23.1310	**LmxM.23.1310**	4757	IDAβ	DNAH2	DHC10
Tb927.3.930	LmjF25.0980	**LmxM.25.0980**	4702	ODAα	DNAH5 / DNAH8	DHC15
Tb927.7.920	LmjF26.1020	**LmxM.26.1020**	4045	IAD5b	n/a	n/a
Tb927.11.2430	LmjF27.1750	LmxM.27.1750	4470	DYNC2H2 (IFT)	DYNC2H1	DHC16
Tb927.11.8160	LmjF28.0610	**LmxM.28.0610**	4231	IDA4a	DNAH1	DHC2
Tb927.11.11220	LmjF28.2880	**LmxM.28.2880**	4230	IAD5c	DNAH6	DHC3 /DHC7
Tb927.4.870	LmjF34.3880	**LmxM.33.3880**	4644	IDAα	DNAH10	DHC1
Tb927.4.560	LmjF34.4160	LmxM.33.4160	4241	DYNC2H1 (IFT)	DYNC2H1	DHC16
Tb927.10.5350	LmjF36.0950	**LmxM.36.0950**	4204	IDA4b	DNAH1	DHC2
Tb927.2.5270	LmjF.27.2590	**LmxM.27.2590**	4337	IDA3	n/a	n/a
		LmxM.29.3410	617	small		

To test whether our gene products of interest localised to the flagellar axoneme, and to assess whether any proximal-distal asymmetries were evident, we targeted all 10 axonemal

DHC genes for endogenous fluorescent tagging of mNG at the C-terminus. Eight tagged cell lines were successfully obtained, and all showed a fluorescent signal enriched along the entire flagellar axoneme Figure 4-3. Furthermore, localisation images in the TrypTag database (187) confirmed that all 9 axonemal DHCs localise to the flagellar axoneme in *T. brucei* Figure 4-4.

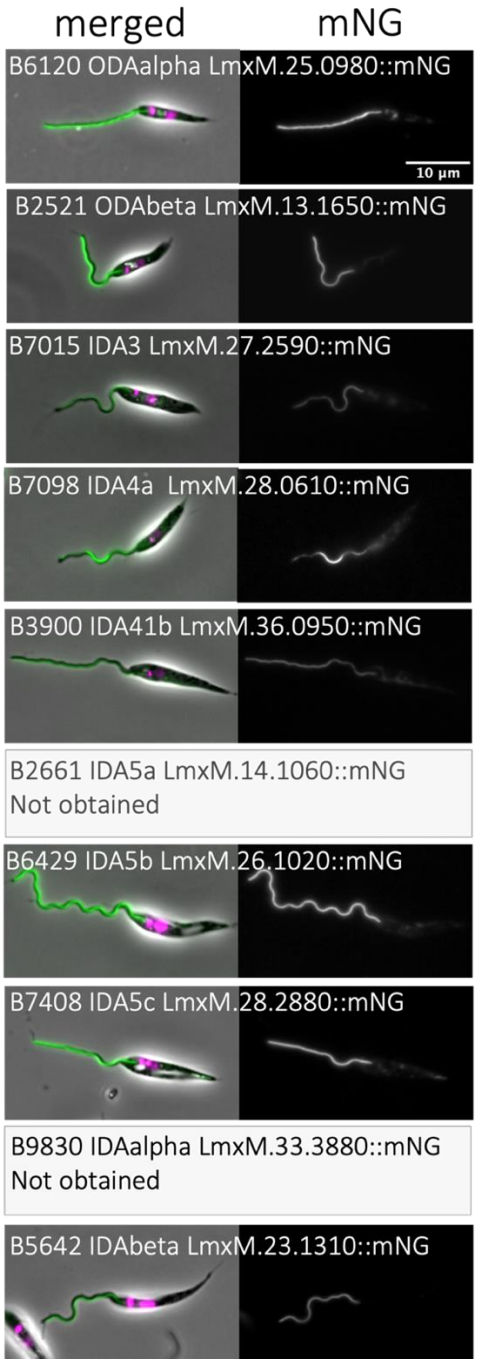


Figure legend on following page.

Figure 4-3: Axonemal dynein localisations in L. mexicana.

Protein localisations of the 8 of the 10 axonemal dyneins addressed in L. mexicana for this study (Table 4-1, column 1). All localisations represent a C-terminal fusion of mNG. Left column presents the merged phase contrast and fluorescence and right column the mNG signal in grey. Annotated on each micrograph is the respective barcode number associated with the null mutant. Scale bar represents 10 µm.

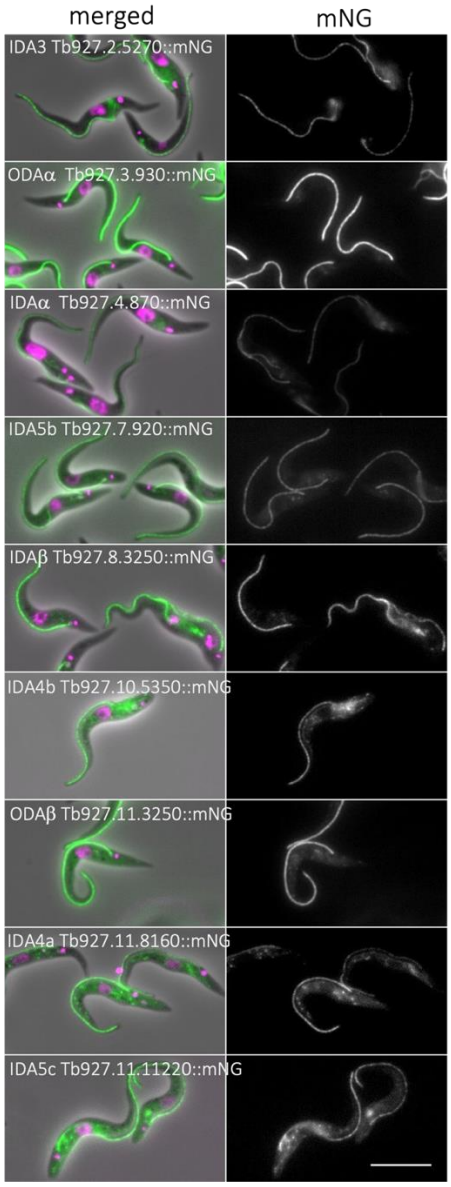


Figure 4-4: Axonemal dynein localisations in T. brucei.

Protein localisations of the syntenic T. Brucei orthologues (Table 4-1, column 1) from the 10 axonemal dyneins addressed in L. mexicana for this study. All tags sourced from Tryptag.org

and represent a C-terminal fusion of mNG. Left column presents the merged phase contrast and fluorescence and right column the mNG signal in grey. Scale bar represents 10 µm.

4.2.1.2. Selection of non-dynein axonemal proteins included in the mutant analysis

Investigation of the contributions of many axonemal structures to ciliary beating has been ongoing since the 1950s (286). In particular, detailed changes in waveform have been documented in *Chlamydomonas* with RS, CP, N-DRC, IDA and ODA deficiencies (69,70). We identified the *Leishmania* orthologs of *Chlamydomonas* genes for which mutant flagellar beat analyses have been published, including *pf1* (RSP4/6), *pf16* (PF16), *pf2* (N-DRC4), *pf3* (IDA LC p28), *oda1/oda38* (ODA-DC), *LC1* and *MBO2* (69,287,288) (Table 4-2). The null mutants for these had already been generated previously in house for previous projects by James Smith and Tom Beneke (Gluenz Lab, Oxford), and thus were already available.

Kinetoplastids have a proximal and distal set of ODA docking components, for which it was shown that deletion of one affects the localisation distribution of the other (46). For this reason, we additionally obtained a double mutant of the proximal and distal docking complex to ensure we had a mutant with entirely absent ODA across the entire length of the flagellum. This cell line was kindly generated and gifted by Dr Cecile Fort (Wheeler lab, Oxford). In addition to this, we chose to include a mutant of the dynein tail structure, intermediate chain 2 (IC2), reported to be needed in assembling the ODA heavy chains onto the A-microtubule and intriguingly highly represented in patients with the ciliopathy Primary Ciliary Dyskinesia (PCD) (276).

From these searches, 12 mutants additional to the dynein mutants were included in our study. They represent key axonemal structures for some of which the waveform contributions have already been characterised in *Chlamydomonas* models (70).

Table 4-2: Non-dynein proteins included in the study.

L. mexicana proteins (column 1) and respective genes IDs (column 2) targeted for deletion are listed with the relevant Chlamydomonas mutants (column 3) and relevant references (column 4). Where two mutants share the same name (e.g., RSP4/6), the chromosome number is listed alongside to distinguish cell lines.

L. mexicana protein name	*L. mexicana* Gene ID	*C. reinhardtii* mutant	Reference
pf3	LmxM.24.0840	*IDA LC p28/IDA4/pf3*	(289,290)
N-DRC4_34	LmxM.34.1810	*pf2*	(47)
N-DRC4_36	LmxM.36.1910	*pf2*	(47)
MBO2	LmxM.33.2480	*MBO2*	(47)
dDC1/2	LmxM.150540/LmxM.31.2900	n/a	
pDC1	LmxM.10.0960	n/a	
pDC1/dDC2	LmxM.10.0960/ LmxM.31.2900	*oda1/oda38 oda41*	(47)
RSP4/6_13	LmxM.13.0430	*pf1*	(291)
RSP4/6_8	LmxM.08_29.0660	*pf1*	(291)
LC1	LmxM.24.1030	*LC1*	(73,292)
IC2	LmxM.24.0280	n/a	n/a
PF16	LmxM.20.1400	*pf16*	(293,294)

4.2.2. The double headed dynein heavy chains of the ODA and IDA are both necessary for forward motility

4.2.2.1. Population overview waveform analysis

To examine how the different *L. mexicana* ODA and IDA proteins contributed to the propagation of flagellar (tip-to-base forward motility) and ciliary (base-to-tip tumbling motility) waveform types, we used the population overview waveform analysis (POWA) (Chapter 5: Methods, Section 5.3.1). Firstly, only *ΔpDC1* and *ΔIDA3* mutants showed comparable proportions of forward motility to parental controls (~75% of cells), suggesting that these components do not significantly contribute to the mechanics of propagating a tip-to-base wave (Figure 4-5). There was, however, a striking reduction in the ciliary beat

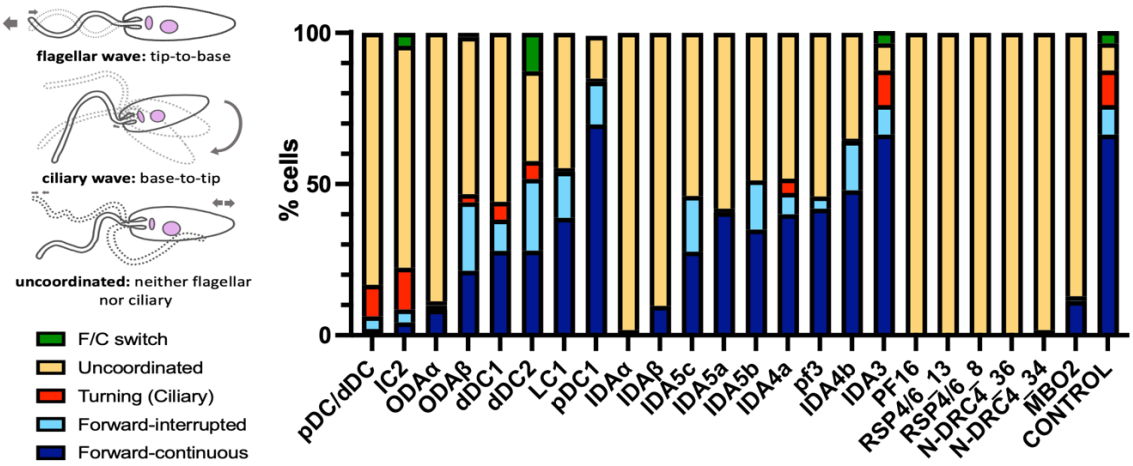


Figure 4-5: Waveform analysis of DHC and DHC associated mutants.

The population overview waveform analysis of dynein heavy chain (DHC) and DHC-associated mutant cell lines including motility control mutants on the right. n > 70 for each population. To the left is a cartoon indicating the waveform categories. Forward motility and tumbling/turning motility represented by dark/ light blue and red respectively. Green

indicated a switch between forward and tumbling motility. Orange represents uncoordinated or static flagella. Data plotted as percentage of the cells within that population.

propagation in *ΔpDC1* (Figure 4-5). Next, we saw that mutants of the single headed IDA dynein-HC (families -4 and -5) *ΔIDA4*, *ΔIDA5,* and ODA mutants *ΔdDC*, *ΔLC1* and *ΔODAβ* displayed moderate decreases in forward motility including a higher proportion of interrupted flagellar waves (combined forward motility ~50% of cells) (Figure 4-5). And lastly, severely diminished (< 10% of cells), or completely abolished flagellar wave propagation was observed in our *ΔMBO2*, both *ΔRSP4/6*, *ΔPF16*, both *ΔN-DRC4* populations, as well as in our *ΔIDAα*, *ΔIDAβ*, *ΔODAα*, *ΔIC2* and *ΔpDC/dDC* double null mutants. We saw a striking lack of ciliary beating in the IDA cohort of mutants, where ciliary beats were only observed in *ΔIDA4a* and *ΔIDA3* populations (Figure 4-5). Interestingly, the *Leishmania ΔMBO2* population, a homologue of *Chlamydomonas* 'moving backwards only' *MBO2* mutant (279) which can only propagate the flagellar wave for photophobic response (*i.e.* no ciliary beat for forward motility), was observed to be propagating the flagellar wave in ~10% of cells where no ciliary wave was observed (Figure 4-5). None of the mutants in our library demonstrated a paralysed static flagellum phenotype, asides from the paralysed control *ΔPF16*.

4.2.2.2. Flagellum length and curling propensity

It was noted during our assessment of waveform types, that in some mutant cell lines, there were apparent morphological phenotypes, such as absent and short flagella (Figure 4-6A) or flagella curling (Figure 4-6B, 6C) (previously described (77,223)). Thus, these were quantified for our cohort of mutants and summarised in Figure 4-7A, 7B and Table 4-3.

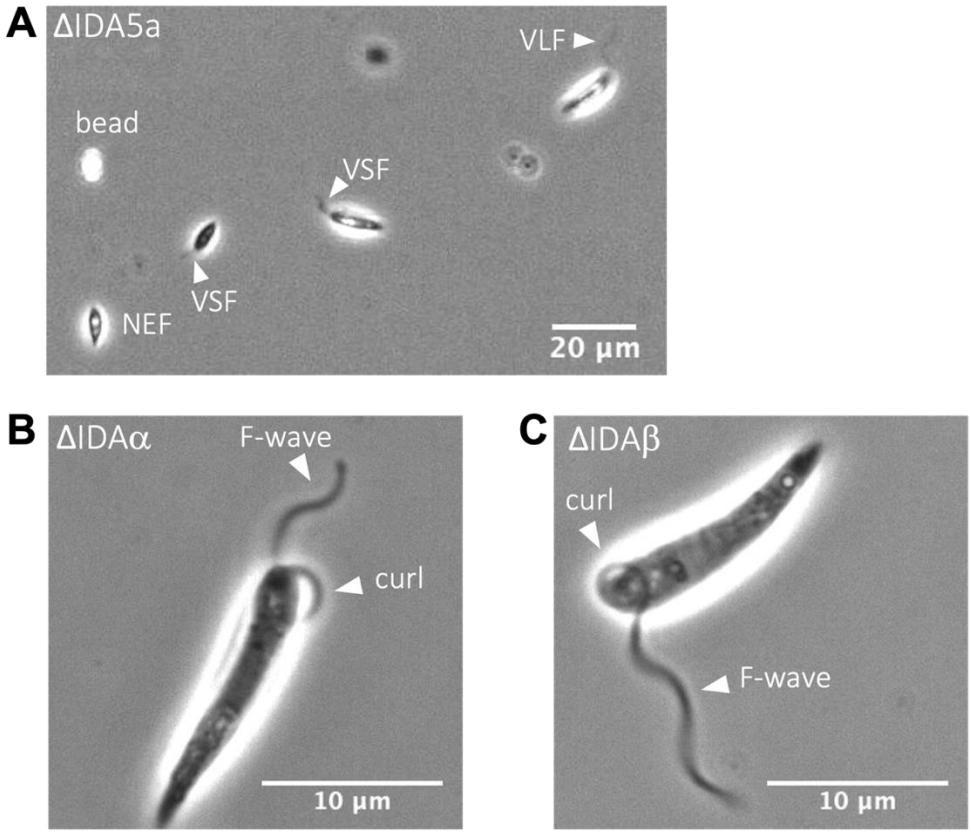


Figure 4-6: Example flagellum morphologies.

(A) example field of view taken from a X20 magnification video used for waveform analysis. The cells shown in the FOV represent a cell with no external flagellum (NEF), visible short flagellum (VSF) or a visible long flagellum (VLF). Scale bar represents 20 µm. Absence in external flagella quantified in Table 4-3. (B) proximal curl in ⊿IDAα flagellum, (C) proximal curl in ⊿IDAβ flagellum. Cells captured with X100 magnification video, where the distal tip is dynamically propagating a normal flagellar wave. White arrows point towards the curl and flagellar wave (F-wave). Scale bars represent 10 µm.

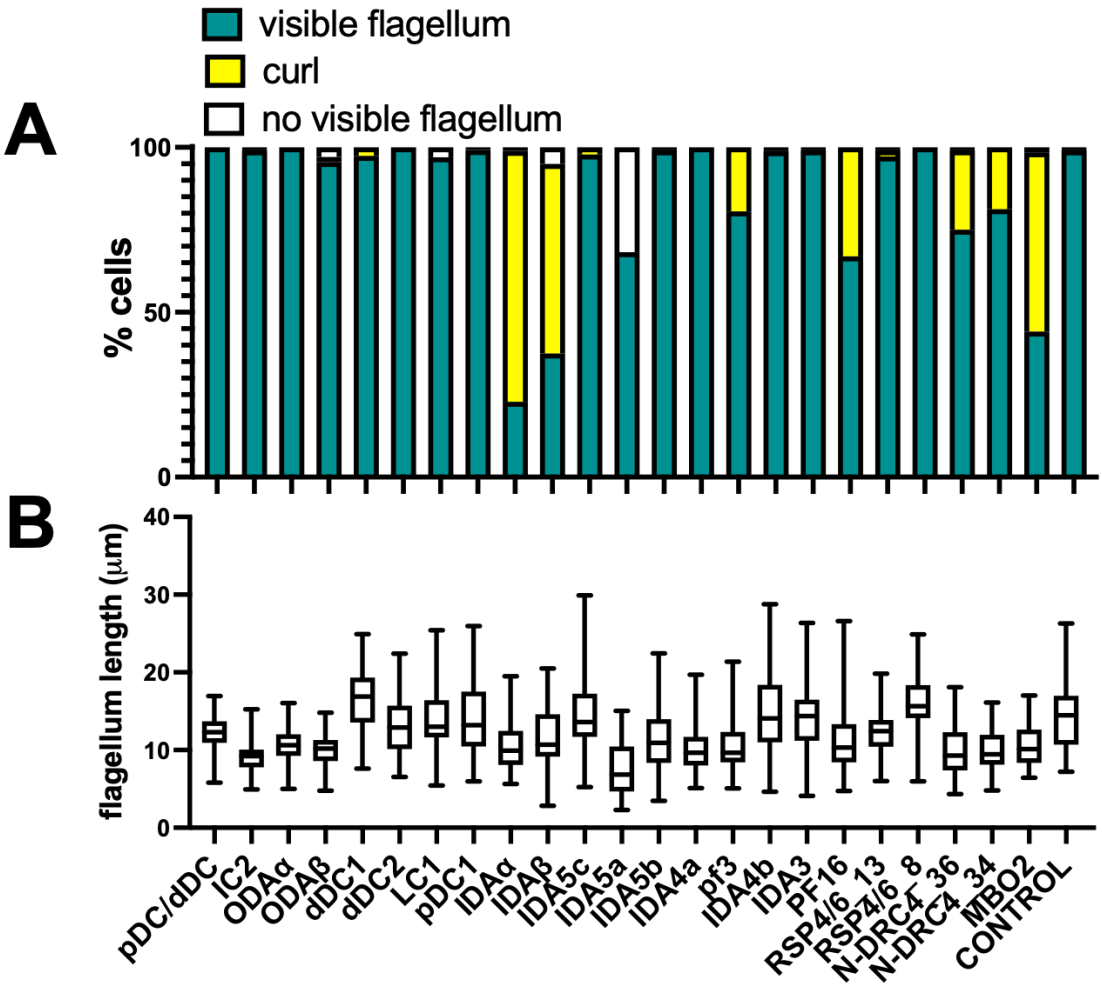


Figure 4-7: Absent and curled flagella quantification.

(A) Curling (yellow) and absent external flagella (white) quantified in non-dividing cells. Green represents a visible external flagellum. Example cells for each category shown in Figure 4-6. (B) Box and whiskers plot of flagellar length for each cell line where the line is at the mean. Each dataset measured in ImageJ from stills obtained from the x20 magnification high speed video capture. Number of cells for each population summarised in Table 4-3.

Firstly, absence of IDA5a appeared to diminish the chance of constructing an external flagellum for 30% of the population and produced significantly shorter flagella in the remaining population (an example field of view shown in Figure 4-6A, proportions quantified in Table 4-3). Moreover, we found among the mutants with the shortest flagella were *ΔIC2* (9.18 µm), and the *ΔN-DRC4* mutants (9.92 and 9.96 µm) compared to the parental control

average flagellar length of 14.36 µm (Table 4-3). It was noted that mutants which exhibited significant curling rates (Figure 4-7A, Table 4-3), *i.e., ΔIDAα* (76% of flagella curled), *ΔIDAβ* (58%), *ΔMBO2* (54%), *ΔN-DRC4* (~20%) and *Δpf3* (19%) mutants, also had reduced flagellar lengths of about 10 - 12 µm (Figure 4-7B, C; Table 4-3). Note, this represents the length of the non-curled flagella in these populations, as the length of curled flagella could not be measured as the visibility is obscured (*e.g.,* Figure 4-6B). This difference in flagellum length could suggest that the flagellum must reach a certain length for the curl to be stable and our flagellar length quantification may have been biased towards visible short, uncurled flagella in each population.

We observed that mutants of the ODA showed no flagella curling and did not have defects in constructing a visible external flagellum (Figure 4-7A, 7B).

Table 4-3: Quantification of flagellum length, absence, and curling.

The table shows for each mutant population the average flagellar length (F-length), standard deviation (St Dev) of length, percentage of cells with a visible uncurled external flagellum, with a flagellar curl and without a visible flagellum. The number of flagella observed for each mutant is indicated (n cells). Flagellar length measurements were done on visible non-curled flagella only, with n > 50 cells for all cell lines except IDA-beta (n = 26) and MBO2 (n = 30). The percentage of each population with visible flagella (column 4), curled flagella (column 5), and no visible external flagella (column 6). Column 7 shows how many cells were observed per population.

Deleted gene	F-length (µm)	St Dev length	(%) visible flagellum	(%) complete curl	(%) no external flagellum	n cells
pDC1/dDC2	12.16	2.37	100	0	0	115
IC2	9.18	2.01	99	0	1	108
ODA-alpha	10.65	1.97	100	0	0	107
ODA-beta	10.16	2.06	96	1	3	68
dDC1	16.38	3.93	97	3	0	115
dDC2	13.07	3.44	100	0	0	71
LC1	13.84	3.67	97	0	3	99
pDC1	13.83	4.76	99	0	1	122
IDA-alpha	10.36	3.18	23	76	1	92
IDA-beta	11.64	4.06	38	58	5	80
IDA5c	14.57	4.31	98	2	0	91
IDA5a	7.41	3.17	68	0	32	110
IDA5b	11.46	4.13	99	0	1	109
IDA4a	10.04	2.67	100	0	0	112
pf3	10.52	3.02	81	19	0	108
IDA4b	15.14	5.26	99	0	1	90
IDA3	14.14	3.96	99	0	1	116
PF16	11.07	4.00	67	33	0	106
RSP4/6_08	12.30	3.07	97	2	1	109
RSP4/6_13	15.76	3.58	100	0	0	102
NDRC4_34	9.92	3.18	75	24	1	112
NDRC_36	9.96	2.68	81	19	0	123
MBO2	10.52	3.08	44	54	1	68
CONTROL	14.36	3.97	99	1	0	112

4.2.2.3. *Mutant population displacement fitness*

We next assessed the population swim speed and directionality to investigate how cell displacement correlated with the observed flagellar morphologies and waveform preferences of the mutants. Raw motility measurements are summarised in Table 4-4.

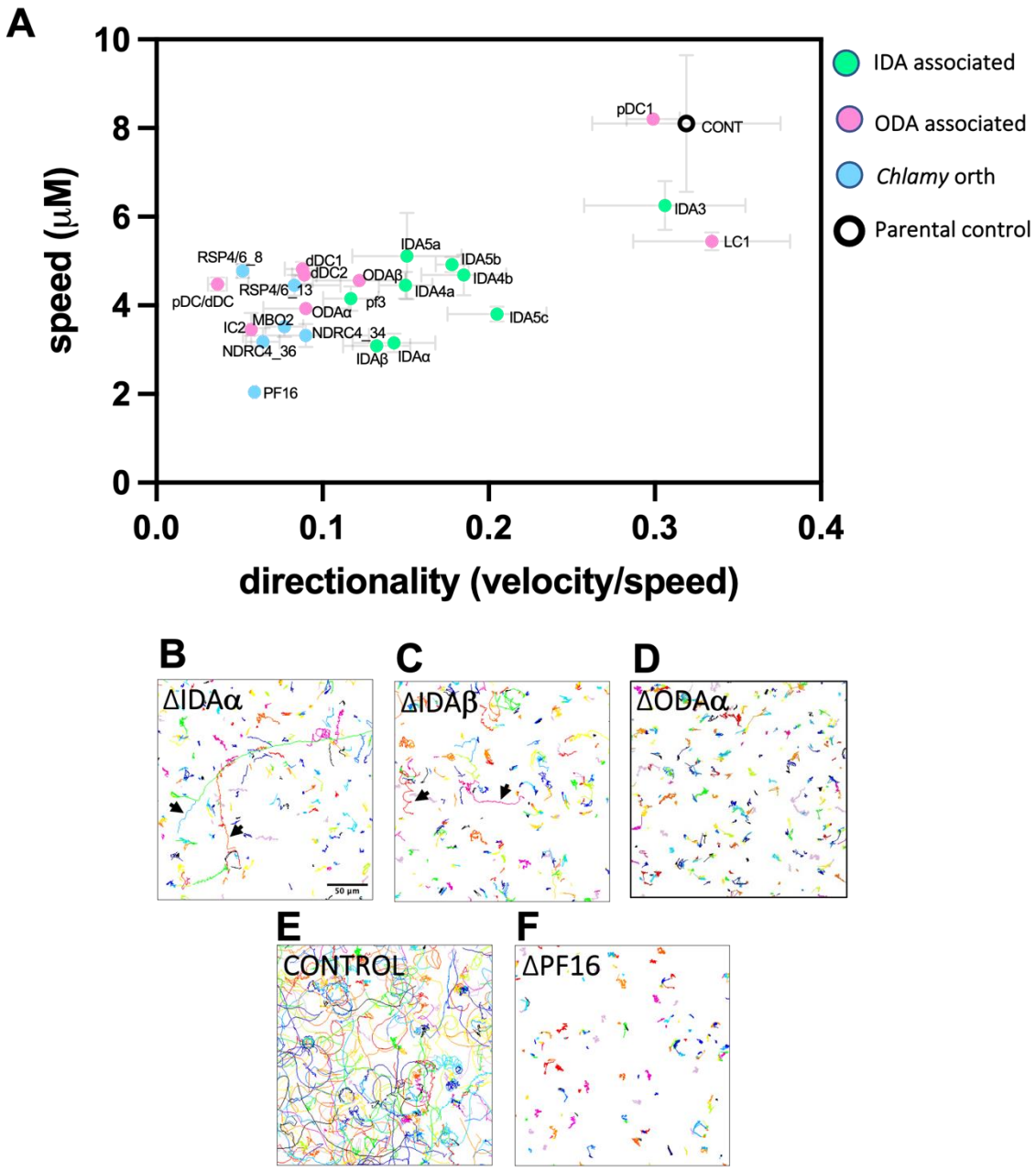


Figure legend on following page.

Figure 4-8: Population motility assay of DHC and dynein associated component.

Plot summarising the speed and directionality measurements gained from performing the motility assay on null mutant populations in parallel to parental controls. Raw measurements including the respective controls are listed in Table 4-4. Blue points are control mutants lacking core axonemal structures known to be essential for coordinated motility. Pink points are ODA associated mutants. Mint points are IDA associated mutants. Each point represents the average of three replicates. Data point represents the mean from three triplicate measurements, whilst the error bars represent standard deviation. (B-F) Individual swim tracks of ΔIDAα, ΔIDAβ, ΔODAα, parental control and paralysed negative control ΔPF16 respectively. Black arrows highlight coordinated displacement by a small minority of the ΔIDAα and ΔIDAβ mutant populations. Scale bar represents 50 µm.

Table 4-4: Population motility measurements.

Measurements were performed in three different labs (Oxford, Sir William Dunn School of Pathology (DUNN), Oxford, Peter Medawar Building (PMD) and Glasgow) by two different researchers (Sophia Fochler (SF) or Cecile Fort (CF)). Since variations were noted in the mean speed of the parental controls between locations, the measurements are shown here grouped by location. The table shows for each mutant three independent measurements of swim speeds and the average of the triplicates (Av S), three measurements of directionality (velocity/speed) and the average directionality (Av D). p-value S (speed) and p-value D (directionality) were calculated using a Students unpaired t-test assuming equal variance.

(i)

OXFORD DUNN SF	speed (µm/s)			Av S	directionality			Av D	p-value S	p-value D
RSP4/6_08	4.88	4.60	4.87	4.78	0.05	0.05	0.06	0.05	0.011	0.001
RSP4/6_13	4.62	4.19	4.55	4.45	0.11	0.08	0.06	0.08	0.012	0.006
N-DRC4_36	3.53	2.96	3.04	3.18	0.08	0.06	0.06	0.06	0.007	0.001
IDAβ	3.11	3.08	3.08	3.09	0.16	0.12	0.12	0.13	0.001	0.007
LC pf3 p28	4.36	4.26	3.84	4.15	0.13	0.12	0.10	0.12	0.008	0.002
ODAα	3.90	3.97	3.92	3.93	0.12	0.08	0.07	0.09	0.002	0.006
IDA5b	4.92	4.76	5.09	4.92	0.18	0.17	0.19	0.18	0.010	0.010
IDA3	6.79	6.28	5.69	6.25	0.36	0.30	0.26	0.31	0.347	0.402
IDA4a	4.43	4.77	4.17	4.46	0.15	0.16	0.13	0.15	0.006	0.001
IDA5c	3.95	3.84	3.61	3.80	0.23	0.18	0.20	0.20	0.005	0.064
dDC2	4.91	4.51	4.65	4.69	0.10	0.09	0.08	0.09	0.014	0.000
MBO2	3.65	3.24	3.66	3.52	0.08	0.06	0.08	0.08	0.006	0.003
IDAα	3.39	3.08	2.98	3.15	0.16	0.11	0.16	0.14	0.005	0.018
N-DRC4_34	3.62	3.22	3.13	3.32	0.13	0.07	0.07	0.09	0.006	0.013
CONTROL	6.51	6.95	6.81	6.76	0.28	0.29	0.27	0.28		

(ii)

GLASGOW SF	speed (µm/s)			Av S	directionality			Av D	p-value S	p-value D
IDA4b	4.73	4.21	5.12	4.69	0.20	0.16	0.20	0.18	0.003	0.008
IDA5a	6.20	4.32	4.82	5.11	0.19	0.13	0.13	0.15	0.141	0.021
CONTROL	7.03	7.02	7.71	7.25	0.37	0.29	0.33	0.33		

(iii)

OXFORD PMB SF	speed (µm/s)			Av S	directionality			Av D	p-value S	p-value D
ODAβ	4.55	4.49	4.65	4.56	0.10	0.12	0.15	0.12	0.010	0.029
IC2	3.63	3.02	3.71	3.45	0.06	0.06	0.05	0.06	0.009	0.000
CONTROL	11.10	9.39	9.62	10.04	0.44	0.35	0.35	0.38		

(iv)

OXFORD PMB CF	speed (µm/s)			Av S	directionality			Av D	p-value S	p-value D
pDC1	**8.11**	**8.21**	**8.30**	**8.21**	**0.28**	**0.30**	**0.32**	**0.30**	**0.073**	**0.064**
CONTROL	**10.05**	**9.22**	**9.08**	**9.45**	**0.36**	**0.35**	**0.35**	**0.35**		
pDC1/dDC2	*4.52*	*4.31*	*4.60*	*4.48*	*0.04*	*0.03*	*0.04*	*0.04*	*0.079*	*0.007*
CONTROL	*7.72*	*7.74*	*5.63*	*7.03*	*0.28*	*0.26*	*0.22*	*0.25*		

ODA mutant motility

Figure 4-8A clearly shows that most mutants of the ODA (pink data points) cluster with our motility defective controls (blue data points). Strikingly in the case of *ΔIC2* and *ΔpDC/dDC* double mutant, the change in directionality was as low as that of *ΔPF16* paralysed mutant (Figure 4-8). It has been shown that population speed and directionality tightly correlate in the majority of flagellar mutants (77). Our *ΔdDC*, *ΔODAα* and *ΔpDC/dDC* double mutant had disproportionately lower directionality measurements respective to their speed reduction, clustering with the *ΔRSP4/6, ΔNDRC4* and *ΔMBO2* motility control mutants (blue data points, Figure 4-8). Inspection of the cell tracks from *ΔODAα* confirmed that cells appeared as immotile in forward motility as the paralysed *ΔPF16* population. Interestingly, this population motility assay highlighted that *ΔpDC1* swam comparable to the parental controls, and *ΔLC1* retained a normal population directionality, however had a significant reduction in population speed (Figure 4-8). So far, these observations suggest that the ODA is indispensable for forward motility and are largely more defective than the cohort of IDA mutants in directionality (compare pink and green data points, Figure 4-8A).

IDA mutant motility

Contrastingly, all of the IDA mutants, asides from *ΔIDA3*, showed proportional reductions in population speed and directionality (green data points in Figure 4-8A). *ΔIDA3* retained a normal population directionality, however a diminished speed. We saw that *Δpf3* had the lowest directionality and all IDA mutants demonstrated milder defects in directionality, but similar reductions in speed to our cohort of ODA and reference mutants (Figure 4-8).

It was apparent that the IDA double headed dyneins contributed the most to population motility out of all the IDA mutants, where *ΔIDAα* and *ΔIDAβ* demonstrated the lowest

population swim speed. This corroborated the POWA outcome where the flagellar wave is very rarely propagated, and flagellum movement is restricted by the flagellar curl present in > 60% of both *ΔIDAα* and *ΔIDAβ* populations (Figure 4-7B). Although IDA double headed dynein mutants are hindered by the structural phenomenon of flagellar curling (Table 4-3, Figure 4-6B, 6C and Figure 4-7B), it was noticed during population overview waveform analysis that in less than 0.5% of the population, a rapid rhythmic tip-to-base flagellar beat was being propagated in *ΔIDAα* mutants. Thus, we inspected individual cell motility tracks of *ΔIDAα* and *ΔIDAβ* mutant populations to identify whether this rarely propagated wave for forward motility amounted in effective cell displacement. Figure 4-8B, 8C demonstrate example cell tracks with directional cell displacement for *ΔIDAα* and *ΔIDAβ* populations, compared to the positive motile control population and the negative immotile control population *ΔPF16*.

As a whole so far, our observations suggest that loss of components within the IDA are less defective in motility relative to the loss of components within the ODA.

4.2.3. Flagellar waveform parameters

4.2.3.1. ODA deficiency causes reduced dominant beat frequency and elevated beat amplitude

For mutants which retained the capacity for the flagellar wave used for forward motility, we investigated whether the waveform parameters deviated from those reached by parental control cells. We used high speed video microscopy (HSVM), automated cell tracing and Fourier decomposition of the wave to compare the dominant frequency, angular amplitude and phase cycles(waves)/flagellum. Our parental control flagella reached an average of 26

Hz (range 17 – 32Hz), with 1.18 radians angular amplitude (~68 degrees) (Figure 4-9A). And of the nine parental control cells captured, the average flagellar length was 17.15 µm with 1.4 waves per flagellum (Figure 4-9B). These parameters were positively coupled with a Spearman's r of 0.67. The flagellar beating parameters of our parental control cells are in agreement to those described previously for *Leishmania* spp (58,60).

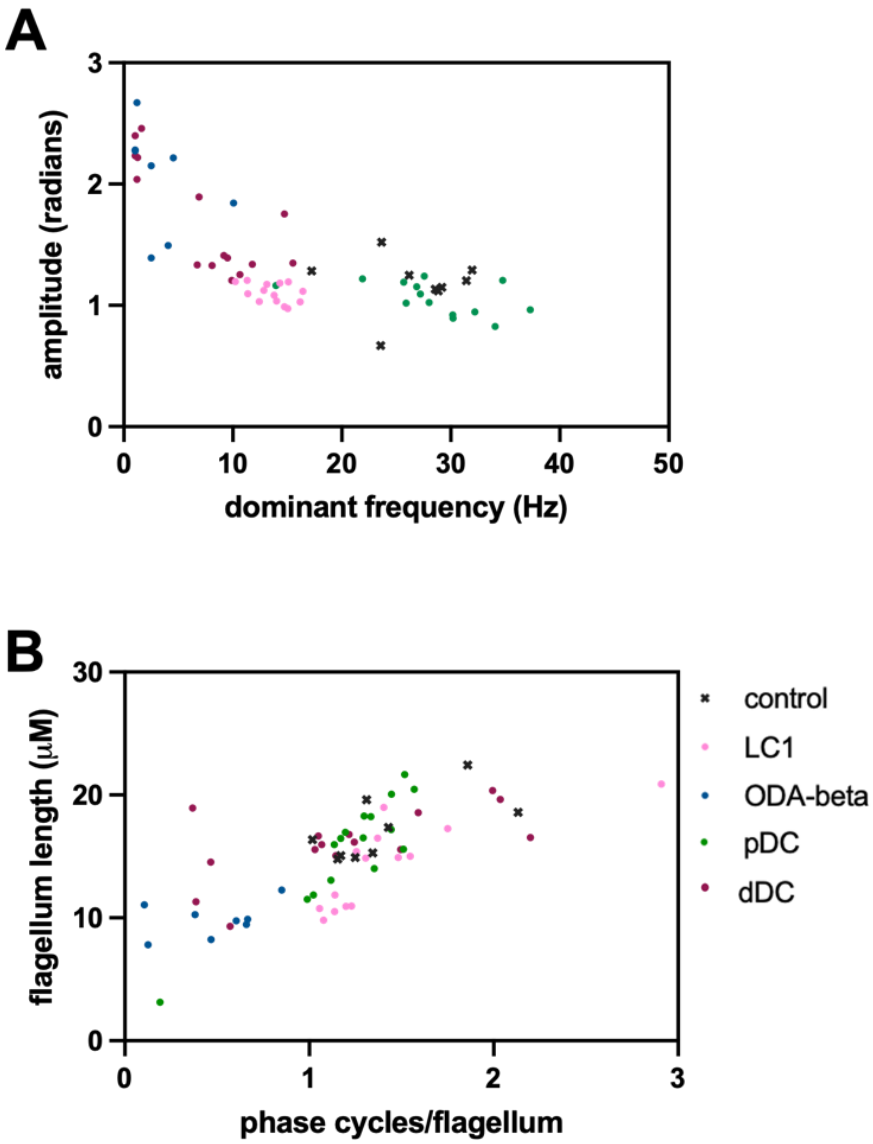


Figure 4-9: Fourier analysis of waveforms from ODA mutants.

(A) beat frequency (Hz) plotted against amplitude (radians) and (B) waves per flagellum plotted against flagellum length (µm) for ODA associated mutant cells. Each point represents 1 cell, where the waveform parameters are taken from an average of five phase cycles per

cell. The parental control datapoints are represented by black crosses. MATLAB was used to extract wave information by scripts written by Dr Ben J Walker.

As it is documented that *dDC1* and *dDC2* form an interdependent complex (46), we combined the datapoints from *ΔdDC1* and *ΔdDC2* cells under the label *ΔdDC* in Figure 4-9. In *ΔODAβ* and *ΔdDC* flagella, we saw a striking decrease in dominant beat frequency by less than half (ranging from 2-17 Hz), and an elevated beat amplitude to ~ 1.7 radians average (Figure 4-9A). The *ΔODAβ* cells were also unable to reach the normal 1-2 waves/flagellum where the flagella captured had much shorter flagella compared to control cells (Figure 4-9B). Interestingly, LC1 appeared to contribute specifically to reaching normal higher beat frequency (average 13.6 Hz), but not to amplitude (1.1 rad) or regulating waves per flagellum (1.4 w/f) (pink dataset in Figure 4-9A, 9B). Lastly, it appears the pDC machinery is dispensable for the propagation of a normal tip-to-base wave, however this may be explained by the finding that the dDC complex redistributes to the entire axoneme in pDC mutants (227). *ΔpDC* flagella beat with normal beat amplitude, frequency, and waves/flagella (Figure 4-9).

Table 4-5: Waveform parameters of mutant flagella.

Fourier decomposition of the flagellar waves for each of the listed gene deletion mutants (column 1). Measurements are shown for the dominant frequency and standard deviation (Dom Freq and StDev_Hz), angular amplitude plus standard deviation (Ang Amp and StDev_Ang Amp) in radians (rads), waves per flagellum and standard deviation (w/f and StDev_w/f), flagellum length in µm and standard deviation (F-length and StDev_F-length). The correlation between flagellar length and waves per flagellum (Fl : w/f) was determined by performing a Spearman's rank correlation (r). Lastly the number (n) of cells analysed for each mutant is indicated. Flagellar length measurements were done from the high magnification (X100) videos captured for waveform parameter extraction, independent of the length measurements reported in Table 4-3.

Mutant name	Dom Freq	StDev_Hz	Ang Amp (rad)	StDev_Ang Amp (rad)	w/f	StDev_w/f	F-length	StDev_F-length	Fl : w/f r	Cells (n)
LC1	13.64	1.79	1.10	0.08	1.42	0.45	14.19	3.34	0.88	15
ODAβ	2.70	2.49	2.04	0.43	0.48	0.27	9.84	1.44	0.24	8
pDC1	26.87	7.80	1.00	0.26	1.22	0.33	15.68	4.44	0.79	16
dDC	6.04	5.06	1.71	0.46	1.19	0.59	16.07	2.92	0.52	15
IDA3	21.02	14.12	0.95	0.06	1.68	0.35	15.57	3.20	0.67	9
IDA4a	25.29	10.94	1.13	0.47	0.94	0.45	14.37	1.92	0.77	7
IDA4b	28.97	6.37	0.96	0.15	1.19	0.37	14.42	3.31	0.92	10
IDA5a	28.76	3.79	1.14	0.16	0.99	0.21	11.62	2.57	0.95	11
IDA5b	25.53	5.33	0.98	0.35	1.64	0.46	16.84	3.79	0.38	12
IDA5c	13.66	7.81	1.30	0.20	1.17	0.48	15.43	4.38	0.34	12
p28	24.45	12.84	0.92	0.33	1.32	0.47	12.35	4.18	0.35	10
CONTROL	26.07	4.88	1.18	0.23	1.41	0.36	17.16	2.63	0.67	9

4.2.3.2. Single headed IDA dynein IDA5c contributes to beat frequency only, whilst IDA3, IDA4b and IDA5b contribute to angular amplitude only

Figure 4-10A shows that *ΔIDA5c* flagella had a diminished average beat frequency of 13.7 Hz (maximum 24.4 Hz), making it the only IDA DHC mutant that did not reach high beat

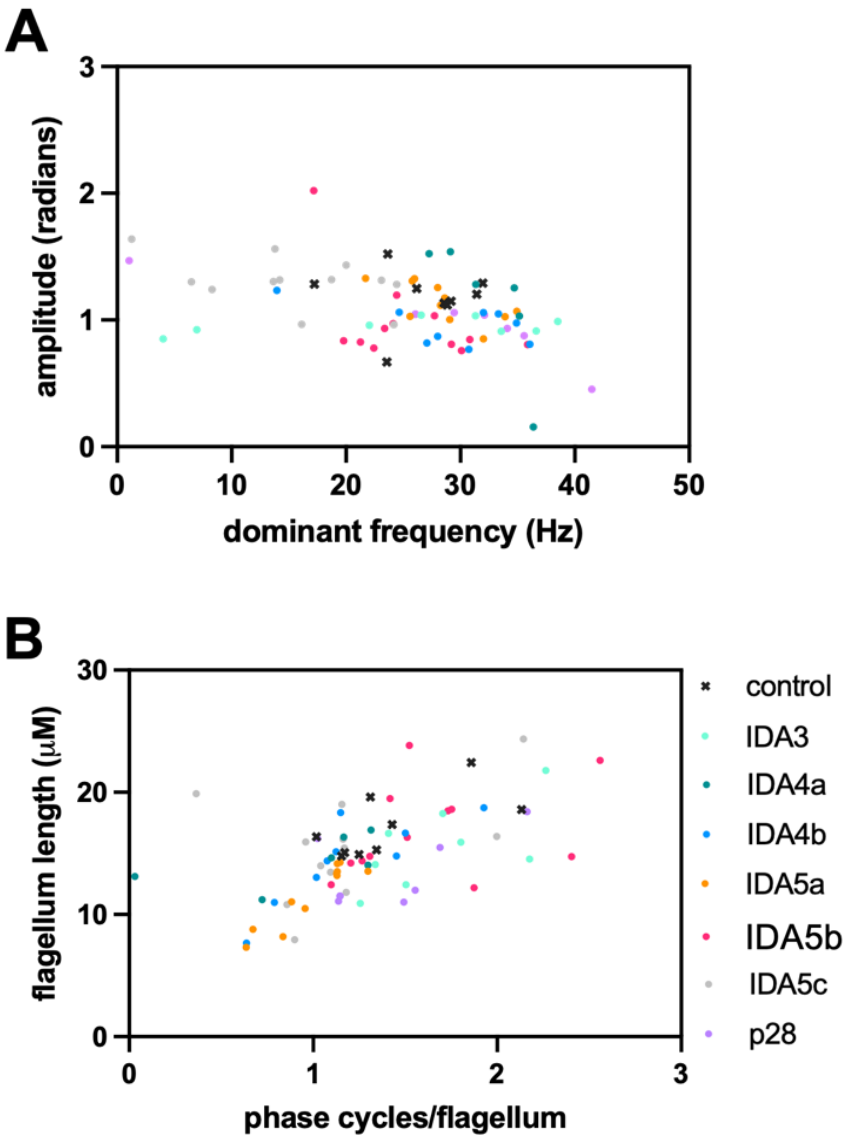


Figure 4-10: Fourier analysis of waveforms from IDA mutants.

(A) beat frequency (Hz) plotted against amplitude (radians) and (B) waves per flagellum plotted against flagellum length (μm) for IDA associated mutant cells. Each point represents 1 cell, where the waveform parameters are taken from an average of five beat cycles per cell. The parental control datapoints are represented by black crosses. Matlab was used to extract wave information by scripts written by Dr Ben J Walker.

frequencies, but it did retain a normal beat amplitude (1.3 rad) and waves per flagellum (1.2 w/f) (grey points Figure 4-10B). Moreover, we found that *ΔIDA3, ΔIDA4b* and *ΔIDA5b* had lower beat amplitudes (< 1 rad) but retained a normal beat frequency (20-30 Hz) (Figure 4-

10A, 10B). It is documented that the flagellar length, although highly variable in *Leishmania* spp., positively correlates with the waves per flagellum in wild type cells (58). We saw here that although *ΔIDA5a* cells had shorter flagella with fewer waves per flagellum (Figure 4-10B), the parameters were still tightly coupled (Spearman's correlation r = 0.95, Table 4-5). The *ΔIDA5a* flagella were also able to reach a normal beat frequency (28.7 Hz average) and amplitude (1.14 rad) (Figure 4-10A). The same could not be said for *ΔIDA5b* and *ΔIDA5c* which demonstrated a much weaker correlation (r = 0.38 and 0.34 respectively, Table 4-5) between flagellum length and waves/flagellum parameters, suggesting these two dyneins may contribute towards the coupling of these parameters.

Lastly, we saw that *ΔIDA4a* flagella beat with a normal frequency (25.3 Hz) and amplitude (1.13 rad) and correlating flagellum length and waves/flagellum (Spearman's r = 0.77, Table 4-5) (Figure 4-10A, 10B).

4.2.3.3. Rare propagation of rhythmic tip-to-base flagellar movement by ΔIDAα and ΔIDAβ cells when unhindered by flagellar curl

Although a rare event, we were able to capture one example cell for each *ΔIDAα* and *ΔIDAβ* with high magnification HSVM where Figure 4-11A show the video stills depicting the wave travelling from tip-to-base and the kymographs below demonstrate periodic beating for 1.28 seconds without interruption (Figure 4-11B). The *ΔIDAα* cell beat with 30.5 Hz with an amplitude of 0.86 rad, whilst the *ΔIDAβ* cell beat with 18.8 Hz and an amplitude of 0.86 rads (Figures 4-11B and 4-12).

Although a rare occurrence, it appears the IDA double headed dyneins are not necessarily required to propagate a normal tip-to-base symmetric wave, however it is apparent that

they are needed to maintain a mechanical or signalling balance within the axoneme, which, when disrupted, locks the flagellum in a tight curl.

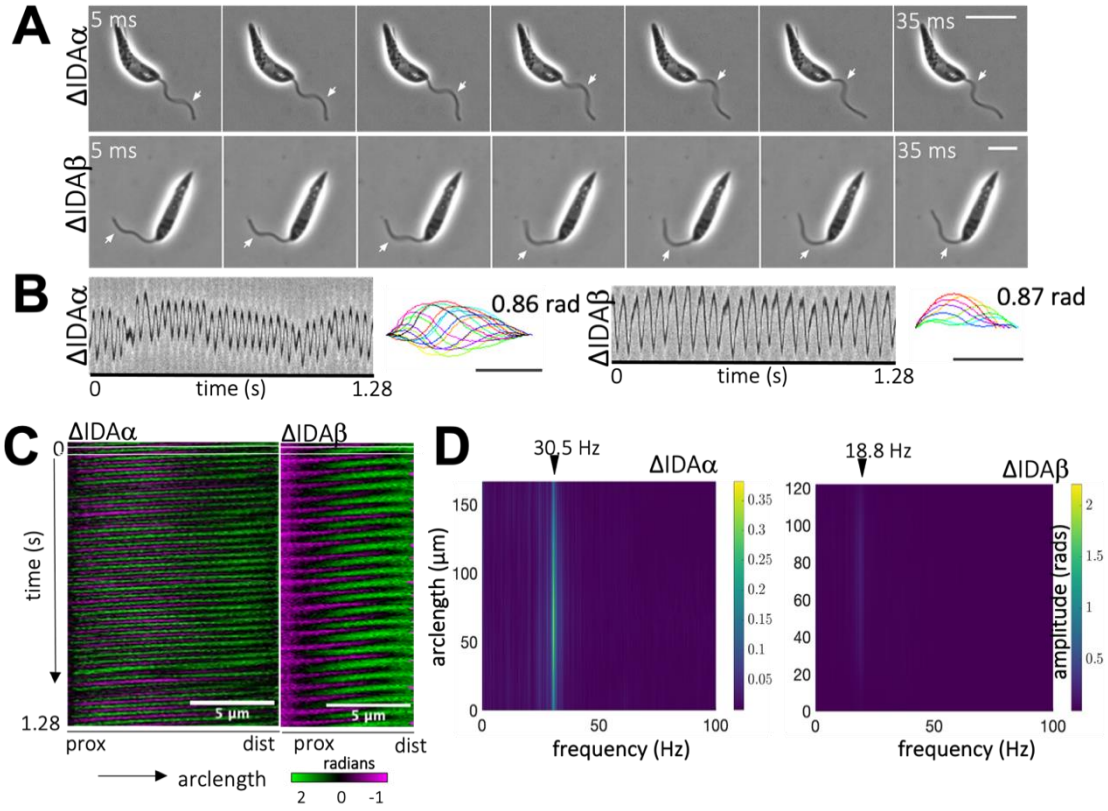


Figure 4-11: Rare flagellar wave of IDAalpha and IDAbeta.

High magnification high speed video microscopy capture of ΔIDAα and ΔIDAβ mutant cells propagating a rhythmic tip-to-base flagellar beat. (A) Still frames micrographs demonstrating movement of flagellar wave moving from tip-to-base with (B) complementary kymograph demonstrating a constant rhythmic beat for 1.28 seconds. Right of each kymograph is a computer-generated beat reconstruction of flagellum movement. The beat amplitude determined by Fourier analysis is displayed above the reconstructed beat. Scale bars represent 10 µm. (C) curvature kymograph of example cells propagating symmetric flagellar beat. White lines indicate where micrographs taken from in previous series. Green and pink colouration indicative of plus and minus wave, intensity representing amplitude in radians. Depth of colour proportional to amplitude in radians. Y-axis represents time in seconds. White lines indicate where the wave information was taken for beat reconstruction

displayed in Figure 4-11B. X-axis represent the arclength (distance along the flagellum). Scale bar represents 5 µm. (D) Fourier frequency spectrum of respective ΔIDAα and ΔIDAβ cells, black arrows highlighting the beat frequency (x-axis) along the arclength (flagellum length) in µm (y-axis).

4.3. Discussion

We combined targeted gene deletions and video capture of cells to address the long-standing question of how the outer and inner dynein arms contribute to flagellar motility, using *Leishmania* flagella as our model. Specifically, we assessed for a panel of dynein and non-dynein flagellar mutants the changes in population motility, the change in proportions of flagellar or ciliary waveforms propagated and the waveform parameters of the flagellar wave.

Contributions of the ODA dyneins

It is widely accepted that the ODA are required for reaching normal beat frequency, but are otherwise dispensable for wave formation (69,81). Firstly, we saw that ODA DHC mutants were equally as defective in population speed as the IDA DHC mutants, however ODA DHC displayed a larger decrease in directionality, and thus, clustered with our reference mutants lacking RSP4/6 and N-DRC (Figure 4-8). Moreover, we observed that the *ΔODAα* demonstrated a more pronounced motility phenotype than *ΔODAβ*. *ΔODAβ* mutants demonstrated an extremely diminished proportion of flagellar waveform, with only ~10% of flagella propagating a symmetric tip-to-base flagellar beat, compared to >40% of ΔODAβ flagella propagating a tip-to-base flagellar wave (Figure 4-5). As there are only two ODA DHC in *Trypanosoma* species (24), and EM/Cryo-EM work in *Chlamydomonas* describe a hierarchy between docking of the outermost dynein (ODAα) on the presence of the middle and inner dyneins (ODAβ and ODAγ respectively) (295–297), we hypothesise that this may explain the disparity between motility phenotypes of *ΔODAβ* and *ΔODAα*. In *Trypanosoma*

spp, ODAα is the innermost dynein. We can speculate that loss of ODAα resulted in a concomitant loss of *ODAβ* from the *L. mexicana* axoneme, and thus it makes sense for the ΔODAα phenotype to be more severe, with a lower proportion of coordinated flagellar beats compared to *ΔODAβ*, where remaining ODAα still contributes to flagellar movement. Given more time, it would be informative to express ΔODAα with a fluorescent tag and delete *ODAβ*, and *vice versa*, to test this hypothesis.

Combining this finding with the phenotype of the *ΔIC2* and *ΔpDC/dDC* double null mutant which had similar diminished propensities for forward motility (< 10% of flagella propagating a symmetric tip-to-base flagellar beat) to *ΔODAα,* we see that our data thus far points toward the ODA being an essential axonemal component for forward motility, contrasting to what is described in *Chlamydomonas* (69), but agreeing with findings in *T. brucei* (85,86). That said, when we assess the waveform parameters of ODA mutants which do retain an ability to propagate the flagellar wave *(i.e., ΔdDC, ΔLC1, ΔODAβ*), we see a decrease in beat frequency by about 50% (Figure 4-9A). This finding is consistent with the work described in *Chlamydomonas* (69) and sea urchin sperm (81) where full removal or partial removal of the ODA respectively, result in a halved beat frequencies. As the work from sea urchin only describe a partial removal of ODA apparatus (81), it remains to be answered whether the flagellar wave of sea urchin sperm can tolerate the complete loss of ODA, as we see here in *Leishmania*. Moreover, our work here corroborates more closely the phenotype described from the first *Chlamydomonas* ODA mutant characterised by Kamiya and Okamoto in 1985, which retains the asymmetric ciliary beat but its symmetric flagellar wave is abolished (84).

Our analysis interestingly highlighted a unique role for LC1. *ΔLC1* retained a normal beat amplitude however shared a similar reduction in beat frequency than *ΔdDC* and *ΔODAβ* cells (Figure 4-9A). This was unexpected, as it has been shown in *T. brucei*, that the ODA DHC

docking to the A-tubule is abolished in LC1 knockdown cell lines (86). If this was the case in *L. mexicana*, we would have expected the *ΔLC1* to phenocopy the *ΔpDC/dDC* double null or *ΔODAα* populations. Thus, we hypothesis that the LC1 protein, recently described to localise to the microtubule binding domain of the ODAγ in *Chlamydomonas* (ODAα in *L.mexicana*), is not required for the full assembly of ODA DHCs to the axoneme, but may reduce docking or reduce ODA DHC contribution to the rhythmic beat dynamics. As the recent published work describes a role for LC1 in weakening the interaction between ODA DHC and the adjacent microtubule, it is tempting to speculate that the ODAα DHC in *ΔLC1* flagellar axonemes bind the adjacent microtubules with too much strength, and this disrupts (perhaps slows) the bind-pull-release iteration where the release is slowed. However, much work would be needed to unpick this mechanistic detail. Lastly, we saw that mutants lacking the proximal and distal ODA docking complex, *ΔpDC/dDC,* retained the ability to propagate a ciliary beat agreeing with previous work (227). Follow up work to elucidate the knock-on effect of targeted removal of each of the axonemal DHCs will help us understand just how completely the ODA structure is removed in each of our mutant cell lines. Such techniques as EM visualisation, proteomics and reciprocal protein tag and deletion may be appropriate for this purpose.

From the experimental approaches used thus far, it appears overall that the *Leishmania* ODA are indeed required for reaching normal beat frequencies, where even removal of the associated light chain LC1 is enough to observe the halved beat frequency phenotype documented for *Chlamydomonas* (69) and sea urchin (81). However, in *Leishmania,* the ODA structure itself appears much more important for generation of a flagellar waveform than the 'dogma' would suggest, however appears dispensable for the ciliary beat.

Contributions of the IDA dyneins

According to the dogma for axonemal dynein contributions, it is thought that the IDA are essential for wave propagation and shape (69).

Our results suggest specific roles for the single headed dynein IDA5c in beat frequency, and IDA4b and IDA5b in beat amplitude. Additionally, several IDA mutants (*ΔIDA5b*, *ΔIDA5c*) exhibited an uncoupling of phase cycles per flagellum and flagellar length. However, all of the single-headed dynein mutants were observed to propagate a classical flagellar wave in a significant minority of the population, suggesting they are not essential for propagation of the flagellar wave. Most of the flagella of IDA double head dynein (*ΔIDA*α and *ΔIDA*β) mutants were hindered by high prevalence of flagellar curling (Figure 4-7B), a phenotype first described in *Leishmania* hydin mutants and further characterised in CP and IDA mutants { Tom Beneke PhD thesis}, yet still we found around 1% of the populations were able to propagate a tip-to-base rhythmic symmetric beat (Figure 4-6B, 6C) where cell swim tracks demonstrate occasional efficient forward displacement (Figure 4-13). We note that the curl event always occurs at the proximal flagellum, often leaving the distal flagellum to propagate a flagellar wave of normal beat frequency (Figures 4-12).

It is hard to know with these findings, whether the loss of a large structure around the IDA, or the removal of a core signalling domain are responsible for causing the curl phenomenon. It is possible that the curl is a consequence of dyneins being disproportionally dominant on one side (potentially locked on), however, if this was the case throughout the entire axoneme, we would see the entire flagellum participate in the curl. Instead, we only see a curl in the proximal half, suggesting that this region is particularly sensitive to the loss of the IDA structure.

Given more time, it would be worth exploring a targeted mutational approach for functional disruption of the IDA double headed dyneins, as opposed to whole gene deletion. If mutant flagella harbouring catalytically dead *ΔIDAα* or *ΔIDAβ* equally result in a proximal curl propensity, then we may be more certain that these DHCs specifically contribute to a pathway which switches opposing dyneins on/off appropriately. It may prove that the IDA double head dyneins partake in the recently described 'switch-inhibition' model for flagellar beat dynamics, where DHCs are demonstrated to exist mostly in the pre-power stroke conformation, *i.e*. primed and active, however DHC-microtubule binding is inhibited by spatial restriction in a bend dependent manner. Loss of the IDA may result in aberrant spatially restricted inhibition and result in a dominantly locked bending conformation.

Strikingly, we made observations that IDA5a DHC is required for normal flagellar construction, where 30% of the mutant population did not poses a visible external flagellum (Figures 4-6A, 4-7B). However, where a flagellum was constructed and a flagellar wave propagated, Fourier analysis revealed normal wave amplitude and frequency, and an appropriately correlative phase cycle/flagellum for the shorter flagellar lengths reached in *ΔIDA5a* (Figure 4-10A, 10B). This potentially could be explained by the relationship unveiled between IDA5 and Centrin3 of *T. brucei* and *Tetrahymena* which are interdependently linked to the flagellar axoneme and proposed to communicate calcium signals to dynein activity (211,298). Although shorter or absent flagella have not been described in *T. brucei* Centrin3 knockdown mutants, variable flagella numbers have been described in *Chlamydomonas* centrin mutants (299). Alternatively, it may be plausible for IDA5a to be linked to the function of IFT dyneins, which are required for flagellum assembly (280).

Does CARP1 act through the ODA?

Chapter 2 concluded that there was one likely cAMP transducer in the axoneme of *Leishmania*, CARP1, which was required for reaching normal population motility speed and directionality. The flagellar wave of ΔCARP1 mutants demonstrated a significantly lower beat frequency, with a normal beat amplitude. We showed that axonemal localisation of CARP1 was retained when we disrupted proteins of the radial spokes, central pair, outer dynein arms or dynein regulatory complex/IDA, indicating CARP1 could be associated with an axonemal structure we did not explore, such as the Microtubule Inner Protein (MIPs), or a minor structure of the axoneme which isn't yet fully described. Does CARP1 influence directly or indirectly the activity of dyneins? Does loss of CARP1 phenocopy any of the dynein mutants? From assessing the contribution of axonemal dyneins to the flagellar wave formation, we summarise that these data alone do not answer the question whether CARP1 is acting to modulate activity of the inner or outer dynein arms. A hypothesis that remains to be tested is the possible localisation of CARP1 to the outer microtubule lumen where it could act to influence the dynein activity through the protofilaments, as described already for interactions of MIPs with the IDA and ODA apparatus (38,235). In the future, finding the precise localisation of CARP1 within the flagellar axoneme will be key to integrating two main threads of the PhD project, namely how individual dyneins modulate the flagellar waveforms and how their activities are regulated by incoming signals that ultimately determine the cell's response to environmental cues.

5. Materials and Methods

5.1. Cell culturing, mutant production and genotype verification

5.1.1. Cell culturing

A *Leishmania mexicana* (WHO strain MNYC/BZ/62/M379) cell line expressing Cas9 and T7 RNA polymerase (221) was used as a parental cell line throughout this thesis unless stated otherwise. Promastigote form cells were cultured exactly as described in (221). In brief, cells were incubated at 28 ^{o}C and maintained in M199 (Life Technologies) medium supplemented with 2.2 g/L sodium bicarbonate between $1x10^5$ and $2x10^7$ cells/ml with regular sub-culturing.

Gene knockouts and cell lines expressing endogenously fused fluorescent gene products were essentially created as outlined by Beneke *et al*., (221). An online resource for automated primer design (www.LeishGEdit.net) was used to obtain primer sequences for the replacement of target gene ORFs with drug resistance cassettes (pT plasmids used to create donor products) or insertion of either mCherry or mNeonGreen (pPLOT plasmids used to create donor products) to the endogenous gene locus (221). Promastigote populations transfected with DNA donor and guide constructs were maintained in M199 medium supplemented with relevant selection drugs (either 20 µg/ml puromycin, 5 µg/ml Blasticidin or 40 µg/ml G418) for 3 culture passages before performing a PCR based knockout verification.

5.1.2. PCR based gene knockout validation

Primers used to confirm the absence of the target open reading frame (ORF) were designed by LeishGEdit and sourced from ThermoFisher. PCR amplifications using ORF Forward/Reverse (F/R) primers targeting (a) the GOI on parental genomic DNA were run alongside (b) genomic DNA from the knockout mutant. A positive control PCR reaction was run in parallel, whereby (c) PCR amplification targeting a fragment within the IFT88 or PF16 ORF was used as a DNA quality control performed on the genomic DNA of mutant cell lines. Master mixes for the PCR reactions constituted the FastGene Optima HotStart Ready Mix sourced from Nippon Genetics containing either (a) 4 ng/µl parental control gDNA with 2.5 µM ORF F/R primers targeting the GOI (final concentration) (b) 4 ng/µl mutant cell line gDNA with 2.5 µM ORF F/R primers targeting the GOI or (c) 4 ng/µl mutant cell line gDNA with 2.5 µM ORF F/R primers targeting a housekeeping gene, according to the reactions listed above. For all diagnostic PCRs, the following PCR program steps were used. Step 1: First denaturation at 95 ^{o}C for 3 minutes. Step 2: denaturation at 95 ^{o}C for 15 seconds. Step 3: 58 ^{o}C for 15 seconds. Step 4: 72 ^{o}C for 30 seconds. Step 5: repeat steps 2-4 for 30 cycles. Step 6: 72 ^{o}C for 1 minute.

Where one drug resistance cassette was used to replace both target alleles, limiting dilution (*i.e.,* 1:10E6, 1:10E5 and 1:10E4 dilutions) of the transfected parasite population in the presence of drug selection pressure on 96-well plates was used to obtain the desired genotype. A clonal cell line was achieved if less than 5% of wells contained drug resistant parasites.

In some cases, bespoke ORF F/R primer design was needed where highly similar genes were targeted and ORF primer specificity was not sufficient. Table 5-1 summarises the genes and ORF primer sequences where the LeishGEdit database was not used.

Once the genotype had been verified by these methods, mutant cell lines were sub-cultured in the absence of drug selection pressure for the purposes of phenotypic observation.

Table 5-1: Bespoke primer design for knockout verification.

Column 1 lists the gene IDs, column 2 the given gene names plus ORF primer direction, forward (F) or reverse (R), and column 3 contains the primer sequences. Firstly, gene sequence similarity was assessed by performing a nucleotide sequence alignment using clustal (300). The least similar section of the gene open reading frames were input into Primer 3 (301) with the desired fragment length set to between 100 – 300 nucleotides. Primer positioning was checked using the Benchling software Benchling ([Biology Software]. (2022). Retrieved from https://benchling.com). Primer compatibility was always checked on parental genomic DNA in parallel to its use on target mutant genomic DNA.

GENE ID	GENE/ORF NAME	PRIMER	PRIMER SEQUENCE
LmxM.15.1480	PDE B2_F		atgggacatttaacggtcaagagagtgttc
LmxM.15.1480	PDE B2_R		gctgcgtggccagagatgctag
LmxM.15.1481	PDE B1_F		ggagaagtttggttgccgtgag
LmxM.15.1481	PDE B1_R		cggtggttctcgttctcctgat
LmxM.34.4010	PKAC1_F		tcattgggccaactcagcagc
LmxM.34.4010	PKAC1_R		catttggcgtgacagccccct
LmxM.34.3960	PKAC2_F		tggagccgaaacctgaggtggc
LmxM.34.3960	PKAC2_R		ccgcgtacactcgtcctcctgg

5.2. Microscopy

5.2.1. Fluorescence microscopy of live cells

For fluorescence microscopy, 1 ml of mid-logarithmic growth (between $1x10^6$ – $1x10^7$ cells/ml) culture was spun at 800 g for 5 minutes and the pellet resuspended in 100 µl of PBS and Hoechst 33342 (ThermoFischer) stock (at 10 mg/ml). A volume of 0.7 µl was spread onto a poly-lysine coated glass slide, bordered (~ 5 x 2 cm rectangle) with the hydrophobic fat pen (Dako pen). A glass coverslip, thickness 1 or 1.5 was used to cover the slide. Live cell imaging was typically done with a Zeiss Axioimager.Z2 microscope with a Hamamatsu ORCA-Flash4.0 camera, x63 oil objective lens with numerical aperture (NA) 1.4, and phase contrast illumination. Fluorescence channel was acquired with between 0.5 and 3 seconds of excitation depending on the brightness of the fluorescent signal.

5.2.2. Imaging axenic amastigotes

Axenic amastigotes were produced in either flasks (5 ml volume) or 24 well plates (2 ml volume) where 500 µl or 20 µl of mid-log promastigote culture was inoculated into a flask or well respectively, containing Schneider's Drosophila medium (Life Technologies) supplemented with 20% heat-inactivated foetal bovine serum (FBS) (Gibco) and adjusted to pH 5.5 with concentrated HCl. Cultures were incubated at 34 ^oC with 5% $CO_2$for 72 hours prior to imaging. 1 ml of sample culture was pelleted by centrifugation at 800 g for 5 minutes, pellet washed with PBS, spun again, then the washed pellet resuspended in 50 µl of PBS plus Hoechst 33342 (10 µg/ml). A volume of 20 µl was placed on the poly-lysine

coated glass slide and left inside a humid chamber for 10 minutes to settle. Excess liquid was gently removed by pipetting and the cover slide placed on top.

5.2.3. Cytoskeleton preparation in a tube

Promastigote cytoskeletons were prepared by washing between 1 – 5 ml (depending on the cell culture density assessed by eye) of mid-log cells with PBS once then resuspended the washed pellet in 100 µl (or 1 ml if > 15E7 cells are in the sample) PEME [100 mM Pipes, 2 mM EGTA, 1 mM MgSO4 and 100 nM EDTA] with 0.1% NP-40. Once homogenous and the solution turns clear, the sample is spun at 2 ^{o}C at 10,000 g for 5 minutes. Supernatant is removed and pellet is washed with PEME then resuspended finally in PEME or PBS with Hoechst. Where the fluorescent signal in the cytoskeletons is assessed in combination of pharmacological intervention, the drug is added at 1:1000 ratio (drug stocks made at 1000x final desired concentration at 1:1000 ratio) to the PEME used during the wash steps after cytoskeletons have been extracted. If the drug is dissolved in DMSO, then the control cytoskeletons have the respective amount of DMSO (0.1%) added to the same mixture.

5.2.4. Salt extraction of cytoskeletons settled on a slide

Firstly, 1 ml of mid-log promastigote culture was washed with PBS then resuspended in 100 µl PEME buffer and left to settle for 10 minutes on a glass slide bordered with Dako hydrophobic pen inside a humid chamber. Excess liquid was gently removed by pipetting, then the membrane extraction solution (PEME with 0.1% NP-40) was added to the slide and left for 10 minutes. The sample was washed by passing PEME solution over the

cytoskeletons several times. Cytoskeleton sample quality was confirmed by observing the slide under the light microscope at x40 magnification. If less than 20 cytoskeletons were in each field of view, the process would be repeated with a larger starting volume of cell culture to gain a more concentrated sample. Next, 100 µl of the desired salt solution was pipetted on top of the cytoskeleton samples and left inside a humid chamber for 5 minutes. The solution was washed off by passing over 1 ml PEME solution containing (10 µg/ml Hoechst 33342) three times. Excess liquid was tapped off and a coverslip added. The samples were then assessed by fluorescence microscopy. The same 2 second excitation time was used for all salt conditions, and ImageJ was used to standardise the min-max of the mNG fluorescence channel micrographs to 9000min – 30,000max to allow for slide-to-slide comparisons.

5.3. Waveform analysis

5.3.1. Population Overview Waveform analysis (POWA)

For POWA, 1 ml of promastigote cells in logarithmic growth ($1x10^6$ – $1x10^7$ cells/ml) was gently centrifuged for 5 minutes at 800 g. Between 600 – 900 µl supernatant was removed and the cells resuspended in the remaining 400 – 100 µl of M199 medium, effectively concentrating the cells. 1 µl of 1:100 bead mix (Sigma 79633 polystyrene microparticle beads (5 µm size) in M199 medium) was added to cell suspension and mixed gently until homogenous. 1 µl of cell sample was added to the centre of a glass microscope slide bordered by a Dako hydrophobic pen (~5 cm by 2 cm rectangle). A glass coverslip of 1.0 or 1.5 thickness bordered by a similar Dako hydrophobic pen rectangle was placed gently on

top of the sample slide, effectively creating a sealed chamber. Videos with phase contrast illumination were captured with an Andor Neo 5.5 camera at 200 frames/s for 0.5 seconds, using a x20 NA 0.3 objective lens on a Leica Inverted microscope. Manual categorisation of waveforms was performed in ImageJ or Fiji (302,303) for non-dividing cells only. Categories included flagellar wave tip-to-base (continuous and interrupted), ciliary asymmetric wave base to tip and uncoordinated which is neither flagellar nor ciliary. Phenotypes such as flagellar curling, flagellar length and absent flagella were also categorised from these videos.

5.3.2. High Speed Video Microscopy

Process of capturing videos for waveform analysis was exactly as above (Section 5.3.1), with the exception of using X63 NA 1.4 or X100 NA 1.4 oil immersion objectives and capturing videos for 5 seconds. Samples were never videoed after more than 10 minutes on the slide. Obtaining tangent angle kymographs from phase contrast video micrographs was done as previously described (61) with the addition of generating raw x y coordinates representing the positioning of cell body and flagellum over each video frame.

For the datasets presented in Chapters 2-3, waveform parameters were gained as follows. From the 5 second phase contrast videos captured of swimming cells (see above, Section 5.3.6), an automated cell tracing script named FlagellumBeatStats_Trace1_PhaseTrace_FAST.ijm (stored on the SS-GLuenz Glasgow University server space, can be provided upon request) was run in ImageJ, yielding a tangent kymograph, which was cropped to exclude the cell body and to a length of either 128 (0.64 seconds) frames or 256 (1.28 seconds) frames which were then saved as tiff files. As *Leishmania* cells can change their swimming behaviour several times during a 5 second

video, each datapoint on the plots present a unit of time (as above), where several datapoints (up to three) could derive from one cell. The fast Fourier transform (FFT) script is then run on the tangent kymograph which yields an FFT output. Finally, the PowerPlotter script is run on the FFT output, which determines all averages of amplitudes using power space, then squares the amplitude to obtain the power. The dominant beat frequency was obtained by determining the highest frequency peak from the FFT output, then capturing 10% tolerance either side of the peak. Data obtained from the Fourier analysis parameters were put into Excel and plotted using GraphPad Prism 9. Amplitude measurements along each flagellum were averaged and plotted against the dominant frequency.

For the dataset presented in Chapter 4, the x, y coordinates obtained from cell tracing was used as an input for an automated workflow in Matlab written by Dr Benjamin Walker. 200 interpolated sample points are analysed along each flagellum, where a cut-off for acceptable flagellum tracing was set at 90%. We compared the relationship between flagellum length (arc length) and waves per flagellum (phase cycles), as well as the beat frequency (as above) and angular amplitude, defined to be half the range of theta for each arclength over the data. Data plotted is extracted from five phase cycles of each flagellum analysed.

5.4. Growth curves

All cell densities were determined using the CASY counter (OMNI Life Science) with a viable cell cut-off pseudo-diameter of below 2 and over 10 µm. Initial cell culture densities were measured, then the appropriate cell culture volume was added to fresh M199 medium

(Section 5.1) (final volume 5ml) in triplicate flasks to achieve a starting cell culture density of either $1x10^5$ or $1x10^6$ cells/ml. Measurements were recorded post dilution, then once every 24 hours until the growth curve was concluded. Where the effect of a drug was being assessed, the M199 medium was supplemented with the desired drug at 1:1000 so that the solvent (water or DMSO) never exceeded 0.1% v/v. All media containing drugs were filter sterilised by filtration through a 0.2 µm filter.

5.5. Motility assay with pharmacological intervention

Motility assays were performed as described in (61) with one alteration. Where the acute effect of drugs on cell motility was being assessed, we incubated 1 ml of mid-log culture in a 1.5 ml Eppendorf tube with the desired drug added 1:1000 v/v for at least 30 minutes before performing the motility assay. Samples were kept in the 28 ^oC incubator and never assayed after more than 1 hour incubation.

5.6. Phylogenetic tree for the novel axonemal dynein (LmxM.27.2590)

A phylogenetic tree was calculated from the following protein sequences. Firstly, the full protein sequences were for all 13 dynein heavy chains (DHCs) listed in Table 4-1, collected from TriTrypDB (304). Protein sequences of dyneins from *Chlamydomonas* and *H. sapiens* were identified from published work (22,282,283) and retrieved from Genbank (305) and Uniprot (306) to add full-length amino acid sequences for 16 DHCs from *C. reinhardtii* (Tables5-2) and 15 DHCs from *H. sapiens* (Table 5-3) to our list. Cobalt (281,284) was used to create a multiple sequence alignment of these combined 44 protein sequences, to construct a Fast Minimum-Evolution phylogenetic tree with a max sequence difference of 0.85 and distance set as Kimura. The Newick file was opened in iTOL (285) for visualisation and figure creation.

Table 5-2: Accession numbers for Chlamydomonas DHCs used in the phylogenetic tree.

Column 1 contains the accession numbers for protein sequences sourced from Genbank, where column 2 lists the nomenclature established by (282). Other names for the DHCs are listed in column 3. Phylogenetic tree displayed in Figure 4-1.

Genbank accession	*Gene name (282)*	*Other names*
Q9SMH3.1	DHC1	IDAalpha_f
XP_1694660.1	DHC2	d
XP_1696272.1	DHC3	MINOR
EDP07657.1	DHC4	MINOR
XP_1699742.1	DHC5	b
XP_1700741.1	DHC6	a
XP_1692695.1	DHC7	g
XP_1692092.1	DHC8	e
BAE19786.3	DHC9	c

Q9MBF8.1	DHC10	IDAbeta_f
XP_1694047.1	DHC11	MINOR
EDP05194.1	DHC12	MINOR
Q39610.2	DHC13	ODAalpha
Q39565.1	DHC14	ODAbeta
Q39575.1	DHC15	ODAgamma
EDP05194.1	DHC12	MINOR

Table 5-3: Accession numbers for H. sapiens DHCs used in the phylogenetic tree.

Columns 1 and 2 summarise the Genbank accession numbers and nomenclature established by (283), respectively, for the 15 DHCs identified using searches outlined in Section 5.6 above. Phylogenetic tree displayed in Figure 4-1.

Genbank accession	*Gene name*
Q9P2D7	DNAH1
Q9P225	DNAH2
Q8TD57	DNAH3
Q8TE73	DNAH5
Q9C0G6	DNAH6
Q8WXX0	DNAH7
Q96JB1	DNAH8
Q9NYC9	DNAH9
Q8IVF4	DNAH10
Q96DT5	DNAH11
E9PG32	DNAH12
Q0VDD8	DNAH14
Q9UFH2	DNAH17
Q14204	DYNC1H1
Q8NCM8	DYNC2H1

5.7. Homology modelling and ligand docking to assess CNBDs

Firstly, InterProScan (215) (https://www.ebi.ac.uk/interpro/search/sequence/) was used to define the protein sequences of cyclic nucleotide binding domains (CNBDs) in the analysed proteins. Next, the sequences were put into SWISS-MODEL (307) (https://swissmodel.expasy.org/interactive) and the best template selected on the highest

QMEANDisCo score (308). The resulting PyMOL files were uploaded to Swiss Dock (309,310) (http://www.swissdock.ch/) along with the cAMP molecule sourced from the ZINC upload feature in Swiss Dock. From the output of Swiss Dock, the position with the lowest Delta G or the position closest to the binding pocket (according to a reference panel of proteins co-crystalised with a cAMP molecule, see Chapter 2; Section 2.2.1.1, Figure 2-3) were chosen to display. This was done by editing the cluster.dock4.pdb PyMOL output file to only include the desired cAMP docking position. Adapted cluster.dock4.pdb files were opened alongside the homology modelled target protein in PyMOL to assess predicted hydrogen bond formation. Final figures were achieved in PyMOL by labelling residues, aligning different protein structures, and colouring protein sequences as desired.

6. References

1. Satir P. Studies on cilia. 3. Further studies on the cilium tip and a 'sliding filament' model of ciliary motility. J Cell Biol. 1968 Oct;39(1):77–94.

2. Brokaw CJ. Bend Propagation by a Sliding Filament Model for Flagella. Journal of Experimental Biology. 1971 Oct 1;55(2):289–304.

3. Lin J, Nicastro D. Asymmetric distribution and spatial switching of dynein activity generates ciliary motility. Science. 2018 Apr 27;360(6387):eaar1968.

4. Bardy SL, Ng SYM, Jarrell KFY. Prokaryotic motility structures. Microbiology. 2003;149(2):295–304.

5. Soh AWJ, Pearson CG. Ciliate cortical organization and dynamics for cell motility: Comparing ciliates and vertebrates. Journal of Eukaryotic Microbiology. 2022;69(5):e12880.

6. Pettitt ME, Orme BAA, Blake JR, Leadbeater BSC. The hydrodynamics of filter feeding in choanoflagellates. European Journal of Protistology. 2002 Jan;38(4):313–32.

7. Kosaki K, Casey B. Genetics of human left-right axis malformations. Semin Cell Dev Biol. 1998 Feb;9(1):89–99.

8. Bustamante-Marin XM, Ostrowski LE. Cilia and Mucociliary Clearance. Cold Spring Harb Perspect Biol. 2017 Jan 4;9(4):a028241.

9. Kumar V, Umair Z, Kumar S, Goutam RS, Park S, Kim J. The regulatory roles of motile cilia in CSF circulation and hydrocephalus. Fluids and Barriers of the CNS. 2021 Jul 7;18(1):31.

10. Russo A, Burdette JE. Isolation of Fallopian Tube Epithelium for Assessment of Cilia Beating Frequency (CBF). Methods Mol Biol. 2022;2424:179-187. doi: 10.1007/978-1-0716-1956-8_12.

11. Teves ME, Guidobaldi HA, Uñates DR, Sanchez R, Miska W, Publicover SJ, et al. Molecular Mechanism for Human Sperm Chemotaxis Mediated by Progesterone. PLoS One. 2009 Dec 8;4(12):e8211.

12. Beneke T, Demay F, Hookway E, Ashman N, Jeffery H, Smith J, et al. Genetic dissection of a Leishmania flagellar proteome demonstrates requirement for directional motility in sand fly infections. PLOS Pathogens. 2019 Jun 26;15(6):e1007828.

13. Pazour GJ, Agrin N, Leszyk J, Witman GB. Proteomic analysis of a eukaryotic cilium. J Cell Biol. 2005 Jul 4;170(1):103–13.

14. Subota I, Julkowska D, Vincensini L, Reeg N, Buisson J, Blisnick T, et al. Proteomic Analysis of Intact Flagella of Procyclic Trypanosoma brucei Cells Identifies Novel Flagellar Proteins with Unique Sub-localization and Dynamics. Mol Cell Proteomics. 2014 Jul;13(7):1769–86.

15. Nakachi M, Nakajima A, Nomura M, Yonezawa K, Ueno K, Endo T, et al. Proteomic profiling reveals compartment-specific, novel functions of ascidian sperm proteins. Molecular Reproduction and Development. 2011;78(7):529–49.

16. Lindemann CB, Lesich KA. Flagellar and ciliary beating: the proven and the possible. J Cell Sci. 2010 Feb 15;123(4):519–28.

17. Ishikawa H, Marshall WF. Intraflagellar Transport and Ciliary Dynamics. Cold Spring Harb Perspect Biol. 2017 Jan 3;9(3):a021998.

18. Lechtreck KF. IFT-cargo interactions and protein transport in cilia. Trends Biochem Sci. 2015 Dec;40(12):765–78.

19. Wang W, Jack BM, Wang HH, Kavanaugh MA, Maser RL, Tran PV. Intraflagellar Transport Proteins as Regulators of Primary Cilia Length. Frontiers in Cell and Developmental Biology. 2021;9:1064.

20. Dai D, Ichikawa M, Peri K, Rebinsky R, Huy Bui K. Identification and mapping of central pair proteins by proteomic analysis. Biophys Physicobiol. 2020 Jun 16;17:71-85.

21. Gui M, Ma M, Sze-Tu E, Wang X, Koh F, Zhong ED, et al. Structures of radial spokes and associated complexes important for ciliary motility. Nat Struct Mol Biol. 2021 Jan;28(1):29–37.

22. Wickstead B, Gull K. Dyneins Across Eukaryotes: A Comparative Genomic Analysis. Traffic. 2007 Dec;8(12):1708–21.

23. Woolley DM. Studies on the eel sperm flagellum. I. The structure of the inner dynein arm complex. Journal of Cell Science. 1997 Jan 1;110(1):85–94.

24. Imhof S, Zhang J, Wang H, Bui KH, Nguyen H, Atanasov I, et al. Cryo electron tomography with volta phase plate reveals novel structural foundations of the 96-nm axonemal repeat in the pathogen Trypanosoma brucei. Carter AP, Kuriyan J, Engel BD, Morriswood B, editors. eLife. 2019 Nov 11;8:e52058.

25. Inaba K. Calcium sensors of ciliary outer arm dynein: functions and phylogenetic considerations for eukaryotic evolution. Cilia. 2015 Apr 30;4(1):6.

26. Rao Q, Han L, Wang Y, Chai P, Kuo Y wei, Yang R, et al. Structures of outer-arm dynein array on microtubule doublet reveal a motor coordination mechanism. Nat Struct Mol Biol. 2021 Oct;28(10):799–810.

27. Ma M, Stoyanova M, Rademacher G, Dutcher SK, Brown A, Zhang R. Structure of the Decorated Ciliary Doublet Microtubule. Cell. 2019 Oct;179(4):909-922.e12.

28. Dai D, Ichikawa M, Peri K, Rebinsky R, Bui KH. 1 Identification and mapping of central pair proteins by proteomic 2 analysis. 2019;40.

29. Summers KE, Gibbons IR. Adenosine triphosphate-induced sliding of tubules in trypsin-treated flagella of sea-urchin sperm. Proc Natl Acad Sci U S A. 1971 Dec;68(12):3092–6.

30. Heuser T, Raytchev M, Krell J, Porter ME, Nicastro D. The dynein regulatory complex is the nexin link and a major regulatory node in cilia and flagella. J Cell Biol. 2009 Dec 14;187(6):921–33.

31. Gui L, Song K, Tritschler D, Bower R, Yan S, Dai A, et al. Scaffold subunits support associated subunit assembly in the Chlamydomonas ciliary nexin–dynein regulatory complex. PNAS. 2019 Nov 12;116(46):23152–62.

32. Walton T, Wu H, Brown A. Structure of a microtubule-bound axonemal dynein. Nat Commun. 2021 Jan 20;12(1):477.

33. Goodenough U, Heuser J. Structural comparison of purified dynein proteins with in situ dynein arms. J Mol Biol. 1984 Dec 25;180(4):1083–118.

34. Fabritius AS, Bayless BA, Li S, Stoddard D, Heydeck W, Ebmeier CC, et al. Proteomic analysis of microtubule inner proteins (MIPs) in Rib72 null Tetrahymena cells reveals functional MIPs. MBoC. 2021 Nov 1;32(21):br8.

35. Maheshwari A, Obbineni JM, Bui KH, Shibata K, Toyoshima YY, Ishikawa T. α- and β-Tubulin Lattice of the Axonemal Microtubule Doublet and Binding Proteins Revealed by Single Particle Cryo-Electron Microscopy and Tomography. Structure. 2015 Sep 1;23(9):1584–95.

36. Stoddard D, Zhao Y, Bayless BA, Gui L, Louka P, Dave D, et al. Tetrahymena RIB72A and RIB72B are microtubule inner proteins in the ciliary doublet microtubules. Mol Biol Cell. 2018 Oct 15;29(21):2566–77.

37. Miki-Noumura T, Kamiya R. Conformational change in the outer doublet microtubules from sea urchin sperm flagella. J Cell Biol. 1979 May;81(2):355–60.

38. Ichikawa M, Khalifa AAZ, Kubo S, Dai D, Basu K, Maghrebi MAF, et al. Tubulin lattice in cilia is in a stressed form regulated by microtubule inner proteins. PNAS. 2019 Oct 1;116(40):19930–8.

39. Kirima J, Oiwa K. Flagellar-associated Protein FAP85 Is a Microtubule Inner Protein That Stabilizes Microtubules. Cell Struct Funct. 2018 Feb 16;43(1):1–14.

40. Portman N, Gull K. The paraflagellar rod of kinetoplastid parasites: From structure to components and function. Int J Parasitol. 2010 Feb;40(2):135–48.

41. Broadhead R, Dawe HR, Farr H, Griffiths S, Hart SR, Portman N, et al. Flagellar motility is required for the viability of the bloodstream trypanosome. Nature. 2006 Mar;440(7081):224–7.

42. Santrich C, Moore L, Sherwin T, Bastin P, Brokaw C, Gull K, et al. A motility function for the paraflagellar rod of Leishmania parasites revealed by PFR-2 gene knockouts. Molecular and Biochemical Parasitology. 1997 Dec 1;90(1):95–109.

43. Maga JA, Sherwin T, Francis S, Gull K, LeBowitz JH. Genetic dissection of the Leishmania paraflagellar rod, a unique flagellar cytoskeleton structure. J Cell Sci. 1999 Aug;112 (Pt 16):2753–63.

44. Samsel Z, Sekretarska J, Osinka A, Wloga D, Joachimiak E. Central Apparatus, the Molecular Kickstarter of Ciliary and Flagellar Nanomachines. International Journal of Molecular Sciences. 2021 Jan;22(6):3013.

45. Smith EF, Yang P. The Radial Spokes and Central Apparatus: Mechano-Chemical Transducers That Regulate Flagellar Motility. Cell Motil Cytoskeleton. 2004 Jan;57(1):8–17.

46. Edwards BFL, Wheeler RJ, Barker AR, Moreira-Leite FF, Gull K, Sunter JD. Direction of flagellum beat propagation is controlled by proximal/distal outer dynein arm asymmetry. PNAS. 2018 Jul 31;115(31):E7341–50.

47. Geyer VF, Sartori P, Friedrich BM, Jülicher F, Howard J. Independent Control of the Static and Dynamic Components of the Chlamydomonas Flagellar Beat. Current Biology. 2016 Apr 25;26(8):1098–103.

48. Satir P, Heuser T, Sale WS. A Structural Basis for How Motile Cilia Beat. Bioscience. 2014 Dec 1;64(12):1073–83.

49. Nakajima M, Iizuka K, Ueki N, Isu A, Yoshimura K, Nakagaki T, et al. Basis for the phototaxis sign reversal in the green alga Chlamydomonas reinhardtii studied by high-speed observation.
bioRxiv 2020.12.06.414052; doi: https://doi.org/10.1101/2020.12.06.414052 2020 [cited 2022 Sep 20].

50. Schmidt JA, Eckert R. Calcium couples flagellar reversal to photostimulation in Chlamydomonas reinhardtii. Nature. 1976 Aug;262(5570):713–5.

51. Berthold P, Tsunoda SP, Ernst OP, Mages W, Gradmann D, Hegemann P. Channelrhodopsin-1 Initiates Phototaxis and Photophobic Responses in Chlamydomonas by Immediate Light-Induced Depolarization. The Plant Cell. 2008 Jun 1;20(6):1665–77.

52. Brokaw CJ, Luck DJL. Bending patterns of chlamydomonas flagella I. Wild-type bending patterns. Cell Motility. 1983;3(2):131–50.

53. Puga Molina LC, Luque GM, Balestrini PA, Marín-Briggiler CI, Romarowski A, Buffone MG. Molecular Basis of Human Sperm Capacitation. Frontiers in Cell and Developmental Biology. 2018;6:72.

54. Suarez S, Ho HC. Hyperactivated Motility in Sperm. Reproduction in Domestic Animals. 2003;38(2):119–24.

55. Torrezan-Nitao E, Guidobaldi H, Giojalas L, Barratt C, Publicover S. Behavioural switching during oscillations of intracellular Ca2+ concentration in free-swimming human sperm. Reproduction and Fertility. 2021 Mar 9;2(1):L5–7.

56. Makin L, Gluenz E. cAMP signalling in trypanosomatids: role in pathogenesis and as a drug target. Trends Parasitol. 2015 Aug;31(8):373–9.

57. Shaw S, DeMarco SF, Rehmann R, Wenzler T, Florini F, Roditi I, et al. Flagellar cAMP signaling controls trypanosome progression through host tissues. Nat Commun. 2019 Feb 18;10(1):803.

58. Gadelha C, Wickstead B, Gull K. Flagellar and ciliary beating in trypanosome motility. Cell Motility. 2007;64(8):629–43.

59. Mukhopadhyay AG, Dey CS. Reactivation of flagellar motility in demembranated Leishmania reveals role of cAMP in flagellar wave reversal to ciliary waveform. Scientific Reports. 2016 Nov 16;6(1):37308.

60. Walker BJ, Wheeler RJ, Ishimoto K, Gaffney EA. Boundary behaviours of Leishmania mexicana: A hydrodynamic simulation study. Journal of Theoretical Biology. 2019 Feb;462:311–20.

61. Wheeler RJ. Use of chiral cell shape to ensure highly directional swimming in trypanosomes. PLOS Computational Biology. 2017 Jan 31;13(1):e1005353.

62. Wang Z, Beneke T, Gluenz E, Wheeler RJ. The single flagellum of Leishmania has a fixed polarisation of its asymmetric beat. J Cell Sci. 2020 Oct 22;133(20):jcs246637.

63. Gui M, Farley H, Anujan P, Anderson JR, Maxwell DW, Whitchurch JB, et al. De novo identification of mammalian ciliary motility proteins using cryo-EM. Cell. 2021 Nov 11;184(23):5791-5806.e19.

64. Dutta M, Jana B. Role of AAA3 Domain in Allosteric Communication of Dynein Motor Proteins. ACS Omega. 2019 Dec 3;4(26):21921-21930.

65. Carter AP. Crystal clear insights into how the dynein motor moves. Journal of Cell Science. 2013 Feb 1;126(3):705–13.

66. Cho C, Vale RD. The mechanism of dynein motility: Insight from crystal structures of the motor domain. Biochimica et Biophysica Acta (BBA) - Molecular Cell Research. 2012 Jan 1;1823(1):182–91.

67. Carter AP, Garbarino JE, Wilson-Kubalek EM, Shipley WE, Cho C, Milligan RA, et al. Structure and functional role of dynein's microtubule-binding domain. Science. 2008 Dec 12;322(5908):1691–5.

68. Roberts AJ, Numata N, Walker ML, Kato YS, Malkova B, Kon T, et al. AAA+ Ring and Linker Swing Mechanism in the Dynein Motor. Cell. 2009 Feb 6;136(3):485–95.

69. Brokaw CJ, Kamiya R. Bending patterns of Chlamydomonas flagella: IV. Mutants with defects in inner and outer dynein arms indicate differences in dynein arm function. Cell Motility. 1987;8(1):68–75.

70. Brokaw CJ, Luck DJL. Bending patterns of Chlamydomonas flagella: III. A radial spoke head deficient mutant and a central pair deficient mutant. Cell Motility. 1985;5(3):195–208.

71. Rupp G, Porter ME. A subunit of the dynein regulatory complex in Chlamydomonas is a homologue of a growth arrest–specific gene product. J Cell Biol. 2003 Jul 7;162(1):47–57.

72. Mutations in the 'dynein regulatory complex' alter the ATP-insensitive binding sites for inner arm dyneins in Chlamydomonas axonemes. J Cell Biol. 1994 Jun 1;125(5):1109–17.

73. Patel-King RS, King SM. An outer arm dynein light chain acts in a conformational switch for flagellar motility. Journal of Cell Biology. 2009 Jul 27;186(2):283–95.

74. Yamamoto R, Obbineni JM, Alford LM, Ide T, Owa M, Hwang J, et al. Chlamydomonas DYX1C1/PF23 is essential for axonemal assembly and proper morphology of inner dynein arms. PLOS Genetics. 2017 Sep 11;13(9):e1006996.

75. Huang B, Piperno G, Luck DJ. Paralyzed flagella mutants of Chlamydomonas reinhardtii. Defective for axonemal doublet microtubule arms. Journal of Biological Chemistry. 1979 Apr;254(8):3091–9.

76. Ralston KS, Lerner AG, Diener DR, Hill KL. Flagellar Motility Contributes to Cytokinesis in Trypanosoma brucei and Is Modulated by an Evolutionarily Conserved Dynein Regulatory System. Eukaryot Cell. 2006 Apr;5(4):696–711.

77. Beneke T, Demay F, Hookway E, Ashman N, Jeffery H, Smith J, et al. Genetic dissection of a Leishmania flagellar proteome demonstrates requirement for directional motility in sand fly infections. Hill KL, editor. PLoS Pathog. 2019 Jun 26;15(6):e1007828.

78. Sunter JD, Gull K. The Flagellum Attachment Zone: 'The Cellular Ruler' of Trypanosome Morphology. Trends Parasitol. 2016 Apr;32(4):309–24.

79. Halliday C, Billington K, Wang Z, Madden R, Dean S, Sunter JD, et al. Cellular landmarks of Trypanosoma brucei and Leishmania mexicana. Molecular and Biochemical Parasitology. 2019 Jun 1;230:24–36.

80. Walker BJ, Ishimoto K, Wheeler RJ. Automated identification of flagella from videomicroscopy via the medial axis transform. Scientific Reports. 2019 Mar 21;9(1):5015.

81. Gibbons BH, Gibbons IR. The Effect of Partial Extraction of Dynein Arms on the Movement of Reactivated Sea-Urchin Sperm. Journal of Cell Science. 1973 Sep 1;13(2):337–57.

82. Summers KE, Gibbons IR. Effects of trypsin digestion on flagellar structures and their relationship to motility. J Cell Biol. 1973 Sep;58(3):618–29.

83. Gibbons BH, Gibbons IR. The Effect Of Partial Extraction Of Dynein Arms On The Movement Of Reactivated Sea-Urchin Sperm. :22.

84. Kamiya R, Okamoto M. A Mutant Of Chlamydomonas Reinhardtii That Lacks The Flagellar Outer Dynein Arm But Can Swim. J Cell Sci. 1985;74:181–91.

85. Branche C, Kohl L, Toutirais G, Buisson J, Cosson J, Bastin P. Conserved and specific functions of axoneme components in trypanosome motility. Journal of Cell Science. 2006 Aug 15;119(16):3443–55.

86. Ralston KS, Kisalu NK, Hill KL. Structure-function analysis of dynein light chain 1 identifies viable motility mutants in bloodstream-form Trypanosoma brucei. Eukaryot Cell. 2011 Jul;10(7):884–94.

87. Lucas JS, Adam EC, Goggin PM, Jackson CL, Powles-Glover N, Patel SH, et al. Static respiratory cilia associated with mutations in Dnahc11/DNAH11: A mouse model of PCD. Human Mutation. 2012;33(3):495–503.

88. Satir P. STUDIES ON CILIA : II. Examination of the Distal Region of the Ciliary Shaft and the Role of the Filaments in Motility. J Cell Biol. 1965 Sep 1;26(3):805–34.

89. Brokaw CJ. Computer simulation of flagellar movement. VI. Simple curvature-controlled models are incompletely specified. Biophysical Journal. 1985 Oct;48(4):633–42.

90. Lindemann CB. A 'Geometric Clutch' Hypothesis to Explain Oscillations of the Axoneme of Cilia and Flagella. Journal of Theoretical Biology. 1994 May 21;168(2):175–89.

91. Lindemann CB. A model of flagellar and ciliary functioning which uses the forces transverse to the axoneme as the regulator of dynein activation. Cell Motil Cytoskeleton. 1994;29(2):141–54.

92. Lindemann CB. Testing the geometric clutch hypothesis. Biol Cell. 2004 Dec;96(9):681–90.

93. Cibert C, Heck JV. Geometry drives the 'deviated-bending' of the bi-tubular structures of the 9 + 2 axoneme in the flagellum. Cell Motil Cytoskeleton. 2004 Nov;59(3):153–68.

94. Omoto CK, Witman GB. Functionally significant central-pair rotation in a primitive eukaryotic flagellum. Nature. 1981 Apr 23;290(5808):708-10.

95. Omoto CK, Kung C. The pair of central tubules rotates during ciliary beat in Paramecium. Nature. 1979 Jun 7;279(5713):532-4.

96. Tamm SL, Tamm S. Ciliary reversal without rotation of axonemal structures in ctenophore comb plates. J Cell Biol. 1981 Jun;89(3):495–509.

97. Tamm SL, Horridge GA. The relation between the orientation of the central fibrils and the direction of beat in cilia of Opalina. Proceedings of the Royal Society of London Series B Biological Sciences. 1970 Aug 4;175(1040):219–33.

98. Gibbons IR. The relationship between the fine structure and direction of beat in gill cilia of a lamellibranch mollusc. J Biophys Biochem Cytol. 1961 Oct;11:179–205.

99. Wais-Steider J, Satir P. Effect of vanadate on gill cilia: Switching mechanism in ciliary beat. Journal of Supramolecular Structure. 1979;11(3):339–47.

100. Schmidt H, Carter AP. Review: Structure and mechanism of the dynein motor ATPase. Biopolymers. 2016 Aug;105(8):557–67.

101. Aoki F, Sakai S, Kohmoto K. Regulation of flagellar bending by cAMP and Ca2+ in hamster sperm. Molecular Reproduction and Development. 1999;53(1):77–83.

102. Kinukawa M, Oda S, Shirakura Y, Okabe M, Ohmuro J, Baba SA, et al. Roles of cAMP in regulating microtubule sliding and flagellar bending in demembranated hamster spermatozoa. FEBS Letters. 2006;580(5):1515–20.

103. Smith EF. Regulation of Flagellar Dynein by Calcium and a Role for an Axonemal Calmodulin and Calmodulin-dependent Kinase. Mol Biol Cell. 2002 Sep;13(9):3303–13.

104. Mukhopadhyay A, Dey C. Role of calmodulin and calcineurin in regulating flagellar motility and wave polarity in Leishmania. Parasitology research. 2017 Sep 7;116.

105. Stival C, Ritagliati C, Xu X, Gervasi MG, Luque GM, Graf CB, et al. Disruption of protein kinase A localization induces acrosomal exocytosis in capacitated mouse sperm. Journal of Biological Chemistry. 2018 Jun 15;293(24):9435–47.

106. Balbach M, Beckert V, Hansen JN, Wachten D. Shedding light on the role of cAMP in mammalian sperm physiology. Mol Cell Endocrinol. 2018 Jun 15;468:111–20.

107. Achikanu C, Correia J, Guidobaldi HA, Giojalas LC, Barratt CLR, Da Silva SM, et al. Continuous behavioural 'switching' in human spermatozoa and its regulation by Ca2+-mobilising stimuli. Molecular Human Reproduction. 2019 Aug 1;25(8):423–32.

108. King SM, Patel-King RS. Identification of a Ca(2+)-binding light chain within Chlamydomonas outer arm dynein. Journal of Cell Science. 1995 Dec 1;108(12):3757–64.

109. Ichikawa M, Bui KH. Microtubule Inner Proteins: A Meshwork of Luminal Proteins Stabilizing the Doublet Microtubule. BioEssays. 2018;40(3):1700209.

110. Mukhopadhyay AG, Dey CS. Reactivation of flagellar motility in demembranated Leishmania reveals role of cAMP in flagellar wave reversal to ciliary waveform. Sci Rep. 2016 16;6:37308.

111. Mukhopadhyay AG, Dey CS. Role of calmodulin and calcineurin in regulating flagellar motility and wave polarity in Leishmania. Parasitol Res. 2017 Nov 1;116(11):3221–8.

112. Brokaw CJ. Calcium-induced asymmetrical beating of triton-demembranated sea urchin sperm flagella. Journal of Cell Biology. 1979 Aug 1;82(2):401–11.

113. Kung C, Naito Y. Calcium-induced ciliary reversal in the extracted models of "Pawn", a behavioral mutant of Paramecium. Science. 1973 Jan 12;179(4069):195-6.

114. Iwadate Y. Photolysis of caged calcium in cilia induces ciliary reversal in Paramecium caudatum. Journal of Experimental Biology. 2003 Apr 1;206(7):1163–70.

115. Shiba K, Baba SA, Inoue T, Yoshida M. Ca2+ bursts occur around a local minimal concentration of attractant and trigger sperm chemotactic response. Proc Natl Acad Sci U S A. 2008 Dec 9;105(49):19312–7.

116. Mizuno K, Shiba K, Okai M, Takahashi Y, Shitaka Y, Oiwa K, et al. Calaxin drives sperm chemotaxis by Ca2+-mediated direct modulation of a dynein motor. Proc Natl Acad Sci U S A. 2012 Dec 11;109(50):20497–502.

117. Mizuno K, Padma P, Konno A, Satouh Y, Ogawa K, Inaba K. A novel neuronal calcium sensor family protein, calaxin, is a potential Ca2+-dependent regulator for the outer arm dynein of metazoan cilia and flagella. Biology of the Cell. 2009;101(2):91–103.

118. Schmid A, Bai G, Schmid N, Zaccolo M, Ostrowski LE, Conner GE, et al. Real-time analysis of cAMP-mediated regulation of ciliary motility in single primary human airway epithelial cells. Journal of Cell Science. 2006 Oct 15;119(20):4176–86.

119. Ma W, Silberberg SD, Priel Z. Distinct Axonemal Processes Underlie Spontaneous and Stimulated Airway Ciliary Activity. J Gen Physiol. 2002 Dec;120(6):875–85.

120. Hamasaki T, Barkalow K, Richmond J, Satir P. cAMP-stimulated phosphorylation of an axonemal polypeptide that copurifies with the 22S dynein arm regulates microtubule translocation velocity and swimming speed in Paramecium. Proc Natl Acad Sci U S A. 1991 Sep 15;88(18):7918–22.

121. Christensen ST, Guerra C, Wada Y, Valentin T, Angeletti RH, Satir P, et al. A Regulatory Light Chain of Ciliary Outer Arm Dynein inTetrahymena thermophila *. Journal of Biological Chemistry. 2001 Jan 1;276(23):20048–54.

122. Rall TW, Sutherland EW. Formation Of A Cyclic Adenine Ribonucleotide By Tissue Particles. Journal of Biological Chemistry. 1958 Jun;232(2):1065–76.

123. Berthet J, Rall TW, Sutherland EW. The relationship of epinephrine and glucagon to liver phosphorylase. IV. Effect of epinephrine and glucagon on the reactivation of phosphorylase in liver homogenates. J Biol Chem. 1957 Jan;224(1):463–75.

124. Walsh DA, Perkins JP, Krebs EG. An Adenosine 3′,5′-Monophosphate-dependant Protein Kinase from Rabbit Skeletal Muscle. Journal of Biological Chemistry. 1968 Jul;243(13):3763–5.

125. Berman HM, Eyck LFT, Goodsell DS, Haste NM, Kornev A, Taylor SS. The cAMP binding domain: An ancient signaling module. PNAS. 2005 Jan 4;102(1):45–50.

126. Salmon D. Adenylate Cyclases of Trypanosoma brucei, Environmental Sensors and Controllers of Host Innate Immune Response. Pathogens. 2018 Jun;7(2):48.

127. Naqvi S, Martin KJ, Arthur JSC. CREB phosphorylation at Ser133 regulates transcription via distinct mechanisms downstream of cAMP and MAPK signalling. Biochem J. 2014 Mar 15;458(3):469–79.

128. Zhang H, Kong Q, Wang J, Jiang Y, Hua H. Complex roles of cAMP–PKA–CREB signaling in cancer. Exp Hematol Oncol. 2020 Dec;9(1):32.

129. Sassone-Corsi P. The Cyclic AMP Pathway. Cold Spring Harb Perspect Biol. 2012 Dec;4(12):a011148.

130. Jackson PK. cAMP Signaling in Nanodomains. Cell. 2020 Sep 17;182(6):1379-1381.

131. Conti M, Mika D, Richter W. Cyclic AMP compartments and signaling specificity: Role of cyclic nucleotide phosphodiesterases. J Gen Physiol. 2014 Jan;143(1):29–38.

132. Dong A, Malecki JM, Lee L, Carpenter JF, Lee JC. Ligand-Induced Conformational and Structural Dynamics Changes in *Escherichia coli* Cyclic AMP Receptor Protein. Biochemistry. 2002 May 1;41(21):6660–7.

133. McKay DB, Steitz TA. Structure of catabolite gene activator protein at 2.9 A resolution suggests binding to left-handed B-DNA. Nature. 1981 Apr 30;290(5809):744–9.

134. Shabb JB, Ng L, Corbin JD. One amino acid change produces a high affinity cGMP-binding site in cAMP-dependent protein kinase. J Biol Chem. 1990 Sep 25;265(27):16031–4.

135. Shabb JB, Buzzeo BD, Ng L, Corbin JD. Mutating protein kinase cAMP-binding sites into cGMP-binding sites. Mechanism of cGMP selectivity. J Biol Chem. 1991 Dec 25;266(36):24320–6.

136. Fahmi T, Port GC, Cho KH. c-di-AMP: An Essential Molecule in the Signaling Pathways that Regulate the Viability and Virulence of Gram-Positive Bacteria. Genes (Basel). 2017 Aug 7;8(8):197.

137. Valentini M, Filloux A. Biofilms and Cyclic di-GMP (c-di-GMP) Signaling: Lessons from Pseudomonas aeruginosa and Other Bacteria. J Biol Chem. 2016 Jun 10;291(24):12547–55.

138. Sogin ML. Early evolution and the origin of eukaryotes. Current Opinion in Genetics & Development. 1991 Dec 1;1(4):457–63.

139. Tamaki H. Glucose-stimulated cAMP-protein kinase a pathway in yeast Saccharomyces cerevisiae. Journal of Bioscience and Bioengineering. 2007 Oct 1;104(4):245–50.

140. Kimmel AR, Parent CA. The Signal to Move: D. discoideum Go Orienteering. Science. 2003 Jun 6;300(5625):1525–7.

141. Tagoe D, Kalejaiye T, De Koning H. The ever unfolding story of cAMP signaling in trypanosomatids: vive la difference! Frontiers in Pharmacology. 2015;6:185.

142. Bachmaier S, Volpato Santos Y, Kramer S, Githure GB, Klöckner T, Pepperl J, et al. Nucleoside analogue activators of cyclic AMP-independent protein kinase A of Trypanosoma. Nat Commun. 2019 Dec;10(1):1421.

143. Shakur Y, de Koning HP, Ke H, Kambayashi J, Seebeck T. Therapeutic Potential of Phosphodiesterase Inhibitors in Parasitic Diseases. Handbook of Experimental Pharmacology. 2011;(204)487-510.

144. de Koning HP, Gould MK, Sterk GJ, Tenor H, Kunz S, Luginbuehl E, et al. Pharmacological validation of Trypanosoma brucei phosphodiesterases as novel drug targets. J Infect Dis. 2012 Jul 15;206(2):229–37.

145. Schoijet AC, Miranda K, Medeiros LCS, de Souza W, Flawiá MM, Torres HN, et al. Defining the role of a FYVE domain in the localization and activity of a cAMP phosphodiesterase implicated in osmoregulation in Trypanosoma cruzi. Molecular Microbiology. 2011;79(1):50–62.

146. Kramer S. Developmental regulation of gene expression in the absence of transcriptional control: The case of kinetoplastids. Molecular and Biochemical Parasitology. 2012 Feb 1;181(2):61–72.

147. Alvar J, Vélez ID, Bern C, Herrero M, Desjeux P, Cano J, et al. Leishmaniasis Worldwide and Global Estimates of Its Incidence. PLoS One. 2012 May 31;7(5):e35671.

148. World Health Organisation (WHO). Leishmaniasis [Internet]. [cited 2022 Apr 11]. Available from: https://www.who.int/news-room/fact-sheets/detail/leishmaniasis

149. Irish A, Whitman JD, Clark EH, Marcus R, Bern C. Updated Estimates and Mapping for Prevalence of Chagas Disease among Adults, United States. Emerg Infect Dis. 2022 Jul;28(7):1313–20.

150. Büscher P, Cecchi G, Jamonneau V, Priotto G. Human African trypanosomiasis. The Lancet. 2017 Nov 25;390(10110):2397–409.

151. World Health Organisation (WHO). Trypanosomiasis, human African (sleeping sickness) [Internet]. [cited 2022 Jan 10]. Available from: https://www.who.int/news-room/fact-sheets/detail/trypanosomiasis-human-african-(sleeping-sickness)

152. Ooi CP, Bastin P. More than meets the eye: understanding Trypanosoma brucei morphology in the tsetse. Front Cell Infect Microbiol. 2013 Nov 13;3:71.

153. Clayton J. Chagas disease 101. Nature. 2010 Jun;465(7301):S4–5.

154. Sunter J, Gull K. Shape, form, function and Leishmania pathogenicity: from textbook descriptions to biological understanding. Open Biology. 7(9):170165.

155. Rojas F, Silvester E, Young J, Milne R, Tettey M, Houston DR, et al. Oligopeptide Signaling through TbGPR89 Drives Trypanosome Quorum Sensing. Cell. 2019 Jan 10;176(1–2):306-317.e16.

156. Pereira SS, Jackson AP, Figueiredo LM. Evolution of the variant surface glycoprotein family in African trypanosomes. Trends in Parasitology. 2022 Jan 1;38(1):23–36.

157. Hurley JH. Structure, Mechanism, and Regulation of Mammalian Adenylyl Cyclase *. Journal of Biological Chemistry. 1999 Mar 19;274(12):7599–602.

158. Durante IM, Butenko A, Rašková V, Charyyeva A, Svobodová M, Yurchenko V, et al. Large-Scale Phylogenetic Analysis of Trypanosomatid Adenylate Cyclases Reveals Associations with Extracellular Lifestyle and Host–Pathogen Interplay. Genome Biol Evol. 2020 Oct 26;12(12):2403–16.

159. Saada EA, Kabututu ZP, Lopez M, Shimogawa MM, Langousis G, Oberholzer M, et al. Insect Stage-Specific Receptor Adenylate Cyclases Are Localized to Distinct Subdomains of the Trypanosoma brucei Flagellar Membrane. Eukaryot Cell. 2014 Aug;13(8):1064–76.

160. Lopez MA, Saada EA, Hill KL. Insect Stage-Specific Adenylate Cyclases Regulate Social Motility in African Trypanosomes. Eukaryot Cell. 2015 Jan;14(1):104–12.

161. Oberholzer M, Lopez MA, McLelland BT, Hill KL. Social Motility in African Trypanosomes. PLOS Pathogens. 2010 Jan 29;6(1):e1000739.

162. Shaw S, Knüsel S, Abbühl D, Naguleswaran A, Etzensperger R, Benninger M, et al. Cyclic AMP signalling and glucose metabolism mediate pH taxis by African trypanosomes. Nat Commun. 2022 Feb 1;13(1):603.

163. Bachmaier S, Giacomelli G, Calvo-Alvarez E, Vieira LR, Van Den Abbeele J, Aristodemou A, et al. A multi-adenylate cyclase regulator at the flagellar tip controls African trypanosome transmission. Nat Commun. 2022 Sep 16;13(1):5445.

164. Oberholzer M, Marti G, Baresic M, Kunz S, Hemphill A, Seebeck T. The Trypanosoma brucei cAMP phosphodiesterases TbrPDEBl and TbrPDEB2: flagellar enzymes that are essential for parasite virulence. The FASEB Journal. 2007;21(3):720–31.

165. Sen Santara S, Roy J, Mukherjee S, Bose M, Saha R, Adak S. Globin-coupled heme containing oxygen sensor soluble adenylate cyclase in Leishmania prevents cell death during hypoxia. Proc Natl Acad Sci U S A. 2013 Oct 15;110(42):16790–5.

166. Kumar M, Das S, Sen A, Abhishek K, Shafi MdT, Bamra T, et al. Oxidant activated soluble adenylate cyclase of Leishmania donovani regulates the cAMP–PKA signaling axis for its intra-macrophage survival during infection. Journal of Cellular Biochemistry. 2021;122(10):1413–27.

167. Sanchez MA, Zeoli D, Klamo EM, Kavanaugh MP, Landfear SM. A Family of Putative Receptor-Adenylate Cyclases from Leishmania donovani. Journal of Biological Chemistry. 1995 Jul 21;270(29):17551–8.

168. Structural analysis of adenylate cyclases from Trypanosoma brucei in their monomeric state. The EMBO Journal. 2001 Feb 1;20(3):433–45.

169. Naula C, Schaub R, Leech V, Melville S, Seebeck T. Spontaneous dimerization and leucine-zipper induced activation of the recombinant catalytic domain of a new adenylyl cyclase of Trypanosoma brucei, GRESAG4.4B. Mol Biochem Parasitol. 2001 Jan 15;112(1):19–28.

170. Voorheis HP, Martin BR. Characteristics of the Calcium-Mediated Mechanism Activating Adenylate Cyclase in Trypanosoma brucei. European Journal of Biochemistry. 1981;116(3):471–7.

171. D'Angelo MA, Montagna AE, Sanguineti S, Torres HN, Flawiá MM. A Novel Calcium-stimulated Adenylyl Cyclase fromTrypanosoma cruzi, Which Interacts with the Structural Flagellar Protein Paraflagellar Rod. Journal of Biological Chemistry. 2002 Sep 20;277(38):35025–34.

172. Voorheis HP, Martin BR. 'Swell dialysis' demonstrates that adenylate cyclase in Trypanosoma brucei is regulated by calcium ions. Eur J Biochem. 1980 Dec;113(1):223-7.

173. Salmon D, Vanwalleghem G, Morias Y, Denoeud J, Krumbholz C, Lhommé F, et al. Adenylate Cyclases of *Trypanosoma brucei* Inhibit the Innate Immune Response of the Host. Science. 2012 Jul 27;337(6093):463–6.

174. Alexandre S, Paindavoine P, Hanocq-Quertier J, Paturiaux-Hanocq F, Tebabi P, Pays E. Families of adenylate cyclase genes in Trypanosoma brucei. Molecular and Biochemical Parasitology. 1996 May 1;77(2):173–82.

175. Gerisch G, Heuser J, Clarke M. Tubular-vesicular transformation in the contractile vacuole system of Dictyostelium. Cell Biol Int. 2002;26(10):845–52.

176. Demmel L, Schmidt K, Lucast L, Havlicek K, Zankel A, Koestler T, et al. The endocytic activity of the flagellar pocket in Trypanosoma brucei is regulated by an adjacent phosphatidylinositol phosphate kinase. J Cell Sci. 2014 May 15;127(10):2351–64.

177. Rohloff P, Docampo R. A contractile vacuole complex is involved in osmoregulation in Trypanosoma cruzi. Exp Parasitol. 2008 Jan;118(1):17–24.

178. Rohloff P, Montalvetti A, Docampo R. Acidocalcisomes and the Contractile Vacuole Complex Are Involved in Osmoregulation in Trypanosoma cruzi. Journal of Biological Chemistry. 2004 Dec 10;279(50):52270–81.

179. Kunz S, Oberholzer M, Seebeck T. A FYVE-containing unusual cyclic nucleotide phosphodiesterase from Trypanosoma cruzi. The FEBS Journal. 2005;272(24):6412–22.

180. Bao Y, Weiss LM, Braunstein VL, Huang H. Role of Protein Kinase A in Trypanosoma cruzi. Infect Immun. 2008 Oct;76(10):4757–63.

181. Johner A, Kunz S, Linder M, Shakur Y, Seebeck T. Cyclic nucleotide specific phosphodiesterases of Leishmania major. BMC Microbiol. 2006 Mar 8;6:25.

182. Wang H, Kunz S, Chen G, Seebeck T, Wan Y, Robinson H, et al. Biological and Structural Characterization of Trypanosoma cruzi Phosphodiesterase C and Implications for Design of Parasite Selective Inhibitors. J Biol Chem. 2012 Apr 6;287(15):11788–97.

183. Wang H, Kunz S, Chen G, Seebeck T, Wan Y, Robinson H, et al. Biological and Structural Characterization of Trypanosoma cruzi Phosphodiesterase C and Implications for Design of Parasite Selective Inhibitors. J Biol Chem. 2012 Apr 6;287(15):11788–97.

184. Blaazer AR, Singh AK, de Heuvel E, Edink E, Orrling KM, Veerman JJN, et al. Targeting a Subpocket in Trypanosoma brucei Phosphodiesterase B1 (TbrPDEB1) Enables the Structure-Based Discovery of Selective Inhibitors with Trypanocidal Activity. J Med Chem. 2018 May 10;61(9):3870–88.

185. Veerman J, van den Bergh T, Orrling KM, Jansen C, Cos P, Maes L, et al. Synthesis and evaluation of analogs of the phenylpyridazinone NPD-001 as potent trypanosomal TbrPDEB1 phosphodiesterase inhibitors and in vitro trypanocidals. Bioorganic & Medicinal Chemistry. 2016 Apr 1;24(7):1573–81.

186. Gould MK, Bachmaier S, Ali JAM, Alsford S, Tagoe DNA, Munday JC, et al. Cyclic AMP effectors in African trypanosomes revealed by genome-scale RNA interference library screening for resistance to the phosphodiesterase inhibitor CpdA. Antimicrob Agents Chemother. 2013 Oct;57(10):4882–93.

187. Dean S, Sunter JD, Wheeler RJ. TrypTag.org: A Trypanosome Genome-wide Protein Localisation Resource. Trends Parasitol. 2017 Feb;33(2):80–2.

188. Suzuki T, Delgado-Escueta AV, Aguan K, Alonso ME, Shi J, Hara Y, et al. Mutations in EFHC1 cause juvenile myoclonic epilepsy. Nat Genet. 2004 Aug;36(8):842–9.

189. Suzuki T, Inoue I, Yamakawa K. Epilepsy protein Efhc1/myoclonin1 is expressed in cells with motile cilia but not in neurons or mitotic apparatuses in brain. Sci Rep. 2020 Dec 16;10(1):22076.

190. Jäger AV, De Gaudenzi JG, Mild JG, Mc Cormack B, Pantano S, Altschuler DL, Edreira MM. Identification of novel cyclic nucleotide binding proteins in Trypanosoma cruzi. Mol Biochem Parasitol. 2014 Dec;198(2):104-12.

191. Gonzales-Perdomo M, Romero P, Goldenberg S. Cyclic AMP and adenylate cyclase activators stimulate Trypanosoma cruzi differentiation. Experimental Parasitology. 1988 Aug 1;66(2):205–12.

192. Rangel-Aldao R, Allende O, Triana F, Piras R, Henriquez D, Piras M. Possible role of cAMP in the differentiation of Trypanosoma cruzi. Molecular and Biochemical Parasitology. 1987 Jan 2;22(1):39–43.

193. Rangel-Aldao R, Triana F, Comach G, Abate T, Fernández V, McMahon-Pratt D. Intracellular signaling transduction in the differentiation of Trypanosoma cruzi: role of cAMP. Arch Biol Med Exp. 1988 Dec;21(3–4):403–8.

194. Garcia ES, Gonzalez MS, de Azambuja P, Baralle FE, Fraidenraich D, Torres HN, et al. Induction of Trypanosoma cruzi metacyclogenesis in the gut of the hematophagous insect vector, Rhodnius prolixus, by hemoglobin and peptides carrying alpha D-globin sequences. Exp Parasitol. 1995 Nov;81(3):255–61.

195. Rose C, Casas-Sánchez A, Dyer NA, Solórzano C, Beckett AJ, Middlehurst B, Marcello M, Haines LR, Lisack J, Engstler M, Lehane MJ, Prior IA, Acosta-Serrano Á. Trypanosoma brucei colonizes the tsetse gut via an immature peritrophic matrix in the proventriculus. Nat Microbiol. 2020 Jul;5(7):909-916.

196. Bhattacharya A, Biswas A, Das PK. Identification of a protein kinase A regulatory subunit from Leishmania having importance in metacyclogenesis through induction of autophagy. Molecular Microbiology. 2012;83(3):548–64.

197. Biswas A, Bhattacharya A, Das PK. Role of cAMP Signaling in the Survival and Infectivity of the Protozoan Parasite, Leishmania donovani. Mol Biol Int. 2011;2011:782971.

198. Genestra M, Cysne-Finkelstein L, Leon L. Protein kinase A activity is associated with metacyclogenesis in Leishmania amazonensis. Cell Biochemistry and Function. 2004;22(5):315–20.

199. Bachmaier S, Witztum R, Tsigankov P, Koren R, Boshart M, Zilberstein D. Protein kinase A signaling during bidirectional axenic differentiation in Leishmania. International Journal for Parasitology. 2016 Feb;46(2):75–82.

200. Mancini PE, Patton CL. Cyclic 3′,5′-adenosine monophosphate levels during the developmental cycle of Trypanosoma brucei brucei in the rat. Molecular and Biochemical Parasitology. 1981 May 1;3(1):19–31.

201. Vassella E, Reuner B, Yutzy B, Boshart M. Differentiation of African trypanosomes is controlled by a density sensing mechanism which signals cell cycle arrest via the cAMP pathway. Journal of Cell Science. 1997 Nov 1;110(21):2661–71.

202. Saldivia M, Ceballos-Pérez G, Bart JM, Navarro M. The AMPKα1 Pathway Positively Regulates the Developmental Transition from Proliferation to Quiescence in Trypanosoma brucei. Cell Rep. 2016 Oct 11;17(3):660–70.

203. Laxman S, Riechers A, Sadilek M, Schwede F, Beavo JA. Hydrolysis products of cAMP analogs cause transformation of Trypanosoma brucei from slender to stumpy-like forms. Proc Natl Acad Sci U S A. 2006 Dec 12;103(50):19194-9.

204. Fischer Weinberger R, Bachmaier S, Dandugudumula R, Phan IQ, Almoznino M, Githure GB, et al. A divergent protein kinase A in the human pathogen *Leishmania* is associated with developmental morphogenesis [Internet]. bioRxiv 2021.04.24.440790; doi: https://doi.org/10.1101/2021.04.24.440790

205. Lefièvre L, Jha KN, Lamirande E de, Visconti PE, Gagnon C. Activation of Protein Kinase A During Human Sperm Capacitation and Acrosome Reaction. Journal of Andrology. 2002;23(5):709–16.

206. Baker N, Catta-Preta CMC, Neish R, Sadlova J, Powell B, Alves-Ferreira EVC, et al. Systematic functional analysis of Leishmania protein kinases identifies regulators of differentiation or survival. Nat Commun. 2021 Feb 23;12(1):1244.

207. Alonso CAI, Osycka-Salut CE, Castellano L, Cesari A, Di Siervi N, Mutto A, et al. Extracellular cAMP activates molecular signalling pathways associated with sperm capacitation in bovines. Molecular Human Reproduction. 2017 Aug 1;23(8):521–34.

208. Roles of cAMP in regulating microtubule sliding and flagellar bending in demembranated hamster spermatozoa. FEBS Letters. 2006 Feb 20;580(5):1515–20.

209. Brokaw CJ, Josslin R, Bobrow L. Calcium ion regulation of flagellar beat symmetry in reactivated sea urchin spermatozoa. Biochemical and Biophysical Research Communications. 1974 Jun 4;58(3):795–800.

210. DiPetrillo CG, Smith EF. Pcdp1 is a central apparatus protein that binds Ca(2+)-calmodulin and regulates ciliary motility. J Cell Biol. 2010 May 3;189(3):601–12.

211. Wei Y, Hu H, Lun ZR, Li Z. Centrin3 in trypanosomes maintains the stability of a flagellar inner-arm dynein for cell motility. Nat Commun. 2014 Jun 3;5:4060.

212. Chassy BM, Love LL, Krichevsky MI. The acrasin activity of 3’,5’-cyclic nucleotides. Proc Natl Acad Sci U S A. 1969 Sep;64(1):296–303.

213. Caza M, Kronstad JW. The cAMP/Protein Kinase a Pathway Regulates Virulence and Adaptation to Host Conditions in *Cryptococcus neoformans*. Front Cell Infect Microbiol. 2019 Jun 18;9:212.

214. Shalaby T, Liniger M, Seebeck T. The regulatory subunit of a cGMP-regulated protein kinase A of Trypanosoma brucei. European Journal of Biochemistry. 2001;268(23):6197–206.

215. Blum M, Chang HY, Chuguransky S, Grego T, Kandasaamy S, Mitchell A, et al. The InterPro protein families and domains database: 20 years on. Nucleic Acids Research. 2021 Jan 8;49(D1):D344–54.

216. Hallgren J, Tsirigos KD, Pedersen MD, Armenteros JJA, Marcatili P, Nielsen H, et al. DeepTMHMM predicts alpha and beta transmembrane proteins using deep neural networks [Internet]. bioRxiv 2022.04.08.487609; doi: https://doi.org/10.1101/2022.04.08.487609

217. Chen YS, Kozlov G, Fakih R, Funato Y, Miki H, Gehring K. The cyclic nucleotide–binding homology domain of the integral membrane protein CNNM mediates dimerization and is required for Mg2+ efflux activity. Journal of Biological Chemistry. 2018 Dec 28;293(52):19998–20007.

218. Salmon D, Bachmaier S, Krumbholz C, Kador M, Gossmann JA, Uzureau P, et al. Cytokinesis of Trypanosoma brucei bloodstream forms depends on expression of adenylyl cyclases of the ESAG4 or ESAG4-like subfamily. Mol Microbiol. 2012 Apr;84(2):225–42.

219. Pastan I, Adhya S. Cyclic adenosine 5'-monophosphate in Escherichia coli. Bacteriol Rev. 1976 Sep;40(3):527–51.

220. Paindavoine P, Rolin S, Assel SV, Geuskens M, Jauniaux JC, Dinsart C, et al. A gene from the variant surface glycoprotein expression site encodes one of several transmembrane adenylate cyclases located on the flagellum of Trypanosoma brucei. 1992;12:8.

221. Beneke T, Madden R, Makin L, Valli J, Sunter J, Gluenz E. A CRISPR Cas9 high-throughput genome editing toolkit for kinetoplastids. R Soc open sci. 2017 May;4(5):170095.

222. Wheeler RJ, Gluenz E, Gull K. The cell cycle of Leishmania: morphogenetic events and their implications for parasite biology. Mol Microbiol. 2011 Feb;79(3):647–62.

223. Beneke T, Banecki K, Fochler S, Gluenz E. LAX28 is required for the stable assembly of the inner dynein arm f complex, and the tether and tether head complex in Leishmania flagella. J Cell Sci. 2020 Jan 23;133(2):jcs239855.

224. Grossman-Haham I, Coudray N, Yu Z, Wang F, Zhang N, Bhabha G, et al. Structure of the radial spoke head and insights into its role in mechanoregulation of ciliary beating. Nat Struct Mol Biol. 2021 Jan;28(1):20–8.

225. Lechtreck KF, Witman GB. Chlamydomonas reinhardtii hydin is a central pair protein required for flagellar motility. J Cell Biol. 2007 Feb 12;176(4):473–82.

226. Bazan R, Schröfel A, Joachimiak E, Poprzeczko M, Pigino G, Wloga D. Ccdc113/Ccdc96 complex, a novel regulator of ciliary beating that connects radial spoke 3 to dynein g and the nexin link. PLOS Genetics. 2021 Mar 4;17(3):e1009388.

227. Edwards BFL, Wheeler RJ, Barker AR, Moreira-Leite FF, Gull K, Sunter JD. Direction of flagellum beat propagation is controlled by proximal/distal outer dynein arm asymmetry. Proc Natl Acad Sci USA. 2018 Jul 31;115(31):E7341–50.

228. Binkowski BF, Fan F, Wood KV. Luminescent biosensors for real-time monitoring of intracellular cAMP. Methods Mol Biol. 2011;756:263-71.

229. Massengill CI, Day-Cooney J, Mao T, Zhong H. Genetically encoded sensors towards imaging cAMP and PKA activity in vivo. Journal of Neuroscience Methods. 2021 Oct 1;362:109298.

230. Cordes TJ, Worzalla GA, Ginster AM, Forest KT. Crystal structure of the Pseudomonas aeruginosa virulence factor regulator. J Bacteriol. 2011 Aug;193(16):4069-74.

231. Luginbuehl E, Ryter D, Schranz-Zumkehr J, Oberholzer M, Kunz S, Seebeck T. The N Terminus of Phosphodiesterase TbrPDEB1 of Trypanosoma brucei Contains the Signal for Integration into the Flagellar Skeleton. Eukaryot Cell. 2010 Oct;9(10):1466–75.

232. Souza W de. Secretory organelles of pathogenic protozoa. An Acad Bras Ciênc. 2006 Jun;78:271–92.

233. Dean S, Moreira-Leite F, Gull K. Basalin is an evolutionarily unconstrained protein revealed via a conserved role in flagellum basal plate function. eLife. 2019 Feb 27;8:e42282.

234. Nalefski EA, Wisner MA, Chen JZ, Sprang SR, Fukuda M, Mikoshiba K, et al. C2 Domains from Different Ca2+ Signaling Pathways Display Functional and Mechanistic Diversity. Biochemistry. 2001 Mar 1;40(10):3089–100.

235. Ma M, Stoyanova M, Rademacher G, Dutcher SK, Brown A, Zhang R. Structure of the Decorated Ciliary Doublet Microtubule. Cell. 2019 Oct;179(4):909-922.e12.

236. Aoki F, Sakai S, Kohmoto K. Regulation of flagellar bending by cAMP and Ca2+ in hamster sperm. Molecular Reproduction and Development. 1999;53(1):77–83.

237. Hyams JS, Borisy GG. Isolated flagellar apparatus of Chlamydomonas: characterization of forward swimming and alteration of waveform and reversal of motion by calcium ions in vitro. J Cell Sci. 1978 Oct;33:235-53.

238. Lodh S, Yano J, Valentine MS, Van Houten JL. Voltage-gated calcium channels of Paramecium cilia. J Exp Biol. 2016 Oct 1;219(Pt 19):3028–38.

239. Hennessey TM, Kim DY, Oberski DJ, Hard R, Rankin SA, Pennock DG. Inner arm dynein 1 is essential for Ca++-dependent ciliary reversals in Tetrahymena thermophila. Cell Motility. 2002;53(4):281–8.

240. Boesger J, Wagner V, Weisheit W, Mittag M. Analysis of Flagellar Phosphoproteins from Chlamydomonas reinhardtii. Eukaryotic Cell. 2009 Jul 1;8(7):922–32.

241. Luconi M, Porazzi I, Ferruzzi P, Marchiani S, Forti G, Baldi E. Tyrosine Phosphorylation of the A Kinase Anchoring Protein 3 (AKAP3) and Soluble Adenylate Cyclase Are Involved in the Increase of Human Sperm Motility by Bicarbonate1. Biology of Reproduction. 2005 Jan 1;72(1):22–32.

242. Turner RMO, Eriksson RLM, Gerton GL, Moss SB. Relationship between sperm motility and the processing and tyrosine phosphorylation of two human sperm fibrous sheath proteins, pro-hAKAP82 and hAKAP82. Molecular Human Reproduction. 1999 Sep 1;5(9):816–24.

243. Naaby-Hansen S, Mandal A, Wolkowicz MJ, Sen B, Westbrook VA, Shetty J, Coonrod SA, Klotz KL, Kim YH, Bush LA, Flickinger CJ, Herr JC. CABYR, a novel calcium-binding tyrosine phosphorylation-regulated fibrous sheath protein involved in capacitation. Dev Biol. 2002 Feb 15;242(2):236-54.

244. Zhang Z, Shen X, Jones BH, Xu B, Herr JC, Strauss JF. Phosphorylation of sperm axoneme central apparatus protein SPAG16L by a testis specific kinase, TSSK2. Biol Reprod. 2008 Jul;79(1):75–83.

245. Boesger J, Wagner V, Weisheit W, Mittag M. Application of Phosphoproteomics to Find Targets of Casein Kinase 1 in the Flagellum of Chlamydomonas. International Journal of Plant Genomics. 2012 Dec 18;2012:e581460.

246. Soriano-Úbeda C, Romero-Aguirregomezcorta J, Matás C, Visconti PE, García-Vázquez FA. Manipulation of bicarbonate concentration in sperm capacitation media improves in vitro fertilisation output in porcine species. Journal of Animal Science and Biotechnology. 2019 Mar 11;10(1):19.

247. Visconti PE. Understanding the molecular basis of sperm capacitation through kinase design. Proc Natl Acad Sci U S A. 2009 Jan 20;106(3):667–8.

248. Wakle M, Khole V. A sperm cytoskeletal protein TSA70 is a novel phosphorylated member of Cenexin/odf2 family. Biochemical and Biophysical Research Communications. 2007 Mar 9;354(2):528–34.

249. Rosales J, Sarker K, Ho N, Broniewska M, Wong P, Cheng M, et al. ODF1 Phosphorylation by Cdk5/p35 Enhances ODF1-OIP1 Interaction. Cell Physiol Biochem. 2007;20(5):311–8.

250. Ardito F, Giuliani M, Perrone D, Troiano G, Muzio LL. The crucial role of protein phosphorylation in cell signaling and its use as targeted therapy (Review). Int J Mol Med. 2017 Aug;40(2):271–80.

251. Anand GS, Hotchko M, Brown SHJ, Ten Eyck LF, Komives EA, Taylor SS. R-subunit Isoform Specificity in Protein Kinase A: Distinct Features of Protein Interfaces in PKA

Types I and II by Amide H/2H exchange Mass Spectrometry. J Mol Biol. 2007 Nov 23;374(2):487–99.

252. Scott JD, Fischer EH, Demaille JG, Krebs EG. Identification of an Inhibitory Region of the Heat-Stable Protein Inhibitor of the cAMP-Dependent Protein Kinase. Proceedings of the National Academy of Sciences of the United States of America. 1985;82(13):4379–83.

253. Poteet-Smith CE, Shabb JB, Francis SH, Corbin JD. Identification of Critical Determinants for Autoinhibition in the Pseudosubstrate Region of Type Iα cAMP-dependent Protein Kinase. Journal of Biological Chemistry. 1997 Jan;272(1):379–88.

254. Torres-Quesada O, Mayrhofer JE, Stefan E. The many faces of compartmentalized PKA signalosomes. Cell Signal. 2017 Sep;37:1-11.

255. Carr DW, Stofko-Hahn RE, Fraser ID, Bishop SM, Acott TS, Brennan RG, Scott JD. Interaction of the regulatory subunit (RII) of cAMP-dependent protein kinase with RII-anchoring proteins occurs through an amphipathic helix binding motif. J Biol Chem. 1991 Aug 5;266(22):14188-92.

256. Banky P, Huang LJ, Taylor SS. Dimerization/docking domain of the type Ialpha regulatory subunit of cAMP-dependent protein kinase. Requirements for dimerization and docking are distinct but overlapping. J Biol Chem. 1998 Dec 25;273(52):35048–55.

257. Gaillard AR, Diener DR, Rosenbaum JL, Sale WS. Flagellar Radial Spoke Protein 3 Is an a-Kinase Anchoring Protein (Akap). Journal of Cell Biology. 2001 Apr 16;153(2):443–8.

258. Bandje K, Naissant B, Bigey P, Lohezic M, Vayssières M, Blaud M, et al. Characterization of an A-kinase anchoring protein-like suggests an alternative way of PKA anchoring in Plasmodium falciparum. Malar J. 2016 Dec;15(1):248.

259. Kobe B, Kajava AV. The leucine-rich repeat as a protein recognition motif. Curr Opin Struct Biol. 2001 Dec;11(6):725-32.

260. Siman-Tov MM, Aly R, Shapira M, Jaffe CL. Cloning from Leishmania major of a developmentally regulated gene, c-lpk2, for the catalytic subunit of the cAMP-dependent protein kinase. Mol Biochem Parasitol. 1996 May;77(2):201-15.

261. Baker N, Catta-Preta CMC, Neish R, Sadlova J, Powell B, Alves-Ferreira EVC, Geoghegan V, Carnielli JBT, Newling K, Hughes C, Vojtkova B, Anand J, Mihut A, Walrad PB, Wilson LG, Pitchford JW, Volf P, Mottram JC. Systematic functional analysis of Leishmania protein kinases identifies regulators of differentiation or survival. Nat Commun. 2021 Feb 23;12(1):1244.

262. Oberholzer M, Langousis G, Nguyen H, Saada E, Shimogawa M, Jónsson Z, et al. Independent Analysis of the Flagellum Surface and Matrix Proteomes Provides Insight into Flagellum Signaling in Mammalian-infectious Trypanosoma brucei. Molecular & cellular proteomics : MCP. 2011 Jun 19;10:M111.010538.

263. Tsigankov P, Gherardini PF, Helmer-Citterich M, Späth GF, Myler PJ, Zilberstein D. Regulation Dynamics of Leishmania Differentiation: Deconvoluting Signals and Identifying Phosphorylation Trends. Mol Cell Proteomics. 2014 Jul;13(7):1787–99.

264. Peng M, Aye TT, Snel B, van Breukelen B, Scholten A, Heck AJR. Spatial Organization in Protein Kinase A Signaling Emerged at the Base of Animal Evolution. J Proteome Res. 2015 Jul 2;14(7):2976–87.

265. Etchebehere LC, Bemmelen MXPV, Anjard C, Traincard F, Assemat K, Reymond C, et al. The Catalytic Subunit of Dictyostelium cAMP-Dependent Protein Kinase. European Journal of Biochemistry. 1997;248(3):820–6.

266. Chan TO, Armen RS, Yadav S, Shah S, Zhang J, Tiegs BC, et al. A tripartite cooperative mechanism confers resistance of the protein kinase A catalytic subunit to dephosphorylation. Journal of Biological Chemistry. 2020 Mar;295(10):3316–29.

267. Steinberg RA, Cauthron RD, Symcox MM, Shuntoh H. Autoactivation of catalytic (C alpha) subunit of cyclic AMP-dependent protein kinase by phosphorylation of threonine 197. Mol Cell Biol. 1993 Apr;13(4):2332-41.

268. Steichen JM, Kuchinskas M, Keshwani MM, Yang J, Adams JA, Taylor SS. Structural Basis for the Regulation of Protein Kinase A by Activation Loop Phosphorylation. J Biol Chem. 2012 Apr 27;287(18):14672–80.

269. Yang C, Yang P. The Flagellar Motility of Chlamydomonas pf25 Mutant Lacking an AKAP-binding Protein Is Overtly Sensitive to Medium Conditions. Mol Biol Cell. 2006 Jan;17(1):227–38.

270. Pigino G, Ishikawa T. Axonemal radial spokes. Bioarchitecture. 2012 Feb 1;2(2):50–8.

271. Boitz JM, Ullman B, Jardim A, Carter NS. Purine salvage in Leishmania: complex or simple by design? Trends Parasitol. 2012 Aug;28(8):345–52.

272. Leigh MW, Horani A, Kinghorn B, O'Connor MG, Zariwala MA, Knowles MR. Primary ciliary dyskinesia (PCD): A genetic disorder of motile cilia. Translational Science of Rare Diseases. 2019 Jan 1;4(1–2):51–75.

273. Lucas JS, Burgess A, Mitchison HM, Moya E, Williamson M, Hogg C. Diagnosis and management of primary ciliary dyskinesia. Archives of Disease in Childhood. 2014 Sep 1;99(9):850–6.

274. Zariwala MA, Knowles MR, Leigh MW. Primary Ciliary Dyskinesia. In: Adam MP, Ardinger HH, Pagon RA, Wallace SE, Bean LJ, Gripp KW, et al., editors. GeneReviews® [Internet]. Seattle (WA): University of Washington, Seattle; 1993 [cited 2022 Feb 12]. Available from: http://www.ncbi.nlm.nih.gov/books/NBK1122/

275. Mitchison HM, Schmidts M, Loges NT, Freshour J, Dritsoula A, Hirst RA, et al. Mutations in axonemal dynein assembly factor DNAAF3 cause primary ciliary dyskinesia. Nat Genet. 2012 Mar 4;44(4):381-S2.

276. Raidt J, Wallmeier J, Hjeij R, Onnebrink JG, Pennekamp P, Loges NT, et al. Ciliary beat pattern and frequency in genetic variants of primary ciliary dyskinesia. European Respiratory Journal. 2014 Dec 1;44(6):1579–88.

277. Ludmann SA, Schwandt A, Konc X, Bricker CS, Pennock DG. Biochemical Analysis of a Mutant Tetrahymena Lacking Outer Dynein Arms. Journal of Eukaryotic Microbiology. 1993;40(5):650–60.

278. Gibbons BH, Baccetti B, Gibbons IR. Live and reactivated motility in the 9+0 flagellum of Anguilla sperm. Cell Motil. 1985;5(4):333–50.

279. Tam LW, Lefebvre PA. The Chlamydomonas MBO2 locus encodes a conserved coiled-coil protein important for flagellar waveform conversion. Cell Motility. 2002;51(4):197–212.

280. Adhiambo C, Forney JD, Asai DJ, LeBowitz JH. The two cytoplasmic dynein-2 isoforms in Leishmania mexicana perform separate functions. Mol Biochem Parasitol. 2005 Oct;143(2):216-25.

281. COBALT:Multiple Alignment Tool [Internet]. [cited 2022 Feb 21]. Available from: https://www.ncbi.nlm.nih.gov/tools/cobalt/re_cobalt.cgi

282. Hom EFY, Witman GB, Harris EH, Dutcher SK, Kamiya R, Mitchell DR, et al. A Unified Taxonomy for Ciliary Dyneins. Cytoskeleton (Hoboken). 2011 Oct;68(10):555–65.

283. Braschi B, Omran H, Witman GB, Pazour GJ, Pfister KK, Bruford EA, et al. Consensus nomenclature for dyneins and associated assembly factors. Journal of Cell Biology. 2022 Jan 10;221(2):e202109014.

284. Papadopoulos JS, Agarwala R. COBALT: constraint-based alignment tool for multiple protein sequences. Bioinformatics. 2007 May 1;23(9):1073–9.

285. Letunic I, Bork P. Interactive Tree Of Life (iTOL) v5: an online tool for phylogenetic tree display and annotation. Nucleic Acids Research. 2021 Jul 2;49(W1):W293–6.

286. Gray J. The Movement of Sea-Urchin Spermatozoa. Journal of Experimental Biology. 1955 Dec 1;32(4):775–801.

287. Sartori P, Geyer VF, Scholich A, Jülicher F, Howard J. Dynamic curvature regulation accounts for the symmetric and asymmetric beats of Chlamydomonas flagella. Goldstein RE, editor. eLife. 2016 May 11;5:e13258.

288. Segal RA, Huang B, Ramanis Z, Luck DJ. Mutant strains of Chlamydomonas reinhardtii that move backwards only. J Cell Biol. 1984 Jun;98(6):2026-34.

289. Lin J, Tritschler D, Song K, Barber CF, Cobb JS, Porter ME, et al. Building blocks of the nexin-dynein regulatory complex in Chlamydomonas flagella. J Biol Chem. 2011 Aug 19;286(33):29175–91.

290. Bayly PV, Lewis BL, Kemp PS, Pless RB, Dutcher SK. Efficient Spatiotemporal Analysis of the Flagellar Waveform of Chlamydomonas reinhardtii. Cytoskeleton (Hoboken). 2010 Jan;67(1):56–69.

291. Luck D, Piperno G, Ramanis Z, Huang B. Flagellar mutants of Chlamydomonas: Studies of radial spoke-defective strains by dikaryon and revertant analysis. Proceedings of the National Academy of Sciences. 1977 Aug;74(8):3456–60.

292. Toda A, Nishikawa Y, Tanaka H, Yagi T, Kurisu G. The complex of outer-arm dynein light chain-1 and the microtubule-binding domain of the γ heavy chain shows how axonemal dynein tunes ciliary beating. J Biol Chem. 2020 Mar 20;295(12):3982–9.

293. Dutcher SK, Huang B, Luck DJ. Genetic dissection of the central pair microtubules of the flagella of Chlamydomonas reinhardtii. J Cell Biol. 1984 Jan;98(1):229–36.

294. Smith EF, Lefebvre PA. PF16 encodes a protein with armadillo repeats and localizes to a single microtubule of the central apparatus in Chlamydomonas flagella. J Cell Biol. 1996 Feb;132(3):359–70.

295. Sakakibara H, Takada S, King SM, Witman GB, Kamiya R. A Chlamydomonas outer arm dynein mutant with a truncated beta heavy chain. J Cell Biol. 1993 Aug;122(3):653-61

296. Sakakibara H, Mitchell DR, Kamiya R. A Chlamydomonas outer arm dynein mutant missing the alpha heavy chain. J Cell Biol. 1991 May;113(3):615-22.

297. Liu Z, Takazaki H, Nakazawa Y, Sakato M, Yagi T, Yasunaga T, et al. Partially Functional Outer-Arm Dynein in a Novel Chlamydomonas Mutant Expressing a Truncated γ Heavy Chain. Eukaryot Cell. 2008 Jul;7(7):1136–45.

298. Guerra C, Wada Y, Leick V, Bell A, Satir P. Cloning, localization, and axonemal function of Tetrahymena centrin. Mol Biol Cell. 2003 Jan;14(1):251–61.

299. Silflow CD, LaVoie M, Tam LW, Tousey S, Sanders M, Wu W chien, et al. The Vfl1 Protein in Chlamydomonas Localizes in a Rotationally Asymmetric Pattern at the Distal Ends of the Basal Bodies. J Cell Biol. 2001 Apr 2;153(1):63–74.

300. Sievers F, Wilm A, Dineen D, Gibson TJ, Karplus K, Li W, et al. Fast, scalable generation of high-quality protein multiple sequence alignments using Clustal Omega. Mol Syst Biol. 2011 Oct 11;7:539.

301. Kõressaar T, Lepamets M, Kaplinski L, Raime K, Andreson R, Remm M. Primer3_masker: integrating masking of template sequence with primer design software. Bioinformatics. 2018 Jun 1;34(11):1937–8.

302. Collins TJ. ImageJ for microscopy. BioTechniques. 2007 Jul;43(1S):S25–30.

303. Schindelin J, Arganda-Carreras I, Frise E, Kaynig V, Longair M, Pietzsch T, et al. Fiji: an open-source platform for biological-image analysis. Nature Methods. 2012 Jul;9(7):676–82.

304. Amos B, Aurrecoechea C, Barba M, Barreto A, Basenko EY, Bażant W, et al. VEuPathDB: the eukaryotic pathogen, vector and host bioinformatics resource center. Nucleic Acids Research. 2022 Jan 7;50(D1):D898–911.

305. Clark K, Karsch-Mizrachi I, Lipman DJ, Ostell J, Sayers EW. GenBank. Nucleic Acids Res. 2016 Jan 4;44:D67–72.

306. Wang Y, Wang Q, Huang H, Huang W, Chen Y, McGarvey PB, et al. A crowdsourcing open platform for literature curation in UniProt. PLOS Biology. 2021 Dec 6;19(12):e3001464.

307. Waterhouse A, Bertoni M, Bienert S, Studer G, Tauriello G, Gumienny R, et al. SWISS-MODEL: homology modelling of protein structures and complexes. Nucleic Acids Research. 2018 Jul 2;46:W296–303.

308. Studer G, Rempfer C, Waterhouse AM, Gumienny R, Haas J, Schwede T. QMEANDisCo-distance constraints applied on model quality estimation. Bioinformatics. 2020 Mar 1;36(6):1765–71.

309. Grosdidier A, Zoete V, Michielin O. SwissDock, a protein-small molecule docking web service based on EADock DSS. Nucleic Acids Res. 2011 Jul;39:W270-277.

310. Grosdidier A, Zoete V, Michielin O. Fast docking using the CHARMM force field with EADock DSS. J Comput Chem. 2011 Jul 30;32(10):2149–59.